# Conceptual Design of the $\bar{\text{P}}$ANDA Luminosity Monitor and Reconstruction Strategy to Measure the Width of the $X(3872)$ State

Dissertation zur Erlangung
des Grades eines Doktors der Naturwissenschaften
in der Fakultät für Physik und Astronomie
der Ruhr-Universität Bochum

von


Tsitohaina H. Randriamalala
aus
Antananarivo - Madagaskar


Bochum 2011

**Versicherung gemäß 7 Abs. 2 Nr. 5 Promo 1987**
Hiermit versichere ich, dass ich meine Dissertation selbstständig angefertigt und verfasst und keine anderen als die angegebenen Hilfsmittel und Hilfen benutzt habe. Meine Dissertation habe ich in dieser oder ähnlicher Form noch bei keiner anderen Fakultät der Ruhr-Universität Bochum oder bei einer anderen Hochschule eingereicht.

1. Gutachter: Prof. James Ritman
2. Gutachter: Prof. Ulrich Wiedner
Tag der Disputation: 19.04.2012

***To the memory of my mother***

# Contents

# Abstract


The $\bar{\text{P}}$ANDA experiment has a great potential to test QCD in the low momentum transfer region with unprecedented accuracy by performing very precise hadron spectroscopy. To achieve this goal the resonance scan method will be used to determine the mass and width of variety of hadronic states. This technique requires a precise knowledge of the luminosity. This thesis develops the conceptual design of the detector allowing to measure the absolute luminosity with about 3% precision.

The detector concept is based on the measurement of elastically scattered antiprotons from the interaction region in the Coulomb-nuclear interference region. Due to the finite beam emittance and the finite size of the interaction volume, the track of the antiproton has to be reconstructed in the luminosity monitor, and not just one point. The detector will located between $z = +10\,m$ and $z = +13\,m$ downstream of the interaction point and will consist of four planes of four sensors each covering the polar angular range of $2.8 \leq \theta \leq 7.5\,mrad$.

The performance study of this detector is one of the main topics of this thesis. These studies were done using Monte Carlo simulations within the PandaRoot framework and the results were compared with the measured data obtained from the tracking station beam test performed at COSY with proton beams.

This work then addressed the question of how the performance of the luminosity monitor effects the determination of the mass and width measurements of $X(3872)$ state using the full $\bar{\text{P}}$ANDA setup. The measurements were performed for three different assumed widths. The influences of the signal to background ratio and the uncertainty on the luminosity were investigated.

This thesis is structured as follows:

- **Chapter 1** concerns the physics motivation in which an overview of the Standard Model as well as a discussion of previous measurements and the theoretical interpretations of the $X(3872)$ state are given,
- **Chapter 2** summarizes the general aspects of the FAIR facility, the HESR accelerator and the $\bar{\text{P}}$ANDA experiment,
- **Chapter 3** describes the conceptual design of the $\bar{\text{P}}$ANDA luminosity monitor and the technique of resonance scan,
- **Chapter 4** develops the implementation of the luminosity telescope inside the PandaRoot framework and simulations of the luminosity measurement,
- **Chapter 5** reports the results from the tracking station beam test,
- **Chapter 6** treats the reconstruction strategy of the mass and the width of the $X(3872)$ state,
- **Chapter 7** concludes the main points given in this thesis.

Chapter 1

# Motivation

This chapter introduces the physics motivation of the present thesis. The first part describes the basic aspect of particle physics in the context of the Standard Model. In the second part, the current status of the experimental measurements and theoretical interpretations for the charmonium-like $X(3872)$ will be overviewed.

## 1.1 The Standard Model

In particle physics, the fundamental interaction between elementary particles, is described by a quantum field theory based framework called the *Standard Model* (SM). In the SM, the elementary particles are classified in two categories: fermions, particles of spin 1/2 and bosons with spin 1. The fermions include quarks and leptons, and their respective antiparticles. Other main properties of fermions are given in Table 1.1.

The theoretical description of the interaction is based on the principle of gauge symmetry: particles interact by the exchange of gauge bosons. There are four types of fundamental interactions but only three of them are included in the SM, namely the electromagnetic, weak and strong interactions. A theory of gravity is not a part of the SM due to the very small strength of the force and the spin 2 of the graviton, the mediator particle (not observed yet), thus implies a different mathematical formulation of the interaction. In the electromagnetic interaction, charged particles interact by exchanging photons ($\gamma$), which are neutral and massless bosons. The weak interaction is mediated by 3 massive bosons $W^{\pm}$ and $Z^0$ with masses of about 80 and 91 $GeV/c^2$, respectively [N+10]. These two types of interactions are unified within the *electroweak* theory. In this theory, the mass difference between these bosons and the photon implies the existence of the massive bosons with spin 0, the *Higgs* bosons. It was not yet observed experimentally but is the cornerstone of the large effort at the CERN-LHC. The lower limit of its mass is 114.4 $GeV/c^2$ with 95% confidence level [N+10].

The strong interaction, which concerns only the quarks, is associated with the exchange of gluons, g. There are 8 gluons, all massless and electrically neutral. The theoretical framework describing the interaction between quarks via the strong force is known as *Quantum Chromodynamics* (QCD) in which an additional quantum number, the so-called *color charge*, is assigned to quarks and gluons. There are 3 types of color charges, usually labeled by red, blue and green and their corresponding anticolors. A particular aspect of QCD is that gluons carry also color, thus can interact between themselves leading to a formation of gluonic flux tubes connecting quarks. This self-coupling of the color of gluons increases the color charge between interacting quarks and thus strengthens the force. It increases with the distance separating quarks. At a large-distance scale ($\sim 1\,fm$), quark-antiquark pairs are created which group to neutralize color forming *hadrons*. This phenomenological explanation of the non-observation of free state of quarks refers to *confinement*. There are many ways

| Name | Symbol | Charge [$e$] | Mass [$MeV/c^2$] | $L$ | $B$ |
|---|---|---|---|---|---|
| electron | $e$ | -1 | 0.511 | 1 | 0 |
| electron-neutrino | $\nu_e$ | 0 | $< 2.2 \times 10^{-6}$ | 1 | 0 |
| up | $u$ | 2/3 | $1.7 - 3.3$ | 0 | 1/3 |
| down | $d$ | -1/3 | $4.1 - 5.8$ | 0 | 1/3 |
| muon | $\mu$ | -1 | 105.65 | 1 | 0 |
| muon-neutrino | $\nu_\mu$ | 0 | $< 0.17$ | 1 | 0 |
| strange | $s$ | -1/3 | 101 | 0 | 1/3 |
| charm | $c$ | 2/3 | $1.27 \times 10^3$ | 0 | 1/3 |
| tau | $\tau$ | -1 | $1.77 \times 10^3$ | 1 | 0 |
| tau-neutrino | $\nu_\tau$ | 0 | $< 15.5$ | 1 | 0 |
| bottom | $b$ | -1/3 | $4.19 \times 10^3$ | 0 | 1/3 |
| top | $t$ | 2/3 | $172 \times 10^3$ | 0 | 1/3 |

**Table 1.1**: List of fermions and their basic properties [N+10]. The symbols $L$ and $B$ are the leptonic and baryonic numbers, respectively, indicating if a fermion is either a lepton ($L = 1$) or quark ($B = 1/3$). Fermions are classified into three families which are separated by the horizontal lines.

for nature to realize color neutral hadrons but only systems composed of a quark and an antiquark ($q\bar{q}$), called a *meson*, or 3 quarks of different colors ($qqq$), called a *baryon*, have been clearly identified. At short-distance, the effective coupling of the interaction becomes weaker. Therefore, quarks can be seen as free particles inside hadrons. This corresponds to *asymptotic freedom*, a property of quarks where QCD can be treated using the perturbation method. The strong coupling constant, $\alpha_s$, varies then as a function of the distance between interacting quarks or the momentum transfer $q^2$. This variation is illustrated in Figure 1.1. In this figure, the blue band delimits the perturbative region from the non-perturbative region of QCD. The description of phenomena in the non-perturbative region of QCD involves other theoretical approaches such as lattice QCD (LQCD) and effective field theory (EFT).

The properties of some recently discovered hadronic states such as $X$, $Y$ and $Z$ states are however hardly consistent with the quark model. Other models such as hybrid charmonium or molecular states were proposed. This thesis is focused on the $X(3872)$ meson. In the following section, the measured properties and some theoretical speculation on the nature of the $X(3872)$ state will be overviewed.

## 1.2 The $X(3872)$ state

In 2003, the Belle collaboration [C+03] reported the observation of a charmonium-like state, the $X(3872)$ meson, in the exclusive $B^\pm \to K^\pm J/\psi\pi^+\pi^-$ decays. The mass of the reconstructed final state from the $\pi^+\pi^- J/\psi$ final state was determined to be $3872 \pm 0.55(stat) \pm 0.5(syst)\, MeV/c^2$ and its width is less than $2.3\, MeV/c^2$ at the 90% confidence level.

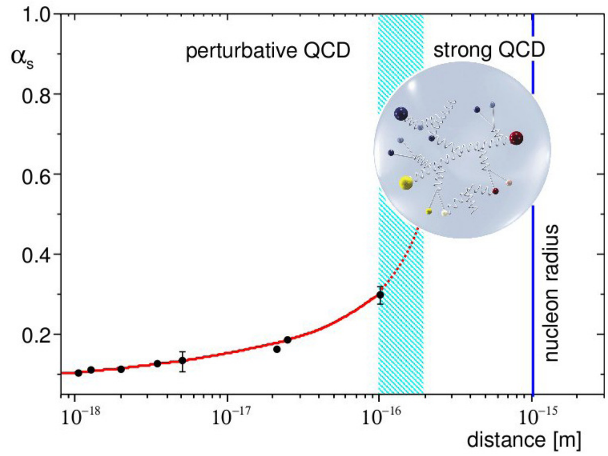


**Figure 1.1**: Variation of the coupling constant of the strong interaction as a function of the distance (red line). Points are data from [N+10]. Picture taken from [pC09b].

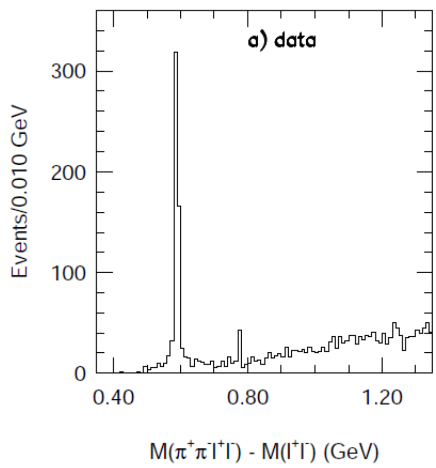


**Figure 1.2**: Discovery of the $X(3872)$ meson in $B \to K\pi^+\pi^- J/\psi$ decays by Belle collaboration. The narrow small peak at about 0.775 $GeV$ corresponds to the $X(3872)$ resonance decaying to $\pi^+\pi^- J/\psi$. Picture taken from [C+03].

Figure 1.2 shows the distribution of the $\pi^+\pi^- e^+ e^-$ invariant mass minus the $e^+e^-$ mass in which the $X(3872)$ meson was discovered. Two significant peaks can be distinguished in the plot. The larger peak at $0.589\,GeV$ corresponds to the $\psi(2S)$ state while the smaller one at $0.775\,GeV$ is the $X(3872)$ state.

The existence of the $X(3872)$ meson state was confirmed by the CDF [A+04b] and D0 [A+04a] collaborations in 2004 in proton-antiproton collisions, and by the BaBar collaboration in 2005 [A+05c] in $B^\pm$ decays to the $\pi^+\pi^- J/\psi$ final state.

In addition to the discovery decay mode, the $X(3872)$ meson has been observed via many other final states which will be quoted next. However, despite the many experimental observations and effort spent in theoretical calculations to identify its properties, the actual nature of the $X(3872)$ state remains unclear. A brief summary of the experimental and theoretical investigations will be given in the following subsections.

### 1.2.1 Overview of experimental results

Several measurements of the $X(3872)$ meson mass have been performed. Different values are obtained depending on the experimental setup and the final state to which the $X(3872)$ is decaying to. The most precise measurement of the $X(3872)$ mass was performed by CDFII in the $X(3872) \to J/\psi\pi^+\pi^-$ decay channel where the obtained value was $3871.61 \pm 0.61(stat) \pm 0.19(syst)\, MeV/c^2$ [A+09a]. The world average mass value of the $X(3872)$, calculated from the recent results from Belle, CDFII, BaBar and D0 collaborations in the $\pi^+\pi^-J/\psi$ decay mode is [N+10]

$$M_X = 3871.56 \pm 0.22\, MeV/c^2. \tag{1.1}$$

Currently, only an upper limit for the total width of $2.3\, MeV/c^2$ at the 90% confidence level exists [C+03]. This corresponds to the Belle detector resolution. Subsequent measurements, with the same decay mode or with other decay modes did not improve the knowledge of the width.

The charge conjugation parity is determined to be $C = +1$ by the observed $X(3872)$ decays to $\gamma J/\psi$ [A+05b] and to $\pi^0\pi^+\pi^-J/\psi$ [A+05b, dAS+10]. The tripion system in the latter decay mode results from the decay of a virtual $\omega$ meson with a relative branching ratio of:

$$\frac{\mathcal{B}(X \to \gamma J/\psi)}{\mathcal{B}(X \to \pi^+\pi^-J/\psi)} = 0.14 \pm 0.05\,, \tag{1.2}$$

$$\frac{\mathcal{B}(X \to \pi^+\pi^-\pi^0 J/\psi)}{\mathcal{B}(X \to \pi^+\pi^-J/\psi)} = \begin{cases} 1.0 \pm 0.4 \pm 0.3 & \text{[A+05b]}\,, \\ 0.8 \pm 0.3 & \text{[dAS+10]}, \end{cases} \tag{1.3}$$

respectively. The Belle final state measurement in the $X(3872) \to J/\psi\pi^+\pi^-$ decay mode suggests that the dipion system is dominated by an intermediate $\rho^0$ resonance [C+03]. The analysis of the angular correlation [A+05a] and on the dipion mass spectrum [A+06] in the same decay mode favor the $J^{PC} = 1^{++}$ or $2^{-+}$ assignments of the $X(3872)$ quantum numbers. The relation (1.3) reflects isospin violation in $X(3872)$ decays.

Decays to $\gamma\psi(2S)$ [A+09b] and $D^0\bar{D}^0\pi^0$ [G+06] were also seen for the $X(3872)$ meson in the $B$ meson decays by the Belle collaboration. The measured branching ratios are

$$\frac{\mathcal{B}(X \to \gamma\psi(2S))}{\mathcal{B}(X \to \gamma J/\psi)} = 3.4 \pm 1.4\,, \tag{1.4}$$

$$\frac{\mathcal{B}(X \to D^0\bar{D}^0\pi^0)}{\mathcal{B}(X \to \pi^+\pi^-J/\psi)} = 8.8^{+3.1}_{-3.6}\,. \tag{1.5}$$

The BaBar collaboration also attributed the observed enhancement near the $D^0\bar{D}^{*0}$ threshold in the $B$ decays to the $X(3872)$ resonance [A+08b]. The measurement in neutral and charged channels lead to the branching ratios of

$$\mathcal{B}(B^0 \to XK^0)\mathcal{B}(X \to D^0\bar{D}^{*0}) = (2.22 \pm 1.05 \pm 0.42) \times 10^{-4}\,, \tag{1.6}$$

$$\mathcal{B}(B^+ \to XK^+)\mathcal{B}(X \to D^0\bar{D}^{*0}) = (1.67 \pm 0.36 \pm 0.47) \times 10^{-4}\,. \tag{1.7}$$

| Decay Channel | Collab. Ref. | Mass [$MeV/c^2$] | Width [$MeV/c^2$] |
|---|---|---|---|
| $B \to J/\psi\pi^+\pi^- K$ | Belle [C+03] | $3872.0 \pm 0.55 \pm 0.5$ | $< 2.3$ |
| $p\bar{p} \to J/\psi\pi^+\pi^- X$ | CDF [A+04b] | $3871.3 \pm 0.7 \pm 0.4$ | resolution |
| $p\bar{p} \to J/\psi\pi^+\pi^- X$ | D0 [A+04a] | $3871.0 \pm 3.1 \pm 3.0$ | resolution |
| $B \to J/\psi\pi^+\pi^- K$ | BaBar [A+05c] | $3873.4 \pm 1.4$ | – |
| $B^+ \to J/\psi\pi^+\pi^- K^+$ | BaBar [A+08a] | $3871.4 \pm 0.55 \pm 0.1$ | $< 3.3$ |
| $B^0 \to J/\psi\pi^+\pi^- K^0_S$ | BaBar [A+08a] | $3868.7 \pm 1.5 \pm 0.4$ | $< 3.3$ |
| $p\bar{p} \to J/\psi\pi^+\pi^- X$ | CDF [A+09a] | $3871.61 \pm 0.16 \pm 0.19$ | – |
| $B \to \omega J/\psi K$ | Belle [A+05b] | – | – |
| $B \to \omega J/\psi K$ | BaBar [dAS+10] | – | – |
| $B \to \gamma J/\psi K$ | Belle [A+05b] | – | – |
| $B \to \gamma\psi(2S) K$ | BaBar [A+09b] | – | – |
| $B \to D^0\bar{D}^0\pi^0 K$ | Belle [G+06] | $3875.2 \pm 0.7 \pm 0.8$ | $5.7 \pm 1.3$ |
| $B \to \bar{D}^{*0} D^0 K$ | BaBar [A+08a] | $3875.1^{+0.7}_{-0.5} \pm 0.4$ | $3.0^{+1.9}_{-1.4} \pm 0.9$ |

**Table 1.2**: Overview of the experimental observations and measurements of the $X(3872)$ meson. Here, $X$ refers to an unmeasured state.

in which the $\bar{D}^{*0}$ in the final state can decay into either $\bar{D}^0\gamma$ or $\bar{D}^0\pi^0$ with a relative branching ratio of

$$\frac{\mathcal{B}(X \to D^0\bar{D}^0\pi^0)}{\mathcal{B}(X \to D^0\bar{D}^0\gamma)} = 1.37 \pm 0.56\,. \tag{1.8}$$

In these decay modes, a mass of around 3875 $MeV/c^2$ was measured. Table 1.2 gives a summary of the observed $X(3872)$ meson decay channels and the corresponding mass and width measurements.

### 1.2.2 Overview of theoretical interpretations

As it can be drawn from the previous section, the experimental results are not sufficient to allow an identification of the $X(3872)$ state. Several theoretical models were developed in order to describe the structure of the $X(3872)$ meson. An overview of some of these models is given below.

#### Charmonium state

It was suggested that the $X(3872)$ meson could be a conventional charmonium state, since its final state contains $c\bar{c}$. The measured $X(3872)$ mass, as given by Table 1.2, lies between the predicted masses of the conventional $1D$ and $2P$ charmonium states. Referring to the $J^{PC}$ quantum number, the $X(3872)$ meson can only be assigned to the $2^3P_1$ (or the first radially excited state of the conventional $\chi_{c1}$ charmonium state) and the $1^1D_2$ states where their quantum numbers are $1^{++}$ and $2^{-+}$, respectively. The theoretical mass ranges were estimated to be $3929 - 3990$ $MeV/c^2$ for the the $2^3P_1$ state and $3765 - 3872$ $MeV/c^2$ for the $1^1D_2$ state. These states were also expected to decay with total widths of about 1.72 $MeV/c^2$ and 0.86 $MeV/c^2$, respectively [BG03].

Investigations on the $E1$ radiative decays of the $X(3872)$ meson, assuming it to be $\chi_{c1}(2P)$, was investigated and described in [WW11]. A numerical result on the ratio of the branching

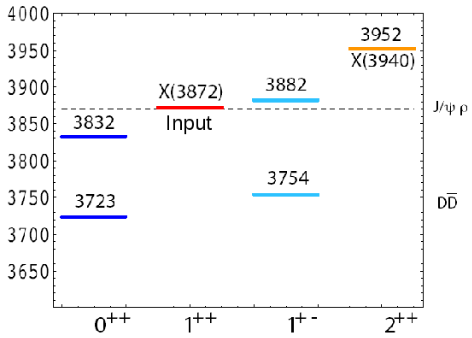


**Figure 1.3**: Spectrum of the $X$ states interpreted as diquark-antidiquark states. Picture taken from [M+05].

ratios $\mathcal{B}(X \to \gamma\psi(2S))/\mathcal{B}(X \to \gamma J/\psi) = 4.4$ was reported. This result is in good agreement with the BaBar measurement given above.

### Hybrid charmonium state

A hybrid charmonium state is a $c\bar{c}$ system with valence gluons, i.e $c\bar{c}$g. In this model, the two pions in the $\pi^+\pi^- J/\psi$ final state are from a two gluon intermediate state, i.e. the decay chain is $X(3872) \to J/\psi$gg, gg $\to \pi^+\pi^-$ with which the decay width is expected to be narrow on the order of the existing upper limit [Li05]. The lightest hybrid charmonium states are expected to have masses of about 4.1 to 4.2 $GeV/c^2$ [PPE10]. Calculations within the so-called *flux tube model* predict the existence of hybrid states with $J^{PC}$ quantum numbers of $1^{++}$ and $2^{-+}$ [GO08].

### Diquark-antidiquark state

A tetraquark model treats the $X(3872)$ meson as a diquark-antidiquark system [M+05], $[cq][\bar{c}\bar{q}]$ where $q = \{u, d\}$. Therefore, it predicts the existence of two neutral $X(3872)$ meson states and their two charged partner states defined as

$$X_u = [cu][\bar{c}\bar{u}] \qquad X_d = [cd][\bar{c}\bar{d}]\,, \tag{1.9}$$

$$X^+ = [cu][\bar{c}\bar{d}] \qquad X^- = [cd][\bar{c}\bar{u}]\,. \tag{1.10}$$

The two neutral states are both produced from $B$ decays but then decay differently as the $X_d$ state decays to $\pi^+\pi^- J/\psi$ and the $X_u$ to $D^0\bar{D}^0\pi^0$ [MPR07]. The measured masses of the $X(3872)$ meson via the two decay modes differ by about the expected mass difference between these two neutral states. Also, in this model, the $X_d$ and the $X_u$ are named as the $X(3872)$ and the $X(3876)$ mesons, respectively.

The full spectrum of diquark-antiquark for the $X$ states is shown in Figure 1.3. The state with $J^{PC} = 1^{++}$ is proposed for the $X(3872)$ meson because it matches many of the observed properties of the state especially its narrow width and its capability to decay into $\rho J/\psi$ and $\omega J/\psi$ final states by isospin breaking. The total width of the state was estimated to be around $1.6\, MeV/c^2$ [MPR07].

### Weakly bound $D\bar{D}^*$ molecule state

An important feature of the $X(3872)$ meson is the closeness of its mass to the $D^0\bar{D}^{*0}$ threshold. Using PDG values for the $X(3872)$, $D^0$ and $\bar{D}^{*0}$ masses [N+10], one obtains:

$$M_X - (M_{D^0} + M_{\bar{D}^{*0}}) = 0.23 \pm 0.52\, MeV/c^2. \tag{1.11}$$

This relation led to a natural interpretation of the $X(3872)$ meson being a $D^0\bar{D}^{*0}$ bound state. By analogy with the deuteron, the $X(3872)$ meson has been interpreted as an S-wave $D\bar{D}$ molecule in which the binding is done via light meson exchange ($\pi$, $\sigma$, $\rho$ and $\omega$) [L+09, TÖ4]. The quantum numbers of such a state are $J^{PC} = 1^{++}$. With this model, the relative branching ratio $\mathcal{B}(X \to D^0\bar{D}^0\pi^0)/\mathcal{B}(X \to D^0\bar{D}^0\gamma)$ is expected to be similar to the ratio 62 : 38 which corresponds to the ratio of the branching fractions $\mathcal{B}(D^{*0} \to D^0\pi^0)/\mathcal{B}(D^{*0} \to D^0\gamma)$ [CP04]. The total width should be dominated by the $D^{*0}$ width [BG03] which is estimated to be $65.5 \pm 15.4$ $keV/c^2$ [BL07].

## 1.3 Summary

The nature of many hadronic states are still unclear. One of these states is the $X(3872)$. Its discovery instigated much theoretical speculations on this matter. An overview of some suggested models is given above. Many others exist such as a virtual state [H+07], an exotic glueball [Set05], or an admixture of a conventional charmonium and $D\bar{D}^*$ molecule [L+08]. The common feature between the different theories is the preference of the $J^{PC} = 1^{++}$ quantum number assignment for the $X(3872)$ meson. Also, even if they have significantly different predictions on the width, their calculation are consistent with the PDG upper bound: $\Gamma_X < 2.3$ $MeV/c^2$.

A precise measurement of the line shape of the $X(3872)$ is crucial to shed light on its nature. This requires an experimental setup capable to produce all hadronic states mentioned above and equipped with a spectrometer with excellent mass and width resolution. This was not possible with the $B-$factories since the $e^+e^-$ collisions are dominated by vector states ($J^{PC} = 1^{--}$) formation. However, the $\bar{p}p$ annihilation provides direct formation of all possible fermion-antifermion states. For such processes, the measurement resolution depends strongly on the beam momentum resolution. As a result the antiproton beams of unprecedented quality provided by the **H**igh-**E**nergy **S**trorage **R**ing (HESR) together with the planned anti**P**roton **AN**nihilations at **DA**rmsdadt ($\bar{\text{P}}$ANDA) experiment at the future **F**acility for **A**ntiproton and **I**on **R**esearch (FAIR) have the opportunity to provide additional decisive information on the nature of the $X(3872)$ state.

# Chapter 2
# Experimental Setup

The $\bar{\text{P}}$ANDA experiment is one of the pillar experiments of the FAIR facility. It is an internal experiment in the HESR ring, a major component of FAIR. The two first parts of this chapter are dedicated to basic information about the FAIR facility and the HESR accelerator. Then different target types that will be used in the experiment will be described. In the last part, an overview of the $\bar{\text{P}}$ANDA physics program is given which leads to the detector description.

## 2.1 The FAIR project

FAIR is an upcoming international accelerator facility in Darmstadt. The schematic overview of FAIR is shown in Figure 2.1. It is an upgrade of the existing GSI accelerators. A broad field of physics will be addressed at this new facility, namely nuclear structure physics, physics with antiprotons, nuclear matter physics, plasma physics and atomic physics [FAI]. The FAIR facility consists of eight ring accelerators, two linear accelerators and various experimental halls.

## 2.2 The HESR antiproton beam

The HESR is the accelerator and storage ring component of the FAIR facility dedicated for high-energy antiproton beams. The ring has a circumference of $574\,m$ with two arcs of $155\,m$ length each and two straight sections of $132\,m$ each. One straight section will mainly be occupied by the electron cooler system. The other will be intended for the beam injection, and will host the RF cavities and the $\bar{\text{P}}$ANDA experiment. The schematic layout of the HESR ring is shown in Figure 2.2.

In the start version, a pre-cooled beam of $10^8$ antiprotons coming from CR will be injected into HESR at $3.8\,GeV/c$ momentum. They will be accumulated in HESR until reaching $10^{10}$ antiprotons. The beam will be accelerated or decelerated to the desired momentum within a range from 1.5 to $15\,GeV/c$. The combination of electron and stochastic cooling will be used to ensure a high-quality of the beam the desired luminosity [Mai11]. In the full version, the HESR will operate in two different modes: *high resolution* and *high luminosity* modes. The specifications of each of these modes are given in Table 2.1.

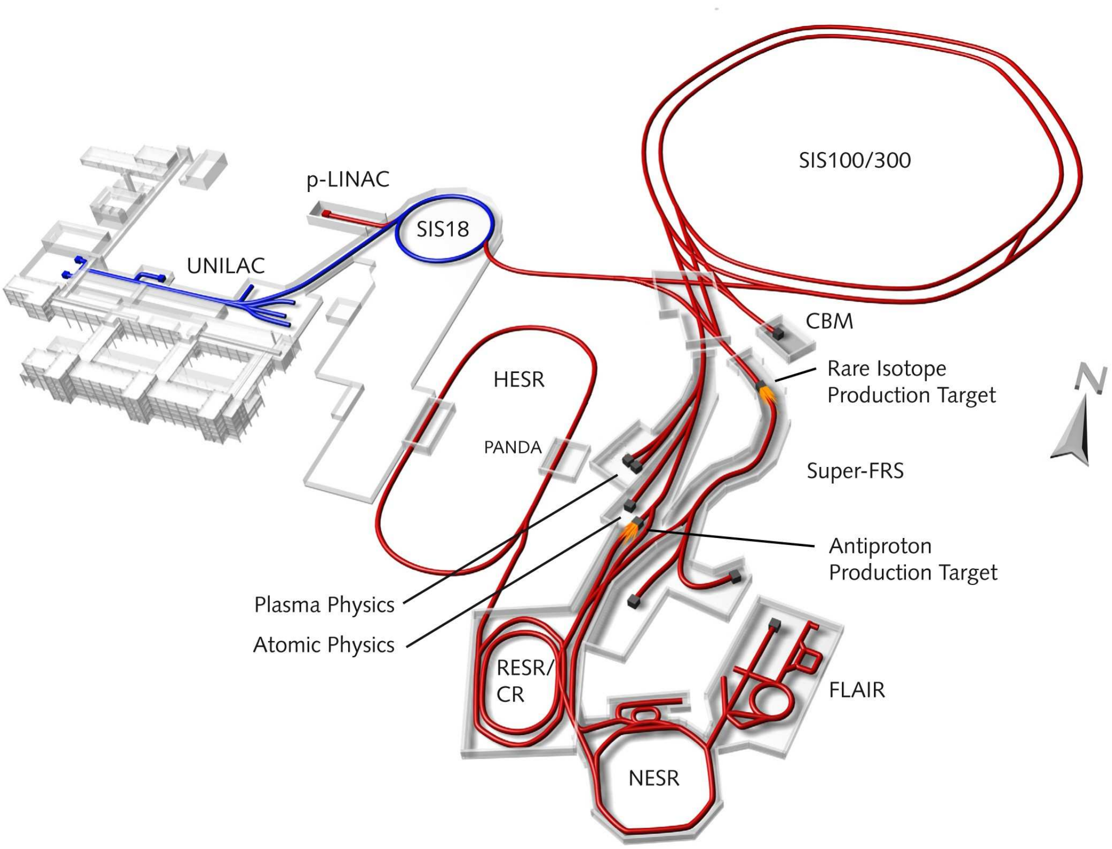


**Figure 2.1**: Schematic overview of the future FAIR facility. Picture taken from [Gia10].

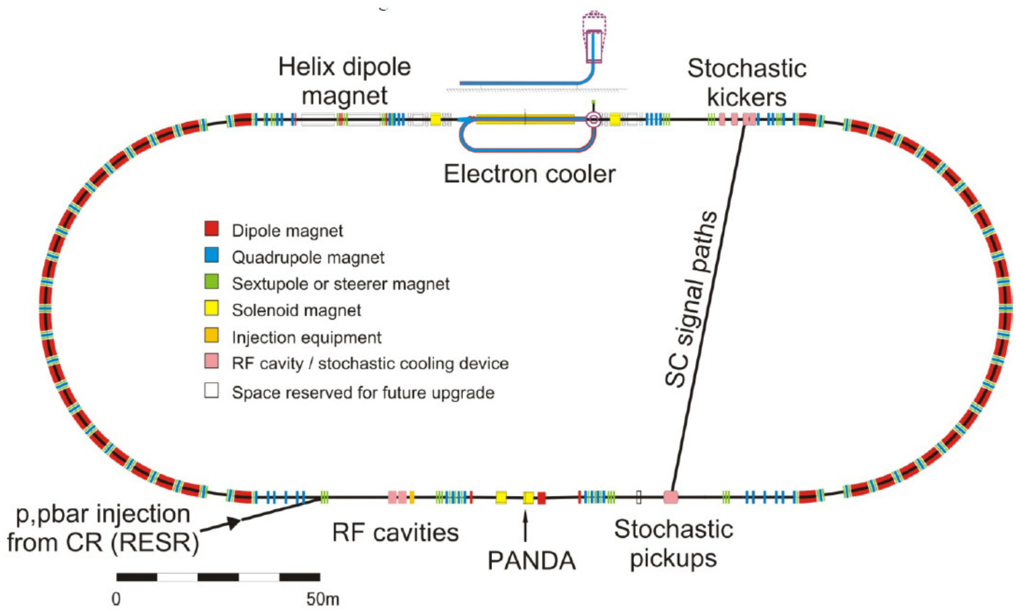


**Figure 2.2**: Layout of HESR accelerator. Picture taken from [Mai11].

| | |
|---|---|
| High resolution | Peak Luminosity of $2 \times 10^{31} cm^{-2}s^{-1}$ for $10^{10}$ $\bar{p}$<br>Target density of $4 \times 10^{15}$ atoms$/cm^2$<br>Momentum resolution $\delta p/p \leq 4 \times 10^{-5}$<br>Momentum range 1.5 to 8.9 $GeV/c$ |
| High luminosity | Peak Luminosity of $2 \times 10^{32} cm^{-2}s^{-1}$ for $10^{11}$ $\bar{p}$<br>Target density of $4 \times 10^{15}$ atoms$/cm^2$<br>Momentum resolution $\delta p/p \sim \times 10^{-4}$<br>Momentum range 1.5 to 15 $GeV/c$ |

**Table 2.1**: Operation modes of HESR.

## 2.3 Target

As seen in Table 2.1, the design luminosity requires a target thickness of about $4 \times 10^{15}$ hydrogen atoms per $cm^2$ for the $10^{10} - 10^{11}$ stored antiprotons in the HESR ring. For the $\bar{p}p$ collisions two different types of hydrogen target are foreseen: a *cluster-jet* and a *pellet* target. Only the pellet target currently provides sufficient target thickness since the current upper limit of the density for the cluster target is $2 \times 10^{15}$ atoms$/cm^2$ [T+11]. Furthermore, they exhibit different properties concerning their effect on the beam quality: cluster jet targets provide a homogeneous and adjustable target density without any time structure and thus without time structure in the luminosity, pellet targets suffer from a non-uniform time distribution which results in considerable variations of the instantaneous luminosity. Therefore the only advantage of the pellet target is the potentially higher average luminosity.

For the hypernuclear studies, a target system consisting of a primary and secondary stationary target is required. And for the $\bar{p}A$ interaction studies, a wire or a foil target will be employed [pC09a].

## 2.4 The $\bar{\text{P}}$ANDA experiment

### 2.4.1 Overview of the physics program

Antiproton-proton collisions allow the $\bar{\text{P}}$ANDA experiment to access various topics in hadron physics. The list of the accessible states within the beam momentum range between 1.5 and 15 $GeV/c$ is shown in Figure 2.3. This list reflects the rich physics program of $\bar{\text{P}}$ANDA which can be divided into several subtopics. Improved knowledge of these states provide a better understanding of the strong interaction and of the hadron structure. The availability of a high antiproton beam quality with a high luminosity endows $\bar{\text{P}}$ANDA the ability to perform very precise measurements at high statistics of these states. Therefore, it has great potential to test with an unprecedented accuracy the theory of the strong interaction. An overview of the main subtopics is given below [pC09a]:

- **QCD bound states**: the key measurements concern charmonium and open-charm states. At full luminosity several thousand $\bar{c}c$ states per day can be detected at $\bar{\text{P}}$ANDA. By means of an adequate experimental method (*cf.* next chapter) accuracies of the order of 100 $keV$ can be achieved for mass and width measurements. $\bar{\text{P}}$ANDA will also search for QCD exotic states in the charmonium mass region. From LQCD calculations, exotic charmonia

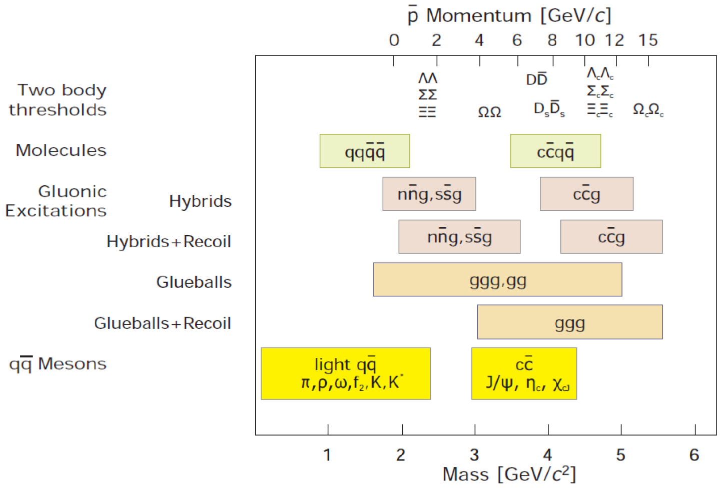


**Figure 2.3**: Hadron physics accessible for $\bar{\mathrm{P}}$ANDA within the HESR beam momentum range of 1.5 to 15 $GeV/c$. Picture taken from [pC05].

are expected to exist in the $3-5\,GeV/c^2$ mass region and the lightest exotic glueball is predicted to have a mass of $4.3\,GeV/c^2$.

- **Non-perturbative QCD dynamics**: the creation mechanism of quark-antiquark pairs measurement and their arrangement to hadrons will be studied through the $\bar{p}p \to \bar{Y}Y$ reaction, where $Y$ is an hyperon. $\bar{\mathrm{P}}$ANDA allows measurements of the cross section production of such stranged and charmed baryon for momenta above $2\,GeV/c$ where essentially no data points exist.

- **Hadron in nuclear medium**: the mass shift of hadron as consequence of chiral dynamics and partial restoration of chiral symmetry in nuclear medium will be measured. In $\bar{\mathrm{P}}$ANDA, extended studies into the charm and strange sectors due to the high-intensity of the HESR antiproton beam up to $15\,GeV/c$ by using antiproton-nucleus reactions is planned.

- **Hypernuclear physics**: although single and double $\Lambda-$hypernulei were discovered many decades ago, only 6 $\Lambda\Lambda-$hypernuclei are identified up to now. $\bar{\mathrm{P}}$ANDA will use a secondary target to capture hyperons produced by $\bar{p}p$ annihilation resulting to excited hypernuclei. The measurements will be performed via the deexcitation of the hypernuclei and the pionic decays to normal nuclei. Thanks to the high beam intensity, copious production of such process at $\bar{\mathrm{P}}$ANDA is expected.

- **Nucleon structure**: it will be investigated by measuring the cross sections of some electromagnetic processes such as $\bar{p}p \to \gamma e^+e^-$, $\bar{p}p \to \gamma\pi^0$, or $\bar{p}p \to \gamma\gamma$ using the Generalized Distribution Amplitude (GDA) or Transition Distribution Amplitude (TDA) approaches. In addition, $\bar{\mathrm{P}}$ANDA will perform the measurement of the cross section of $\bar{p}p \to e^+e^-$ process at large momentum transfer $Q^2 > 20\,GeV^2/c^2$ and with larger statistics. This will allow to separately measure the electric $|G_E|$ and magnetic $|G_M|$ time-like electromagnetic form factor of the proton.

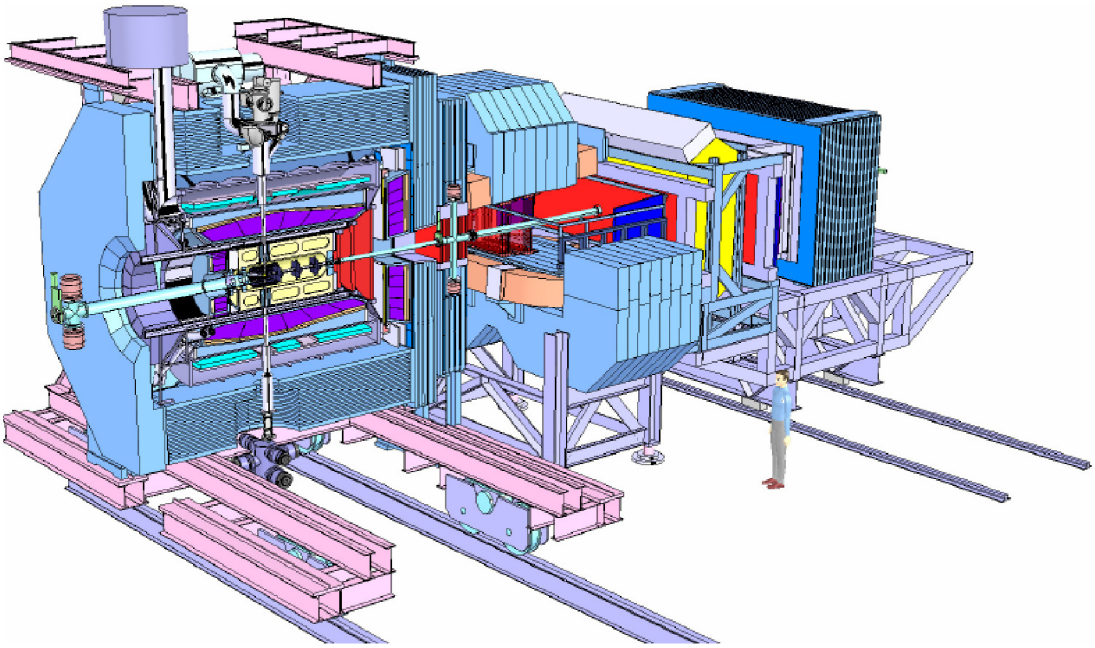

**Figure 2.4**: Picture of the $\bar{\text{P}}$ANDA spectrometer. Picture taken from [PAN].

### 2.4.2 Detector description

In order to cover the rich physics program mentioned above, the $\bar{\text{P}}$ANDA detector must be optimized to exploit as much the high quality and intensity of the HESR antiproton beam as possible. As a consequence, the detector must have a $4\pi$ acceptance, high resolution for tracking, particle identification and energy, good vertex reconstruction, high rate capabilities and a versatile readout and event selection.

The $\bar{\text{P}}$ANDA detector will consist of two magnet spectrometers: the *target spectrometer* and the *forward spectrometer*. A schematic picture of the $\bar{\text{P}}$ANDA detector is shown in Figure 2.4.

#### Target spectrometer

The target spectrometer is based on superconducting solenoid magnet which provides an homogeneous magnetic field of $2\,T$. The subdetectors inside the solenoid magnet are arranged in a shell-like structure surrounding the interaction region cover a total polar angular range from $\theta = 22°$ to $140°$. An additional forward endcap extends the angular coverage down to $5°$ in the vertical and $10°$ in the horizontal plane.

The innermost detector will be the MicroVertex Detector (MVD) surrounding the interaction region. It consists of 4 barrels and 6 disks in the forward direction of silicon sensors. It will be surrounded by the central tracker which consists of a barrel of Straw Tube Tacker (STT) and three layers of Gas Electron Multiplier (GEM) for particles emitted at angles below $22°$. The next layer will be the particle identification devices including the Time-Of-Flight (TOF) and the Detector of Internally Reflected Cherenkov light (DIRC). Then the last layer of subdetector inside the solenoid magnet is the ElectroMagnetic Calorimeters (EMC) composed by a barrel, backward and forward endcaps and will surround the above detectors. Outside of the solenoid there will be an instrumented flux return to measure muons.

### Forward spectrometer

The forward spectrometer will detect particles emitted below 5° and 10° in vertical and horizontal direction, respectively. It has a dipole magnet of $2\,Tm$ bending power at $15\,GeV/c$ beam momentum.

The tracking will be performed by 3 pairs of STT stations placed in front, inside and behind the dipole magnet. The particle identification device will use a TOF system and a Ring Imaging Cherenkov Counter (RICH) which will be placed behind the tracking station. This will be followed by the forward shashlick calorimeter and MUO detectors.

Further details on the $\bar{\text{P}}$ANDA detector can be found elsewhere [PAN, pC09a].

### Luminosity monitor

The most downstream part from the interaction region of the $\bar{\text{P}}$ANDA detector system will be the luminosity monitor (LuMo) at about $z = +10\,m$. It was conceived to determine the absolute luminosity up to a precision of 3% which is required by $\bar{\text{P}}$ANDA to perform a high accuracy on the mass and width measurements.

Since the conceptual design of this detector is one of the topics of this thesis, a detailed description of the LuMo will be presented in the next two chapters.

CHAPTER 3

# Conceptual Design of the $\bar{\text{P}}$ANDA Luminosity Monitor

This chapter focuses on the method which is used to measure the luminosity for the $\bar{\text{P}}$ANDA experiment. As described in detail in the subsequent sections, the measurement will be done by exploiting the $\bar{p}p$ elastic scattering process. The introduction of the chapter motivates the need to measure the absolute luminosity for $\bar{\text{P}}$ANDA, followed by the reason why $\bar{p}p$ elastic scattering has been chosen as the reference channel. Then a description of the channel of interest will be treated. Finally, the different constraints on the detector apparatus on which its design is based will be shown in the last part of the chapter.

## 3.1 Motivation of a precise luminosity measurement

### 3.1.1 Concept of luminosity

The number of interesting particles $dN$ measured by a detector produced by the interaction of a particle beam with a target (or two colliding particle beams) within the time $dt$ is proportional to the probability of producing the particle in a single interaction. Since the cross section $\sigma$ encodes the probability for such a reaction to occur, ignoring the detector acceptance and efficiency, the proportionality constant $\mathcal{L}$, called *luminosity*, defines the rate with which the particles are produced. The relation between these quantities can be then written as:

$$\frac{dN}{dt} = \mathcal{L}\sigma \; . \tag{3.1}$$

Thus, a precise measurement of the cross section requires a correct normalization of the reaction rate and thus an absolute determination of the luminosity. Furthermore, the determination of many physics parameters (e.g. mass and width) which are generally extracted from the cross section line shape, relies on the accuracy with which the luminosity is measured. This is explicitly demonstrated by the so-called *resonance scan* method which is described in the next subsection.

### 3.1.2 Resonance scan technique

With the resonance scan method, the nominal beam energy is stepped through the center-of-mass energy region where the resonance is expected to occur. The number of events $N$ is measured for each considered beam energy. The measured number of events during a beam time $\Delta t = t_1 - t_0$ is connected to the resonance cross section $\sigma_{RES}$ as follows:

$$N(\sqrt{s}) = \varepsilon \int_{t_0}^{t_1} \dot{\mathcal{L}} dt \left[\sigma_{BKG} + (\sigma_{RES} \otimes B)(\sqrt{s})\right] \; , \tag{3.2}$$

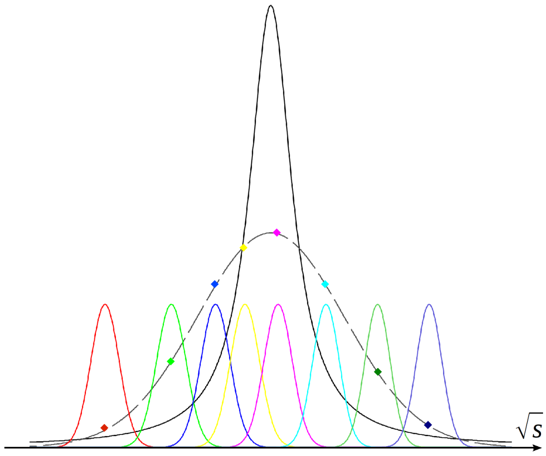


**Figure 3.1**: Sketch of the resonance scan technique. At each nominal center-of-mass energy, the beam energy distribution and the measured rate are represented by the colored curve and the point, respectively. The dashed gray curve shows the profile of the rate distribution within the energy range of the scan. The solid black curve corresponds to the line shape fit to the cross section distribution obtained by the deconvolution of the two first curves.

where $\varepsilon$ is the detector efficiency, $\dot{\mathcal{L}}$ is the instantaneous luminosity, $\sigma_{BKG}$ is the background cross section and $B$ is the function that describes the beam energy distribution at a given $\sqrt{s}$ nominal center-of-mass energy. The resonance cross section is then obtained by the deconvolution of the beam profiles and the measured rate. A fit to the cross section distribution allows the resonance parameters to be extracted. A schematic illustration of the method is shown in Figure 3.1.

The resonance scan technique is widely used in charmonium spectroscopy. Among the first applications of this method was the $J/\psi$ mass measurement formed in $\bar{p}p$ annihilation at the experiment R704 at the CERN Intersecting Storage Ring [B+87]. Then, the method was extensively used by the experiment E760/E835 at the Fermilab Antiproton Accumulator. For example, the cross section distribution as a function of the center-of-mass energy of the $\chi_{c0}(1^3P_0)$ charmonium reconstructed from the $\bar{p}p \to \chi_{c0} \to \gamma J/\psi \to \gamma(e^+e^-)$ reaction by the E835 collaboration is shown in Figure 3.2. The obtained distribution was fit with a non-relativistic Breit-Wigner function allowing the mass and the width of the state as well as the combined branching ratios $\mathcal{B}(\chi_{c0} \to \bar{p}p) \times \mathcal{B}(\chi_{c0} \to \gamma J/\psi) \times \mathcal{B}(J/\psi \to e^+e^-)$ to be determined [B+02].

The main advantage of this technique is that one can essentially eliminate all systematic errors due to the detector resolution. The measurement precision depends strongly on the knowledge of the beam energy distribution and resolution at each individual nominal center-of-mass energy used.

Due to the unprecedented quality of the antiproton beam that HESR will provide, $\bar{\text{P}}$ANDA can perform a very precise spectroscopy of hadronic systems in the charmonium mass range using the resonance scan method. Indeed, one can expect a very high accuracy on the measurement of some very narrow states, especially the new charmonium-like $X$, $Y$, $Z$ states (with predicted widths $\sim 30 - 100\,keV$), or the $D_s$ meson (currently the upper limits to the width are $\simeq 4\,MeV$). A precision of about 3% on the measurement of the absolute luminosity is re-

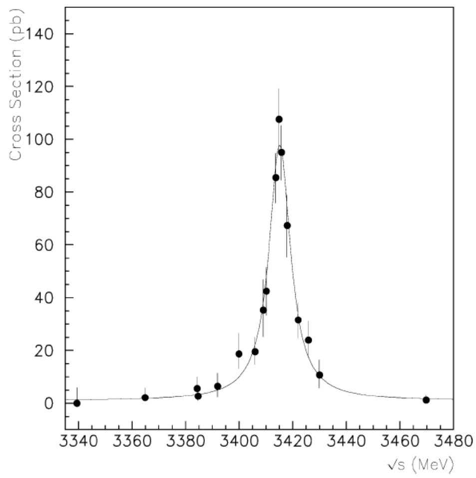


**Figure 3.2**: Cross section distribution of the $\chi_{c0}(1^3P_0)$ charmonium formed in $\bar{p}p$ annihilation measured by the E835 experiment at Fermilab. The mass and width obtained by a fit (solid line curve) to the distribution are $3415.4 \pm 0.4 \pm 0.2\,MeV$ and $9.8 \pm 1.0 \pm 0.1\,MeV$. Figure taken from [B+02].

quired by the $\bar{\text{P}}$ANDA experiment to achieve these goals. In the next section the measurement method to reach this precision is presented.

## 3.2 Methods to measure the absolute luminosity

The determination of the absolute luminosity can be perform by one of the following two methods:

1. using the *optical theorem.* This method consists of measuring the total (inelastic and elastic) $\bar{p}p$ annihilation rate, $R_{tot}$. The luminosity is given by:
$$\mathcal{L} = \frac{R_{tot}}{\sigma_{tot}} = \frac{(R_{inel} + R_{el})}{\sigma_{tot}}. \tag{3.3}$$
According to this relation, the determination of the luminosity requires the knowledge of the total cross section. It can be calculated by exploiting the optical theorem. The basic expression of the optical theorem is given by (3.16). A consequence of the formula is expressed as:
$$\sigma_{tot} = \frac{16\pi}{(\rho^2 + 1)} \cdot \frac{(dR_{el}/dt)_{t=0}}{R_{tot}} \tag{3.4}$$
with
$$\rho = \frac{\Re(f_n(t \to 0))}{\Im(f_n(t \to 0))}, \tag{3.5}$$
where $f_n$ is the forward hadronic amplitude of the $\bar{p}p$ elastic scattering. Thereby, it connects the forward elastic scattering amplitude, extrapolated to small 4-momentum transfer $t$ to the total cross section.

2. comparison to a process with a well known cross section. Here, the known process will serve as the cross section normalization for other processes as follows:
$$\sigma = \frac{R}{\mathcal{L}} = \frac{R}{R_{ref}} \cdot \sigma_{ref} \tag{3.6}$$

The first method based on the optical theorem has several sources of significant uncertainties. The $\rho$ parameter is poorly known in the $\bar{\text{P}}$ANDA beam momentum range. Thus, a simultaneous measurement of $\sigma_{tot}$ and $\rho$ will result in a large uncertainties. Further uncertainty enters by extrapolating the differential elastic rate $dR_{el}/dt$ from the measured region at finite 4-momentum transfer down to $t = 0$. As a result, the second method has been chosen.

The cross section for most hadronic processes that will be measured in the $\bar{\text{P}}$ANDA experiment are not known with sufficient precision to serve as the reference channel for the normalization. An exception is *the elastic $\bar{p}p$ scattering* process. The main characteristic of this process is that it is dominated by Coulomb scattering at very low momentum transfer. Since the electromagnetic amplitude can be calculated precisely, Coulomb elastic scattering allows both the luminosity and total cross section to be determined without measuring the total inelastic rate.

The $\bar{\text{P}}$ANDA LuMo thus aims to determine the rate of the elastic $\bar{p}p$ scattering at the smallest possible values of momentum transfer values. Based on the physics of this reference process, a detector concept has been developed which is presented in the following section.

## 3.3 Basic concept of the $\bar{\text{P}}$ANDA luminosity monitor

The design of the LuMo is optimized to measure the $\bar{p}p$ elastic scattering interaction. Thus, the properties of this process will be presented in the first part of this section.

In order to describe the properties of the elastic $\bar{p}p$ scattering, expressions for the differential cross section are derived. Using this information, the basic concept of the luminosity telescope will then be given.

### 3.3.1 Elastic $\bar{p}p$ scattering process cross section

A sketch of the elastic $\bar{p}p$ scattering process is shown in Figure 3.3. In the laboratory frame, an incident antiproton of four-momentum $p_1 = (E_1, \mathbf{p_1})$ hits a target proton at rest $p_2 = (E_2, \mathbf{p_2}) = (m, \vec{\mathbf{0}})$. After the collision, the antiproton is scattered by a polar angle $\theta$ with a four-momentum $p_3 = (E_3, \mathbf{p_3})$, and the proton is scattered by an angle $\alpha$ (with respect to the plane normal to the beam direction) with 4-momentum $p_4 = (E_4, \mathbf{p_4})$. The angle $\theta_{CM}$ denotes the antiproton scattering angle in the center-of-mass reference frame (see Figure 3.3).

The Mandelstam variable $t$ is defined as:

$$t = (p_4 - p_2)^2 = (p_3 - p_1)^2 \, . \tag{3.7}$$

Using the angles $\theta_{CM}$ and $\alpha$, $t$ can be expressed as the following:

$$t = -2\mathbf{k}^2(1 - \cos\theta_{CM}) \, , \tag{3.8}$$

$$t = -\frac{4m^2 \sin^2\alpha}{\beta^{-2} - \sin^2\alpha}, \tag{3.9}$$

where $\mathbf{k}$ is the momentum in the center-of-mass frame, $m$ is the (anti)proton mass and $\beta = |\mathbf{p_1}|/(E_1 + m)$ is the velocity of the center-of-mass. The angles $\theta_{CM}$ and $\theta$ are related to each other by [DF03]:

$$\tan\theta = \frac{\sin\theta_{CM}}{\gamma(\cos\theta_{CM} + 1)} \tag{3.10}$$

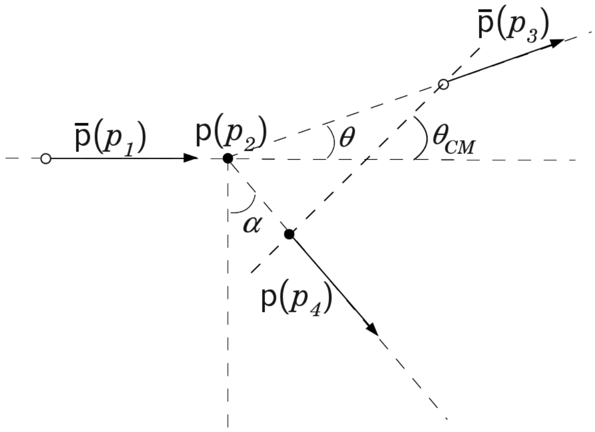


**Figure 3.3**: Description of the $\bar{p}p$ elastic scattering in the laboratory reference frame.

in which $\gamma = (1 - \beta^2)^{-\frac{1}{2}}$.

In scattering theory, the differential elastic cross section $d\sigma_{el}/d\Omega$ is determined by the forward elastic scattering amplitude $f$ defined in center-of-mass frame by the relation [Sch07, BP02]:

$$\frac{d\sigma_{el}}{d\Omega} = |f(\theta_{CM})|^2 \, . \tag{3.11}$$

The differential cross section can be expressed in terms of the 4-momentum transfer $t$ by using the relation (3.8) as:

$$\begin{aligned} \frac{d\sigma_{el}}{dt} &= \frac{d\Omega}{dt} \cdot \frac{d\sigma_{el}}{d\Omega} \\ &= \frac{\pi}{k^2} \cdot |f(t)|^2 \, . \end{aligned} \tag{3.12}$$

Moreover, the forward elastic $\bar{p}p$ scattering amplitude can be expressed as the sum of the Coulomb and hadronic (nuclear) interactions amplitudes, $f_C$ and $f_n$ [A+96]:

$$f(t) = f_C(t)e^{i\delta} + f_n(t) \, , \tag{3.13}$$

where $\delta$ is the relative phase between the nuclear and Coulomb amplitudes. The forward Coulomb amplitude is given by [Sch07, BP02]

$$f_C(t) = -\frac{2\alpha_{em} k G^2}{(\hbar c)\beta|t|}(\hbar c)^2 \tag{3.14}$$

where $\alpha_{em}$ is the electromagnetic fine structure constant and $G(t) = (1 + \Delta)^{-2}$, with $\Delta = \frac{|t|}{0.71}\ GeV^2$, is the proton dipole form factor [A+96].

The forward hadronic amplitude is parametrized in the vicinity of small momentum transfer as following [BP02]:

$$f_n(t) = f_n(t \to 0) \cdot e^{-\frac{b}{2}|t|} \tag{3.15}$$

where $b$ is the nuclear slope parameter. At $t \to 0$, the *optical theorem* connects the total cross section $\sigma_{tot}$ with the imaginary part of the forward hadronic amplitude as:

$$\sigma_{tot} = \frac{4\pi}{k} \Im f_n(t \to 0) \, . \tag{3.16}$$

Writing $f_n(t \to 0)$ as:

$$\begin{aligned} f_n(t \to 0) &= \Re f_n(t \to 0) + \imath \Im f_n(t \to 0) \\ &= \Im f_n(t \to 0)(\rho + \imath). \end{aligned} \tag{3.17}$$

with $\rho$ defined in Equation (3.5), one can obtain the following expression for $f_n$:

$$f_n(t) = \frac{\sigma_{tot} k}{4\pi}(\rho + \imath)e^{-\frac{b}{2}|t|}(\hbar c)^{-1}. \tag{3.18}$$

The factors $\hbar c$ have been introduced in Equations (3.14) and (3.18) in order to express the scattering amplitude in units of length.

The relative phase $\delta$ between the nuclear and Coulomb amplitudes reads [A+96]

$$\delta = \alpha_{em}\left[\gamma_E - \ln\left(\frac{b|t|}{2} + 4\Delta\right) + 4\Delta\ln(4\Delta) + 2\Delta\right] \tag{3.19}$$

where $\gamma_E = 0.577$ is the Euler constant.

Finally, one obtains the expression of the differential elastic $\bar{p}p$ cross section which can be written as a sum of three terms: a pure Coulomb term ($d\sigma_C/dt$), a pure hadronic term ($d\sigma_n/dt$) and the Coulomb-hadronic interference term ($d\sigma_{int}/dt$):

$$\frac{d\sigma_{el}}{dt} = \frac{d\sigma_C}{dt} + \frac{d\sigma_n}{dt} + \frac{d\sigma_{int}}{dt}\ , \tag{3.20}$$

where:

$$\frac{d\sigma_C}{dt} = \frac{\pi}{k^2}|f_C(t)|^2 = \frac{4\pi(\hbar c)^2\alpha_{em}^2 G^4}{\beta^2 t^2}\ , \tag{3.21}$$

$$\frac{d\sigma_n}{dt} = \frac{\pi}{k^2}|f_n(t)|^2 = \frac{(1+\rho^2)\sigma_{tot}^2}{16\pi(\hbar c)^2}e^{-b|t|}\ , \tag{3.22}$$

$$\frac{d\sigma_{int}}{dt} = \frac{2\pi}{k^2}\Re[f_C^*(t)f_n(t)] = -\frac{\sigma_{tot}\alpha_{em}G^2}{\beta|t|}(\rho+\delta)e^{-\frac{b}{2}|t|}. \tag{3.23}$$

One can note from the above formula that the differential cross section depends on three *a priori* unknown parameters: $\sigma_{tot}$, $\rho$ and $b$.

A graphical representation of the differential cross section and the three components as a function of the 4-momentum transfer for an incident antiproton momentum of $6\,GeV/c$ is shown in the left part of Figure 3.4. For these graphs, the values of the three parameters $\sigma_{tot}$, $\rho$ and $b$ were set to 59.30 $mb$ [N+10], $-0.02$ and 12.6 $GeV^{-2}$ [A+96], respectively. In this plot, one can distinguish the $t-$regions where the $\bar{p}p$ elastic scattering process is essentially dominated by the Coulomb interaction ($-t < 6 \times 10^{-4}\ GeV^2$) and by the nuclear interaction ($-t > 10^{-2}\ GeV^2$). The interference term only effects the differential cross section at small $t$ values. This is explicitly shown by the right side plot in Figure 3.4 where $\kappa$, the ratio of the differential cross section without the interference term to the total cross section, rises above 1. It reaches its maximum contribution at the value of $|t| = |t|_{int}$ where $\frac{d\sigma_C}{dt} \simeq \frac{d\sigma_n}{dt}$ and is roughly given by:

$$|t|_{int} \simeq \frac{8\pi\alpha_{em}}{\sigma_{tot}}(\hbar c)^2, \tag{3.24}$$

At this beam energy, this corresponds to $|t|_{int} \simeq 1.2 \times 10^{-3}\ GeV^2$.

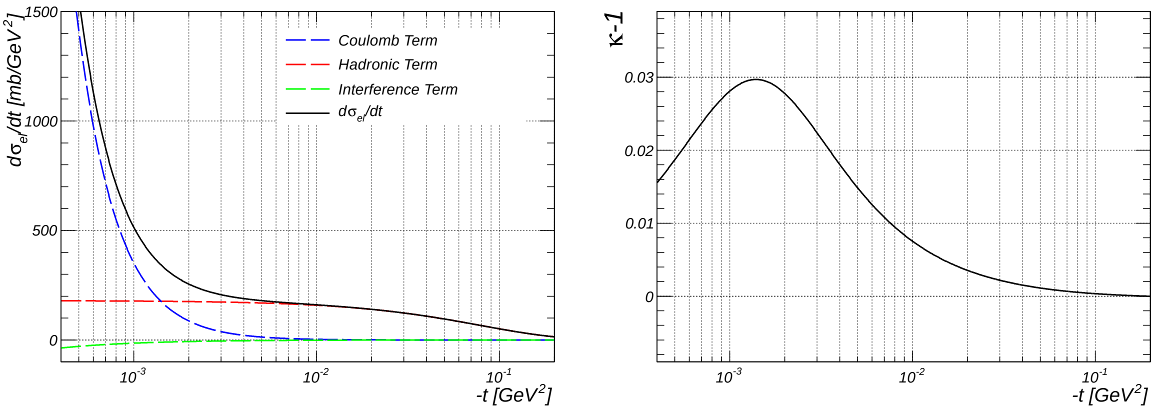


**Figure 3.4**: $\bar{p}p$ elastic differential scattering cross section (*left*) and $\kappa - 1 = (d\sigma_{int}/dt)/(d\sigma_{el}/dt)$ (*right*) variations as a function of the $|t|$ for an antiproton beam momentum of 6 $GeV/c$, $\sigma_{tot} = 59.30\ mb$ [N+10], $\rho = -0.02$ and $b = 12.6\ GeV^{-2}$ [A+96].

## 3.3.2 Detector concept

### 3.3.2.1 Physics constraints

Since Quantum Electrodynamic (QED) can calculate the Coulomb amplitude with very high precision, the measurement of the $\bar{p}p$ elastic rate down to the Coulomb dominated region allows an absolute normalization of the physics cross section. As mentioned above, for an antiproton beam of $6\,GeV/c$ momentum, this corresponds to $-t < 6 \times 10^{-4}\ GeV^2$ which requires measuring the recoil proton in the region of $\alpha < 7\,mrad$ or the scattered antiproton in the forward direction with $\theta < 2\,mrad$.

For the $\bar{\mathrm{P}}$ANDA detector, it is not possible to measure the recoil proton at such small momentum transfers due to the $2\,Tesla$ solenoid field and energy loss in the material of the beam pipe, the MVD and the central tracker. On the other hand, it appears feasible to measure the forward outgoing antiproton. Nevertheless, the region $\theta < 2\,mrad$ can not be measured in $\bar{\mathrm{P}}$ANDA due the finite dimensions of the target and beam pipe. Instead, larger angles must be used.

In practice, it is sufficient to measure the $\bar{p}p$ elastic scattering in the Coulomb-nuclear interference region to determine the absolute luminosity. Such measurements have been performed at e.g. the UA4 [A+94b] and the E760/E835 [T+95] experiments. These experiments measured either the scattered particle with momentum nearly equal to the beam (UA4), or the recoil of the target in the laboratory frame (E760). For a $6\,GeV/c$ antiproton beam, the interference region corresponds to an antiproton scattered at $\theta_{int} \simeq 5.5\,mrad$.

The absolute value of the 4-momentum transfer and the corresponding antiproton scattering angle in the laboratory frame, for which the Coulomb and the nuclear processes have equal contributions to the $\bar{p}p$ elastic scattering are shown by Figure 3.5 for a wide range of antiproton beam momentum. In these plots, points correspond to the beam momenta in which the total cross section $\sigma_{tot}$ were measured and tabulated in [N+10]. The available values of the slope parameter $b$ in the literature show it to be nearly constant in the given beam momentum range

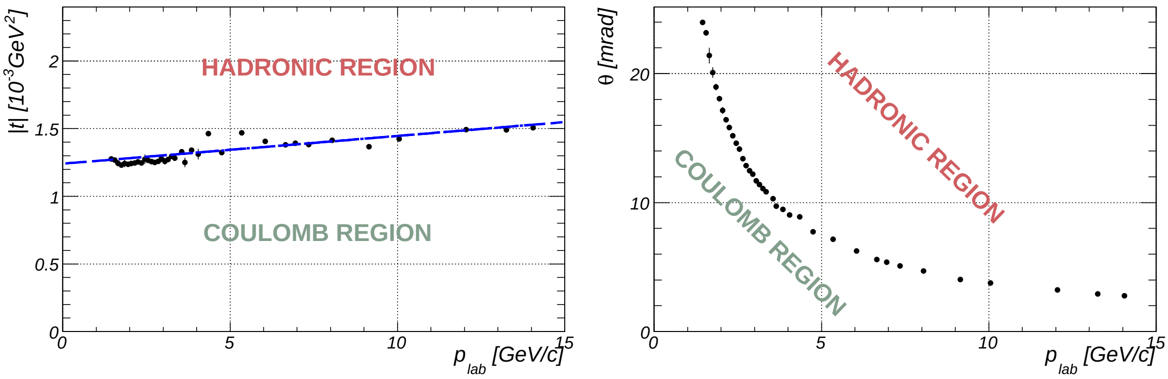


**Figure 3.5**: Distributions of the 4-momentum transfer (*left*) and the scattering angle for $\frac{d\sigma_C}{dt} \simeq \frac{d\sigma_n}{dt}$ (*right*). The blue dashed line on the left plot is a first order polynomial fit to the distribution.

| Momentum range $[GeV/c]$ | $\rho$ |
|---|---|
| $p_{beam} \leq 2$ | 0.15 |
| $2 < p_{beam} \leq 4$ | 0.05 |
| $4 < p_{beam} \leq 7$ | -0.02 |
| $7 < p_{beam} \leq 11$ | -0.12 |
| $p_{beam} \geq 11$ | 0.0 |

**Table 3.1**: Value of the $\rho$ parameter used in Figure 3.5.

[A+96, J+75, D+67, A+74, F+65a, F+65b, B+75, J+77, K+68, F+63, B+69]. The plot showing this variation is presented in Figure 4.37. For this calculation, a mean value of $b$ of 12.64 $GeV^{-2}$ was used. The $\rho$ parameter has only been measured at very few beam momenta [N+10]. Based upon those data, the value of $\rho$ has been assumed over the relevant beam momentum range and the values used are given in Table 3.1.

A first order polynomial fit to the 4-momentum transfer distribution of the Coulomb-nuclear interference range shows that the slope is roughly constant ($\mathcal{O}(10^{-5}\,GeV)$) at approximately $|t| \simeq 1.2 \times 10^{-3}\,GeV^2$ for the whole beam momentum range relevant for $\bar{\text{P}}$ANDA. The corresponding antiproton scattering angles vary from 25 $mrad$ to 3 $mrad$ at the lowest and highest beam momenta, respectively.

#### 3.3.2.2 Constraints imposed by HESR

In the Coulomb-nuclear interference region, the measurement of the antiproton can be performed in $\bar{\text{P}}$ANDA by locating the detector as far downstream from the interaction region as possible. The acceptance of the HESR restricts the lower limit of the polar angle coverage to be 3 $mrad$. The $\bar{\text{P}}$ANDA detector will occupy the region to 10.0 $m$ downstream of the interaction point. The HESR dipole needed to redirect the antiproton beam out of the $\bar{\text{P}}$ANDA chicane back into the direction of the HESR straight stretch is located at $z = +13.0\,m$ downstream of the target. Thus, the available space to measure the scattered antiprotons will be in the region between $z = +10.0\,m$ and $z = +13.0\,m$). At this distance, the minimum radial distance between the luminosity monitor and the beam axis is about 3 $cm$. At $z = +10.0\,m$ the inner beam pipe diameter is about $160\,mm$. This constrains the upper limit of the detector acceptance to be $8\,mrad$.

#### 3.3.2.3 Geometry of the luminosity monitor

The task of the $\bar{\text{P}}$ANDA LuMo is to measure the angle of the scattered antiprotons (and thus $t$). This can be done by reconstructing their trajectories. However, due to the finite size of the target and the non-vanishing beam emittance, the position of the primary vertex is not known with high precision. As a consequence, the trajectory and not just a point must be measured. This is done by using several detector layers. In this case, the luminosity telescope will consist of a sequence of four sensor planes. Four planes are required for sufficient redundancy and background suppression.

The sensors will consist of double-sided silicon microstrip detectors. They will be placed inside a vacuum chamber to minimize scattering of the antiprotons before traversing the four planes. Furthermore, they will be electrically isolated from the beam to avoid impedance jumps that would quickly destroy the beam quality. Therefore a foil will be used to separate the LuMo vacuum from the beam vacuum. The first layer will not be located at exactly $z = +10\,m$. This will result a decrease of the detector acceptance which will not be exactly the expected $\theta = 3$ to $8\,mrad$. An example of a detector geometry is shown in Figure 3.6 where the first layer is located at $z = 10.5m$ which set the lower angular limit to about $2.8\,mrad$.

Up to now, two shapes of sensors have been proposed namely rectangular and trapezoidal. The rectangular shape allows perpendicular strip directions with which the best hit resolution can be achieved. The readout has to be done at two different sides of the rectangle. In contrast, the trapezoidal shape presents the advantage of having the frontend electronic only on one side by placing strips along the direction of the nonparallel sides.

Two different detector concept are under discussion in $\bar{\text{P}}$ANDA four sensors per plane or eight sensors per plane. In the four sensors case, sensors will be arranged radially to the beam axis. This geometry allows systematic error to be strongly suppressed. These effects include finite misalignment of the nominal beam axis and the actual beam direction at the interaction point, and effects arising in the horizontal plane due to the dipole magnet of the forward spectrometer. The eight sensors case will use the trapezoidal sensors shapes and arranged in order to cover the full azimuthal range.

A schematic view of the detector apparatus using rectangular sensors arranged radially relative to the beam axis is shown by Figure 3.6. The three type of sensors with their respective dimensions are pictured in Figures 3.7 to 3.9.

The study of the trapezoidal sensors is not in the scope of this thesis. The following chapter will be devoted to study of the performance of the LuMo consisting of four tracking stations of four rectangular double-sided silicon detector presented in Figure 3.6.

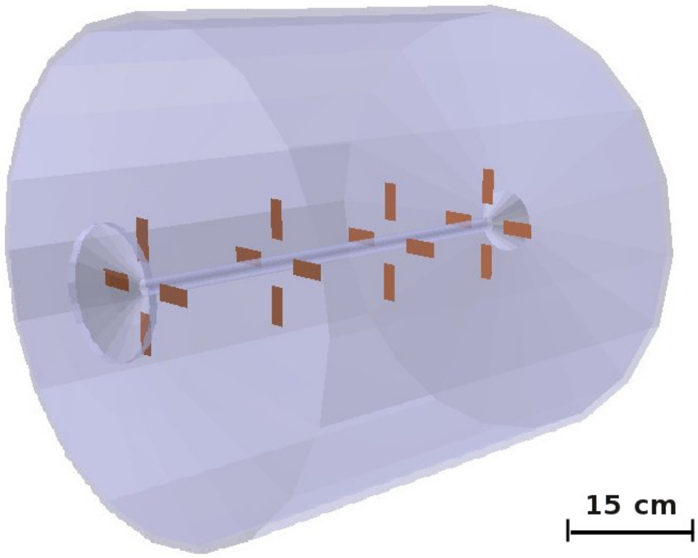


**Figure 3.6**: Schematic view of the LuMo with rectangular sensors. The distance between adjacent planes is $20\,cm$. The vacuum chamber consists of $1\,cm$ thick aluminum. The device has a radius of about $30\,cm$ of radius and a length of about $70\,cm$.

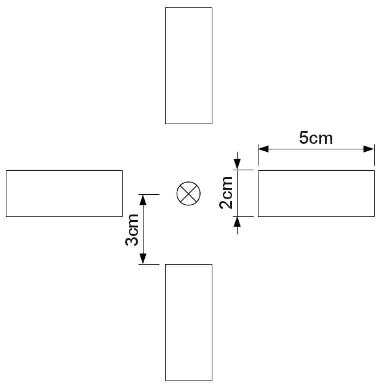


**Figure 3.7**: Four rectangular sensors arranged radially with respect to the beam axis.

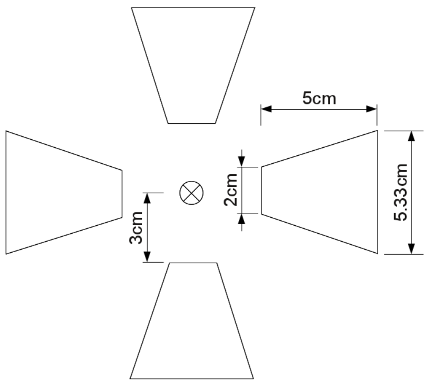


**Figure 3.8**: Four trapezoidal sensors arranged radially with respect to the beam axis.

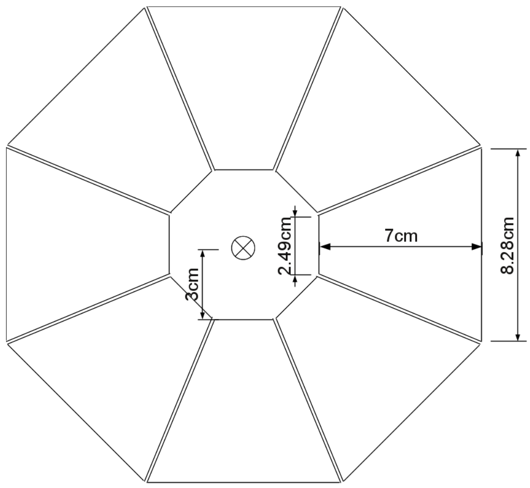


**Figure 3.9**: Eight trapezoidal sensors arranged to complete a disk.

Chapter 4

# Performance Study of the Luminosity Monitor

In this chapter, Monte Carlo performance studies of the LuMo will be presented. As mentioned in the previous chapter, only the rectangular double-sided silicon microstrip sensors sketched in Figure 3.6 will be considered here.

The studies aim to characterize the telescope in terms of $\bar{p}p$ elastic scattering event reconstruction efficiency and resolution. The efficiency refers to the performance of the detector to reconstruct to track of the scattered antiproton. The detector resolution is estimated in terms of the spatial resolution of each individual sensor and the angular resolution after the track reconstruction. Therefore, a full simulation chain including Monte Carlo simulation, digitization, and hit and track reconstruction has been developed.

The first parts of this chapter introduce the structure of the so-called *PandaRoot* simulation framework on which the detector implementation is based, followed by an overview of the available event generators within this framework. The next section gives a detailed description of the LuMo inside the framework and the study of its resolution and its efficiency. This will be illustrated by a simplified simulation in which the effect of external parameters such as the magnetic fields and the beam emittance was excluded. These effects were taken into account in the subsequent section. The description of this simulation is given in Section 4.5. Following this, a study of the rate of the inelastic reactions that would be misinterpreted and reconstructed as elastic scattering events will be discussed. This chapter concludes with a summary.

## 4.1 The PandaRoot framework

PandaRoot is an extension of the FairRoot framework [FRO] which is based on ROOT system [ROO]. FairRoot provides an interface to the ROOT Virtual Monte Carlo (VMC) engine [VMC]. This feature allows users to switch between different transport models without changing the code structure [Hǒ3, Hǒ8]. The two transport models used in the FairRoot framework are GEANT3 and GEANT4. FairRoot also provides generic classes for a track propagation based on GEANE [I+91], an IO Manager based on the ROOT TFolder and TTree classes, an interface parameter to a database and the event display based on EVE [EVE]. Many different tasks invoked during the simulation or analysis as well as the input setups, e.g. event generators and magnetic fields are implemented in FairRoot.

Specific digitization and reconstruction algorithms were implemented for each individual subdetector in PandaRoot. Different types of event generators are needed for the simulation studies. An overview of the available event generators is given in the next section. For the

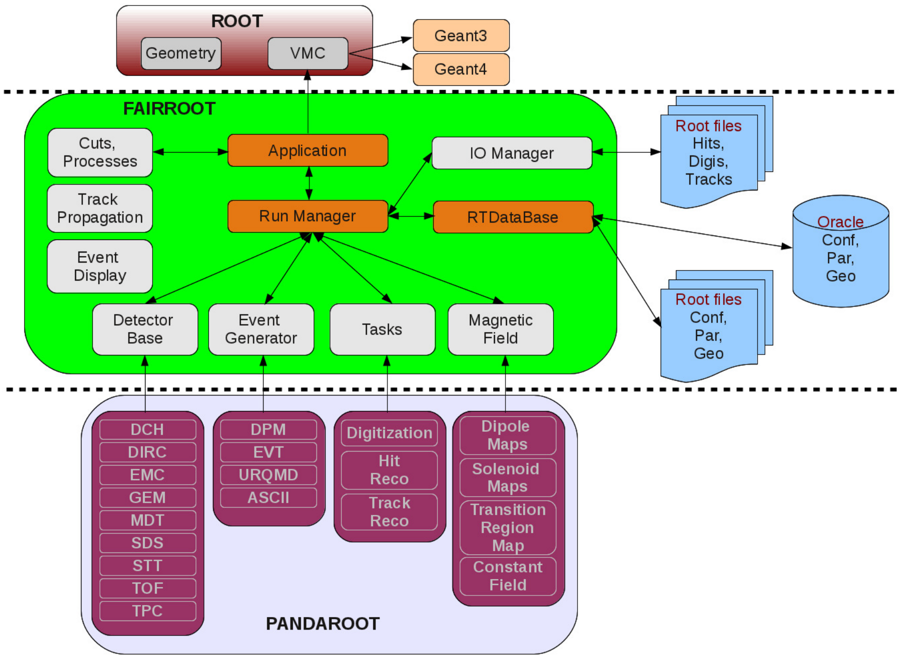


**Figure 4.1**: Diagram illustrating the structures and connections between ROOT, FairRoot and PandaRoot. Picture adapted from [pC09a].

physics analysis, the PandaRoot software comes with the Rho package [RHO] and additional tools for vertex and kinematic fitting [JR10].

Figure 4.1 illustrates how the FairRoot and PandaRoot frameworks are connected together with ROOT.

One important feature of PandaRoot is that it can be compiled on many different Linux flavors and MAC OS systems and compilers, and thus, can easily be employed in a GRID environment.

## 4.2 Event generators

The following generators have been integrated into the PandaRoot framework:

- **Box generator**: single particle generator which generates particles according to uniform distribution within defined ranges of momentum and solid angle. This generator is usually used to study detector efficiency and resolution and test the algorithms.

- **EvtGen generator**: originally designed to study the physics processes relevant to the $B$-meson decays in the $B$-factories, provides the ability to handle complex sequential decay events and generate resonances [Lan01].

- **Dual Parton Model generator (DPM)**: it treats $\bar{p}p$ interactions by parametrizing its cross sections using the synthesis of the Regge theory, the $1/N_f$ expansion of QCD and the parton model [GU05, UG02]. It is especially dedicated to generate the $\bar{p}p$ elastic and inelastic scattering and thus can be used as a background event generator for studies of particular channel.

- **Ultra-relativistic Quantum Molecular Dynamic generator (UrQMD)**: it models the $\bar{p}A$ annihilation processes using a microscopic transport theory based on interaction between all hadrons and their resonances at low and intermediate energies ($\sqrt{s} < 5\,GeV$) and on color string formation and their subsequent fragmentation into hadrons at higher energies [GP03].

## 4.3 Implementation of the telescope in Monte Carlo simulations

This section describes the implementation of the different tasks required for the full simulation chain used for LuMo performance studies. The main features of each task are:

- simulation: description of the detector geometry, definition of the physics processes of interest, generation of primary particles, tracking and hit processing, and computation of the particle-matter interactions,
- digitization: modeling of the charge collection process by the detector, the electronics behavior and the output data flow of the subdetector,
- hit reconstruction: clusterization and reconstruction of the hit position and the deposited energy,
- track reconstruction: track finder and track fitter.

The global coordinate system is a right handed system with the origin at the beam-target interaction point. The $x-$axis is horizontal pointing towards the center of the HESR, the $y-$axis is vertical and the $z-$axis is parallel to the beam direction. This system is shown in Figure 4.2. The output of each task is illustrated in this section with a full simulation using the box event generator. Each event consists of an antiproton emitted from the origin, with a polar angle $\theta$ between 1 and 10 $mrad$ to cover the detector acceptance, an uniform distribution in $\cos\theta$ and full azimuthal angular coverage. Unless otherwise stated, the simulation has been performed for an antiproton momentum of $6.2\,GeV/c$.

### 4.3.1 Simulation: from track propagation to hit processing

The implementation of the detector starts by defining the media used and the geometrical properties. A medium is defined by its name and its physical properties such as the number of component, the atomic (or molecular) weight, the mass density and so on. An ASCII file is provided in which the properties of some materials are listed and in which new materials can be defined.

The geometry of the detector is determined by the assembly of several volumes. A volume is built by defining the shape and the dimensions of each individual component, as well as the material filling it. Basically, there are the mother and the daughter volumes. The positions of the daughter volumes are given by their respective transformation (translation and rotation) matrix with respect to the mother volume. Each volume is flagged as an active or passive volume. Parameters related to the geometry of each individual sensor were given in the previous chapter. For this study since the dipole field is off, the position of the mother volume

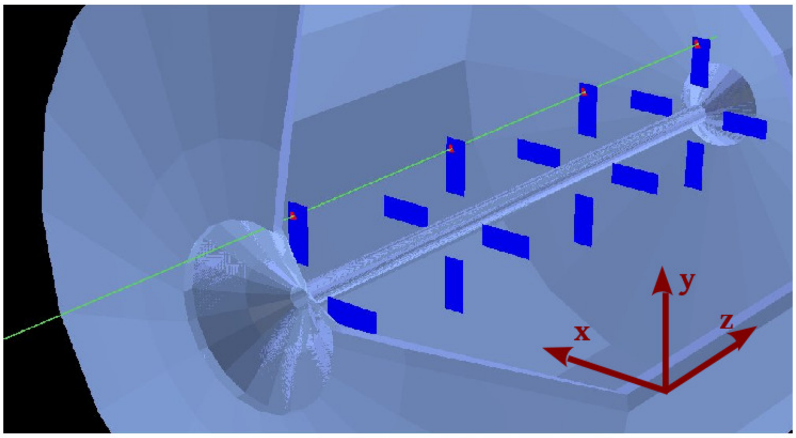


**Figure 4.2**: FairRoot event display [ATU09] illustrating an event corresponding to an antiproton track hitting all four planes. The blue-gray volume represents the aluminum cover and the rectangular dark-blue volumes the silicon sensors. The green line shows the antiproton track and the resulting hits are given by the red points.

was set at $x = 0$, $y = 0$, $z = 10.80\,m$ (i.e. the first plane is located at $z = 10.50\,m$) and each plane is perpendicular to the beam axis.

The tracking is performed by the GEANE package which is implemented in the ROOT VMC [F+08]. The LuMo is located outside of the magnetic field, thus the tracks are straight lines. This is shown in Figure 4.2.

As discussed in the previous chapter, all four planes are needed for sufficient redundancy in order to suppress background. This study focuses only on events in which all four planes have been hit. An illustration of a single event that meets this condition is also shown in Figure 4.2. One can note that the track is nearly normal to the detector plane. As a result, the path length through the detector material is only slightly larger than the sensor thickness.

Figure 4.3 shows two-dimensional distributions of the Monte Carlo hit position at each station. The uniformity of the hit distribution reflects the uniform distribution of the generated particles. The hit occupancies on the $x-$ and $y-$coordinates have the same width for all planes but shift slightly to higher values from one plane to another. This is a consequence of the requirement that a track must hit all four planes. With this condition, the angular coverage of the telescope is obtained. The corresponding $\theta$ polar angle distribution is shown in Figure 4.4. From this distribution the polar angular range of LuMo is between 2.8 and 7.5 $mrad$.

The hit position is defined as the mean of the segment (path) defined by the entry position of a track into the sensitive volume of the detector and the exit position where the particle leaves the volume. These positions are computed by GEANT by taking into account multiple Coulomb scattering within the material. Multiple Coulomb scattering deflects the track direction by an angle $\theta_0$ which follows a Gaussian distribution with a standard deviation $\sigma_{\theta_0}$ given by [N+10]:

$$\sigma_{\theta_0} = \frac{13.6\,MeV}{\beta c p} z \sqrt{x/X_0}\,[1 + 0.038 \ln(x/X_0)] \tag{4.1}$$

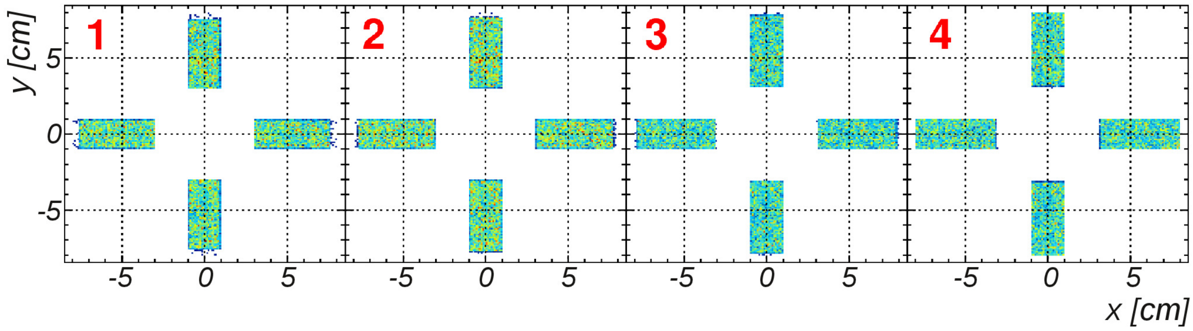


**Figure 4.3**: Two-dimensional hit distributions from tracks that hit all four stations. The numbers in the upper left indicate the plane along the beam direction.

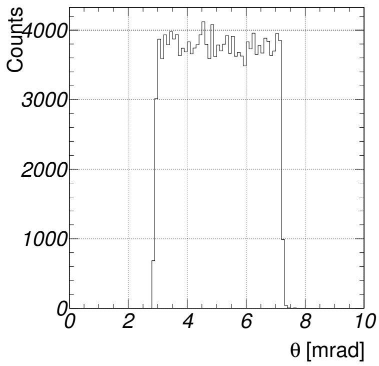


**Figure 4.4**: Angular distribution of events accepted by the LuMo.

where $p$, $\beta c$, and $z$ are the momentum, velocity, and charge number of the incident particle, respectively, and $x/X_0$ is the thickness of the scattering medium in radiation lengths. For the current study, $\sigma_{\theta_0}$ is about $0.1\,mrad$. This corresponds to a Gaussian dispersion of $20\,\mu m$ width of the $x-$ and $y-$coordinates of hits position between adjacent planes. This is shown in Figure 4.5 where the distributions of the difference $\Delta\vec{x}$ between the impact position of the projection of the Monte Carlo track and the hit position at each plane are plotted. In the first plane, the distribution is a $\delta-$function. The effect of the multiple scattering is seen in the three last planes where each histogram follows a Gaussian distribution with standard deviation $\sigma_{x_i}$ at the $i^{th}$ plane which can be parametrized by:

$$\sigma^2_{x_i} = \sum_{j=0}^{i-1} (j \cdot d \cdot \sigma_{\theta_0})^2 \,, \tag{4.2}$$

in which $d = 20\,cm$ is the distance between two adjacent planes.

Charged particles passing through the silicon sensors interact primarily by ionizing the atoms. This causes the incident particle to lose energy, which is computed by the transport model [GEA93, A$^+$03]. The energy loss distribution for $300\,\mu m$ thick silicon is shown in Figure 4.6. In the left part of the figure, the distribution is fit with a Landau function, which approximately describes the energy loss distribution in a thin layer [Bic88]. In the right part,

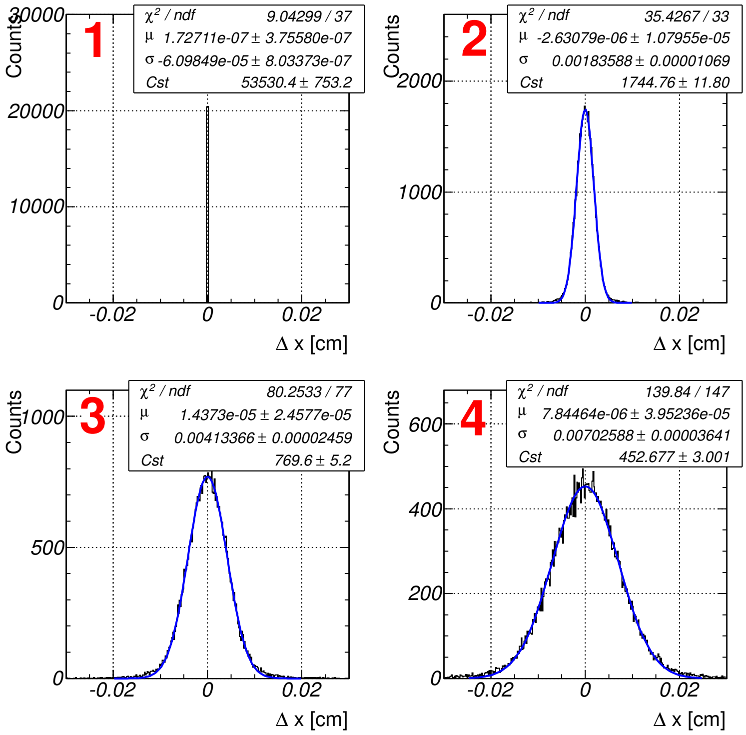


**Figure 4.5**: Distributions of $x-$coordinate of the vector hit residual between the projection of the Monte Carlo track and the Monte Carlo hit position at every detector plane denoted by the number at the top left. The blues lines are Gaussian fits to the corresponding distribution.

a Landau convoluted by Gaussian function is used to fit the energy loss distribution. The convolution with a Gaussian takes into account the effect of distant collisions of the incident particle with the atomic electrons in the inner shells [Ran84].

The Landau function is expressed as [H$^+$84a]:

$$f_L(x, \Delta) = \frac{\phi(\lambda)}{\xi} \,. \tag{4.3}$$

The parameter $\xi$ is defined as:

$$\xi = (2\pi z^2 e^4 / m_e c^2 \beta^2) N_A Z x \rho A \,, \tag{4.4}$$

where $N_A$ is the Avogadro number, $m_e$ and $e$ are the electron mass and charge, respectively, $z$ is the charge of the incident particle, $Z$, $A$ and $\rho$ are the atomic number, atomic number and mass density of the material, and $x$ is the distance traversed. The $\xi$ parameter is connected to the FWHM of the Landau distribution by FWHM$\simeq 4.02 \cdot \xi$ [H$^+$84b]. The function $\phi$ is an universal function of the dimensionless variable $\lambda$ which is defined as:

$$\lambda = \frac{[\Delta - (\Delta_p - \xi\lambda_0)]}{\xi} \tag{4.5}$$

here the parameter $\Delta_p$ is the most probable energy loss and $\lambda_0 \simeq -0.223$ is the value for which $\phi$ is maximum. For a thickness of 300 $\mu m$, $x = 68.9 \, mg \, cm^{-2}$ and the minimum ionization for the silicon $(dE/dx)_{min} = 1.664 \, MeV \, g^{-1} \, cm^2$, $\Delta_p \simeq 79 \, keV$ [N$^+$10].

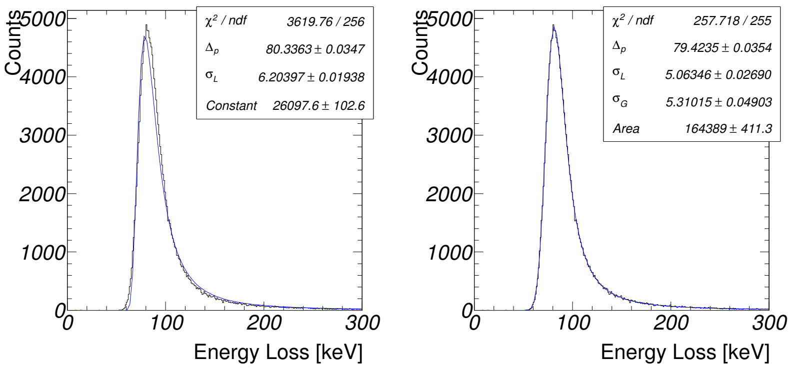


**Figure 4.6**: Energy loss distribution (black line) of $6.2\,GeV/c$ antiprotons in $300\,\mu m$ thickness of silicon fitted with a Landau distribution (*left*) and with a Landau convoluted with a Gaussian (*right*).

The Landau convoluted with a Gaussian is:

$$f(x,\Delta) = \frac{1}{\sigma_G\sqrt{2\pi}} \int_{-\infty}^{+\infty} f_L(x,\Delta') \otimes e^{-(\Delta-\Delta')^2/2\sigma_G^2} d\Delta' \,, \tag{4.6}$$

where $\sigma_G$ is the $r.m.s$ of the Gaussian distribution. If assuming the distant collisions to be dominated by the interaction of the innermost shell (K-shell), then $\sigma_G = \sigma_K = 5.75 \pm 0.5\,keV$ for this simulation setup [H+84b].

One can note from Figure 4.6 that the Landau convoluted with Gaussian fits better the energy loss distribution where $\chi^2/ndf \simeq 1$ (Landau fit results in $\chi^2/ndf \simeq 14.1$). In addition, the most probable energy loss obtained from the second is comparable to the theoretical prediction while the value obtained from the first fit is slightly bigger. Furthermore, the Landau width ($\sigma \equiv \xi$) is bigger for the first fit. Within the error bars, the Gaussian width obtained with the second fit is in good agreement with the value mentioned above.

### 4.3.2 Digitization process

Ionization in the silicon volume generates electron-hole pairs, and the number of pairs created is proportional to the energy loss of the particle. Due to an applied electric field, the electrons and holes drift in opposite directions and are collected in the electrodes before they recombine. The purpose of the digitization is to model the charge collection and charge sharing between strips. The digitization depends on the drift and the diffusion of the charge carriers, as well as the strip pitch, the electronic noise and the charge threshold.

The drift is the average motion of the charge due to the electric field $\vec{E}$. Thus, the charge carrier (electron or hole) drift velocity $\vec{v}_{dr}$ is proportional to the electric field and is expressed as:

$$\vec{v}_{dr} = \pm\mu\vec{E} \tag{4.7}$$

where $\mu$ is the mobility of the charge carrier and the sign is given by the sign of the charge carrier. During their drift, the electrons and the holes do not follow the field line direction, but undergo random motion by multiple collisions. The transverse displacement of charge carrier from the field line follows a Gaussian distribution:

$$\frac{dN}{N} = \frac{1}{\sqrt{4\pi Dt}} e^{-\frac{x^2}{4Dt}} dx\,, \tag{4.8}$$

where $t$ is the drift time and $D$ is called the *diffusion coefficient* which is defined by the Einstein relation:

$$D = \mu \frac{k_B T}{e}\,, \tag{4.9}$$

in which $k_B$ is the Boltzmann constant, $T$ is the temperature and $e$ is the electron charge. Since the mobility and the drift time are inversely proportional, the standard deviation $\sigma_{diff} = \sqrt{2Dt}$ depends only on the temperature and the electric field magnitude but not on the type of the particle. For a $300\,\mu m$ thick silicon sensor, a typical value of $\sigma_{diff}$ for the electron is about 5 to $10\,\mu m$ [Bel83, Pei93].

The drift and diffusion processes need to consider each individual electron and hole. Thus, its implementation is based on dividing the full path length of the track inside the sensor into small segments ($\mathcal{O}(1\,\mu m)$). Each segment corresponds to the same amount of charge carriers ($388\,eV \simeq 107\,electrons$). Electrons and holes in every charge packet are then smeared over a surface parallel of the detector plane, according to the same Gaussian distribution located at the center of the segment and with width $\sigma_{diff}$. As a consequence, the Gaussian distribution is evaluated on the collection plane which is composed of contiguous strips.

The contribution of one charge packet to the total charge collected by the $i^{th}$ strip is given by the cumulative function $\phi_i$ defined as:

$$\begin{aligned} \phi_i(\mu_s, \sigma_{diff}) &= \frac{1}{\sqrt{2\pi}} \int_{x_i-p/2}^{x_i+p/2} exp\left(-\frac{(x-\mu_s)^2}{2\sigma_{diff}^2}\right) dx & (4.10)\\ &= \frac{1}{2}\left[erf\left(\frac{x_i+p/2-\mu_s}{\sigma_{diff}\sqrt{2}}\right) - erf\left(\frac{x_i-p/2-\mu_s}{\sigma_{diff}\sqrt{2}}\right)\right], & (4.11) \end{aligned}$$

where $x_i$ and $p$ are the center position and the pitch of the strip, respectively, and $\mu_s$ is the center of the segment.

Figure 4.7 sketches the drift and diffusion of charges (electrons in this case) inside the detector volume. It also shows the strip charge collection. The process is the same for the holes. This figure is a good illustration of those events where the track hits all four planes i.e. the Monte Carlo track is nearly normal to the detector surface. In this case, the entry and exit positions are within the range of $x_i - p/2$ to $x_i + p/2$, and thus the charge generated should be collected only by the central $i$ strip. However, the charge diffusion will cause some of the charge to be collected on the adjacent strips.

In addition to the charge diffusion process, the effect of the electronic readout associated with each strip is taken into account. Noise has been generated for each individual strip according to a Gaussian function of width $\sigma_{noise}$ and was added to the actual amount of charge at each strip. This leads to a non-zero charge in the strips which were not hit. Hence, a charge threshold is introduced to suppress fake signals. The charge threshold has been set at the same level for each individual strip for every sensor and equal to $3\sigma_{noise}$.

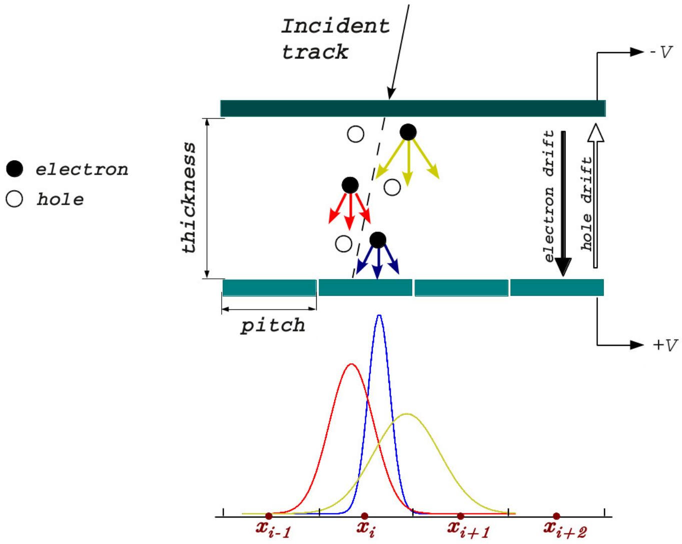


**Figure 4.7**: Strip charge collection and sharing processes taking diffusion into account. The solid black and empty arrows on the right indicate the drift directions of the electrons and the holes, respectively. The colored arrows on the electrons indicate their directions of motion which are due to the combination of the drift and the diffusion processes. Their profiles at the collection plane are represented by the Gauss curves at the bottom of the figure.

| Parameter | Value |
|---|---|
| Pitch | $50\,\mu m$ |
| $\sigma_{diff}$ | $8\,\mu m$ |
| $\sigma_{noise}$ | $3000\,eV$ |
| Threshold | $9000\,eV$ |
| Stereo angle | $90°$ |

**Table 4.1**: Digitization parameters for the silicon strip sensor.

For this simulation, the front strip direction is parallel to the length and the back strip direction is parallel to the width of the rectangular sensor. In total there are 400 and 1000 strips on the front side and back side, respectively. The strips cross with a 90° stereoangle, thus the overlap in the $xy-$plane form $50\,\mu m \times 50\,\mu m$ *virtual pixels*.

A summary of the parameters values for the digitization for the current study is given in Table 4.1.

Taking into account these parameters, the distribution of the charge deposited per strip in the front and back side of a sensor are plotted in Figure 4.8. Profile histograms are drawn on the top of each two-dimensional distribution in order to determine the position of the mean charge collected by each strip on both sides. The values obtained are $71.28 \pm 0.44\,keV$ and $71.76 \pm 0.27\,keV$ for the front and back sides strips, respectively. These two values are consistent with each other within the error bars.

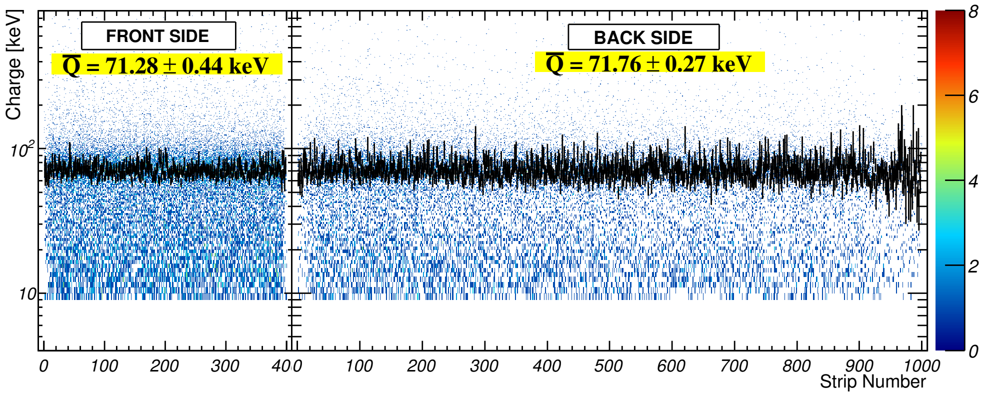


**Figure 4.8**: Distribution of the charge deposited per strip on the front side (left plot) and the back side (right plot) of the silicon strip sensors. The black marks are profile histograms indicating the mean value and the uncertainty of the means. The mean values of the charge deposited in each strip, $\bar{Q}$, on each side of the sensor are printed inside the yellow boxes.

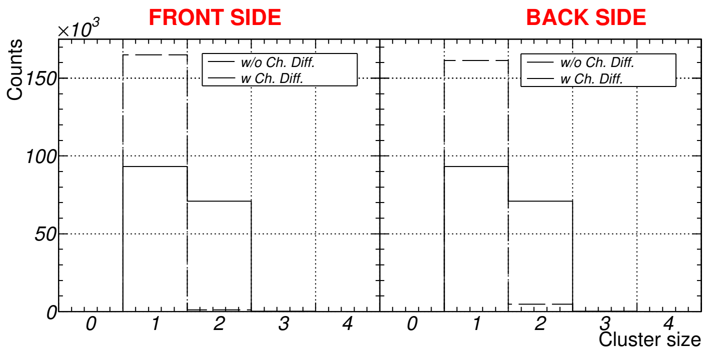


**Figure 4.9**: Cluster size distributions on the front (*left*) and back (*right*) sides of the silicon strip sensors for the two cases: without the charge diffusion (dashed line) and with $\sigma_{diff} = 8\,\mu m$ charge diffusion (solid line).

### 4.3.3 Hit reconstruction

#### 4.3.3.1 Clusterization

Neighboring strips on the same side of the sensor that were fired by a single particle are grouped together to form a *cluster*. The number of the strips involved is called the *cluster size*.

Histograms showing the distributions of the cluster size in the front and back sides are plotted in Figure 4.9. As discussed previously, drift and diffusion of the charge carriers has important effects on the cluster size. To investigate this, two histograms are presented for each side of the sensor, corresponding to the digitization process with and without the charge diffusion, respectively. As expected, the ratio of events with cluster size larger than one shows a significant increase when charge diffusion is considered. In the front side, as in the back side, the ratio increases by about 44% with $\sigma_{diff} = 8\,\mu m$. One can note the slightly higher fraction of cluster size equal to 2 on the back side for the case of digitization without the charge diffusion. This is due to the larger inclination angle $(2.8 - 7.5\,mrad)$ in that direction.

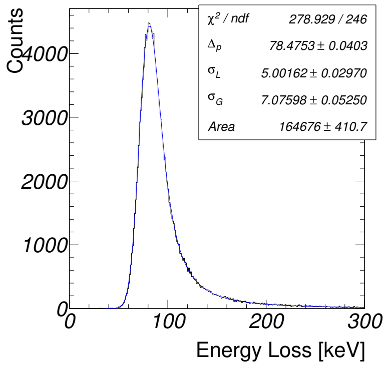


**Figure 4.10**: Distribution of the reconstructed energy loss fit with a Landau convoluted with a Gaussian function.

The deposited charge is determined by the sum of the charges collected by each individual strip involved in the reconstructed cluster. The distribution of the reconstructed energy loss is shown in Figure 4.10. The distribution is fit with a Landau convoluted with a Gaussian. The obtained values for the most probable energy loss and the Landau width are consistent with the Monte Carlo true values. The width of the Gaussian $\sigma_{RECO}$ is larger than $\sigma_{MC}$ obtained in the Monte Carlo simulation. This is due to the contribution of the electronic noise. In fact, the width of the Gaussian noise can be determined by:

$$\sigma_{RECO}^2 = \sigma_{MC}^2 + \sigma_{noise}^2 \,. \tag{4.12}$$

With this equation, one reconstructs $\sigma_{noise} = 3.37 \pm 0.071\, keV$, in reasonable agreement with the input value of $3\, keV$ given in Table 4.1.

#### 4.3.3.2 Position reconstruction in 1-dimension

The first step of the hit position reconstruction is the determination of the mean cluster position. Here two cases are considered:

- *Cluster size equal to 1,* in this case the center of the strip is taken to be the cluster position.
- *Cluster size more than 1.* When the charge is collected by more than 1 strip, there will be a non-linear but monotonic relationship between the position where the charge was deposited and the ratio of the collected charge on the strips.

  The strips of the cluster can be divided into two groups: *left* and *right.* They are defined in ascending order of the strip index. This means that for cluster size equal to 2, the left strip has the lower index. For wider clusters, the groups are defined from the boundary of the two strips with the largest collected charge. This is illustrated in the left picture of Figure 4.11.

  If the amount of charge collected by the right and the left strips are $Q_R$ and $Q_L$, respectively, the ratio of charge collected by the right cluster strips is given by the $\eta-$function which is defined as:

$$\eta = \frac{Q_R}{Q_R + Q_L} \,. \tag{4.13}$$

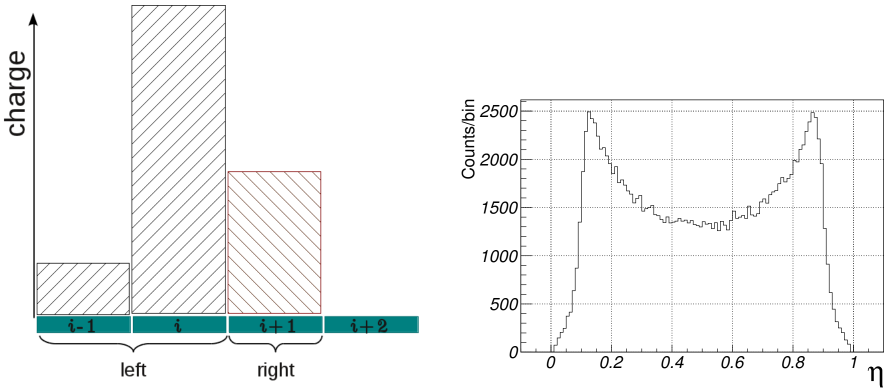


**Figure 4.11**: Charge sharing illustration. (*left*) illustrates how the left and the right groups of strips in the cluster are defined. (*right*) shows the distribution of the $\eta$ function, defined in Equation (4.13).

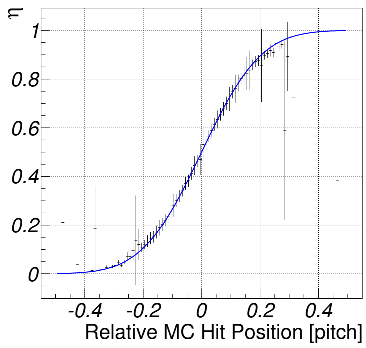


**Figure 4.12**: Variation of $\eta$ as a function of the Monte Carlo hit position (points). The hit position is expressed in units of the pitch. The blue line represents the function in Equation (4.14) which defines the reconstructed position of the multi strip clusters.

The distribution of $\eta$ has two symmetric peaks with one peak well below $\eta = 0.5$ corresponding to the larger fraction of charge being collected by the left strips and another peak at well above $\eta = 0.5$ corresponding to the larger fraction in the right strips. The distribution of the $\eta-$function is shown by the right plot in Figure 4.11 for the parameter values listed in Table 4.1. The peak positions are determined by the ratio of the threshold to the most probable value of the energy loss. For this simulation the ratio is about 11.4%. In the figure the peaks are located at about $\eta = 0.12$ and $\eta = 0.88$.

The mean cluster position is determined by exploiting the distribution of the variable $\eta$. The dependence of $\eta$ on the Monte Carlo track impact position $x$ is shown in Figure 4.12.

The variation $\eta(x)$ is best described by the *cumulative function* since the charge sharing was seeded by the Gaussian distribution i.e. :

$$\eta(x) = \frac{1}{2}\left[1 + erf\left(\frac{x}{\sigma_{diff}\sqrt{2}}\right)\right] . \tag{4.14}$$

This function is plotted as a solid line is Figure 4.12. As observed in this figure, the curve representing Equation (4.14) agrees with the current distribution for $\eta$ values between 0.12

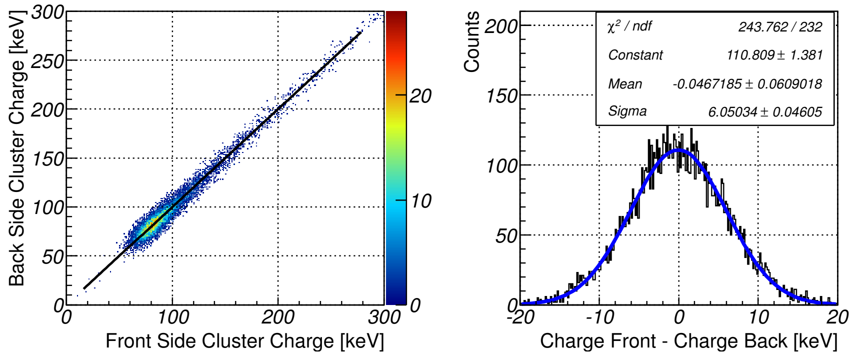


**Figure 4.13**: Correlation between charges on the front and back sides of the sensor. The solid line represents the line of perfect correlation.

and 0.88 (the peaks location in right plot of Figure 4.11) very well. Within this interval, clusters have exactly a size of 2. The points near the edges ($\sim \pm pitch/2$) are poorly described by the function since they typically correspond to clusters with size $> 2$.

As a consequence, the inverse of this function has been used to determine the mean position $x_{reco}$ of the cluster which is:

$$x_{reco} = \sqrt{2\sigma_{diff}^2} \cdot erf^{-1}(2\eta - 1)\,. \tag{4.15}$$

Although the $x_{reco}$ formula precisely reconstructs the position, as will be confirmed by Figure 4.14, the result depends strongly on the determination of $\sigma_{diff}$.

#### 4.3.3.3 Position reconstruction in 2-dimension

The two dimensional hit position is obtained by combining the total charge deposited in the cluster and its average position from both sides of the sensor.

The first step is to match clusters in both sensor sides with similar charges in order to suppress false hits (*"ghost hits"*). This step is in particular necessary for events with high track multiplicity. The charge matching was implemented by selecting on the charge difference. The correlation between the charges deposited on the front and back sides of the sensor can be verified by the scatter plot shown in the left part of Figure 4.13. The distribution is comparable to the perfect correlation represented by the black straight line in the same figure.

The distribution of the difference of the cluster charge on both side is shown in the right part of the same figure. It follows a Gaussian distribution. The mean value of 0 corroborates the perfect correlation. The dispersion of about $\sigma = 6\,keV$ is due to the effects of the noise and the charge diffusion. In this study, only clusters with charge difference within $3\sigma$ of the distribution were considered.

Next, the information of the hit position on both sides is combined to find the intersection which is taken to be the position of the track in the sensor. For the current study, the $x-$ and $y-$coordinates for the up and down sensors are given by the cluster positions at the back and front sides, respectively, and inversely for the left and right sensors.

#### 4.3.3.4 Hit resolution

The bivector hit residual $\Delta\vec{x} = (\Delta x, \Delta y)$ is defined as the difference between the Monte Carlo and the reconstructed hit positions. Similar distributions are obtained $\Delta x$ and $\Delta y$ since the virtual pixels are square and their sides are parallel to the two directions. The $x-$coordinate of the residual for cluster size 1, 2 and $> 2$ are plotted in Figure 4.14. Here, the Monte Carlo hit position is taken as the mean of the entry and exit positions.

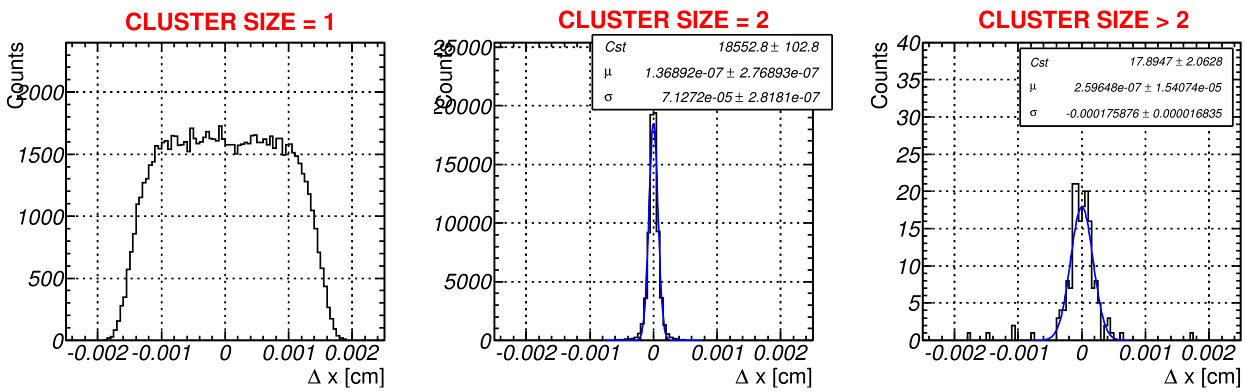


**Figure 4.14**: Distributions of the $x-$coordinate of the hit residual corresponding to clusters size 1 (*left*), 2 (*middle*) and $> 2$ (*right*).

The residual distribution corresponding to the single strip cluster is almost uniform in the center, as expected, for a homogeneous illumination of the sensor. The distribution drops near the edge of the sensor because charge diffusion always converts single hit clusters into two hit clusters. This explains why the full width is $(p - 2\sigma_{diff})$ with $p$ is the strip pitch. The expected resolution $\sigma_1$ for the single hit clusters is given by the following formula, taking charge diffusion into account:

$$\sigma_1^2 = \frac{1}{p - 2\sigma_{diff}} \cdot \int_{-(p/2-\sigma_{diff})}^{+(p/2-\sigma_{diff})} x^2 dx \simeq (14\,\mu m)^2 \,, \tag{4.16}$$

where $x$ is the distance to the center of the strip.

The distributions are narrower for the case of multi strip clusters. This is the consequence of the application of the $\eta$ based position reconstruction algorithm. As mentioned earlier, the algorithm results in a good spatial resolution for hits that fire two strips. The corresponding distribution is a Gaussian of $\sigma_2 = 0.7\,\mu m$ width. The residual distribution corresponding to the cluster size $> 2$ is wider and a Gaussian fit to the distribution gives a resolution of $\sigma_3 = 1.76\,\mu m$.

The spatial resolution of the detector is obtained by the weighted average of the three different type of clusters:

$$\sigma_\Delta = \frac{\sum_{i=1}^{3} w_i \sigma_i}{\sum_{i=1}^{3} w_i} \,. \tag{4.17}$$

In this equation, the number of entries of the distributions were taken as the weights and the obtained resolution is $\sigma_\Delta \simeq 8\,\mu m$.

### 4.3.4 Track reconstruction

#### 4.3.4.1 Track finding

The track finding process consists of identifying all hits in the different planes that were created by the same track.

Within the LuMo region, the tracks are straight lines since there is no magnetic field. However, the tracks do not point to the origin in the global reference system due to the presence of the dipole magnetic field between the interaction point and the LuMo. Thus, the reconstructed hits were transformed so that the detector axis is collinear to the $z-$axis. If $\alpha$ is the bending angle of the dipole magnet located at ($x = 0$, $y = 0$, $z = z_{dipole}$), the transformation is:

$$\begin{pmatrix} x \\ y \\ z \end{pmatrix} = \begin{pmatrix} \cos\alpha & 0 & \sin\alpha \\ 0 & 1 & 0 \\ -\sin\alpha & 0 & \cos\alpha \end{pmatrix} \begin{pmatrix} x' \\ y' \\ z' - (z_{lum} - z_{dipole}) \end{pmatrix}, \tag{4.18}$$

where $(x', y', z')$ is the coordinates of the hit in the LuMo reference system and $z_{lum}$ is the $z-$position of the detector. Numerical calculation of parameters related to the effect of the dipole magnetic field are given in detail in Section 4.4.1.

After making this transformation the tracks are on a line in the global reference system. The position of a point $(x, y, z)$ on a line is parametrized as

$$\begin{cases} x &= x_0 + a_x t \\ y &= y_0 + a_y t \\ z &= z_0 + a_z t \end{cases} \tag{4.19}$$

where $t$ is a parameter, the point $(x_0, y_0, z_0)$ is the initial position of the line and $\vec{v}(a_x, a_y, a_z)$ is the direction vector of the line. The orientation of the line can equivalently be described with the polar $\theta$ and the azimuthal $\phi$ angles which are defined by:

$$\theta = atan\left(\frac{|\vec{v}_{xy}|}{a_z}\right) \tag{4.20}$$

$$\phi = atan\left(\frac{a_y}{a_x}\right). \tag{4.21}$$

Here, $\vec{v}_{xy}(a_x, a_y)$ is the transverse component of $\vec{v}$. As a consequence, a representation of a line will be a point in the $\theta\phi-$plane.

Based on these properties, two different algorithms for track finding have been developed and implemented. The first method is performed in the Cartesian coordinate system $(x, y, z)$ by projection of the straight line in every sensor plane, while the second uses a Hough transformation of the hit positions.

The hit positions after reconstruction are stored in an array. Track finding is only performed if there are hits at each individual plane. In particular if there are no hits on the outer planes then the event is skipped. Descriptions of both algorithms are given below:

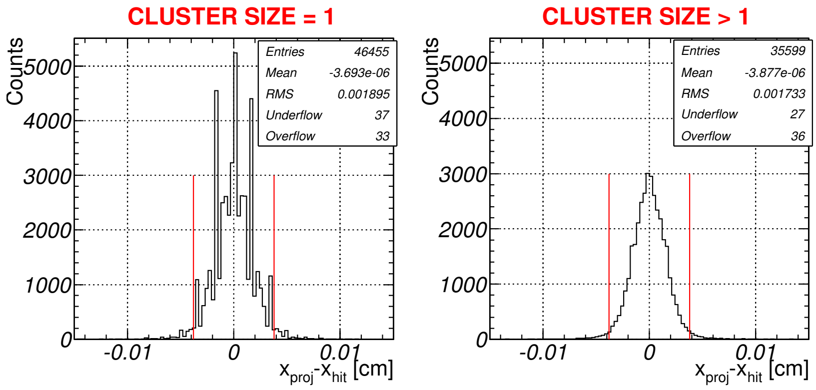


**Figure 4.15**: Distributions of the $x-$coordinate of the residual $\vec{X}_{hit} - \vec{X}_{proj}$ for the cases of single strip clusters (*left*) and multi strip clusters (*right*) reconstructed in the intermediate planes. The red lines define the cut applied on the searching area.

### Line projection method

The first step of this method consists of combining the reconstructed hits of the first and last planes. Then straight lines are constructed between these pairs. The two dimensional position $(x_{proj}, y_{proj})$ corresponding to the intersection of each line with the other sensor planes located at $z$ is calculated by:

$$\begin{cases} x_{proj} &= x_1 + \dfrac{x_4 - x_1}{z_4 - z_1}(z - z_1) \\ y_{proj} &= y_1 + \dfrac{y_4 - y_1}{z_4 - z_1}(z - z_1) \end{cases} \tag{4.22}$$

here the subscripts indicate the index of the sensor plane. Finally, hits in the central planes are searched for within a window centered at that position. This is done by applying cuts on the distributions of the $x-$ and $y-$components of the vector residual $\vec{X}_{hit} - \vec{X}_{proj}$. The distributions are similar for the $x-$ and $y-$directions.

In a given direction, the residual distributions are different depending on the type of the clusters reconstructed in the intermediate planes. As shown in Figure 4.15, the $x-$residual distribution corresponding to multi strip clusters is roughly a smooth Gaussian while the distribution for single strip clusters presents spikes on the Gaussian peak. These spikes are due to the discretization introduced by the hit position reconstruction algorithm corresponding to cluster size 1 acting on both the first and last planes. Nevertheless, the two distributions have similar width.

In this study, the same cut was applied for both components, which corresponds to the window delimited by the two vertical red lines at $\pm 2\sigma$ where $\sigma$ is the $r.m.s.$ of the distribution.

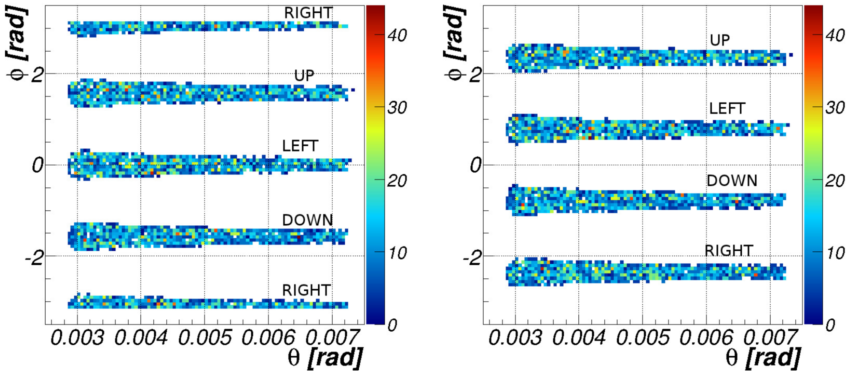


**Figure 4.16**: The hit representation in the Hough Space before (*left*) and after (*right*) the rotation about the $z-$axis by $\phi = \pi/4$.

### Hough transformation

This method exploits the $\theta$ and $\phi$ angles properties of a straight line emitted from the origin. It features the common two dimensional line *Hough transformation*, but in this case, the *Hough space* is referred as the $\theta\phi-$plane.

The angles $\theta$ and $\phi$ are calculated for each hit with respect the origin of the global coordinate system. The angles at the $i^{th}$ plane, $i = \{1, 2, 3, 4\}$ are thus given by:

$$\theta_i = arctan\left(\frac{r_i}{z_i}\right), \tag{4.23}$$

$$\phi_i = arctan\left(\frac{y_i}{x_i}\right), \tag{4.24}$$

where

$$r_i^2 = x_i^2 + y_i^2\,. \tag{4.25}$$

Due to multiple scattering the $\theta_i$'s and $\phi_i$'s of the hits for a given track do not have exactly the same values. Instead they are very close to each other, except when the $\phi$ angle is near the interval bounds ($\phi = \pm\pi$).

The points from tracks with $|\phi| \simeq \pi$ could be separated by about $2\pi$, thereby making it difficult to reconstruct the track. To avoid this, the points are temporarily rotated by an angle of $\pi/4$ about the $z-$axis before the azimuthal angles are calculated. This operation is sufficient and effective since the LuMo covers a discrete azimuthal angle range which does not contains $\phi = \pi/4$. Now, instead of having five discrete regions of finite acceptance, there are four in the Hough space, each one corresponds to a particular row of sensor (up, left, down or right). This modification is illustrated by Figure 4.16, in which the $\theta\phi-$space is plotted for a large number of events with the actual representation of the LuMo hits on the left and the modified ones on the right. The discontinuity in the vicinity of $\pm\pi$ has been removed.

The next step of the process is to search for hits at about the same position in the Hough space. Similar to the first method the search is performed by applying a cut on the coordinate system by taking into account the multiple scattering which causes the tracks to deviate by an angle $\theta_0$. One denotes $\vec{v}_{12}$ and $\vec{v}_{34}$ the direction vectors of the segments formed by the hits on the two first planes and on the two last planes, respectively. The angle formed by these vectors with the direction vector $\vec{v}_{14}$ of the segment formed by the hits on the outer planes follows a Gaussian distribution with $\sigma_{\theta_0}$, defined in Equation (4.1), as a mean. This distribution is shown by Figure 4.17. In this study, the accepted hits on the center planes corresponds to

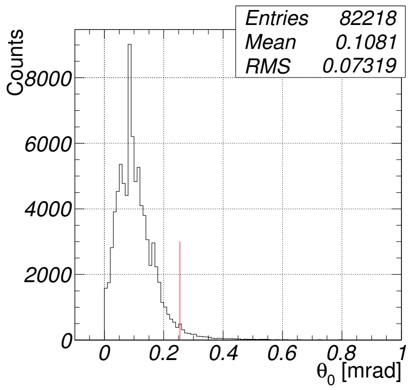


**Figure 4.17**: Distributions of the angle between $\vec{v}_{14}$ and $\vec{v}_{12}$, and $\vec{v}_{14}$ and $\vec{v}_{34}$. The cut applied for the hit finding is indicated by the red line.

$\theta_0 \leq \bar{\theta}_0 + 2\sigma$ where $\bar{\theta}_0$ and $\sigma$ are the mean and the $r.m.s.$ of the distribution, respectively.

The final step consists of rotating the hits about the $z-$axis back to their initial positions.

#### Track finder efficiency

The collection of hits found forms a *track candidate*. A good track candidate is defined as a collection that contains at least one hit per sensor plane.

The efficiency of the track finder algorithm for the LuMo is defined as the ratio between the number of the good tracks candidates to the number of generated tracks that hit all four detector plane:

$$efficiency = \frac{\#\, Good\, Track\, Candidate}{\#\, Good\, MCTrack} \,. \tag{4.26}$$

This efficiency is shown in Figure 4.18 for the beam momentum range of the $\bar{\text{P}}$ANDA experiment and for the two different methods. Both methods have similar efficiency of above 99% over all beam momenta.

The Hough transformation is almost twice as fast. However, the method based on $\theta$ and $\phi$ angles is less effective for the detectors that cover the full $\phi$ range as indicated on Figure 3.9 because of the significant probability to reconstruct hits near $\phi = \pi$ radians.

### 4.3.4.2 Track fitting

After the reconstructed hits have been selected to form a track candidate, their positions are fit to a straight line hypothesis. The parameters to describe the straight line are in Equation (4.19): the components of the initial position, the direction vector, and the parameter $t$.

The number of parameters is reduced by scaling the direction vector by $\frac{1}{a_z}$ for non-zero $a_z$ i.e. :

$$(a_x, a_y, a_z) \longrightarrow \left(\frac{a_x}{a_z}, \frac{a_y}{a_z}, 1\right) \,,$$

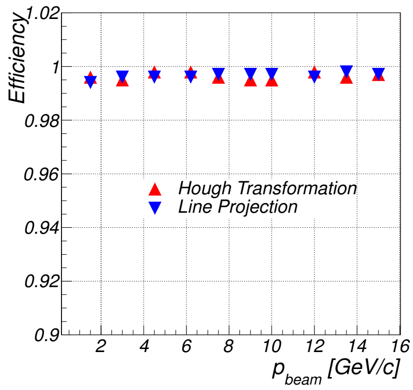


**Figure 4.18**: Track finder efficiency as a function of the beam momentum for the two methods.

and by eliminating $t$ from the third component of the parametric equation. Therefore, the line parametric equation can be rewritten as:

$$\begin{cases} x = x_0 + a_x(z - z_0) \\ y = y_0 + a_y(z - z_0) \end{cases} \tag{4.27}$$

$z_0$ is the position of a reference plane, thus it is fixed. As a result there are only four parameters to be determined, namely $a_x$, $a_y$, $x_0$ and $y_0$.

By design there will be four track points for each good track candidates. The fit procedure adopted is the generalized least-squared method in which the parameters are estimated by minimizing the $\chi^2-$function:

$$\chi^2 = \sum_{j=1}^{j=4} \delta_j^T V^{-1} \delta_j \,, \tag{4.28}$$

where

- $\delta_j$ is a bivector residual, defined as the difference between the intersection of the reconstructed track with the $j^{th}$ sensor plane and the reconstructed hit positions:

$$\delta = \begin{pmatrix} \delta_x \\ \delta_y \end{pmatrix} = \begin{pmatrix} x_{imp} - x_{reco} \\ y_{imp} - y_{reco} \end{pmatrix} . \tag{4.29}$$

  $x_{imp}$ and $y_{imp}$ are calculated from Equation (4.27) where $z$ corresponds to the $z-$position of the plane;

- $V$ is the $8 \times 8$ covariance matrix: its individual elements $V_{nm}$ is the covariance between the residuals at the $n^{th}$ and the $m^{th}$ planes given by :

$$V_{nm} = \rho_{nm}\sigma_n\sigma_m \tag{4.30}$$

  where $\rho_{nm}$ is the correlation coefficient and $\sigma$'s are the residual errors.

### Hit errors and correlation coefficients

Since the $x-$ and $y-$coordinates are independent, they can be separated in the $\chi^2$ formula as

$$\chi^2 = \sum_{j=1}^{4} \delta_{x,j}^T V_x^{-1} \delta_{x,j} + \sum_{j=1}^{4} \delta_{y,j}^T V_y^{-1} \delta_{y,j} \,. \tag{4.31}$$

As a consequence the covariance matrices $V_{x,y}$ are $4 \times 4$ matrices, and are identical for both coordinates. Therefore, the errors and the correlation coefficients need to be determined with respect to only one coordinate.

These values are determined by Monte Carlo simulations. In the first step, the line defined by the hit positions in the two first planes is calculated. The line is projected through the two last planes. The impact position of the line in plane $i$ is the point $\vec{X}_{proj,i} = (x_{proj,i}, y_{proj,i})$. The residual $\Delta_i$ in this plane is defined as:

$$\Delta_i = \begin{pmatrix} \Delta_{x,i} \\ \Delta_{y,i} \end{pmatrix} \equiv \begin{pmatrix} x_{proj,i} - x_{reco,i} \\ y_{proj,i} - y_{reco,i} \end{pmatrix} . \tag{4.32}$$

The hit error at this plane is given by the standard deviation of the residual distribution:

$$\sigma_i = \sigma_{x,i} = \sigma_{y,i} = \sqrt{\frac{\sum\limits_{k=1}^{N} (\Delta_{i,k} - \bar{\Delta}_i)^2}{(N-1)}} \,. \tag{4.33}$$

where $N$ is the number of tracks used and $\bar{\Delta}_i = \dfrac{1}{N} \sum\limits_{k=1}^{N} \Delta_i$.

The hit correlation coefficient between two planes is:

$$\rho_{ij} = \frac{\sum\limits_{k=1}^{N} (\Delta_{i,k} - \bar{\Delta}_i)(\Delta_{j,k} - \bar{\Delta}_j)}{(N-1)\sigma_i \sigma_j} \,. \tag{4.34}$$

The errors and correlation coefficients values obtained for the current simulation setup are:

$$\sigma = \left(8.16 \times 10^{-4}, 8.16 \times 10^{-4}, 2.24 \times 10^{-3}, 5.02 \times 10^{-3}\right) cm \,, \tag{4.35}$$

$$\rho = \begin{pmatrix} 1 & 0 & 0 & 0 \\ 0 & 1 & 0 & 0 \\ 0 & 0 & 1 & 0.6 \\ 0 & 0 & 0.6 & 1 \end{pmatrix} . \tag{4.36}$$

The distributions used to determine these values are shown in Figure 4.19 and Figure 4.20.

The upper distributions in Figure 4.19 correspond to the residuals of the two first planes. As expected they are similar to the distribution in Figure 4.14 and thus the hit resolution has been taken for the error values. The two last values in Equation (4.35) were determined by the Gaussian fits on the lower two histograms of Figure 4.19.

The fact that the residuals on the two first planes are equal is a direct consequence of the reconstruction technique. Since there is no external reference, the track is assumed to go exactly through the hits in the first two planes. This is the reason why the non-diagonal values

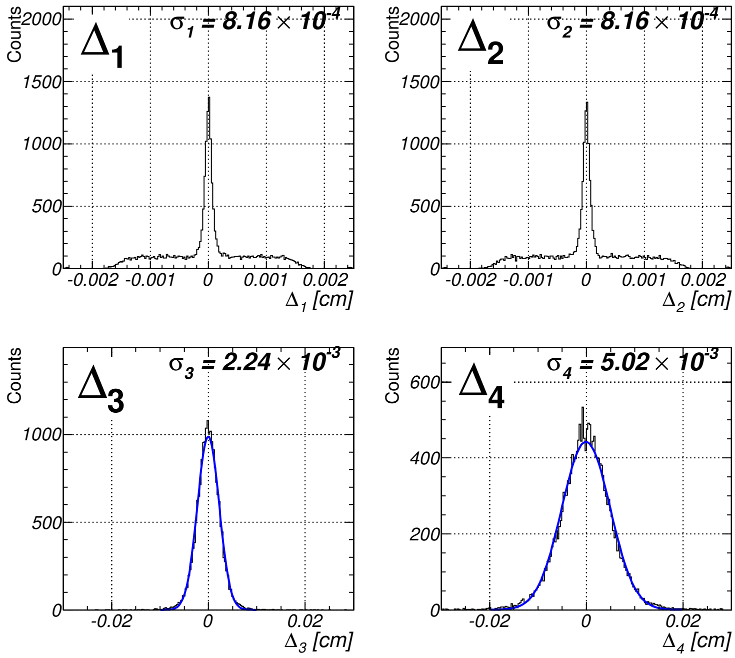


**Figure 4.19**: Distribution of the residuals $\Delta_i$, defined in Equation (4.32) for each plane. The errors $\sigma_i$ are obtained from Gaussian fits.

of the correlation coefficient matrix in Equation (4.36) are all zero except for $\rho_{34}(=\rho_{43})$. This coefficient is not zero and is positive because small angle scattering in the first two planes leads to a displacement in the same direction in subsequent planes. The corresponding plot in Figure 4.20 explicitly shows this.

### Minimization process and fit constraints

The LuMo aims to reconstruct the track without an external reference by using only the four measured hit points. The first plane is taken as the reference plane. This means that $z_0$ is the $z-$position of the first plane and the fit values of the parameters $x_0$ and $y_0$ will be constrained by the measured $x$ and $y-$coordinates of the hit position on this plane.

The fitting process was performed using the *ROOT TMinuit* class where the $\chi^2-$function was minimized via the MIGRAD algorithm and the parameter errors were estimated by the MINOS method [ROO, Jam98]. The distribution of the $\chi^2$ of the fitted tracks is shown in Figure 4.21.

The correctness of the values and error parameters can be judged by the pull distributions. The pull formula, for a given constrained parameter $p$ which has $p_{meas}$ as initial value and $p_{fit}$ as final value, with $\sigma_{meas}$ and $\sigma_{fit}$ as their respective errors, is given by [DL02]

$$Pull = \frac{p_{meas} - p_{fit}}{\sqrt{\sigma^2_{meas} - \sigma^2_{fit}}}\,. \tag{4.37}$$

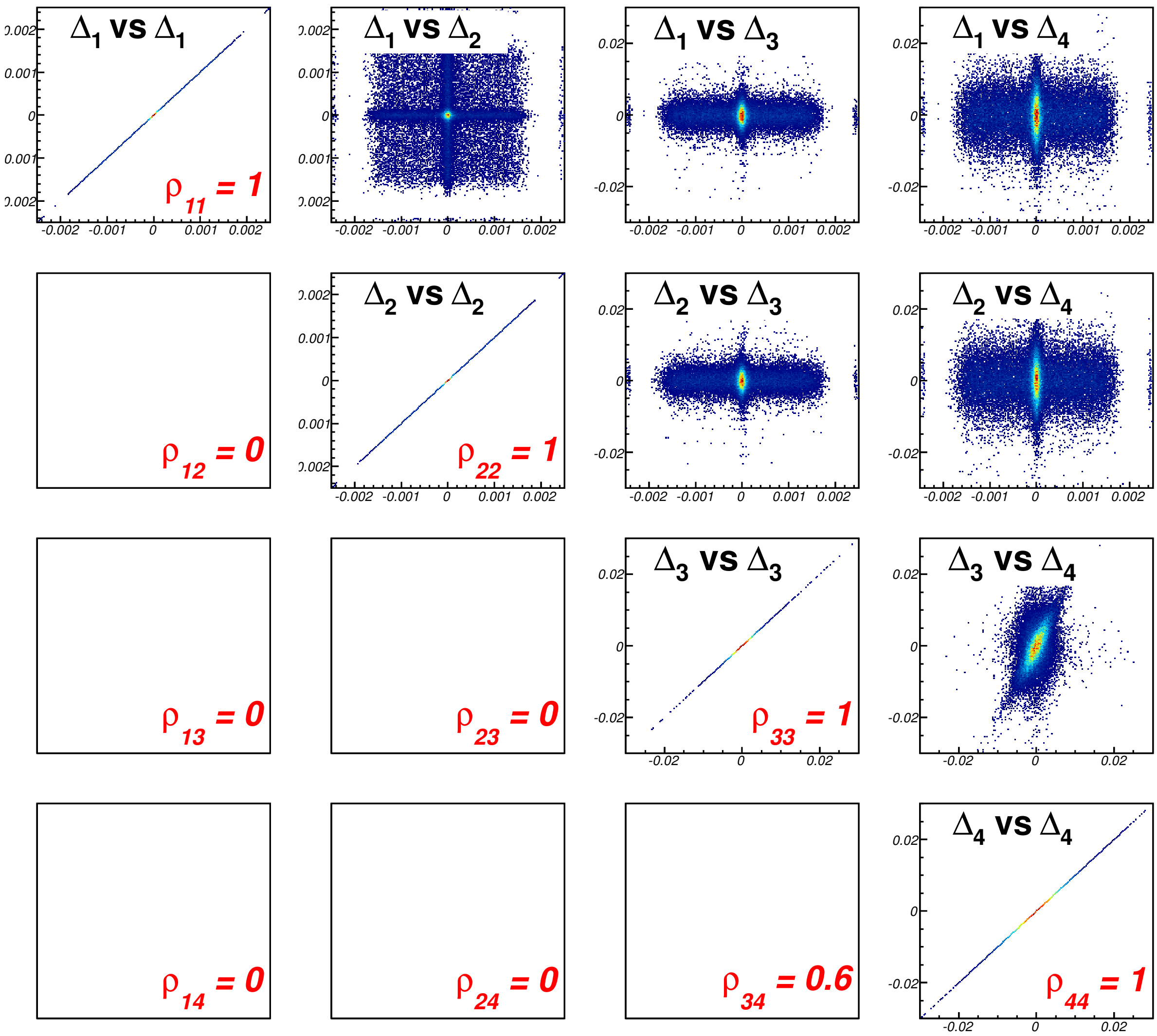


**Figure 4.20**: Scatter plots of the residuals $\Delta_i$'s on the four planes allowing the correlation coefficients $\rho_{ij}$ to be determined. Since the matrix is symmetric, only the diagonal and the upper part is plotted. The corresponding values are printed on the lower part.

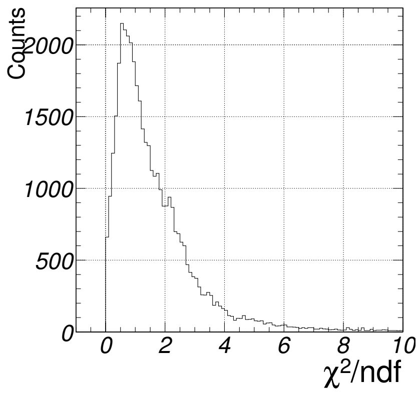


**Figure 4.21**: Distribution of $\chi^2/ndf$ of the reconstructed tracks.

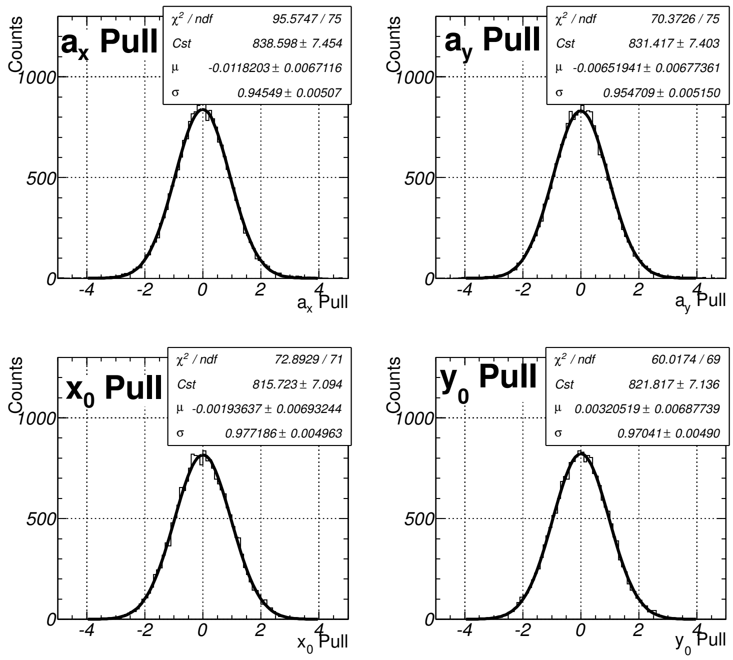


**Figure 4.22**: Fit parameters pull distributions. The solid line on top of each distribution is a Gaussian fit.

For an unconstrained parameter this reduces to

$$Pull = \frac{p_{meas} - p_{fit}}{\sigma_{fit}} . \tag{4.38}$$

In the current case Equation (4.37) was applied for the parameters $x_0$ and $y_0$ where $\sigma_{mes} = 0.8\,\mu m$, and Equation (4.38) was used for the parameters $a_x$ and $a_y$. If the fit is able to correctly determine the track parameters and their errors, the pull distributions will be normal distributions. Any source of systematic error or wrong adaptation of a constraint leads to a shift of the mean and/or change of the standard deviation of the distribution away from 1.

Figure 4.22 shows the pull distributions of the four track parameters after the fit. Gaussian fits have been applied for all distributions. From this figure, it can be seen that all distributions

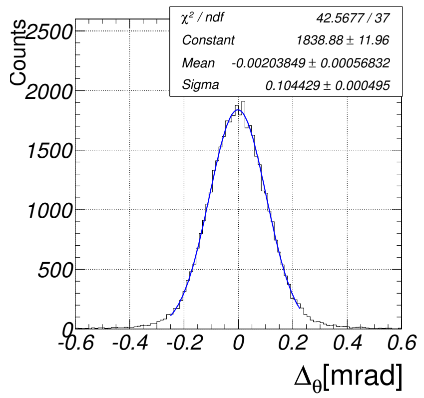


**Figure 4.23**: Angular residual distribution corresponding to the beam momentum of $6.2\,GeV/c$. The curve is a Gaussian fit applied on the distribution with its standard deviation corresponding to the angular resolution.

are centered around 0 and have standard deviation of about 1. This indicates that the fit procedure is working correctly.

### 4.3.5 Angular resolution

The performance of the LuMo can be summarized in terms of the angular resolution. This indicates how well the detector and track reconstruction have performed, given that all physics processes related to the detector have been correctly taken into account.

The LuMo is interested in the polar angle $\theta$ of the scattered antiproton which is sufficient to calculate the 4-momentum transfer $t$. The angular resolution is defined as the standard deviation of the distribution of the residual $\Delta\theta$:

$$\Delta\theta = \theta_{true} - \theta_{reco}\,. \tag{4.39}$$

In the above expression, the angle $\theta_{true}$ is the polar angle of the Monte Carlo generated track. It describes the physics of the process at the generator level. For the current case, it is defined with respect to the antiproton beam direction. The angle $\theta_{reco}$ is the angle obtained after the track reconstruction. It is measured with respect to the global $z-$axis and calculated from the fitted $a_x$ and $a_y$ parameters values according to Equation (4.20). For the determination of the angular resolution, only the reconstructed tracks having $\chi^2/ndf \leq 5$ were used.

The distribution of $\Delta\theta$ is shown in Figure 4.23 for $p_{beam} = 6.2\,GeV/c$. This distribution follows a Gaussian with the angular resolution $\sigma_{\Delta\theta} = 0.11\,mrad$.

The variation of the angular resolution as a function of the beam momentum for the $\bar{\text{P}}$ANDA experiment is presented in Figure 4.24. As expected, the resolution is worse at lower beam momenta where the influence of multiple scattering is stronger. This leads to bigger hit errors on the two last planes and thus a relatively strong correlation between them. Table 4.2 gives the values of these parameters, namely $\sigma_3$, $\sigma_4$ and $\rho_{34}$, for several simulated beam momenta. The remaining parameters are the same for all beam momentum values. This fact also explains the $\frac{1}{p}$-variation of the angular resolution which is a consequence of Equation (4.1). The resolution improves from $0.47\,mrad$ at $1.5\,GeV/c$ to $0.05\,mrad$, at $15\,GeV/c$.

| | Parameter | | |
|---|---|---|---|
| $p_{beam}$ $[GeV/c]$ | $\sigma_3$ $[cm]$ | $\sigma_4$ $[cm]$ | $\rho_{34}$ |
| 1.5 | 0.0098 | 0.0221 | 0.66 |
| 2.5 | 0.0052 | 0.0119 | 0.64 |
| 3.7 | 0.0035 | 0.0079 | 0.63 |
| 4.5 | 0.0029 | 0.0064 | 0.61 |
| 6.2 | 0.0022 | 0.0051 | 0.60 |
| 7.5 | 0.0018 | 0.0038 | 0.58 |
| 9.0 | 0.0016 | 0.0032 | 0.56 |
| 10.5 | 0.0014 | 0.0028 | 0.52 |
| 12.0 | 0.0013 | 0.0025 | 0.49 |
| 13.5 | 0.0012 | 0.0023 | 0.48 |
| 15.0 | 0.0011 | 0.0020 | 0.44 |

**Table 4.2**: Hit errors on the third and forth planes and the correlation coefficients between them for different beam momenta.

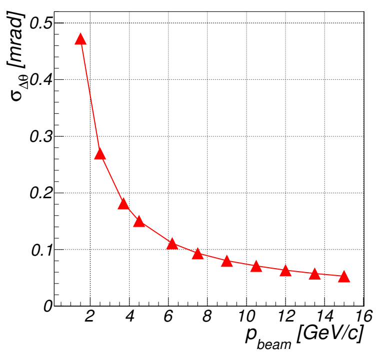


**Figure 4.24**: Variation of the angular resolution in the $\bar{\text{P}}$ANDA beam momentum range.

The angular resolution of the luminosity monitor allows to estimate the measurement precision of the scattered antiproton from the $\bar{p}p$ elastic scattering process. However, in addition to multiple scattering in the detector, there will also be several external factors limiting the precision. For a more realistic case, the influence of external parameters such as the magnetic fields and the beam emittance at the interaction point must be included. These effects will be the topic of the next section.

## 4.4 Study of the effect of the external parameters

### 4.4.1 Effect of the magnetic fields

The magnetic elements in the $\bar{\text{P}}$ANDA detector include the superconducting solenoid which surrounds the interaction region and the dipole magnet of the forward spectrometer.

#### 4.4.1.1 Effect of the dipole magnetic field

**Dipole field and luminosity monitor position**

The dipole field deflects the beam particles and the elastically scattered antiprotons from the interaction region. Therefore, a mismatch of the detector position to the bending power of the field will reduce the detector efficiency.

The integral of the field along the beam axis is chosen so that the bending angle of the beam is the same for all momenta. Its value will be ramped up from 0.2 to $2\,Tm$ as the beam momentum increases from 1.5 to $15\,GeV/c$ [pC09b].

Five dipole field maps are implemented in PandaRoot corresponding to $p_{beam} = 1.5$, 4.06, 8.9, 11.91 and $15\,GeV/c$. For intermediate beam momenta the map corresponding to the closest momentum value is used. The distribution of the field strength along the $z-$axis at the lowest and highest $\bar{\text{P}}$ANDA beam momentum is shown in Figure 4.25. This figure shows a slight change in the shape of the distribution. Moreover, for intermediate beam momenta, the bending power of the dipole field is not constant [pC09b]. As a results, the position of the luminosity telescope will effect the acceptance differently for the various beam momentum settings.

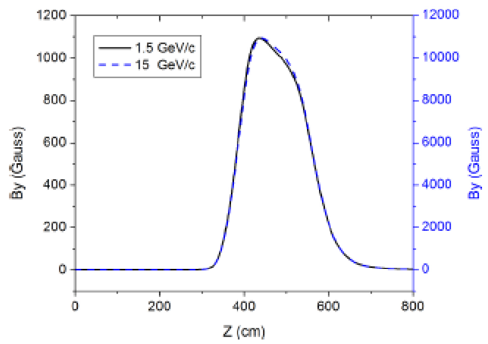


**Figure 4.25**: Dipole field distribution along the $z-$axis for $1.5\,GeV/c$ (solid black line and left scale) and $15\,GeV/c$ (dashed blue line and right scale) beam momenta. Plot taken from [pC09b].

The position of the LuMo will be determined by the average angular deflection of the beam trajectory. The dipole magnetic field requires a shift in the $x-$direction and a rotation about the $y-$axis in order to arrange the detector plane perpendicular to the beam direction. The angular deflection $\alpha$ is

$$\alpha = \frac{D}{\rho} \simeq 40\,mrad\,, \tag{4.40}$$

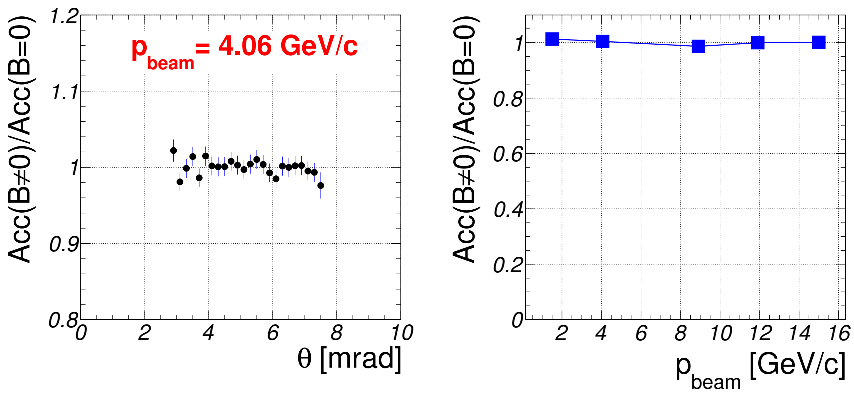


**Figure 4.26**: Distribution of the ratio between the angular acceptances when the dipole field is on and off (*left*) and variation of the ratio of the acceptance as function of the beam momentum (*right*).

where $D = 2.475\,m$ is the dipole length along the $z-$axis, $\rho$ is the radius of curvature:

$$\rho = \frac{p[GeV/c] \times D[m]}{0.3B[Tm]} \simeq 61.87\,m\,, \tag{4.41}$$

with $B = 2\,Tm$ for $p = 15\,GeV/c$.

Based on this value of the angular deflection, the $x-$position of the center of the LuMo volume (mother volume at $z = +1079.52\,cm$) is $x = +24.08\,cm$. At this position, the angle between the detector axis and the $z-$axis is $\alpha$.

### Detector acceptance

In order to estimate the acceptance of the LuMo when the dipole filed is on, simulations have been performed at the five beam momenta for which field maps are calculated in PandaRoot. The angular acceptance distribution obtained from these simulations were compared to the situation where the dipole field is off. The ratio between the acceptances in the two cases as a function of the polar angle is shown in the left plot of Figure 4.26 for $p_{beam} = 4.06\,GeV/c$. This distribution reflects the identical angular distribution for both situations. Similar distributions are obtained for all five beam momenta. In addition, the polar angle coverage is conserved i.e. in both cases the measured tracks have $2.8 < \theta < 7.5\ mrad$.

The variation of the acceptance ratio as a function of the beam momentum is plotted in the right part of Figure 4.26. The ratio is nearly constant and equal to 1 for every beam momentum. A large fluctuation of the ratio of the entries can be used to quickly identify a mislocation of the luminosity monitor when the dipole field is present.

In conclusion, these results demonstrate that the position of the luminosity monitor when the dipole magnetic field is on is correctly assigned. The center of the detector volume is located at $(24.08\,,\,0\,,1079.52)\,cm$. The angle between the detector axis and the global $z-$axis is $\alpha = 40\,mrad$. At this position, the same rate of particles will pass through the detector as when the dipole field is off, and the LuMo is located at $(0,0,1080)cm$.

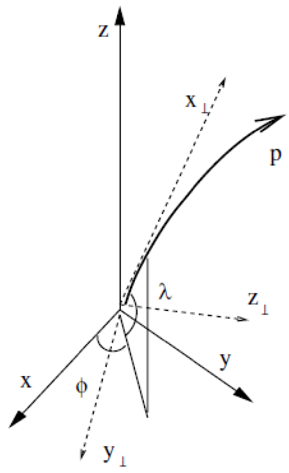


**Figure 4.27**: Transverse representation of the particle trajectory.

### Angular resolution determination

The determination of the angular resolution was discussed above. However, when the dipole field is turned on then $\theta_{reco}$ is no longer a good measure of the produced $\theta_{true}$. Instead the track must be followed back to the interaction point. This is done with the *GEANE* package which is fully integrated into PandaRoot.

GEANE was conceived to perform track following. Basically, it predicts the average trajectory of a particle when it passes through dense materials and/or a magnetic field region by calculating the transport matrix and the propagated errors covariance matrix of the track parameters [I+91, F+07].

Technically, for a single track, as input for GEANE, one needs to define the initial and the final planes from and to which the track will be propagated, respectively, the position and the momentum of the track at the initial plane with their respective errors, and of course the type of particle to be propagated. Here, the direction of the track momentum is given by the reconstruction and the magnitude is similar to the beam momentum. The momentum gives the direction of the propagation of the particle (antiproton) from the initial plane (in this case the first detector plane) back to the $xy-$plane of the primary vertex ($z = 0$). The initial position is the reconstructed hit at the first plane and its error on the $x-$ and $y-$coordinates was set to the hit resolution.

These settings allow the particle trajectory representation to be defined. Here, the transverse representation was used in which the trajectory is represented by five parameters [I+91]:

$$1/p,\ \lambda,\ \phi,\ y_\perp,\ z_\perp\,. \tag{4.42}$$

Here $\lambda$ and $\phi$ are the dip and the azimuthal angles, respectively, $y_\perp$ and $z_\perp$ are the coordinates of the track trajectory in the frame where $x_\perp$ gives the track direction and $y_\perp$ is parallel to the $xy-$ plane, and $1/p$ gives the trajectory curvature where $p$ is the particle momentum. This representation is illustrated by Figure 4.27.

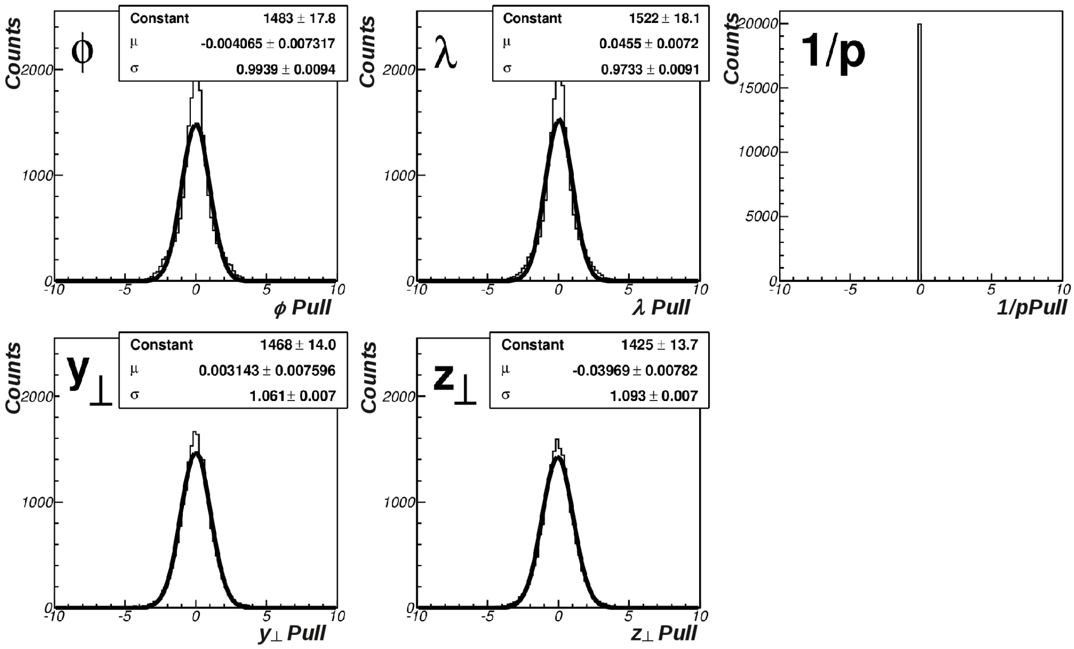


**Figure 4.28**: Pull distributions of the trajectory parameters in the transverse representation. The solid curves on top of the $\lambda$, $\phi$, $y_\perp$ and $z_\perp$ parameter distributions are Gaussian fits. The mean position and the standard deviation are close to the expected values for all distributions.

The pull distributions of all five variables are shown in Figure 4.28. A Gaussian fit is applied on each individual distribution apart from the $1/p$ parameter. Every fit is similar to a normal distribution, which can be interpreted as a correct computation of parameters and their respective errors. The $\delta-$function of the $1/p$ parameter is due to the absence of any material in the propagation region. The magnitude of the momentum will only change if the particle passes through material [F+07].

### Results on vertex and angular resolutions

At the interaction region, the results from GEANE are compared with the true Monte Carlo information. The distribution of the position of the GEANE track on the plane at $z = 0$ around the generated vertex ($x = y = z = 0$) follows a Gaussian distribution. The vertex resolution is given by the standard deviation of this distribution. Similarly, the angular resolution is the standard deviation of the residual ($\theta_{geane} - \theta_{true}$) distribution.

The variations of these resolutions as a function of the beam momentum are shown in Figure 4.29. The two graphs show similar behavior. The poor resolution of the vertex distribution for small beam momenta is connected to the poor angular resolution of the reconstructed tracks within the LuMo.

The right frame of Figure 4.29 compares the angular resolution with and without the dipole field. There is a negligible difference between the two graphs. This implies that the propagation of the particle through the magnetic field by GEANE works well.

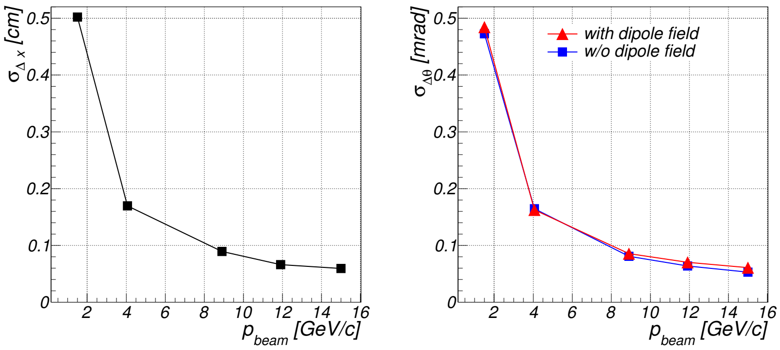


**Figure 4.29**: Position (*left*) and angular (*right*) resolution of the vertex in the presence of the dipole magnetic field as a function of the beam momentum. The angular resolution is in addition plotted without magnetic field the (blue square marker).

#### 4.4.1.2 Effect of the solenoid magnetic field

Investigations on the influence of the solenoid field show that this distorts the direction of the scattered antiproton measured by the luminosity monitor [X+10]. This effect is illustrated by Figure 4.30. The histograms in this figure correspond to two-dimensional hit distributions of simulated antiprotons in the first plane. The antiprotons were emitted from $x = y = z = 0$ and at a fixed angle of $\theta = 5\,mrad$ uniformly distributed in azimuthal $\phi$ angle between $-\pi$ and $+\pi$ for six different beam momenta. Instead of having regular circle shapes, elliptical shapes of the impact positions are obtained. The distributions in Figure 4.30 show that the lower beam momenta are more sensitive on the effect of the solenoid field. At higher beam momentum ($p_{beam} > 9\,GeV/c$), the effect of the field is negligible.

The distortion of the trajectories of the scattered antiproton is due to the geometry of the solenoid. The rectangular opening of the solenoid yoke introduces a quadrupole component to the field. This can be seen through the plot in Figure 4.31 in which the variation of the magnitude of the transverse component $\vec{B}_T = (B_x, B_y)$ of the magnetic field for the full $\phi-$range is shown close to the exit door of the solenoid yoke.

This unavoidably leads to a deterioration of the angular resolution and the detector acceptance. A correction of the shift was performed using GEANE. The results are shown in Figure 4.32 where it is compared to the ideal situation (without any magnetic field). The correction is effective for $p_{beam} > 3\,GeV/c$. Similar values of the angular resolutions with the ideal situation case are obtained. However at $p_{beam} = 1.5\,GeV/c$ the angular resolution worsens significantly from $\sigma_\theta = 0.5$ to $0.8\,mrad$.

### 4.4.2 Effects of the finite beam emittance

Up to now, the ideal situation has been considered, in which the beam-target interaction occurs at exactly $x = y = z = 0$ and the incident particle direction is exactly collinear to the $z-$axis. A correct description of the experiment must consider the non-vanishing beam emittance and the finite size of the target flux. This can be done by eventwise assigning a random shift of the primary vertex and a non-zero incident angle of the beam particle onto the target.

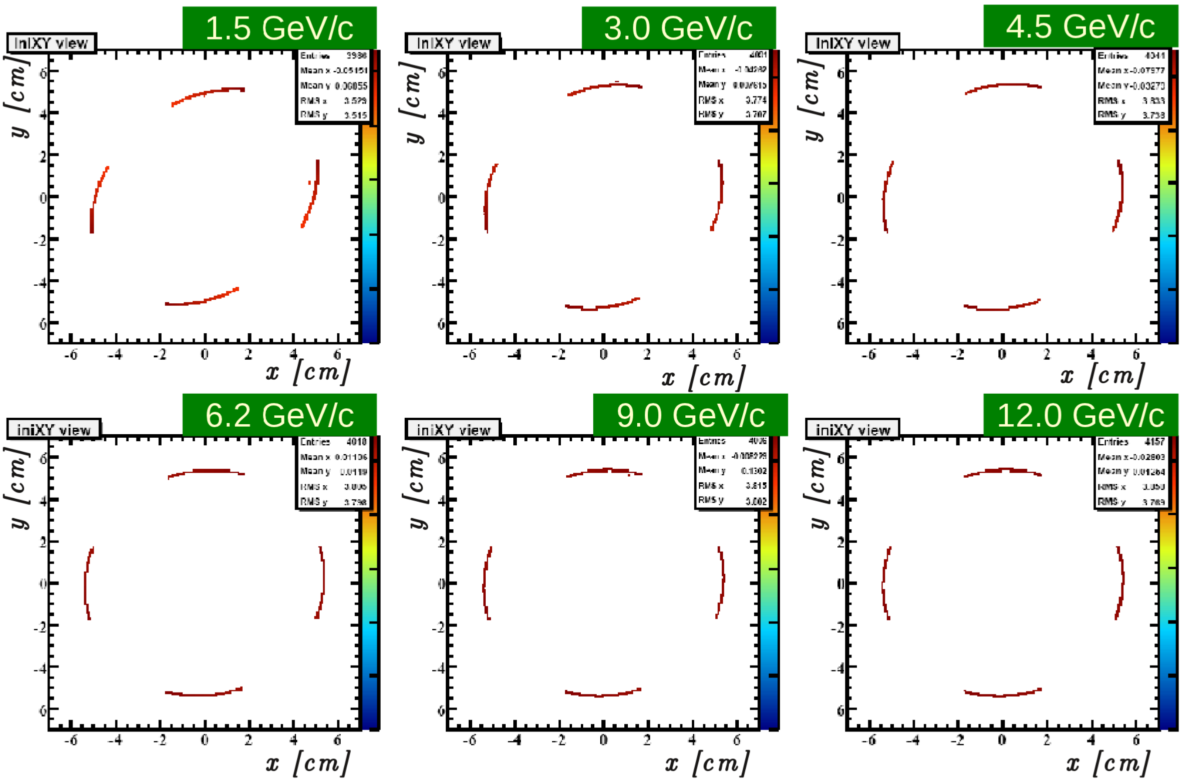


**Figure 4.30**: Two dimensional distributions of the antiproton hits at the luminosity monitor for different beam momenta for antiprotons emitted with $\theta = 5\,mrad$ showing the distortion of the tracks causes by the solenoid field. Figure taken from [X+10].

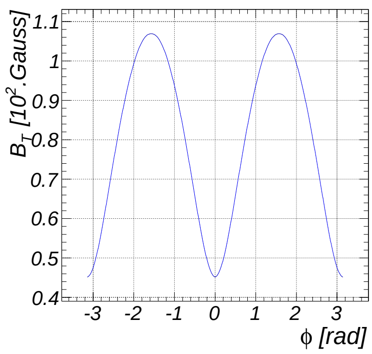


**Figure 4.31**: Variation of the transverse solenoid field $B_T = \sqrt{B_x^2 + B_y^2}$ as a function of the azimuthal $\phi$ angle at $z = +230\,cm$ and with $R = \sqrt{x^2 + y^2} = 1.15\,cm$, corresponding to $\theta = 5\,mrad$.

#### 4.4.2.1 Simulation of the vertex and angular smearing

To match the expected conditions at $\bar{\text{P}}$ANDA, vertex and angular smearing algorithms have been developed according to the expected properties of the HESR antiproton beam and the target at the interaction region.

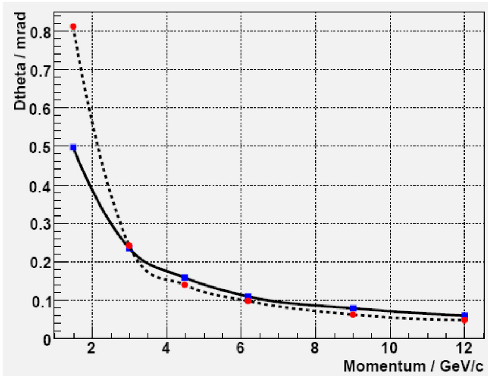


**Figure 4.32**: Angular resolution corresponding to the ideal situation (solid line) and GEANE correction (dotted line). Figure taken from [X+10].

### Beam-target system parameters at the interaction region

The overlap between the beam and the target flux will be optimized to achieve the desired luminosity. Here the conditions for the hydrogen pellet target are considered. The important parameters are the pellet radius $r_p$, the pellet stream radius $R$, and the average vertical separation between the pellets $d$. These parameters were chosen to satisfy the high luminosity requirement by $\bar{\text{P}}$ANDA. For this study their values are taken from [R+07, Zie06] and are tabulated in Table 4.3.

The HESR beam is assumed to have a Gaussian transverse profile with *r.m.s.* width $\sigma_x = \sigma_y = \sigma_{x,y}$ at the target. The average luminosity is proportional to the effective target thickness, $\rho_{eff}$, given by the overlap of the beam with the target stream [R+07]:

$$\rho_{eff}(\sigma_x) = \frac{<\mathcal{R}>}{\sqrt{2\pi}\sigma_x}\int_{-R}^{+R} 2\sqrt{R^2 - x^2} \cdot exp\left(-\frac{x^2}{2\sigma_x^2}\right) dx\,, \tag{4.43}$$

where

$$<\mathcal{R}>= \frac{\frac{4}{3}\pi r_p^3}{\pi R^2 d}\mathcal{R} \tag{4.44}$$

is the average pellet density in the $y-$direction with $\mathcal{R} = 4.3 \times 10^{22}\, atoms/cm^3$. A graph showing the variation of $\rho_{eff}$ as a function of $\sigma_x$ is drawn in Figure 4.33 for the target size given in Table 4.3. According to this graph, the transverse beam *r.m.s.* should be kept less than $0.08\, cm$ in order to achieve an average luminosity of about 80% of the maximum possible.

The angular divergence of the beam $\sigma_\alpha$, is connected to the transverse beam spread $\sigma_x$ by the beam transverse emittance $\varepsilon$ with the following relation:

$$\varepsilon = 2\sigma_x \cdot 2\sigma_\alpha\,. \tag{4.45}$$

At the interaction region, the transverse emittance of the antiproton HESR beam will be $1\, mm \cdot mrad$ [L+06]. Thus, for $\sigma_x = 0.08\, cm$ there will be $\sigma_\alpha = 0.3\, mrad$.

All the parameters mentioned above are summarized in Table 4.3 and are used in the following.

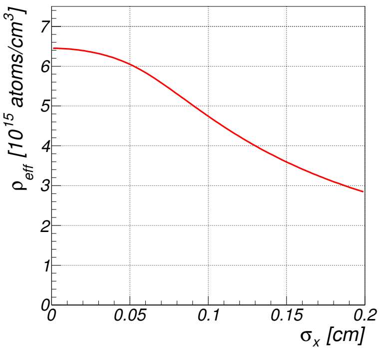


**Figure 4.33**: Effective target thickness as a function of the transverse beam profile.

| Parameter name | Symbol | Value |
|---|---|---|
| Pellet radius (mm) | $r_p$ | 0.015 |
| Pellet flux radius (mm) | $R$ | 1.5 |
| Average vertical distance between pellet (mm) | $d$ | 4 |
| Transverse beam $r.m.s.$ (mm) | $\sigma_{x,y}$ | 0.8 |
| Beam angular divergence (mrad) | $\sigma_\alpha$ | 0.3 |

**Table 4.3**: Beam and target parameters used for the vertex and angular smearing.

### Implementation of the vertex and angular smearings

The vertex and angular smearing processes imply performing a geometrical transformation of the 3-momentum vector of the generated primary particles at the beam-target interaction position. The coordinate shifts of the vertex are limited by the overlap area between the beam and the target. Since $\sigma_x < R$, the $x$ and $y-$shifts will be determined by the HESR beam distribution, and the $z-$shift by the horizontal pellet flux dimension $R$.

At the interaction point, calculations show that the *electron-cooled* antiprotons distribution are rather uniform than Gaussian [R+07]. Therefore, the vertex translations in the $x$ and $y-$coordinates were randomly generated by uniform distributions centered at 0 with width equal to $2 \times \sigma_x = 1.6\,mm$. On the other hand, a random normal translation was applied for the $z-$coordinate with width $\sigma_z = R$.

The consideration of the non-zero beam angular divergence implies changes on the direction of the generated particles. These changes must be in accordance with the orientation of the incident beam particle. The angular smearing corresponds to the incident particle having a polar angle $\delta\alpha$. This angle is generated randomly with a Gaussian distribution centered at 0 and of $\sigma_\alpha$ width. Therefore, a correct description of the angular smearing consists of rotating the incident particle about the $x-$axis by an angle $\delta\alpha$ followed by a rotation about the $z-$axis by an angle $\delta\phi$, generated uniformly between $-\pi$ and $+\pi$. A picture sketching this scenario is shown in Figure 4.34 for the case with two generated particles.

The implementation of the angular smearing in the event generator includes, for the 3-momentum vector of each individual generated particle, the rotation by an angle $-\delta\phi$ about the $z-$axis followed by the rotation by angle $-\delta\alpha$ about the $x-$axis. This has as consequence a change of the polar angle from its initial value for every single particle. The amplitude of

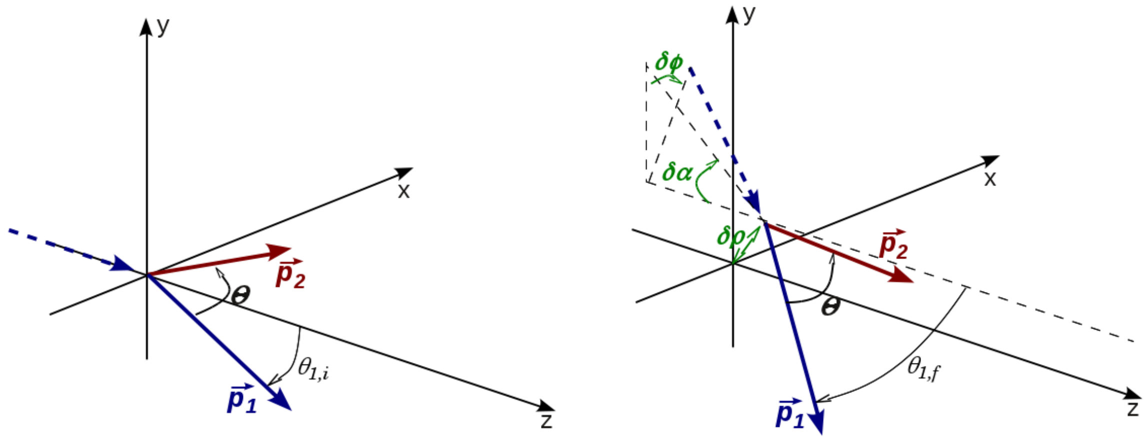


**Figure 4.34**: Sketch illustrating the vertex and angular smearing. Before the smearing acts, the incoming beam, indicated by the blue dashed arrow has a direction collinear to the $z-$axis and the outgoing particles are emitted from $x = y = z = 0$. The introduction of the vertex and angular smearing results in a shift by $\delta\rho = \sqrt{(\delta x)^2 + (\delta y)^2 + (\delta z)^2}$ of the vertex and a change on the direction of each generated particle according to the angular smearing parameters $\delta\alpha$ and $\delta\phi$. The figure corresponds to the case of two primary particles in which the relative angle $\Theta$ between their respective directions is conserved by the operation.

the variation of the polar angle after the angular smearing depends on the initial polar angle and the final azimuthal angle.

In more explicit way, like the situation illustrated by Figure 4.34, one can consider the case where a particle initially generated with a direction lying in the $xz-$plane ($p_y = 0$). The total rotation matrix expressing the angular smearing reads:

$$\mathbf{R}_{xz} = \begin{pmatrix} c_\phi & -s_\phi & 0 \\ c_\alpha s_\phi & c_\alpha c_\phi & -s_\alpha \\ s_\alpha s_\phi & s_\alpha c_\phi & c_\alpha \end{pmatrix} \tag{4.46}$$

where $c_\phi = \cos(-\delta\phi)$, $s_\phi = \sin(-\delta\phi)$, $c_\alpha = \cos(-\delta\alpha)$ and $s_\alpha = \sin(-\delta\alpha)$. Here, the angle $\delta\phi$ corresponds to the final azimuthal angle after smearing. With the current assumption, the final polar angle $\theta_f$ after the operation is given by

$$\cos\theta_f = \sin\theta_i s_\alpha s_\phi + \cos\theta_i c_\alpha\,, \tag{4.47}$$

with the angle $\theta_i$ is the initial polar angle at which the particle is emitted.

For a small beam angular divergence of the order of $0.3\,mrad$, the relative variation of the polar angle due to the angular smearing as functions of $\theta_i$ and $\phi_f$ is shown in Figure 4.35. Due to the smallness of $\delta\alpha$, the variation shows a strong dependence on $\phi_f$ rather than on $\theta_i$. The influence of the polar angle appears mainly in the boundary values, i.e. at $\theta_i = 0$ and $\pi$, for $\phi_f = -\pi$, 0 and $+\pi$ where the relative variation of the polar angle is at its minimum. Nevertheless, the variation can be neglected compared to the global variation in the full $\phi_f$ range. As expected, it reaches its maximum at $\phi_f = -\pm\pi/2$ where the difference between the initial and final polar angles is on the order of the input angle $\delta\alpha$.

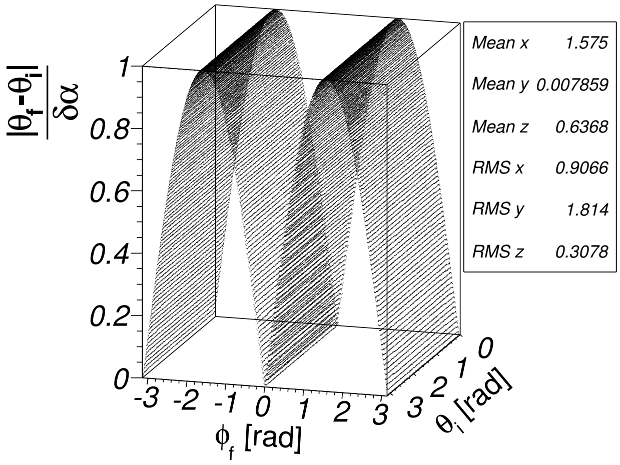


**Figure 4.35**: Relative variation $\frac{|\theta_f - \theta_i|}{\delta\alpha}$ of the polar angle of a generated particle as functions of the initial $\theta_i$ polar angle and the final $\phi_f (= \delta\phi)$ azimuthal angle. This histogram corresponds to an incident beam particle of $\delta\alpha$ polar angle taken to be equal to the angular divergence $\sigma_\alpha = 0.3\,mrad$. The mean value of the relative variation of the polar angle is about 0.64.

#### 4.4.2.2 Consequence on the angular resolution

Unlike the idealistic situation, the introduction of the angular smearing has a consequence that the incoming antiprotons hit the the proton target at a non-zero polar angle. In other words, the angular divergence is involved in the angle $\theta_{true}$.

Taking into account the expected properties of the HESR antiproton beam described previously, the angular resolution variation of the LuMo for the $\bar{\text{P}}$ANDA beam momentum is plotted on the left side of Figure 4.36. For reference, the variation corresponding to the idealistic situation is also represented in the same graph. On the right side of the same figure, the relative contribution of the beam emittance on the angular resolution is plotted. One can conclude from the figure that the beam emittance leads to the deterioration of the angular resolution by about 75% at higher beam momenta and just by 15% for the lowest beam momentum.

Nevertheless, the resolution is always worse at lower beam momentum with a lower limit of about 0.2 *mrad* at higher beam momenta. This corresponds to the best angular resolution of the LuMo. This value is comparable to the mean of the relative variation of the polar angle introduced by the angular smearing process which is given by Figure 4.35. Indeed, referring to this histogram, one obtains the mean relative variation of the $\theta$ angle for an angular divergence of $\sigma_\alpha = 0.3\,mrad$ to be $0.64 \times \sigma_\alpha \simeq 0.2\,mrad$.

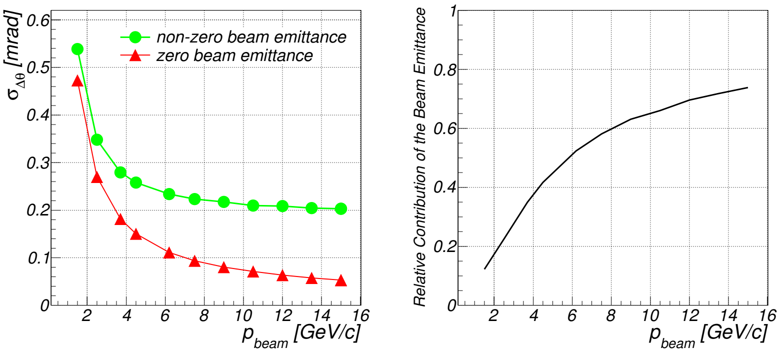


**Figure 4.36**: Variation of the LuMo angular resolution (*left*) corresponding to the non-zero beam emittance (green curve) compared with zero beam emittance (red curve) and the relative contribution of the beam emittance to the resolution (*right*) in the $\bar{\text{P}}$ANDA beam momentum range.

## 4.5 Estimation of the precision to measure the luminosity

In this section a simulation of the luminosity measurement will be presented. The study was Monte Carlo based and was performed by taking into account the full simulation chain developed throughout this chapter.

The $\bar{p}p$ elastic scattering events were generated using the DPM generator [GU05]. The differential and total cross sections parametrization within this generator will be presented in the next subsection. Also, the simulation setup considered that the antiproton beam has a finite emittance corresponding to the expected HESR antiproton beam properties previously described and that the dipole magnet is switched on. For the same reasons discussed in Section 4.4.1, this study focused on the beam momenta 1.5, 4.06. 8.9, 11.91 and 15 $GeV/c$.

### 4.5.1 Generation of $\bar{p}p$ elastic scattering events

Within the DPM generator a function has been implemented to express the variation of the differential cross section $d\sigma_{el}/dt$ for $\bar{p}p$ elastic scattering events with the 4-momentum transfer $t$, given by the relations Equations (3.20) to (3.23). These relations define the probability density function used by the event generator. Since the function diverges in the Coulomb region, $t \simeq 0$ must be omitted. This is done by setting a lower limit on the polar angle of the elastically scattered antiproton.

This lower angular bound has to be optimized by taking into account the dominant process within the geometrical acceptance of the LuMo for the different beam momenta under consideration. A relatively small lower angular limit will decrease the rate of hadronic events compared to Coulomb events. This helps for lower beam energies in which, referred to the right plot of Figure 3.5, the process is dominated by the Coulomb scattering within the acceptance of the LuMo. However, a small bound is not required for the higher beam momenta where the hadronic process is most relevant. Thus, the lower angular limit was set differently for each individual beam momentum in order to get an appropriate lower bound $t_{min}$ on the 4-momentum transfer. The values of the lower angular bound $\theta_{min}$ and its corresponding $t_{min}$ for the simulated beam momenta are given in Table 4.4.

| $p_{beam}$ $[GeV/c]$ | $\theta_{min}[°]$ | $-t_{min}$ $[GeV^2]$ |
|---|---|---|
| 1.5 | 0.20 | $5 \cdot 10^{-6}$ |
| 4.06 | 0.21 | $2 \cdot 10^{-5}$ |
| 8.9 | 0.29 | $1 \cdot 10^{-4}$ |
| 11.91 | 0.25 | $1 \cdot 10^{-4}$ |
| 15 | 0.22 | $1 \cdot 10^{-4}$ |

**Table 4.4**: Angular lower limit and the corresponding 4-momentum transfer used in the DPM generator for the simulated beam momenta.

The values of the the differential cross section parameters $\rho$, $b$ and $\sigma_{tot}$, which depend on the beam momentum, are calculated in the event generator using the following parametrizations:

$$\rho = -\frac{1}{(1-A_2)}\sqrt{\frac{A_3}{A_1}}\,, \tag{4.48}$$

$$b = \frac{A_1}{A_1(1-A_2)^2 + A_3}\left[\frac{1}{T_1} + \frac{A_2^2}{T_2} - A_2\left(\frac{1}{T_1} + \frac{1}{T_2}\right) + \frac{A_3}{A_1 T_2}\right]\,, \tag{4.49}$$

$$\sigma_{tot} = (1-A_2)\sqrt{16\pi(\hbar c)^2 A_1}\,. \tag{4.50}$$

The quantities $A_1$, $A_2$, $A_3$, $T_1$ and $T_2$ in the above relations parametrize the differential $\bar{p}p$ elastic cross section to match the existing experimental data in the $\bar{\text{P}}$ANDA beam momentum range. For a given beam momentum $p_{beam}$, these quantities read:

$$A_1 = 115.0 + 650.0 \cdot e^{-p_{beam}/4.08}\,, \tag{4.51}$$

$$A_2 = 0.0687 + 0.307 \cdot e^{-p_{beam}/2.367}\,, \tag{4.52}$$

$$A_3 = 0.8372 + 39.53 \cdot e^{-p_{beam}/0.765}\,, \tag{4.53}$$

$$T_1 = 0.0899\,, \tag{4.54}$$

$$T_2 = -2.979 + 3.353 \cdot e^{-p_{beam}/483.4}\,. \tag{4.55}$$

Comparisons of the differential cross section parameters used by the event generator with the existing data compiled by the Particle Data Group [N+10] are shown in Figure 4.37 for the relevant $\bar{\text{P}}$ANDA beam momenta.

The top plots of Figure 4.37 show a comparison of the $\rho$ parameter. A discrepancy is observed between the DPM parametrization and the data. The parametrization used by the event generator agrees with the measured data for only a couple of points with absolute errors less than 0.05. Moreover, at low momenta the variations of the data and the parametrization go in opposite directions and at $p_{beam} = 1.5\,GeV/c$ a maximum absolute error of 0.3 is reached. One can note from these plots that there are very few measured values of this parameter for the considered beam momenta range, thus it is difficult to achieve the correct parametrization.

The middle plots of Figure 4.37 are related to the nuclear slope parameter $b$. Within the error bars, the value of the parameter from the event generator agrees with the existing data. For most points, the relative errors are less than 5%, its maximum value is about 14% at $p_{beam} = 7\,GeV/c$ and for the beam momenta used in the current study, the relative errors are about 4%. However, even though more points have been measured for this parameter than for $\rho$, there are still several beam momentum intervals relevant for $\bar{\text{P}}$ANDA with no data points.

The comparison of the total cross section $\sigma_{tot}$ is shown by the bottom plots of Figure 4.37. There are many data points at low beam momenta ($p_{beam} < 3\,GeV/c$) where its variation is

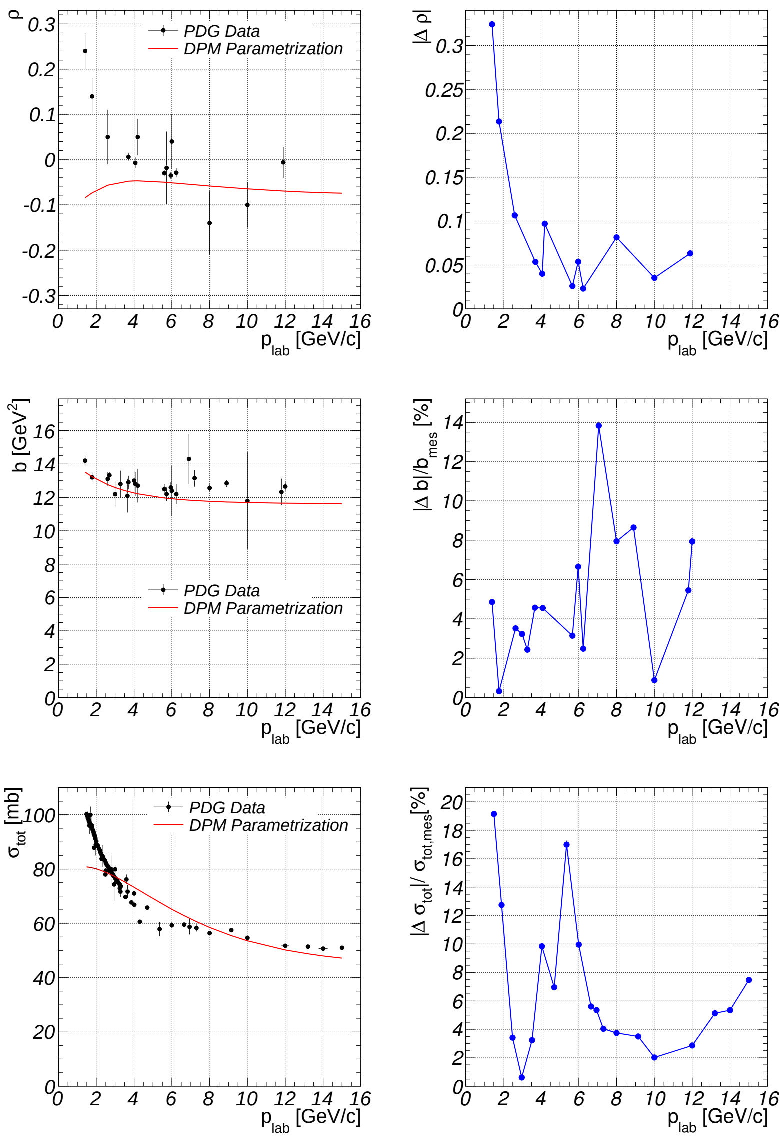


**Figure 4.37**: Comparison of the values of the parameters $\rho$ (*top*), $b$ (*middle*) and $\sigma_{tot}$ (*bottom*) computed by the DPM generator (red curves) with the world data in [N+10]. (*left*) shows the data and DPM parametrization as a function of the beam momentum. (*right*) shows the absolute errors for $\rho$ and the relative errors for $b$ and $\sigma_{tot}$ between the two distributions. In case many data points with similar beam momentum exist, their means were used.

stronger than that of the parametrization which is roughly constant. In this range of momentum, the relative error of $\sigma_{tot}$ increases from nearly 0 to 20%. A strong disagreement is also observed in the intermediate energies where the relative errors are about 12%. For $p_{beam} > 7\,GeV/c$, the two results seem consistent with each other. Nevertheless, the relative differences are about 4% and there is a lack of measured data at high beam momenta.

As a conclusion for this comparison, the parametrizations used by the DPM generator show slight differences compared to the world measured data for the beam momenta relevant for $\bar{\text{P}}$ANDA. The reason for this discrepancy may be because the quantities $A_1$, $A_2$, $A_3$, $T_1$

| Parameter | Beam momentum $[GeV/c]$ | | | | |
|---|---|---|---|---|---|
| | 1.5 | 4.06 | 8.9 | 11.91 | 15 |
| $\rho$ | -0.138 | -0.061 | -0.072 | -0.080 | -0.085 |
| $b\,[GeV^2]$ | 13.442 | 12.253 | 11.729 | 11.656 | 11.619 |
| $\sigma_{tot}[mb]$ | 80.818 | 73.066 | 56.123 | 50.374 | 47.217 |

**Table 4.5**: Differential $\bar{p}p$ elastic cross section parameters used by the DPM generator for different beam momenta.

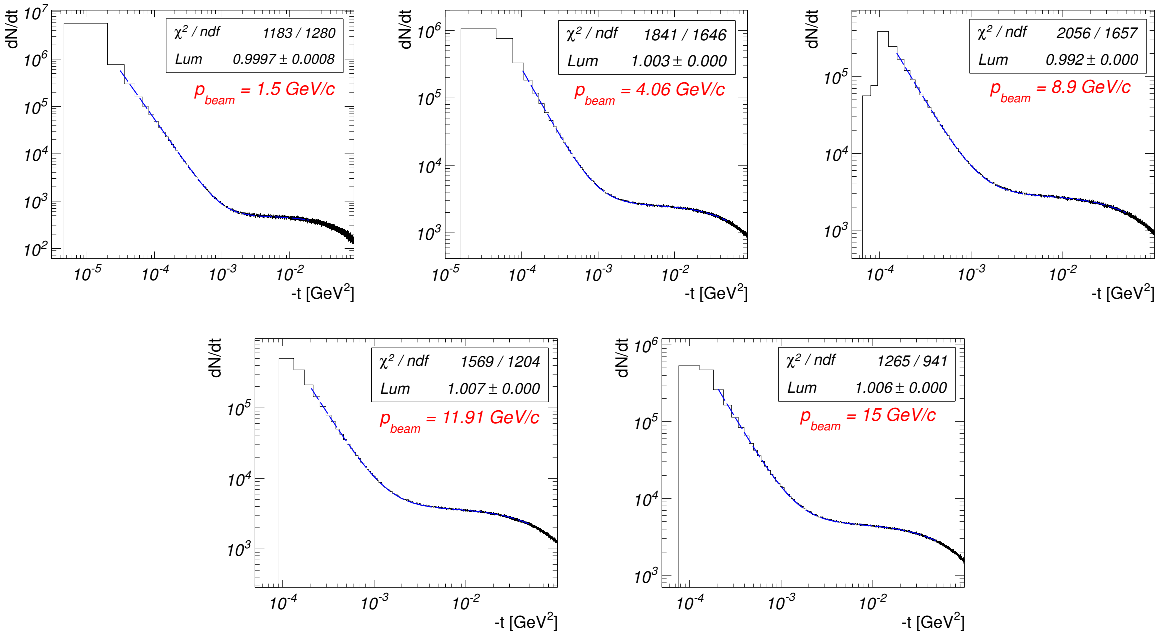


**Figure 4.38**: Distribution of the antiprotons generated elastically by the DPM generator as a function of the 4-momentum transfer $t$ for the five simulated beam momenta. The dashed blue lines are fits to the distributions using the function defined in Equation (4.56). The fitted values of the luminosity are expressed in units of $10^{31}cm^{-2}s^{-1}$.

and $T_2$ have only been determined for specific beam momenta and for a wider range of the momentum transfer up to $|t| \simeq 2\,GeV^2$ [G+08]. For this study, the values of the $\rho$, $b$ and $\sigma_{tot}$ parameters calculated by the DPM generator were used as start values which are listed in Table 4.5 for the five different beam momenta studied.

Based on the values in Table 4.5, the $\bar{p}p$ elastic scattering spectra at the event generator level are obtained from the distribution of the scattered antiproton as a function of the 4-momentum transfer. These distributions are shown in Figure 4.38 for the five simulated beam momenta.

The distributions have been fit with the function $dN/dt$ given by:

$$\frac{dN}{dt} = \mathcal{L} \times \frac{d\sigma_{el}}{dt} \times \Delta\tau\,, \tag{4.56}$$

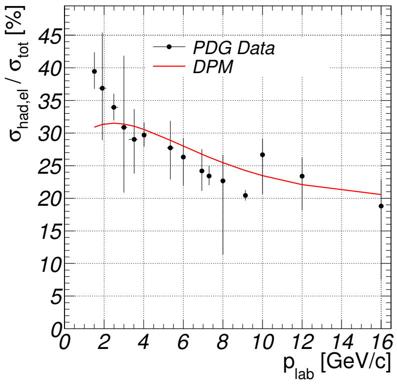


**Figure 4.39**: Ratio of the integrated hadronic cross section to the total cross section.

where $d\sigma_{el}/dt$ is the differential $\bar{p}p$ elastic cross section which contains the three parameters described in the text, $\mathcal{L} = \int \mathring{\mathcal{L}} d\tau$ is the integrated luminosity and $\Delta\tau$ the experimental running time. This latter is calculated using the hadronic process in which the corresponding cross section has a finite value i.e.:

$$\Delta\tau = \frac{n_{had}}{\mathcal{L} \cdot \sigma_{had}} . \tag{4.57}$$

Here $\sigma_{had}$ is the hadronic elastic cross section integrated over the range of the 4-momentum transfer in which events are generated. The ratio of the integrated hadronic cross section to the total cross section calculated within the DPM generator is compared with the ratio obtained from the experimental measurements in [N+10] in Figure 4.39. A good agreement is noted for the two sets of measurements. The hadronic cross section contributes about $30-35\%$ of the total cross section at lower momentum to 20% at higher beam momentum in the considered beam momentum range.

The rate of hadronic events $n_{had}$ is obtained by:

$$n_{had} = n_{event} \cdot \frac{\sigma_{had}}{\sigma_{had} + \sigma_{coul}} , \tag{4.58}$$

where $\sigma_{coul}$ is the integrated Coulomb cross section and $n_{event}$ is number of generated events. For each individual beam momentum setup, the simulation was performed with $n_{event} = 10^7$ events and assuming the luminosity $\mathcal{L} = 10^{31} cm^{-2} s^{-1}$. The values of $\Delta\tau$, $\sigma_{coul}$ and $\sigma_{had}$ for the five simulated beam momenta are listed in Table 4.6.

In summary, the fit function contains five parameters namely $\rho$, $b$, $\sigma_{tot}$, $\Delta\tau$ and $\mathcal{L}$. The $\Delta\tau$ parameter is the time during which the measurement is performed and thus is known *a priori*. Therefore, it behaves like a constant parameter in the fit function. In the case of Figure 4.38, the remaining fit parameters were kept fixed apart from the luminosity $\mathcal{L}$. One can note the perfect fit to the distributions by the function in which the $\chi^2/ndf < 1.3$, the relative differences $\Delta\mathcal{L}/\mathcal{L} < 0.8\%$ and precisions are better than $10^{-3}$. Throughout this study, the luminosity parameter is expressed in units of $10^{31} cm^{-2} s^{-1}$.

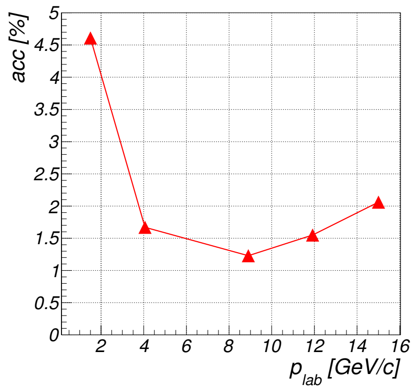


**Figure 4.40**: Variation of the acceptance of the LuMo as function of the beam momentum.

| $p_{beam}$ $[GeV/c]$ | 1.5 | 4.06 | 8.9 | 11.91 | 15 |
|---|---|---|---|---|---|
| $\sigma_{coul}$ $[mb]$ | 72.55 | 13.46 | 2.62 | 2.60 | 2.61 |
| $\sigma_{had}$ $[mb]$ | 26.23 | 21.61 | 13.53 | 11.02 | 9.74 |
| $\Delta\tau$ $[s]$ | 10.12 | 28.51 | 61.91 | 73.38 | 80.91 |
| $n_{det}$ | 461611 | 166991 | 123051 | 155366 | 205726 |
| $Rate$ $[/s]$ | 45613 | 5776 | 1987 | 2117 | 2542 |

**Table 4.6**: Values of the integrated cross section of the Coulomb and hadronic processes, $\sigma_{coul}$ and $\sigma_{had}$, respectively, the experimental running time $\Delta\tau$, the number of detected tracks $n_{det}$ and the antiproton rate in the LuMo for $10^7$ elastic events generated at a luminosity of $10^{31} cm^{-2} s^{-1}$ with the DPM event generator.

### 4.5.2 Detector acceptance

The acceptance of the LuMo is defined as the fraction of the simulated tracks within the geometric coverage of the detector i.e. the fraction of the generated tracks that hit all four detector planes for a given simulation setup. It allows to determine the rate of the antiprotons elastically scattered in the detector.

The acceptance $acc$ and the rate are then calculated as:

$$acc = \frac{n_{det}}{n_{event}}, \quad (4.59)$$

$$Rate = \frac{n_{det}}{\Delta\tau}, \quad (4.60)$$

where $n_{det}$ is the number of tracks detected by the LuMo. The plot showing the variation of the acceptance as function of the beam momentum for this simulation is drawn in Figure 4.40. The acceptance drops between the two lowest simulated beam momenta because the Coulomb region goes to the smaller angles at $p_{beam} = 4.06\,GeV/c$. It rises for higher beam momenta because with the same value of $t_{min}$ set for these beam momenta, the LuMo $t-$range increases with the beam momentum. The expected rate and the number of detected tracks corresponding to the simulation setups described above are given in Table 4.6 for the five considered beam energies. In this table the integrated cross sections of the Coulomb process $\sigma_{coul}$ are related to the $\theta_{min}$ values given in Table 4.4.

For this study, it is essential to have the distribution of the acceptance as a function of the 4-momentum momentum which will be used as normalization factor for the fit procedure. It is obtained by dividing the $t-$spectrum of the $\bar{p}p$ elastic scattering for the simulated tracks within the detector acceptance by the spectrum of all propagated tracks from the interaction region. This latter is different from the *true* spectrum generated by at the event generator level because it includes the effect of the beam smearing. Such distributions are shown in Figure 4.41. Here, to show the difference, the same fit settings applied on the distributions in Figure 4.38 were used and result in larger $\chi^2/ndf$ values.

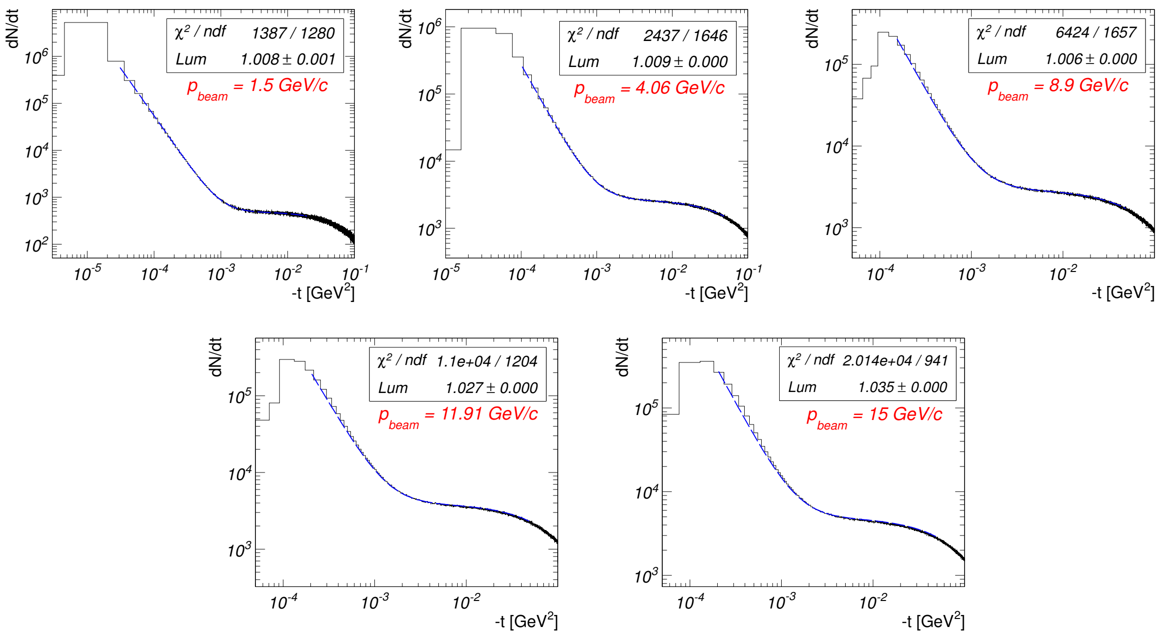


**Figure 4.41**: Spectra of the $\bar{p}p$ elastic scattering determined from the output of the simulation for the five simulated beam momenta. The dashed blue lines are fits to the distributions with the same settings as the fit on the distributions of Figure 4.38. The fitted values of the luminosity are expressed in units of $10^{31}cm^{-2}s^{-1}$.

The distributions of the scattered antiprotons in the $t-$ranges covered geometrically by the LuMo for the five simulated energies are shown in the left group of plots of Figure 4.42. The $t-$range coverage of the detector are different from one beam momentum setup to another. Referring to Figure 3.5 where the Coulomb-nuclear interference corresponds to $-t \simeq 10^{-3}\,GeV^2$, the luminosity monitor is in the Coulomb dominance region for the lowest beam momentum ($p_{beam} = 1.5\,GeV/c$), in the interference region for the intermediate beam momenta ($p_{beam} = 4.06$ and $8.9\,GeV/c$) and mostly in the nuclear region for the higher beam momenta ($p_{beam} \geq 11.91\,GeV/c$).

The $t-$acceptance spectra of the LuMo for the five beam momenta are shown by the histograms in the right part of Figure 4.42. One can observe the similarity of the behavior between all distributions in which the acceptance decreases at high values of $|t|$. This is because at larger radial distance from the beam axis, the azimuthal angular coverage of the detector decreases.

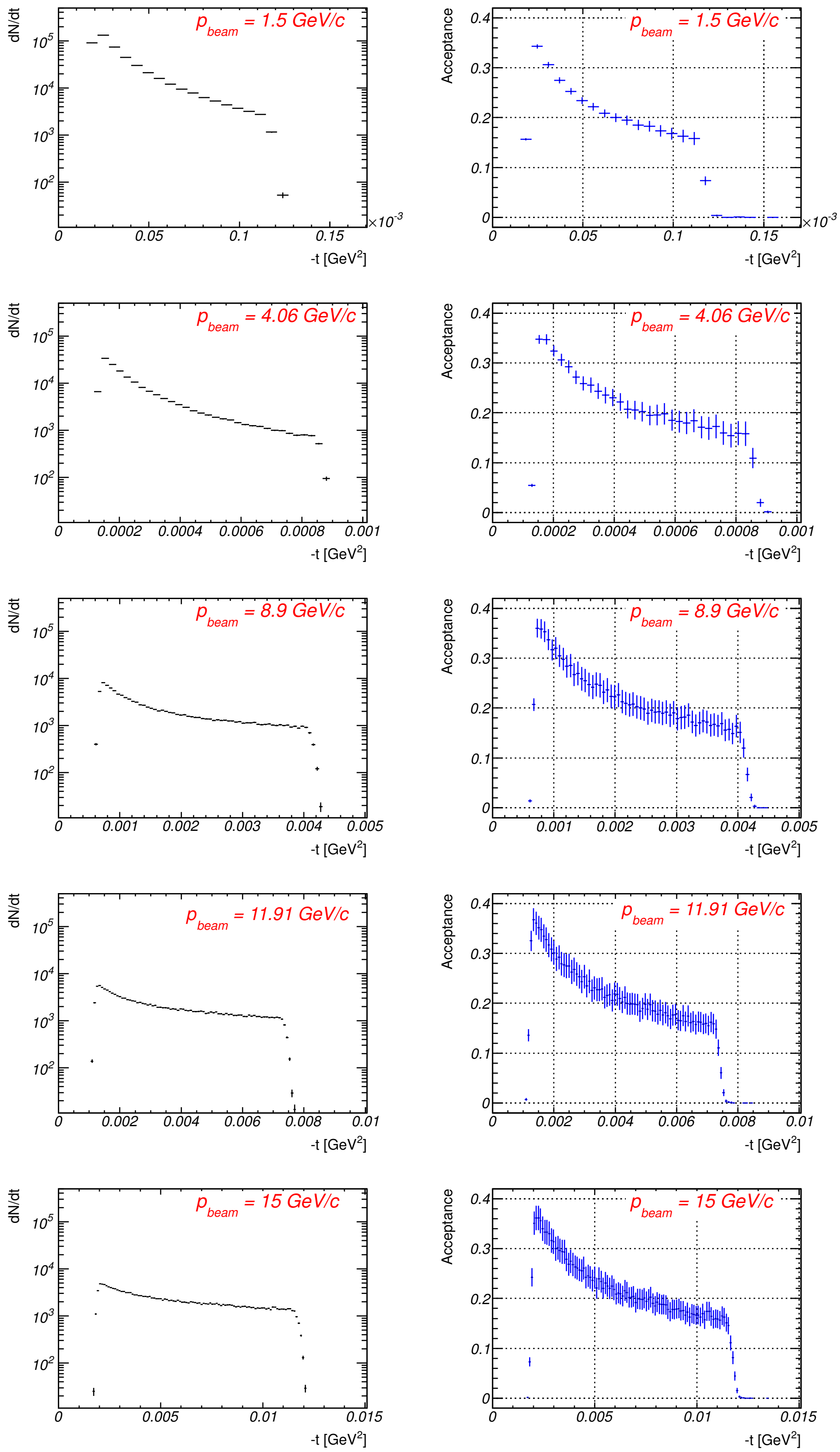


**Figure 4.42**: Spectra of the $\bar{p}p$ elastic scattering in the LuMo (*left*) and acceptance of the detector (*right*) for the five simulated beam momenta.

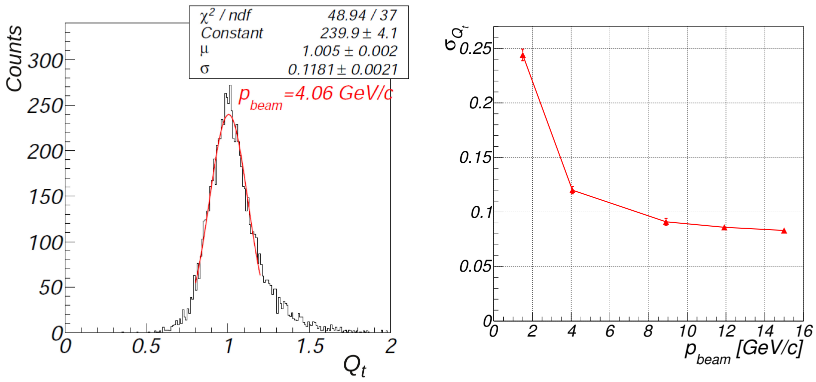


**Figure 4.43**: Distribution of the quotient $Q_t$ for $p_{beam} = 4.06\,GeV/c$ *(left)*. The red line is a Gaussian fit to the distribution. The variation of the 4-momentum transfer resolution as a function of the beam momentum *(right)*.

## 4.5.3 Reconstruction of the $\bar{p}p$ elastic scattering spectrum

### 4.5.3.1 Momentum transfer resolution

The value of the reconstructed 4-momentum transfer $t_{reco}$ is deduced from the polar angle $\theta$ of the reconstructed track by means of the relations Equation (3.8) and Equation (3.10). To determine the 4-momentum transfer resolution, one needs to define the quotient $Q_t$ given by:

$$Q_t = \frac{t_{true}}{t_{reco}}\,, \tag{4.61}$$

where $t_{true}$ is the 4-momentum transfer calculated at the event generator level. The distribution of $Q_t$ is nearly a Gaussian centered at 1 and with standard deviation of $\sigma_{Q_t}$ as it is shown in the left picture of Figure 4.43. Its standard deviation defines the resolution of the LuMo in terms of 4-momentum transfer $t$.

The variation of the resolution for the simulated beam momenta is plotted in the right part of Figure 4.43. As expected, the resolution worsens from 0.083 at $p_{beam} = 15\,GeV/c$ to 0.244 at $p_{beam} = 1.5\,GeV/c$.

### 4.5.3.2 Determination of the luminosity

The luminosity is determined from the reconstructed spectrum of the $\bar{p}p$ elastic scattering by the LuMo by fitting this latter with the function defined above. In order to fit the reconstructed spectrum properly, it has to be corrected by dividing it with the acceptance spectrum (right plots of Figure 4.42). This has only been performed for bins in the $t-$acceptance spectrum above 15% to reduce error at the edges of the distributions. The distributions of the measured antiproton as a function of the reconstructed 4-momentum transfer are shown by the left plots of Figure 4.44. The spectra resulting from the operation are shown by the right plots of Figure 4.44.

In the case of the right plots of Figure 4.44, the fits to the corrected spectra were performed with only one parameter allowed to vary freely, the luminosity. The other parameters ($\rho$, $b$ and $\sigma_{tot}$) were kept fixed. Thus, the obtained precision on the luminosity can be interpreted

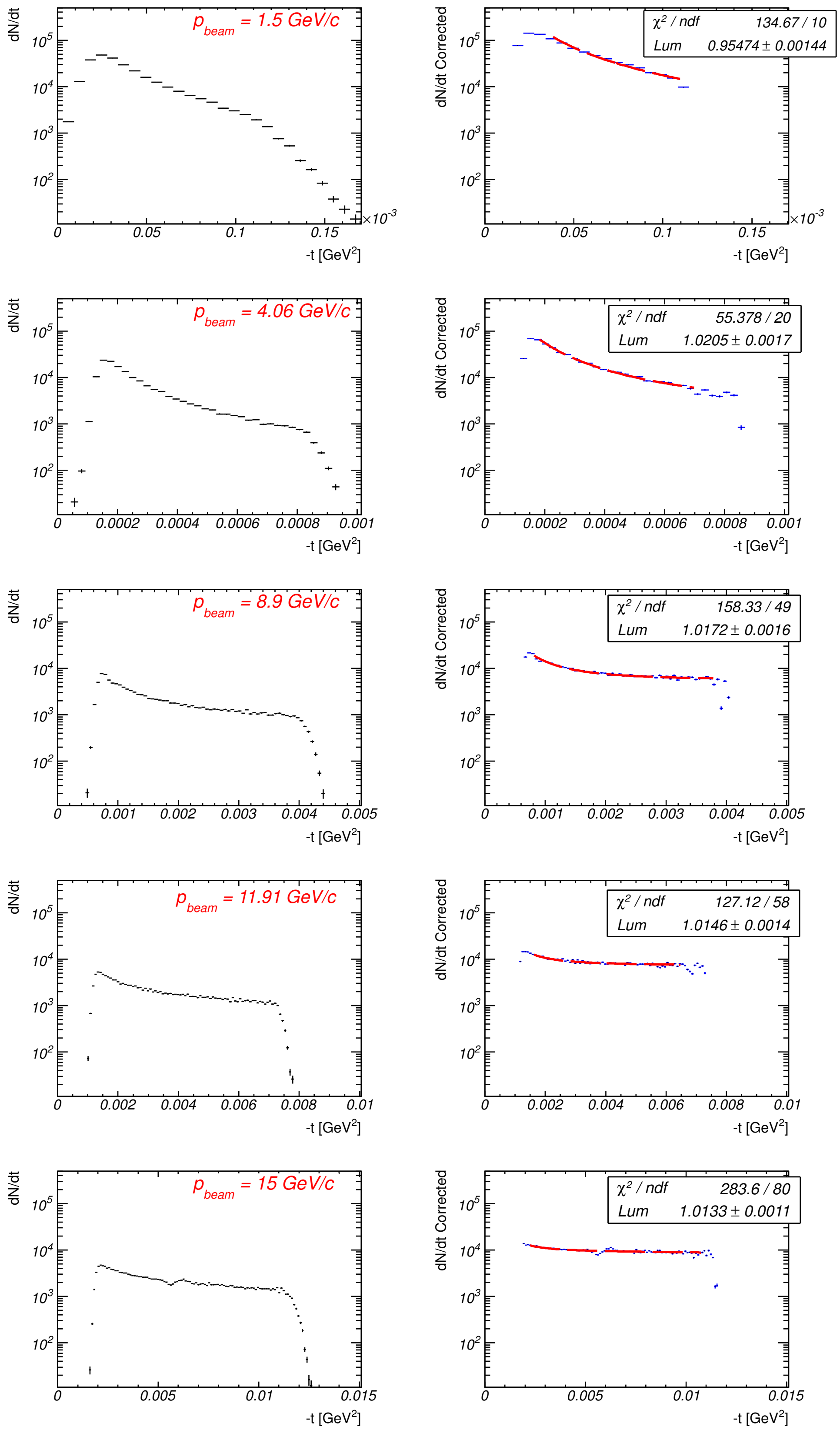


**Figure 4.44**: Reconstructed $t-$spectrum (*left*) and the corrected $t-$spectrum (*right*) with the LuMo. The corrected spectrum is fit with the function defined in Equation (4.56) (dashed red line) in which only the luminosity parameter is released. The luminosity is expressed in units of $10^{31} cm^{-2}s^{-1}$.

as the effect of the intrinsic detector resolution and the beam emittance. As a consequence, the relative errors on the luminosity increases at lower beam momentum. Its biggest value is about $\Delta\mathcal{L}/\mathcal{L} = 4.5\%$ at the lowest beam momentum and the most precise value, achieved at the highest beam momentum corresponds to $\Delta\mathcal{L}/\mathcal{L} = 1.3\%$. In addition, for $p_{beam} \geq 8.9\,GeV/c$, the relative errors on the luminosity are similar and $\Delta\mathcal{L}/\mathcal{L} < 2.0\%$.

### 4.5.4 Systematic uncertainties on the luminosity measurement

Apart from the detector resolution, the effect of different factors judged to be the main sources of systematic uncertainties connected with the measurement method previously described was investigated. These factors include the poor knowledge of the differential cross section parameters $\rho$, $b$ and $\sigma_{tot}$ and the $\bar{p}p$ inelastic background contamination on the elastic process spectrum.

The estimation of the systematic errors on the luminosity performed as functions of these factors is given later on this section. Before this, the study of the correlation of the luminosity with the cross section parameters and the determination of the rate of the $\bar{p}p$ inelastic process are presented in the subsequent subsections.

#### 4.5.4.1 Study of the correlation between the luminosity and the cross section parameters

The study performed previously assumes that the parameters connected with the differential cross section ($\rho$, $b$ and $\sigma_{tot}$) are absolutely known and the error on the measurement of the luminosity is uniquely the result of the detector resolution. However, these parameters are not known with arbitrary precision. Instead, very few measurements in the beam momentum range relevant for $\bar{\text{P}}$ANDA exist, thus they must be determined.

One method consists of a determination of the luminosity simultaneously with the three parameters $\rho$, $b$ and $\sigma_{tot}$ by means of the fit to the (corrected) reconstructed spectrum in the LuMo. This method requires the consideration of any existing correlation between these four fit parameters. The correlation can be determined by releasing all parameters during the fit procedure. The correlation coefficients between parameters obtained from the fit on the reconstructed spectrum within the $t-$range relevant for a given beam momentum of the LuMo are given in Table 4.7. This table exhibits the strong correlations between each individual parameter for all considered beam momenta.

By focusing only on the luminosity, one can note the following aspects. The luminosity is highly correlated with the $\rho$ parameter within the five different fit ranges, with the correlation coefficient $\rho_{\mathcal{L}\rho} \geq 0.91$. In particular, the correlation between these two parameters is stronger at $p_{beam} = 8.9\,GeV/c$ where $\rho_{\mathcal{L}\rho} = 0.99$. This is due to the fact that at this beam momentum the detector acceptance contains the Coulomb-nuclear interference region where the effect of the $\rho$ parameter on the shape of the differential cross section variation is the most relevant. As one moves away from this region, $\rho_{\mathcal{L}\rho}$ decreases. That is why $\rho_{\mathcal{L}\rho}$ has a minimum of 0.91 at $p_{beam} = 15\,GeV/c$.

The nuclear slope parameter $b$ and the total cross section $\sigma_{tot}$ are rather more sensitive to the nuclear region i.e. they influence the differential cross section for relative higher values

$\mathbf{p_{beam} = 1.5\,GeV/c}$

| | $\mathcal{L}$ | $\rho$ | $b$ | $\sigma_{tot}$ |
|---|---|---|---|---|
| $\mathcal{L}$ | 1.00 | 0.94 | -0.21 | -0.69 |
| $\rho$ | - | 1.00 | 0.98 | 0.14 |
| $b$ | - | - | 1.00 | 0.95 |
| $\sigma_{tot}$ | - | - | - | 1.00 |

$\mathbf{p_{beam} = 4.06\,GeV/c}$

| | $\mathcal{L}$ | $\rho$ | $b$ | $\sigma_{tot}$ |
|---|---|---|---|---|
| $\mathcal{L}$ | 1.00 | 0.94 | 0.50 | -0.64 |
| $\rho$ | - | 1.00 | -0.72 | 0.88 |
| $b$ | - | - | 1.00 | 0.94 |
| $\sigma_{tot}$ | - | - | - | 1.00 |

$\mathbf{p_{beam} = 8.9\,GeV/c}$

| | $\mathcal{L}$ | $\rho$ | $b$ | $\sigma_{tot}$ |
|---|---|---|---|---|
| $\mathcal{L}$ | 1.00 | 0.99 | 0.80 | -0.95 |
| $\rho$ | - | 1.00 | -0.68 | 0.87 |
| $b$ | - | - | 1.00 | 0.94 |
| $\sigma_{tot}$ | - | - | - | 1.00 |

$\mathbf{p_{beam} = 11.91\,GeV/c}$

| | $\mathcal{L}$ | $\rho$ | $b$ | $\sigma_{tot}$ |
|---|---|---|---|---|
| $\mathcal{L}$ | 1.00 | 0.94 | 0.84 | -0.98 |
| $\rho$ | - | 1.00 | -0.62 | 0.85 |
| $b$ | - | - | 1.00 | 0.93 |
| $\sigma_{tot}$ | - | - | - | 1.00 |

$\mathbf{p_{beam} = 15\,GeV/c}$

| | $\mathcal{L}$ | $\rho$ | $b$ | $\sigma_{tot}$ |
|---|---|---|---|---|
| $\mathcal{L}$ | 1.00 | 0.91 | 0.91 | -1.00 |
| $\rho$ | - | 1.00 | -0.67 | 0.88 |
| $b$ | - | - | 1.00 | 0.93 |
| $\sigma_{tot}$ | - | - | - | 1.00 |

**Table 4.7**: Correlation matrices between the four parameters obtained from fits on the reconstructed spectra in the LuMo for the five simulated beam momenta.

of the 4-momentum transfer. This fact explains the increase in correlation between these parameters and the luminosity as long as the detector $t-$range approaches the nuclear region. The correlation coefficient $\rho_{\mathcal{L}b}$ between the luminosity and the slope parameter rises from $\rho_{\mathcal{L}b} = -0.21$ at the lowest beam momentum to $\rho_{\mathcal{L}b} = 0.91$ at the highest beam momentum. Similarly, the luminosity and the total cross section correlation coefficient $\rho_{\mathcal{L}\sigma}$ is minimum and $\rho_{\mathcal{L}\sigma} = -0.69$ at lower $t-$values. At $p_{beam} = 15\,GeV/c$, it reaches its maximum of $\rho_{\mathcal{L}\sigma} = -1$. This is due to the fact that at this beam momentum, the $\bar{p}p$ elastic scattering is mostly dominated by the nuclear process where the differential cross section is proportional to $\sigma_{tot}$.

#### 4.5.4.2 Rate of $\bar{p}p$ inelastic background

The estimation of the $\bar{p}p$ inelastic rate which constitutes the main background of the luminosity measurement was investigated. A full simulation was performed in which the $\bar{p}p$ inelastic events were generated using the DPM generator. Within the model, the $\bar{p}p$ annihilation final state is determined by the parametrization of the cross sections of various processes leading to string formation [GU05, UG02]. The cross section of the different processes are given in Table 4.8.

The main goal here is to determine the ratio of the inelastic events to the elastic events in the LuMo. At each of the five beam momenta used previously $n_{inel} = 2 \cdot 10^6$ $\bar{p}p$ inelastic events were generated. The corresponding distributions with $\theta$ from 0 to $10\,mrad$ are shown in Figure 4.45. Each distribution is compared with the corresponding $\bar{p}p$ elastic scattering spectrum. The number of the simulated elastic events $n_{el}$ was deduced using the following

| $p_{beam}$ $[GeV/c]$ | 1.5 | 4.06 | 8.9 | 11.91 | 15 |
|---|---|---|---|---|---|
| $\sigma_{tot}$ $[mb]$ | 80.818 | 73.066 | 56.123 | 50.374 | 47.217 |
| $\sigma_{had,el}$ $[mb]$ | 26.23 | 21.61 | 13.53 | 11.02 | 9.74 |
| $\sigma_{inel}$ $[mb]$ | 54.59 | 51.39 | 42.59 | 39.35 | 37.48 |
| $n_{el}$ | $3.62 \cdot 10^6$ | $1.36 \cdot 10^6$ | $7.6 \cdot 10^5$ | $7 \cdot 10^5$ | $6.6 \cdot 10^5$ |

**Table 4.8**: Total cross section, hadronic elastic cross section, inelastic cross sections for the simulated beam momenta and the number of generated elastic events corresponding to $2 \cdot 10^6$ inelastic events.

| $p_{beam}$ $[GeV/c]$ | 1.5 | 4.06 | 8.9 | 11.91 | 15 |
|---|---|---|---|---|---|
| Rate for $\vec{B}_{dip} \neq \vec{0}$ | 19 | 51 | 122 | 175 | 321 |
| Rate for $\vec{B}_{dip} = \vec{0}$ | 67 | 267 | 852 | 1546 | 2244 |

**Table 4.9**: Rates of $\bar{p}p$ inelastic events in the LuMo for the different simulated beam momenta for the two cases of dipole field $\vec{B}_{dip}$ is switched on and off.

equation:

$$n_{el} = n_{inel} \cdot \frac{(\sigma_{had,el} + \sigma_{coul,el})}{\sigma_{inel}}, \tag{4.62}$$

and its value is given in Table 4.8 for all considered beam momenta.

Two different simulation were performed: one has the dipole field switched off and another with dipole field on. The consideration of the these two setups allows to investigate the role of the dipole field in the background suppression. For both configurations the HESR antiproton beam properties were taken into account.

In order to estimate the rate of the inelastic background in the luminosity monitor, the reconstructed tracks are pointed back onto the interaction region (the $xy-$plane at $z = 0$) using GEANE. In this case, the tracks are assigned the same momenta as the beam. The rates of inelastic events in the detector obtained with the two simulation setups are given in Table 4.9. The existence of the dipole field reduces the rate of the background by a factor of about 3.5 at lower beam momenta to about 8 at higher beam momenta. But at $p_{beam} = 1.5\,GeV/c$, the relative ratio of the inelastic background events in the LuMo compared to the elastic events for both simulation setups is less than 1% as shown in Figure 4.46. The ratio of about 17% in case where the dipole is off at $p_{beam} = 15\,GeV/c$ is reduced to less than 3% when the field is on.

Furthermore, the distributions of the reconstructed vertices from inelastic events at the interaction region are compared with those of the elastic events. In Figure 4.47, the distributions of the $x-$positions of the projected reconstructed tracks onto the plane $z = 0$ for all five simulated beam momenta for elastic and inelastic events are shown. Here, only the simulation corresponding to dipole field on was considered since this matches the reality of the experiment. These histograms show a central Gaussian distributions corresponding to the elastic events and long inelastic tails. This demonstrates the high discriminator power of the dipole field. In this case, for each individual distribution, a cut of $3 \cdot \sigma$ was applied to reduce the amount of inelastic background where $\sigma$ is the vertex resolution corresponding to the $\bar{p}p$ elastic scattering events which is also given in the figure.

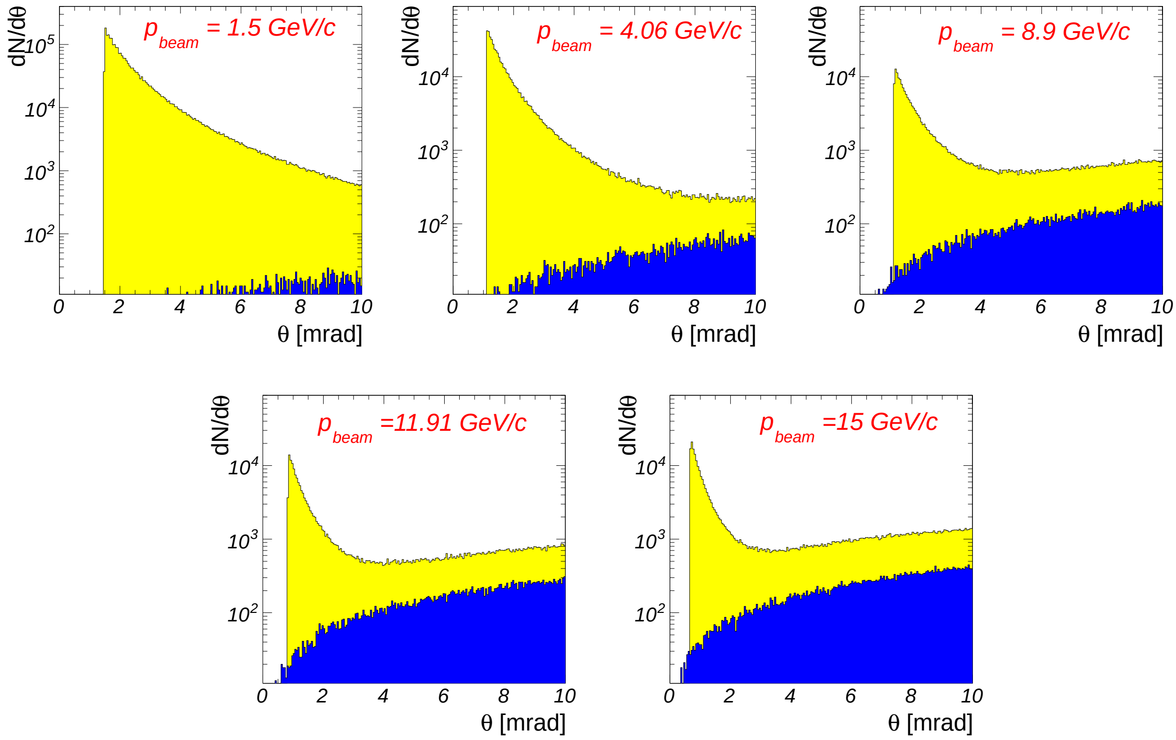


**Figure 4.45**: Distributions of the $\bar{p}p$ inelastic events (blue filled area) and the $\bar{p}p$ elastic events (yellow filled area) generated by the DPM generator in the vicinity of the angular acceptance of the LuMo.

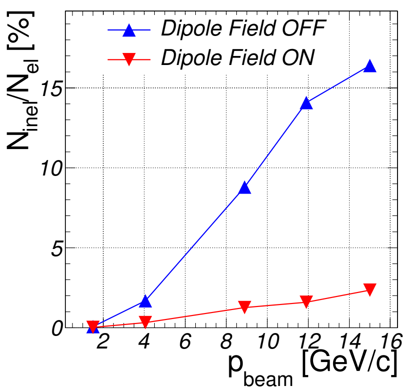


**Figure 4.46**: Ratio of the number of $\bar{p}p$ inelastic background to the number of elastic scattering events in the LuMo.

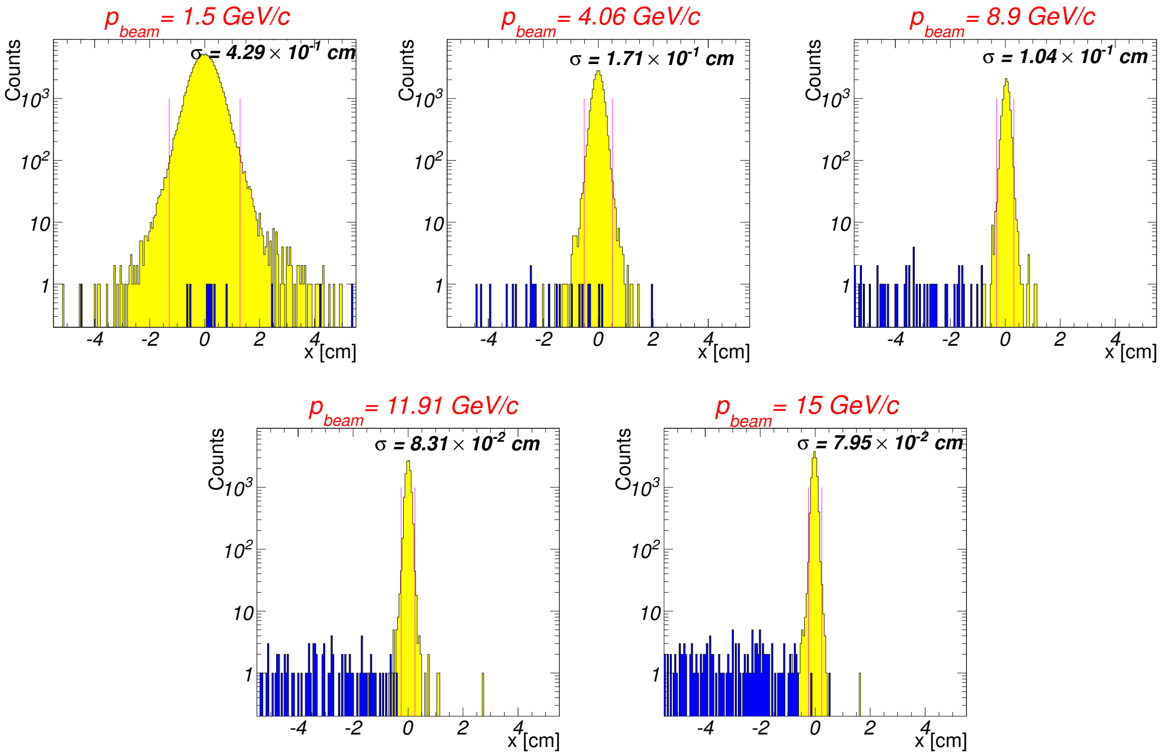


**Figure 4.47**: Distributions of the $x-$coordinate of the reconstructed vertex for the elastic events (yellow filled area) and inelastic events (blue filled area) for the case where the dipole field on. The magenta lines corresponds to the cut of $3 \cdot \sigma$.

#### 4.5.4.3 Results of the study of the systematic errors

Firstly, the impact of the systematic uncertainties on the different differential cross section parameters on the precision of the luminosity measurement in the relevant $t-$range for the LuMo was investigated. The influences of the $\rho$, $b$ and $\sigma_{tot}$ were taken separately as the luminosity (and its relative error) was measured for an uncertainty assigned to each individual parameter. For the $\rho$ parameter, the study was performed by adding 0.05 to true value which represents the average absolute fluctuation of the measured value in the $\bar{\text{P}}$ANDA beam momentum range (see Figure 4.37). For the other parameters, a relative uncertainty of 1% was considered.

Then, a systematic study of the influence of inelastic events was performed. For each simulated beam momentum, the distribution of the 4-momentum transfer $t$ is reconstructed at the LuMo for both elastic and inelastic events. Their respective $t-$spectra are shown separately in Figure 4.48 for different beam momenta. For a particular beam momentum, in the $t-$range of the antiproton scattered elastically in the luminosity monitor, there are very few entries corresponding to inelastic events.

For each individual study, the relative error on the luminosity was calculated with respect to the results with zero systematic error on each individual cross section parameter with pure $\bar{p}p$ elastic events obtained in Figure 4.44. The results for different settings are summarized in

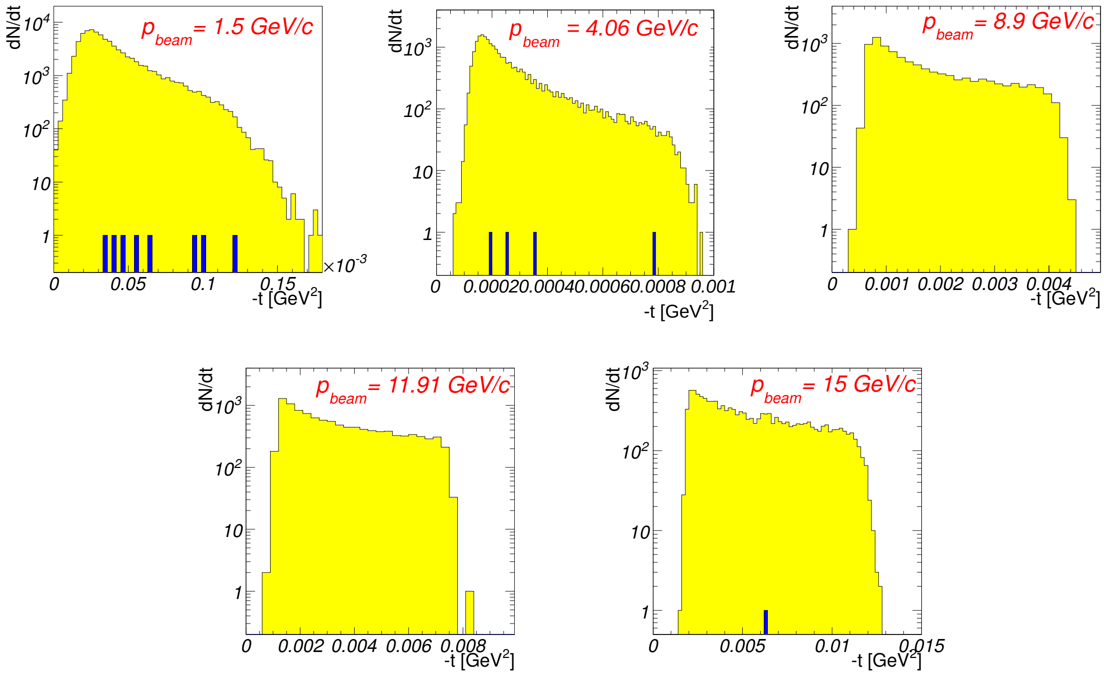


**Figure 4.48**: Reconstructed $t-$spectrum at the LuMo for the $\bar{p}p$ inelastic (blue area) and elastic (yellow area) events.

Table 4.10. The total systematic error was calculated by the square root of the sum of the squared errors from each individual measurement.

In most of the cases, the total systematic uncertainty on the luminosity is mainly dominated by the uncertainty due to the intrinsic detector resolution and the beam emittance. As results, as expected the systematic uncertainty is the largest for $p_{beam} = 1.5\,GeV/c$.

The second most important parameter is the parameter $\sigma_{tot}$. Its contribution on the uncertainty increases with the beam momentum, similar to the correlation coefficient $\rho_{\mathcal{L}\sigma}$. As a consequence, for $p_{beam} \geq 11.91\,GeV/c$ it becomes the dominating source of uncertainty on the measurement.

The change on the $\rho$ parameter has also a significant consequence on the luminosity measurement. Its effect are quite similar for all simulated beam momenta. It is slightly stronger at $p_{beam} = 8.9\,GeV/c$. This corroborates the observation that the correlation between this parameter with the luminosity is maximum ($\rho_{\mathcal{L}\rho} = 0.99$) at this beam momentum and almost the same for the other beam momenta.

The modification performed on the $b$ parameter did not have a significant effect on the deduced luminosity. A rough calculation indicates that a relative error of about 1% on the luminosity is obtained by an uncertainty of 60% on this parameter at $p_{beam} = 15\,GeV/c$ at which the correlation between these two parameters is the strongest ($\rho_{\mathcal{L}b} = 0.91$).

As seen in Figure 4.48, the rate of the inelastic events in the relevant $t-$range for the LuMo is very small, so that its effect is negligible on the luminosity measurement.

| | Beam momentum $[GeV/c]$ | | | | |
|---|---|---|---|---|---|
| | 1.5 | 4.06 | 8.9 | 11.91 | 15 |
| Detector resolution & beam emittance $\Delta\rho = \Delta b = \Delta\sigma_{tot} = 0$ | | | | | |
| $\mathcal{L}$ $[10^{31} cm^{-2} s^{-1}]$ | 0.9547 | 1.0205 | 1.0172 | 1.0146 | 1.0133 |
| $\Delta\mathcal{L}/\mathcal{L}$ [%] | 4.53 | 2.05 | 1.72 | 1.46 | 1.33 |
| $\rho \to \rho + 0.05$ | | | | | |
| $\mathcal{L}$ $[10^{31} cm^{-2} s^{-1}]$ | 0.9605 | 1.0276 | 1.0242 | 1.0221 | 1.0201 |
| $\Delta\mathcal{L}/\mathcal{L}$ [%] | 0.61 | 0.69 | 0.77 | 0.74 | 0.67 |
| $\Delta b/b = 1\%$ | | | | | |
| $\mathcal{L}$ $[10^{31} cm^{-2} s^{-1}]$ | 0.9547 | 1.0205 | 1.0172 | 1.0146 | 1.0133 |
| $\Delta\mathcal{L}/\mathcal{L}$ [%] | $< 10^{-4}$ | $< 10^{-4}$ | $< 10^{-4}$ | $< 10^{-4}$ | $< 10^{-4}$ |
| $\Delta\sigma_{tot}/\sigma_{tot} = 1\%$ | | | | | |
| $\mathcal{L}$ $[10^{31} cm^{-2} s^{-1}]$ | 0.9549 | 1.0223 | 1.0311 | 1.0325 | 1.0326 |
| $\Delta\mathcal{L}/\mathcal{L}$ [%] | 0.02 | 0.27 | 1.37 | 1.76 | 1.90 |
| Inelastic background | | | | | |
| $\mathcal{L}$ $[10^{31} cm^{-2} s^{-1}]$ | 0.9547 | 1.0205 | 1.0172 | 1.0146 | 1.0133 |
| $\Delta\mathcal{L}/\mathcal{L}$ [%] | $< 10^{-4}$ | $< 10^{-4}$ | $< 10^{-4}$ | $< 10^{-4}$ | $< 10^{-4}$ |
| Total systematic error [%] | 4.57 | 2.18 | 2.27 | 2.40 | 2.41 |

**Table 4.10**: Results on the study of the systematic errors connected with the measurement of the luminosity.

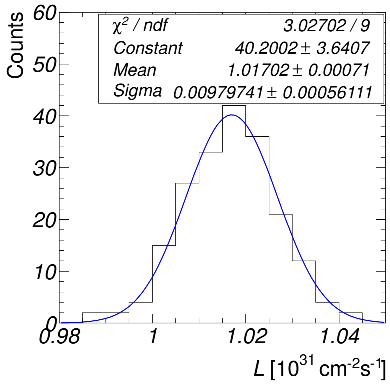


**Figure 4.49**: Distribution of the measured values of the luminosity corresponding to $N = 200$ data sets of $4 \cdot 10^6$ generated $\bar{p}p$ elastic events.

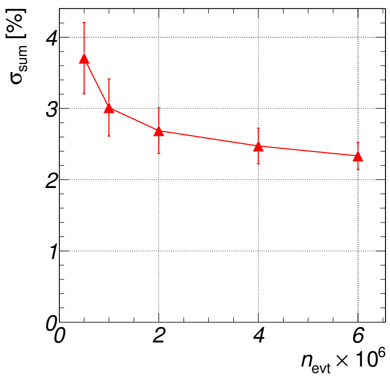


**Figure 4.50**: Total uncertainty on the luminosity measurement for different number of generated events.

### 4.5.5 Statistical errors on the measurement

The statistical error was investigated by measuring the luminosity for $N = 200$ data sets of $\bar{p}p$ elastic scattering events. The fit used to determine the luminosity takes the true values of the cross section parameters. This was only done for $p_{beam} = 8.9\,GeV/c$. The distribution of the measured luminosity from the simulations corresponding to $4 \cdot 10^6$ generated events, which takes about 25 seconds, at $\mathcal{L} = 10^{31}\,cm^{-2}s^{-1}$, to collect , per data set is shown in Figure 4.49. The measured luminosity values are distributed according to a Gaussian. The statistical uncertainty is given by the standard deviation of the fit to the distribution. In the current case, it is about 0.98%.

The same study was performed for different number of generated events. The results are shown in Figure 4.50. In this graph, the total uncertainty $\sigma_{sum}$ includes both systematic and statistic uncertainties and was calculated as:

$$\sigma^2_{sum} = \sigma^2_{stat} + \sigma^2_{syst}\,. \tag{4.63}$$

## 4.6 Summary and discussion

The implementation of the LuMo consisting of four tracking stations of four rectangular double-sided silicon strip detectors in the PandaRoot framework has been described here in detail. It allows the performance of the LuMo detector for $\bar{p}p$ elastic scattering event to be estimated in order to determine the precision with which the absolute luminosity can be measured. A full simulation chain has been performed in order to determine the resolution of the detector in terms of the polar angle $\theta$ for the $\bar{\text{P}}$ANDA beam momentum range. At $p_{beam} = 1.5\,GeV/c$, the angular resolution is about $0.5\,mrad$. A higher resolution of better than $0.1\,mrad$ was achieved for $p_{beam} > 6\,GeV/c$. This corresponds to the ideal situation without the influence of external parameters, e.g. magnetic fields, beam emittance. In this case, the parameters that mostly influence the performance are the small angle scattering and the charge smearing width. The first parameter reflects the multiple scattering that the track undergoes when it traverses the detector planes. That calculation is performed by the transport engine. The charge smearing width characterizes the drift of charge carriers inside the detector volume and was implemented in the digitization process. The introduction of this process allows to determine the actual number of strips fired. Due to this mechanism, the probability to register charge in a more than one strip increases from 0.04 to 0.4. A consequence of that is an improvement of the hit resolution: for a single strip fired which corresponds to a hit resolution of about $14\,\mu m$ and multi strip cluster with a resolution of about $0.7\,\mu m$, an average spatial resolution of $8\,\mu m$ is obtained.

The consideration of the magnetic fields and the beam emittance deteriorates the angular resolution of the LuMo. For the case of the magnetic fields, a correction on the track direction using the GEANE package leads to a negligible effect especially for beam momentum above $3\,GeV/c$. However, a strong effect is obtained when including the beam emittance in the simulation. The angular resolution is limited by the angular divergence of the beam. For the expected HESR antiproton beam properties, the best resolution achieved at the highest beam momentum is about $0.2\,mrad$. At the lowest beam momentum the angular resolution worsens to about $0.5\,mrad$.

To improve the angular resolution for the lower beam momenta, one must reduce the effect of the multiple scattering in the first plane. Such optimization can be achieved by using a thinner sensor for this plane. Small angle scattering of about $0.1\,mrad$ is obtained for $p_{beam} = 1.5\,GeV/c$ for a $50\,\mu m$ thick silicon sensor.

The simulation of the luminosity measurement was developed using the DPM event generator. The method consists essentially of the fit the reconstructed spectrum corrected by the acceptance of the $\bar{p}p$ elastic scattering in the LuMo. Three different studies were performed to estimate the total uncertainty on the measurement. In the first study, it was assumed that all three cross section parameters ($\rho$, $b$ and $\sigma_{tot}$) have zero systematic uncertainties. In addition, simulated events were purely elastic processes. This allows to evaluate the uncertainty on the luminosity caused by the detector resolution, the magnetic fields and the beam emittance. In this case, an absolute precision between 1.33% and 4.53% was achieved corresponding to the highest and lowest beam momenta, respectively.

The second study was the determination the systematic errors connected with the measurement method. This consists of the estimation of the contribution of the systematic uncertainty

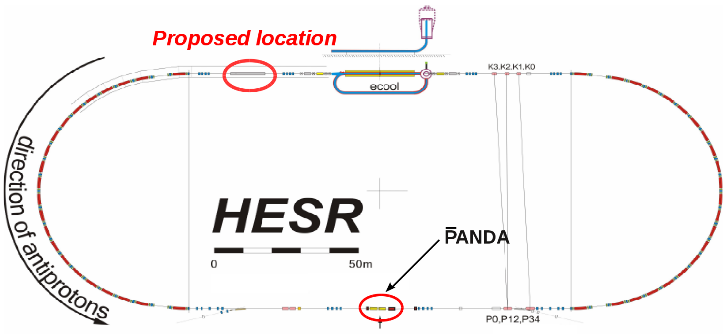


**Figure 4.51**: Proposed location of the day one experiment in the HESR. Picture taken from [X+11].

on each individual cross section parameter. The relative contribution of a given parameter depends on its correlation strength with the luminosity within the relevant $t-$range of a given beam momentum. However, unlike the parameters $\rho$ and $\sigma_{tot}$ which affect strongly the luminosity measurement, this latter has very low sensitivity to the parameter $b$. The systematic errors due to the $\bar{p}p$ inelastic background events have also been investigated. Due to the very low rate of such events in the relevant $t-$range for the LuMo, its effect appears to be negligible on the luminosity determination.

The statistical error was determined for different generated number of events. An error of about 1% was obtained for $4 \times 10^6$ generated $\bar{p}p$ elastic scattering events. This corresponds to about 25 seconds of measurement for a luminosity of $\mathcal{L} = 10^{31} cm^{-2} s^{-1}$.

The detector resolution is usually the most dominant source of uncertainty and is less than 2%. The statistical error can easily be less than 1%. Thus the expected precision on the luminosity measurement depends upon the precise determination of the parameters $\rho$, $\sigma_{tot}$ and $b$. The method of simultaneous determination of the three parameters with the luminosity will unavoidably deteriorate the precision due to the strong correlations between them. Instead, the *HESR Day-One Experiment* proposes an independent measurement of each of the cross section parameters. An overview of this proposal is presented in the next section.

## 4.7 Outlook: The HESR Day One Experiment

This experiment aims at a precise measurement of the $\bar{p}p$ differential cross section parameters, $\rho$, $b$ and $\sigma_{tot}$ in the beam momenta relevant for P̄ANDA during its initial running phase. This is required since a good knowledge of these parameters is mandatory for the absolute determination of the luminosity, and also since there are very few measured data of these parameters in the P̄ANDA beam momentum range. The proposed location of the experiment in the HESR accelerator is shown by Figure 4.51.

The measurement will reconstruct the $\bar{p}p$ elastic scattering spectrum for a large $t-$range from $-t = 8 \times 10^{-4}\, GeV^2$ to $-t = 0.1\, GeV^2$ [X+11]. Within this range the correlation between the $\rho$, $b$ and $\sigma_{tot}$ parameters can be significantly reduced. This can be achieved by measuring the recoil proton target within the energy range of 0.4 to 60 $MeV$.

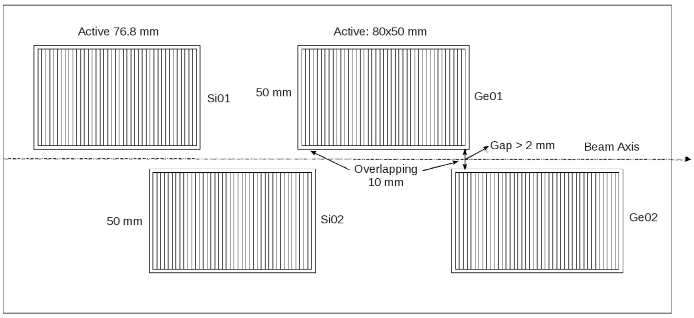


**Figure 4.52**: Layout of the recoil proton detector.

The measurement of the recoil proton will be performed by an array solid state detectors placed nearly perpendicular to the beam direction which has an effective area of $24\,cm \times 5\,cm$ as shown Figure 4.52. To suppress background, a coincidence measurement with the forward scattered antiproton may be required. An a consequence, the detector is sketched in Figure 4.53 and consists of two arms, one to measure the recoil target and one to measure the forward scattered antiproton.

The measurement will be performed in two steps. First, the slope parameter $b$ will be determined at large $t-$values, $0.05 < -t < 1\,GeV^2$, to reduce the influence of the other parameters. In this range, the $\bar{p}p$ elastic scattering is a pure nuclear process where the differential cross section can be parametrized as [A+94a]:

$$\frac{d\sigma_n}{dt} = \sigma_{OP} \cdot e^{bt+ct^2} \tag{4.64}$$

where $\sigma_{OP}$ is called the *optical point* determined by the extrapolation of the elastic nuclear cross section to $-t = 0$ i.e.:

$$\sigma_{OP} = \left(\frac{d\sigma_n}{dt}\right)_{t=0} . \tag{4.65}$$

Then, the $\rho$ and $\sigma_{tot}$ parameters will be measured at very small 4-momentum transfer using the optical point. The method used will be the so-called *luminosity independent method*. In this case, $t$ will be calculated from the kinetic energy $T_p$ of the recoils proton target as:

$$-\,t = 2m_pT_p \tag{4.66}$$

In order to measure the kinetic energy, the recoil arm detector will be relatively thick to stop the recoil proton.

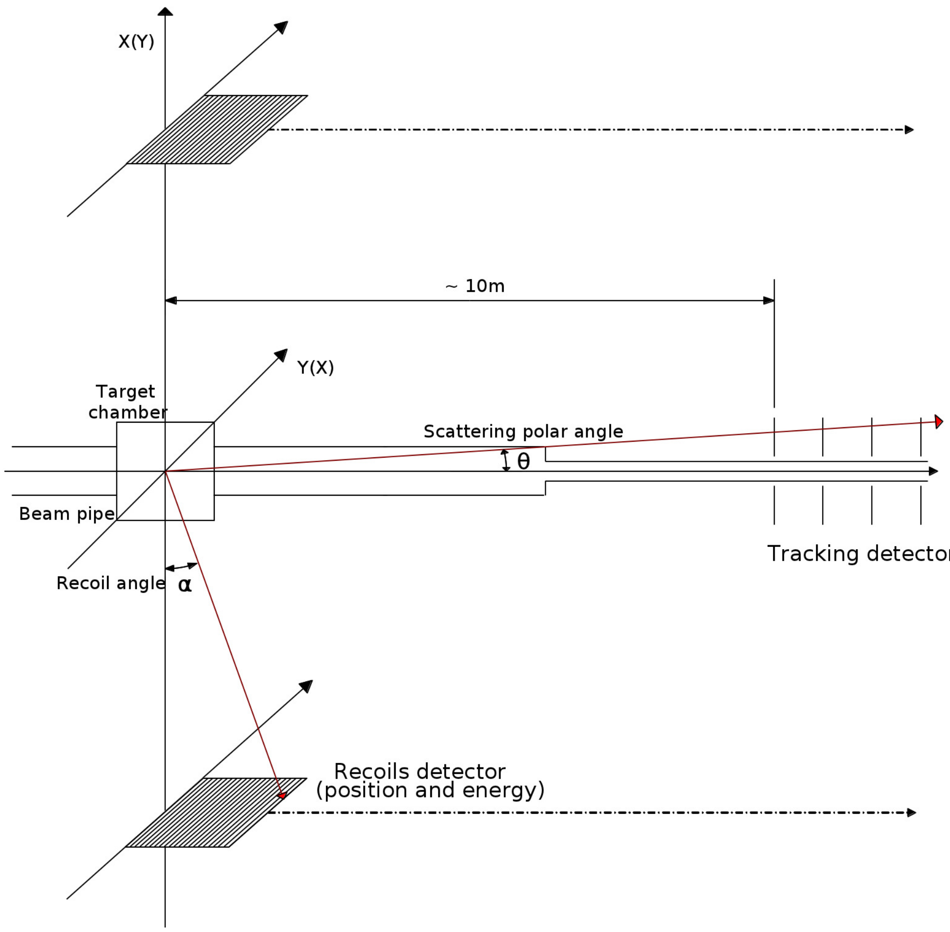


**Figure 4.53**: Sketch of the detector setup for the day one experiment. Picture taken from [X+11].

Chapter 5

# Proton Beam Test of a Silicon Strip Tracking Station

In February 2010, a prototype of the silicon strip tracking system has been setup at COSY and tested with a proton beam. With the strong participation of the $\bar{\text{P}}$ANDA group from HISKP Bonn, who designed and build the apparatus, this beam test allowed investigations of the $\bar{\text{P}}$ANDA MVD, the LuMo and their respective frontend electronics. Therefore, the goal was a full characterization of the silicon strip sensors and readout electronics and a benchmarking of the simulations results with real data. For the LuMo study more emphasis was put on the latter aspect of the beam test. In particular, it allows the implemented reconstruction method for the LuMo presented in the previous chapter to be validated.

This chapter reports on the beam test analysis results. The offline analysis has been carried out with the LuMo simulation software in PandaRoot. A brief overview of the experimental and detector setups will be given in the first section. The second section will focus on describing the data structure and the offline analysis results. In particular, the cluster behavior as functions of the beam momentum and the angle of incidence will be discussed, and also a method to calibrate geometry misalignment will be presented. Finally, this information will be summarized.

## 5.1 Experimental setup

The tracking station was tested with proton beams of $2.95\,GeV/c$ and $0.893\,GeV/c$ delivered by the COSY accelerator at Jülich at a rate of about $4 \cdot 10^3/s$. It consisted of four modules of silicon strip sensors and two pairs of scintillating hodoscopes as the trigger system. The four modules included two double-sided and two pairs of single-sided modules.

The four sensor modules were arranged sequentially along the beam direction and between the pairs of the scintillators. Initially, without a dedicated alignment procedure, the detector system, sensor modules and trigger system, were placed manually normal to the beam direction.

The whole system was supported by a $2\,m$ long frame with a height adjusted to the beam pipe level. It has been specially designed to easily perform shifts of each individual sensor module along the three Cartesian directions. One frame could rotate in order to vary the incident angle of the beam to the sensor module. Two pairs of scintillators were used as an event trigger and were placed at the edges of the frame and were kept fixed during the experiment. A picture of the experimental setup is displayed in Figure 5.1.

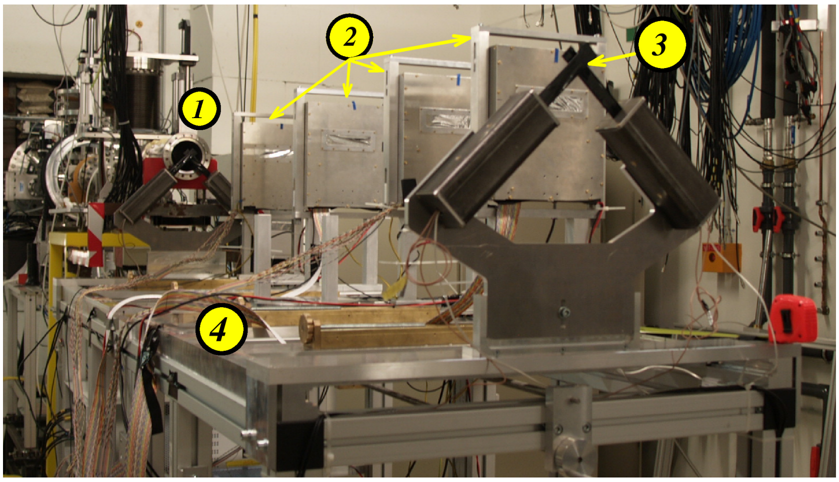


**Figure 5.1**: Photograph of the silicon strip tracking system setup during the beam test at COSY. In this picture the numbers 1, 2, 3 and 4 indicate the beam pipe, the four sensor modules, the downstream pair of scintillator and the support frame, respectively.

### 5.1.1 Detector setup

Each individual scintillating hodoscope was $2\,cm$ wide and $20\,cm$ long. The individual scintillators were rotated by about 90 relative to each other to generate a square overlap region.

All six silicon strip sensors have the dimension of $2\,cm \times 2\,cm \times 300\,\mu m$ with $50\,\mu m$ pitch. Each module was put in a lighttight aluminum box, where the connection with the frontend electronics is done. The front and the back of the sensitive area of the module was covered by a thin aluminum foil ($\sim 20\,\mu m$ thickness) to completely isolate the module from the outside environment. The gap between the two single sided sensors was about $4\,mm$ with a stereo angle of 90 degrees. Figure 5.2 shows a sketch of the system including the global coordinate system $(x, y, z)$. The beam direction is parallel to the $z-$axis, and $z = 0$ corresponds to the end of the beam pipe. The front and back strips are parallel to the global $x-$ and $y-$axis, respectively.

Two different detector configurations were adopted during the beam test as shown in Figure 5.2. In the first configuration, the incident proton beam was normal to the sensor surfaces. With this setup, data for the two beam momenta were collected in order to analyze the detector response as a function of the beam momentum.

The second scenario moved module 4 to the second position and rotated it about the global $y-$axis by an angle $\omega$ between 0 and 45 degrees. These measurements were only performed for $p_{beam} = 2.95\,GeV/c$. In this case, the detector performance as a function of the rotation angle was investigated. The $z-$positions of the modules for the two setups are given in Table 5.1.

### 5.1.2 Frontend and readout electronics

A module readout was performed using APV25-S1 [Jon01] frontend chips with 128-channels each. Each active sensor side was read out by three chips. This one-side sensor readout system was mounted in a *L-shaped* board. This shape has been designed to allow a common readout for a double-sided sensor. On the same board, a high voltage sensor supply connector and

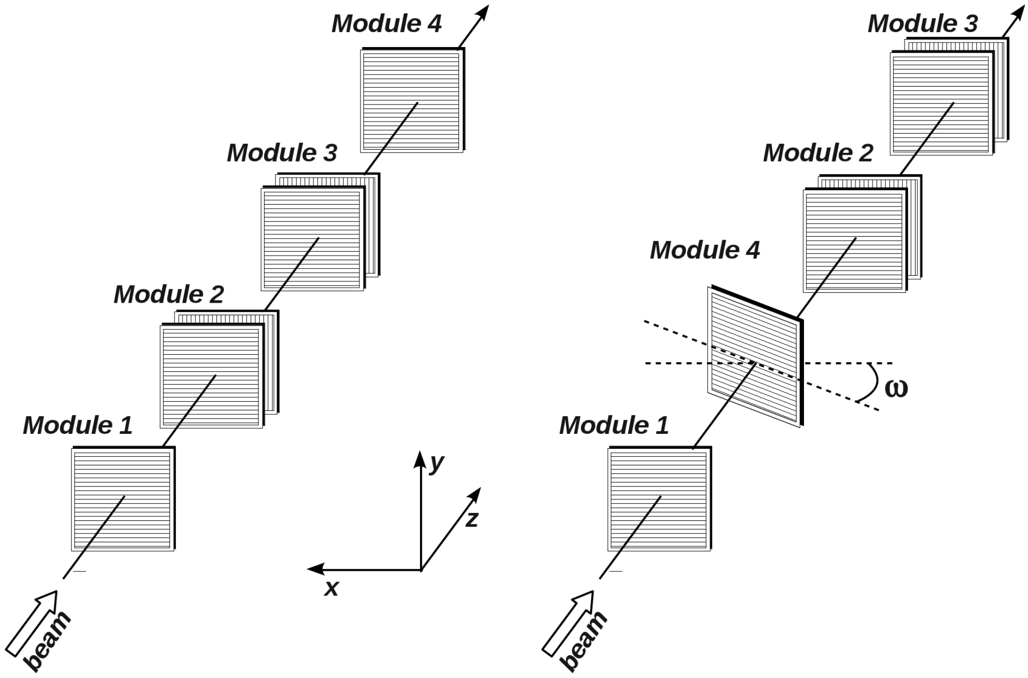


**Figure 5.2**: Sketch illustrating the two configurations of the tracking station beam test: Setup 1 is on the left and Setup 2 is on the right . The global coordinate system is indicated. In this reference system, the beam direction is parallel to the $z-$axis. Parallel lines inside the squares shape indicate the strip directions. The trigger system is not drawn in the figure.

| | $z-$position $(mm)$ | |
|---|---|---|
| Module Number | Setup 1 | Setup 2 |
| 1 | 110 | 165 |
| 2 | 807 | 1750 |
| 3 | 1390 | 1872 |
| 4 | 1832 | 1150 |

**Table 5.1**: Positions of the modules with respect to the end of the beam pipe for the two different detector setups.

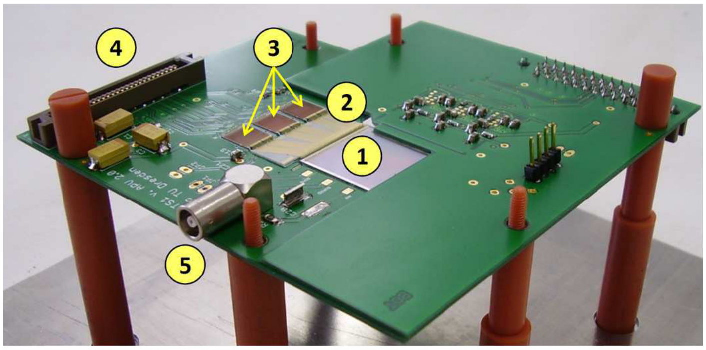


**Figure 5.3**: Picture of a complete double-sided sensor module equipped with two identical L-shaped PCBs. Main components of each individual sensor bord are: (1) double-sided sensor, (2) pitch adapter, (3) three APV25-S1s chips, (4) high density connector (for chips power supply, slow control, data output) and (5) sensor HV connector (only in one board). Picture taken from [W+10].

a high density connector needed for the data flows were also mounted. A photograph of a double-sided module is presented in Figure 5.3.

The on-detector readout was connected with a supply board which provided the operating voltage and acted as repeater and transition card for the frontend signals. The clock and trigger signals were generated by a FPGA mounted in a VME board allowing an adjustable clock frequency between 0.5 and 50 $MHz$. Slow control for the frontend chips, supply board and FPGA was implemented using the standard $I^2C$ [W+10]. For the digitization, a commercial ADC card was used. The whole test station was controlled by a standard computer.

### 5.1.3 Online monitoring and data acquisition

The DAQ flow was initiated by the coincidence of three scintillators hits. The trigger signal is then delivered by the FPGA. This leads to the pulse preamplification and shaping processes through the frontend pipeline incorporated in the APVs. The resulting analog signals, with digital headers are then sent to the ADC where the digitization is performed. The digitized data are transferred to the VME board and stored temporarily.

The stored data undergo several processing steps within the VME-FPGA board. To begin with the FPGA performs a frontend identification, followed by the signal extraction: the signal is separated from the header. Then, the pedestal correction and the noise suppression are performed. The resulting signals are finally written and stored in a FIFO.

The digitized data are transferred to the computer via an Ethernet network. The computer itself runs a dedicated software for the online data acquisition monitoring. During the beam test, a total of about 85 million events have been recorded.

Another type of data results from the online cluster finder algorithm, that was also implemented at the FPGA data processing level. In this case, information belonging to the same sensor side, resulting from a single beam particle crossing is merged together to form the cluster data. A more detail description of the beam telescope can be found at [W+10].

In the following, only the digitized data will be taken into account in order to validate the LuMo reconstructed method.

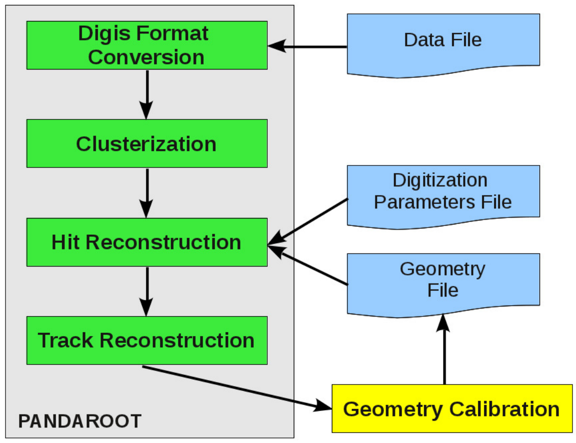


**Figure 5.4**: Flow diagram of the beam test data analysis chain.

## 5.2 Offline analysis and results

The offline analysis for this study used the LuMo reconstruction algorithm implemented in PandaRoot. A detailed description of the algorithm was given in the previous chapter.

The analysis starts by taking the beam test data file. The data format had to be restructured in order to be consistent with the PandaRoot software. This operation will be described in more detail in the upcoming section. The output is used as input to first perform the clusterization and then the hit reconstruction. At this level, a complete description of the detector setup is needed. Thus, two files, one containing the digitization parameters such as the pitch, the strip orientation on each side, and another giving the detector geometry, were provided. The next step is the track reconstruction. The output of this process allows the calibration of the detector geometry to be performed. This process was necessary to correct the relative misalignment between the sensor planes allowing a better estimate of the detector resolution and efficiency. The alignment method was developed for this beam test and is described later in this chapter. The geometry file is updated according to the modification in the alignment process. This process is iterated until the resolution of the alignment is optimized. A flow diagram summarizing the analysis chain is shown in Figure 5.4.

### 5.2.1 Raw data restructuring

The output raw data from the beam test was stored in ASCII files in which a hit is represented by the trigger identification, the frontend and channel fired and the amplitude of the charge collected in ADC channels. The restructuring of the data consists of converting the frontend number into the module and side numbers, the channel number into the strip number and performing the gain calibration.

In the raw data file, the frontends are labeled 0 to 23 and the channels 0 to 127. Each group of six consecutive frontend numbers represents a module with three consecutive frontends per side. The strip number corresponding to the channel $c_j$ of the frontend $fe_k$ in a side is calculated as $(fe_k - fe_0) \times 128 + c_j + 1$, where $fe_0$ is the number of the first frontend on the same side. Thus, after the conversion the strips from each side of the sensor are numbered

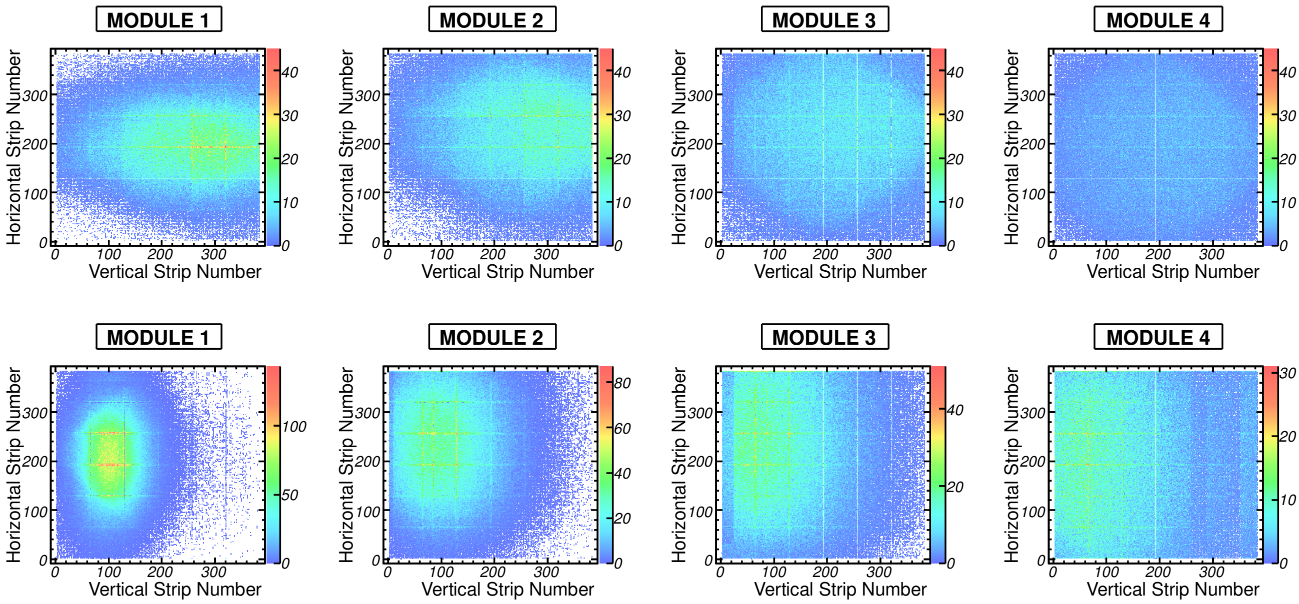


**Figure 5.5**: Typical strip fired distributions of the four stations for the data at $p_{beam} = 2.95\,GeV/c$ (*upper row*) and $p_{beam} = 0.893\,GeV/c$ (*lower row*). These histograms correspond to detector Setup 1.

from 1 to 384. The two dimensional histograms in Figure 5.5 show the distributions of the frequency each strip fired for all four modules for the two beam momentum setups.

The histograms on the figure are ordered from the left to the right according to the module positions along the beam direction. On the histogram corresponding to module 1, the beam spot shape can be seen which represents the overlap area of the trigger hodoscopes. The beam impact spot on the sensor surface widens from one station to the next. This is mainly due to the combination of the beam divergence and small angle scattering effects.

The different shape of the beam spot for the $2.95\,GeV/c$ and the $0.893\,GeV/c$ data is most likely the result of different focus properties of the beam at different momenta.

One can also observe the positions of the beam axis on the different sensor modules. This reflects the limited precision with which the modules were mounted on the frame. The determination of the actual positions of each station will be the purpose of the alignment procedure presented later in this chapter.

The offline gain calibration was performed for all readout channels in each individual sensor side. The calibration coefficient for each channel was calculated by the quotient of the average deposited charge on the sensor side to the average charge collected by this channel. In this case, only the hits from tracks that went through all four stations were considered. Furthermore, among these hits, only those ones which fired a single strip were used i.e. the amount of charge deposited in the sensor are collected by only one strip, were used. The consequence of these cuts is that the long tail of the Landau distribution of the charges was significantly reduced. This is explicitly shown by Figure 5.6. As a result, the position of the mean position of the distribution becomes stable and thus corresponds to the average deposited charges in all strips of the sensor side.

The calibration has only been performed for strips that have more than 150 entries. For other strips (mainly those ones at the edges) the calibration coefficient was set to 1.

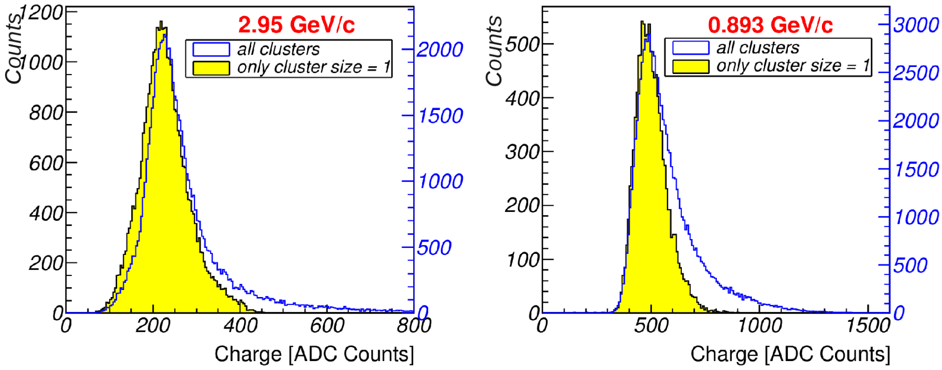


**Figure 5.6**: Charge distributions of all reconstructed clusters and clusters of size 1 (yellow area), for the two beam momenta. The left scale corresponds to the single-strip cluster charge distribution and the right scale to the distribution of all cluster charge. This figure correponds to the P-side of the double-sided sensor in module 1.

Figure 5.7 shows the mean deposited charge per strip for strips satisfying the conditions mentioned above after calibration for both beam momenta and for each sensitive sensor side. The collected charges are slightly higher on the back side than in the front side of the double-sided module. This is because the front side corresponds to the P-side and the back side to the N-side of the sensor, and the N-side is effected by higher noise. Similar values are obtained for the single-sided modules. The average charge per sensor side is about 237 ADC counts and 516 ADC counts for the 2.95 $GeV/c$ and 0.893 $GeV/c$ beam momenta, respectively. The deposited charge at lower beam momentum is higher than for the higher beam momentum, as expected. Fluctuations from one side to another of about 9% and about 4% around the averages are observed for the first three modules, for the 2.95 $GeV/c$ and 0.893 $GeV/c$ beam momenta, respectively. The mean charge values in the sensor side of module 4 were not included in these average values because the gain was a factor two lower for the corresponding channels. Furthermore, the gain of the last 128 channels of the N-side of module 4 was lower during the 0.893 $GeV/c$ beam momentum data taking.

The analysis of the charge distributions per strip per sensor side was used to determine the charge threshold for the different running conditions. The threshold corresponds to the minimum charge that can be collected on the strip. Histograms in the upper row of Figure 5.8 show the typical distributions of the charge per strip in a sensor side for the Setup 1 at the 2.95 $GeV/c$ beam momentum (left) and for the Setup 1 with the 0.893 $GeV/c$ beam momentum and the Setup 2 (right). The distributions of the corresponding minimum charges for all channels are plotted in the lower row of the same figure. Gaussian fits to these distributions were used to estimate the charge thresholds for these two experimental conditions. For geometry Setup 1 at 2.95 $GeV/c$ beam momentum, the threshold of about 64 ADC channels was found with a spread of about 2 ADC channels. For Setup 1 with $p_{beam} = 0.893\,GeV/c$ and for Setup 2, it is about 32 ADC channels with a spread of about 1 ADC channel. For this latter case, the last 128 strips of module 4 were not taken into account in the calculation.

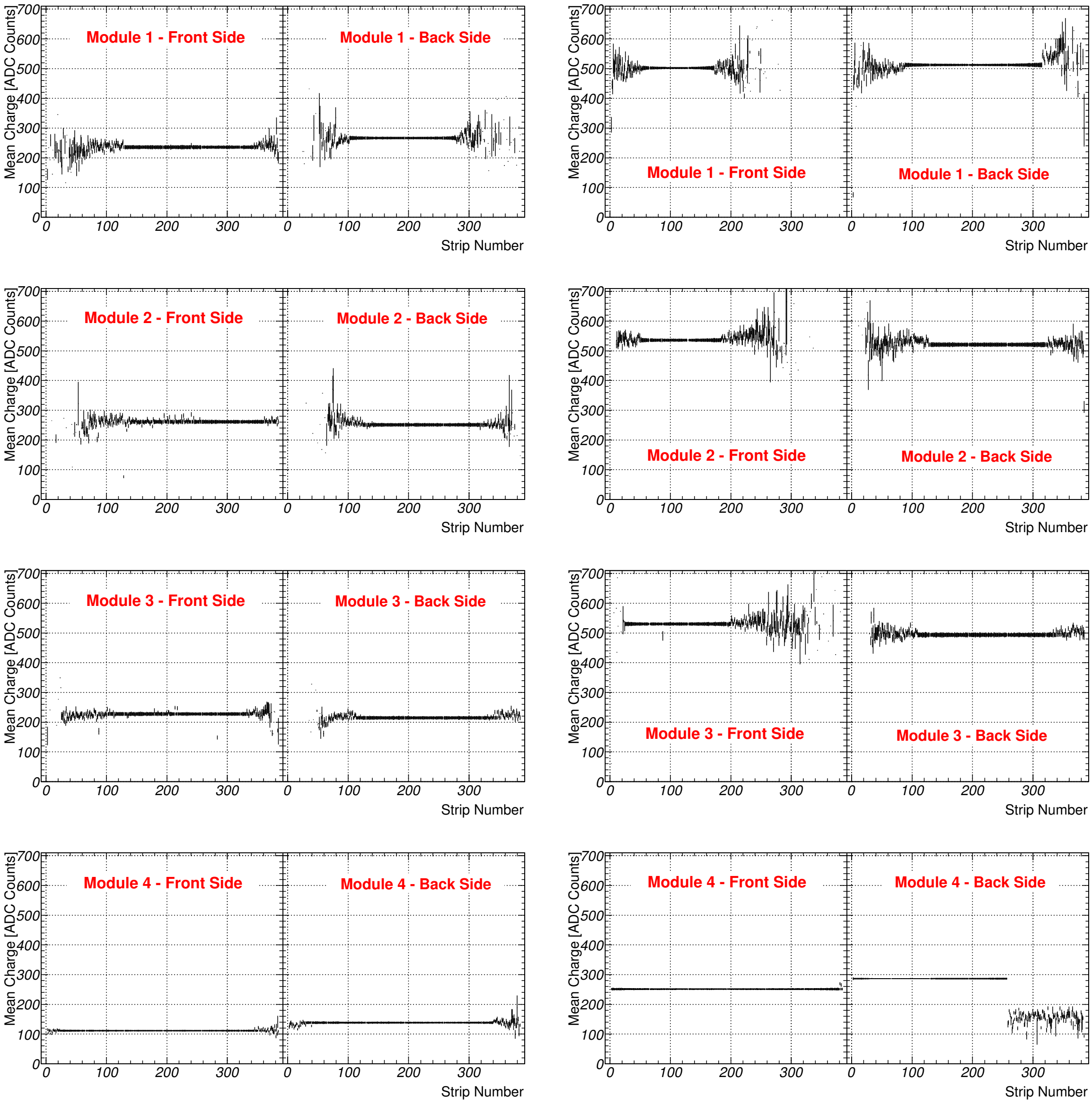


**Figure 5.7**: Distribution of the mean deposited charge for each strip at (*left column*) $p_{beam} = 2.95$ $GeV/c$ and (*right column*) $p_{beam} = 0.893$ $GeV/c$ corresponding to single-strip cluster.

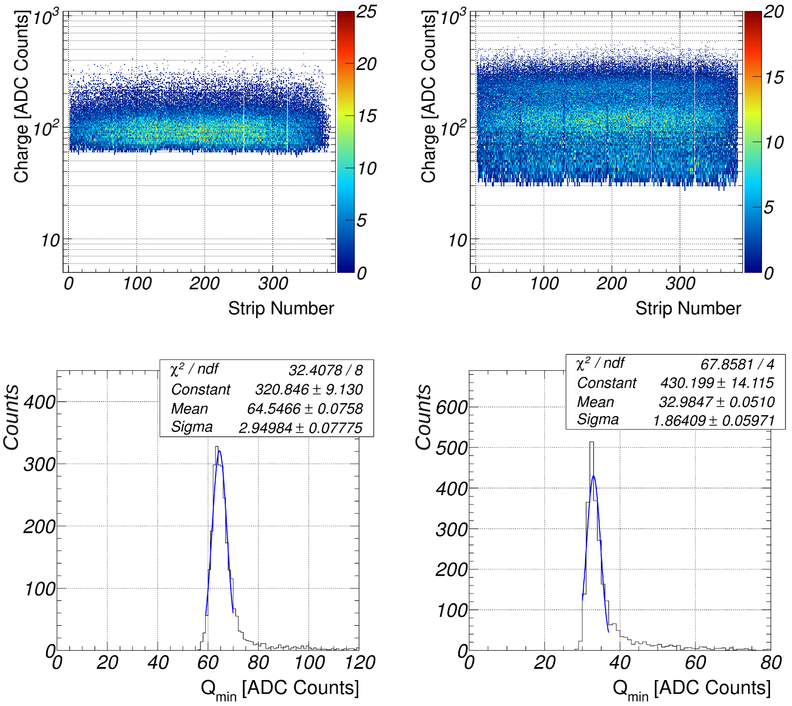


**Figure 5.8**: *Upper row:* Typical distribution of the deposited charge for each strip in a given sensor side (in this case the P-side of module 4) corresponding to the the Setup 1 at the 2.95 $GeV/c$ beam momentum (*left*) and for the Setup 1 with the 0.893 $GeV/c$ beam momentum and the Setup 2 (*right*). *Lower row:* Distributions of the minimum deposited charge per strip for all four modules for these two experimental setups. The blue lines on top of the lower figure part are Gaussian fits to the distribution. The means of the fits give the thresholds values.

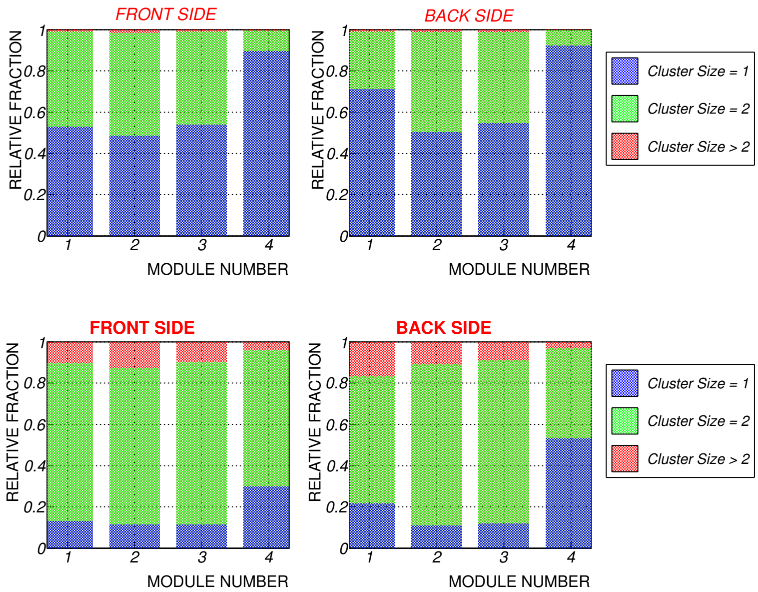


**Figure 5.9**: Relative fraction of the cluster size at each sensitive sensor side of the tracking station. The upper and lower rows are for data taken at 2.95 and 0.893 $GeV/c$, respectively.

### 5.2.2 Reconstructed cluster properties

The cluster size and charge have been investigated as functions of the beam momentum (Setup1) and the angle of incidence (Setup 2). All results presented in this section were obtained from incident tracks that hit all four stations.

#### 5.2.2.1 Cluster properties as function of the beam momentum

**Cluster size**

Histograms showing the relative fraction of clusters having size of 1, 2 and $> 2$ in each individual sensitive sensor side of the tracking station and for both beam momenta are plotted in Figure 5.9.

For the single-sided modules, the front and back side clusters have equal size. In contrast, the P-side clusters are wider than the N-side clusters in the double-sided modules. This might be the consequence of the higher noise on the N-side. In fact, the same charge threshold applied on both sides reduces much more the size of the clusters on the N-side than on the P-side due the lower signal to noise ratio on the N-side.

The clusters in module 4 are narrower than the clusters in the other three modules for both beam momenta. This is mainly a consequence of the lower gain on the channels on this module. In fact, the number of strips fired during the passage of a single track depends on several aspects such as noise and the incident track angle. The noise is expected to be similar for all sensors. Due to the condition that the tracks hit all four planes, the incident angle is nearly 90° for all modules despite the small misalignment of the modules. Another important factor discussed previously is the charge diffusion. Assuming that the sensors have similar

| | Reconstructed value of $\sigma_L$ $(keV)$ | | | |
|---|---|---|---|---|
| | 2.95 $GeV/c$ | | 893 $MeV/c$ | |
| Module Number | Front Side | Back Side | Front Side | Back Side |
| 1 | $5.87 \pm 0.07$ | $7.05 \pm 0.08$ | $12.03 \pm 0.10$ | $14.05 \pm 0.11$ |
| 2 | $6.48 \pm 0.07$ | $6.32 \pm 0.07$ | $12.97 \pm 0.11$ | $12.19 \pm 0.11$ |
| 3 | $6.41 \pm 0.07$ | $6.60 \pm 0.07$ | $12.09 \pm 0.10$ | $12.57 \pm 0.10$ |
| 4 | $8.58 \pm 0.11$ | $9.57 \pm 0.12$ | $11.92 \pm 0.13$ | $13.13 \pm 0.13$ |

**Table 5.2**: The fitted value of the width parameter $\sigma_L$ of the Landau distribution.

physical properties, the charge diffusion should not cause a strong difference of the cluster size for different sensors. The cluster size also depends strongly on the ratio of the mean charge to the threshold. If referred to Figure 5.7 with the threshold values given in Figure 5.8, this ratio is a factor of two bigger in the three first modules than in the module 4 due to the lower gain on the corresponding channels. A similar factor is noted in the relative fraction of clusters size equal to 1 in the front side part of Figure 5.9 for the two beam energies.

For all modules, at $p_{beam} = 2.95\,GeV/c$, there is a higher fraction of cluster size $= 1$. Despite the threshold being set to half the value for $p_{beam} = 0.893$ $GeV/c$ beam momentum, the relative ratio of the single-strip clusters of the $p_{beam} = 2.95$ to the 0.893 $GeV/c$ data is still larger than 2. This reflects the widening of the clusters when the deposited charge increases.

### Cluster charge

Figure 5.10 shows the distributions of the deposited charge of the reconstructed clusters for each sensor side of the four detector modules and for both beam energies. Each individual distribution has been fit with a Landau distribution convoluted with a Gaussian as given by Equation (4.6).

Fits to the data to determine the values of the $\Delta_p$, $\sigma_G$ and $\sigma_L$ are shown in Figure 5.10. The conversion of the collected charge in ADC counts to the deposited energy in eV was performed by setting the most probable energy loss $\Delta_p$ to 76 $keV$ and 144 $keV$ for the higher and lower beam momenta, respectively. These values were taken from the theoretical expectation of $\Delta_p$ shown in Figure 5.11 [N+10]. The calibration coefficients were calculated for each sensor of single-sided modules. For double-sided modules, the coefficient in the P-side was used for both side. Other parameters were determined using these calibrations.

The measured values of the width parameter $\sigma_L$ of the Landau distribution for every sensor side are given in Table 5.2. For $p_{beam} = 2.95\,GeV/c$, the fitted value has an average of $6.47\,keV$ except the last module in which big values of $\chi^2/ndf$ were obtained. This value is in good agreement with the existing value of about $6\,keV$ for $300\mu m$ thick silicon [H+84a]. The value of $\sigma_L$ extrapolated to the lower beam momentum is about 12.0 $keV$. The measured value is consistent with this value.

Assuming the distant collisions to be dominated by the interaction of the innermost shell (K-shell), then $\sigma_K$ will be similar for the two beam momenta and roughly equal to 5.7 $keV$

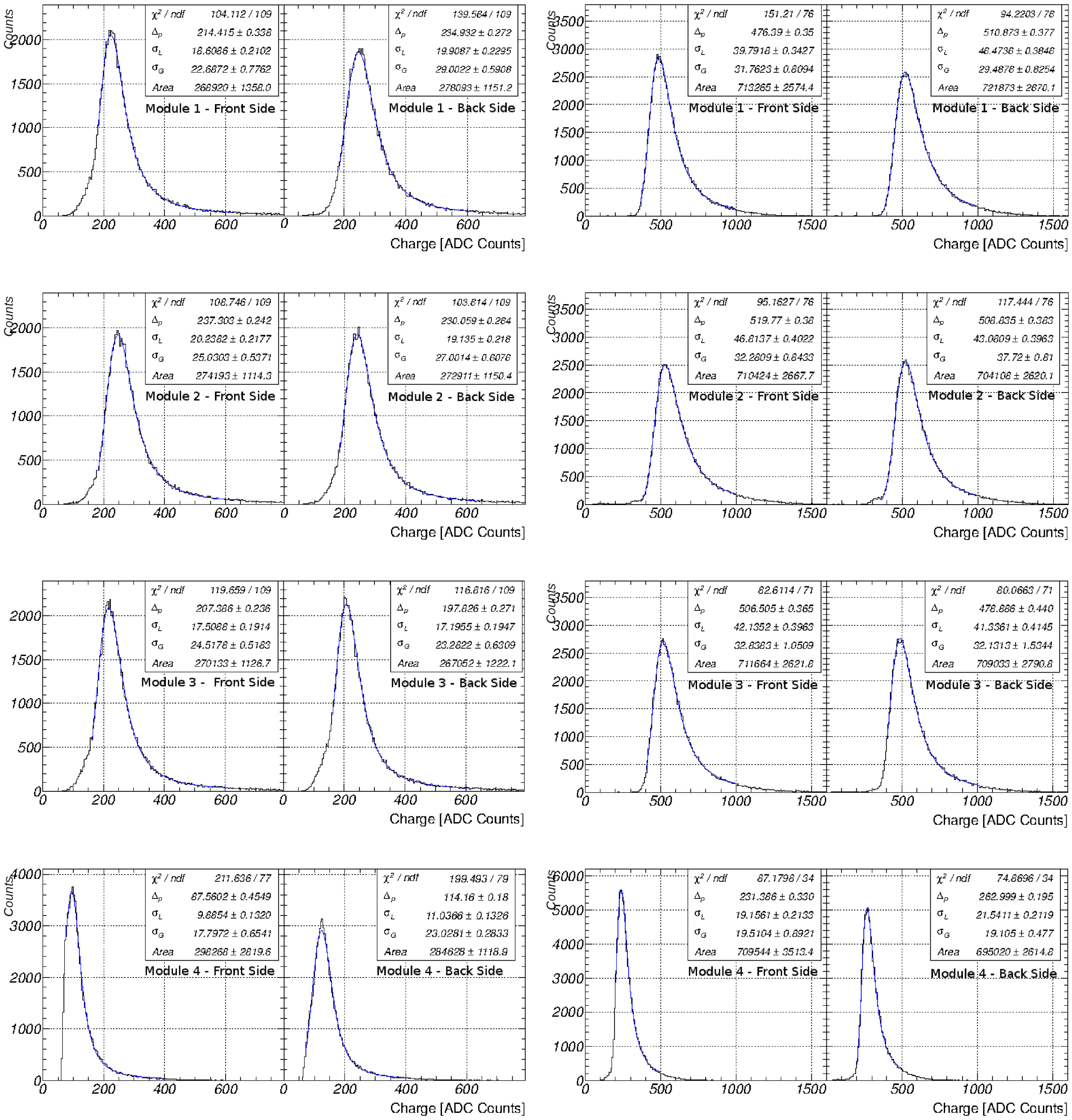


**Figure 5.10**: Distributions of the deposited charge per cluster for each sensitive side of all four detector modules for $p_{beam} = 2.95\,GeV/c$ (*left column*) and $p_{beam} = 0.893\,GeV/c$ (*right column*). Blue curves are fits to the data with a Landau function convoluted with a Gaussian.

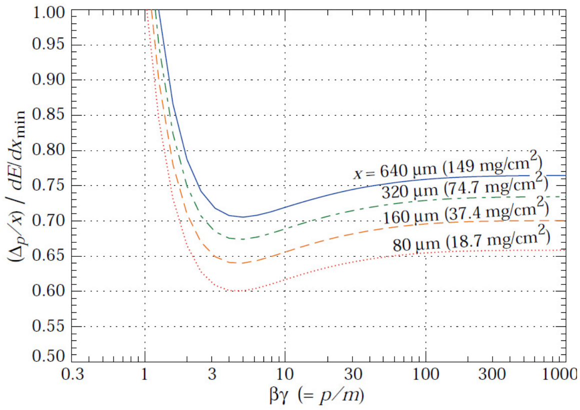


**Figure 5.11**: Most probable energy loss in silicon, scaled to the mean loss of a minimum ionizing particle, 388 $eV/\mu m$ ($1.66\,MeV \cdot g^{-1} \cdot cm^2$). Picture taken from [N+10].

| | Reconstructed value of $\sigma_{noise}$ $(keV)$ | | | |
|---|---|---|---|---|
| | 2.95 $GeV/c$ | | 893 $MeV/c$ | |
| Module Number | Front Side | Back Side | Front Side | Back Side |
| 1 | $5.67 \pm 0.27$ | $8.55 \pm 0.21$ | $7.71 \pm 0.24$ | $6.85 \pm 0.25$ |
| 2 | $5.64 \pm 0.17$ | $6.86 \pm 0.20$ | $6.89 \pm 0.23$ | $9.02 \pm 0.23$ |
| 3 | $6.94 \pm 0.19$ | $6.89 \pm 0.24$ | $6.70 \pm 0.21$ | $6.59 \pm 0.26$ |
| 4 | $14.35 \pm 0.57$ | $19.15 \pm 0.25$ | $10.72 \pm 0.55$ | $10.43 \pm 0.30$ |

**Table 5.3**: The *r.m.s.*'s of the Gaussian distributions representing the electronic noise at each individual sensitive side of the four modules of the tracking station.

[H+84b]. The electronic noise contribution can be estimated by :

$$\sigma_{noise} = \sqrt{\sigma_G^2 - \sigma_K^2}\,. \tag{5.1}$$

The reconstructed value of $\sigma_{noise}$ on each sensor side is given in Table 5.3. In the double-sided modules, the noise on the P-side is expected to be smaller than in the N-side. This is the case for the noise reconstructed in the module 1 for the $2.95\,GeV/c$ beam momentum setup. In the same module, the contrary is observed for the lower beam energy which may due to the poor quality of the fit to the P-side charge distribution. For the module 4, the big values of the noise are the consequence of the abnormal fit to the distributions for both beam momenta. For the single-sided module 2, the discrepancy of the noise in the front and back sides is not clear. However, similar noise values are measured in the module 3 for the front and back sides. Considering only good $\chi^2/ndf$ fits, average noise values of $6.4\,keV$ and $6.7\,keV$ are measured for the higher and lower beam momenta, respectively. These values are consistent with each other taking into account the average fit error of about $0.2\,keV$. Here, the difference may be due to the uncertainties in the charge calibration or the values of the charge threshold.

#### 5.2.2.2 Dependence of the cluster properties on the sensor rotation

In this section, the analysis was focused on the behavior of the reconstructed clusters in the module 4, which was rotated about the global $y-$axis by an angle $\omega$ between 0 to 45 degrees (as illustrated Figure 5.2) for the $2.95\,GeV/c$ beam momentum setup. Basically, the fact of rotating the sensor leads to changes of its geometry relative to the incident particle. These changes include the increase of the effective thickness of the sensor and the narrowing of the effective pitch of the strips of the side where their direction is parallel to the rotation axis. Here, this side corresponds to the N-side of the sensor.

A straightforward consequence of the thickening of the sensor is the increase of the path length of the track inside the sensor. The deposited charge is also expected to increase accordingly since these two observables are proportional to each other, as illustrated in Figure 5.12. In this figure the distributions of the cluster charge for both sides are shown. In particular for the P-side sensor where the charge distributions have been fitted with Landau convoluted with a Gaussian, one can observe the shift of the most probable deposited charge, determined by the fit to a higher charge value when the incidence angle increases. In this case, the change of the deposited charge for an incident angle $\omega$ is proportional to the factor $1/\cos(\omega)$ by which the path length increases with respect to the normal incidence.

The same behavior is not observed for the N-side cluster charge in particular for higher polar angles ($\omega > 10°$). For this angular range, the decrease of the strip width has a more significant effect on the charge collection. Indeed, a similar amount of charge collected by mostly one or two strips for nearly normal incident tracks is shared by several strips and thus is more strongly effected by the threshold. This explains the presence of the several peaks in these distributions. This is also confirmed by the variation of the cluster width as a function of the incident angle plotted in the left part of Figure 5.13.

The left part of Figure 5.13 represents the variation of the mean cluster width as a function of the incident angle. In this figure, the P- and N-side clusters have identical widths for small incident angles ($\omega \leq 10°$). The total amount of deposited charge is collected mostly by one strip for $\omega = 0°$, $5°$ and by either one or two strips for $\omega = 10°$. Above this angle the P-side cluster width varies only slightly with the angle. However the N-side cluster widens: the mean cluster width increases linearly with the angle and reached a value of about 2.7 strips at $\omega = 35°$. Then it drops for even higher incident angle because the charges that spread over the further strips are below the charge threshold. Thus there is more pronounced peak in the lower charge value as shown Figure 5.12.

The effect of the incident angle on the properties of the clusters on both sides are summarized in Figure 5.13. The right plot of this figure shows the relative variation of the most probable deposited charge with respect to the normal incident angle as a function of $1/\cos(\omega)$ for the P-side clusters. A straight line was drawn with the points to show the linear behavior of the variation. The two first points corresponding to $\omega = 0°$ and $\omega = 5°$ do not fit on the line. This is due to the altered distribution of the deposited charge (see the two top plots of Figure 5.12) and thus falsified the determination of the most probable value by the fit. This is also the reason why the slope of the line differs from 1.

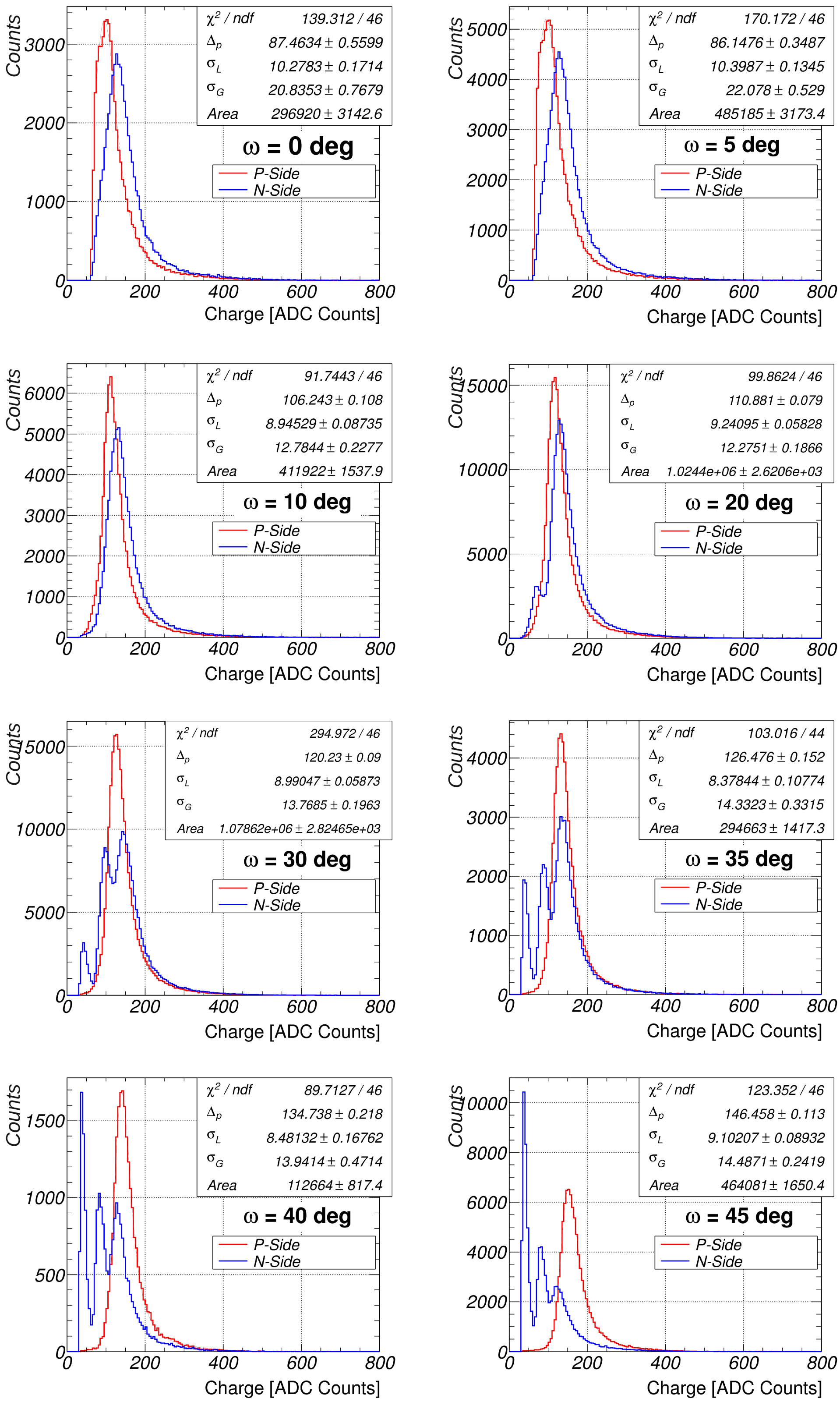


**Figure 5.12**: Distributions of the deposited charge in reconstructed clusters for different angles of incidence $\omega$ relative to the normal of the sensor.

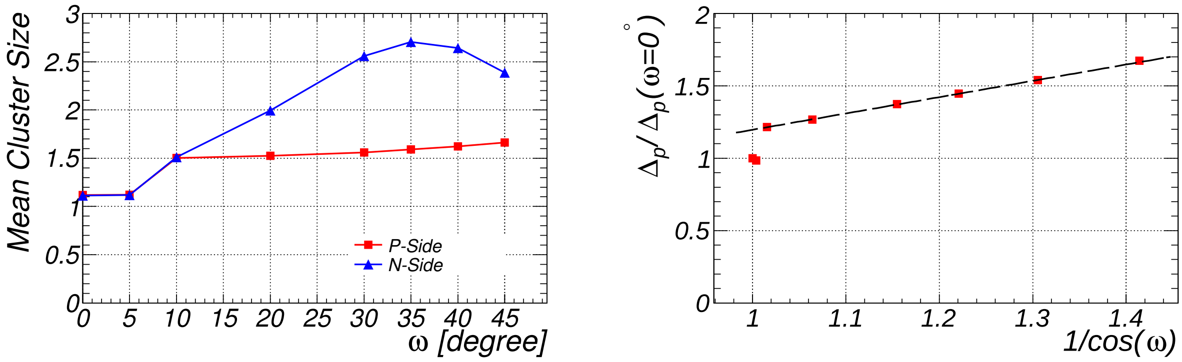


**Figure 5.13**: Graphs showing the mean cluster size as a function of the incident angle $\omega$ (*left*) and the most probable deposited charge on the P-side as a function of $1/\cos(\omega)$ (*right*). The dashed line represents the expected proportionality of the deposited charge with $1/\cos(\omega)$.

The optimal situation is at $\omega = 10°$. At this incident angle, the clusters on both sides of the sensor have the same mean size of 1.5 strips. This situation corresponds to a transverse path length comparable to the strip pitch when tracks pass through the sensor such as:

$$\tan(10°) \simeq \frac{pitch}{thickness} . \tag{5.2}$$

Therefore the total amount of deposited charge was collected by either 1 or 2 strips. The cluster size 1 corresponds to tracks which enter and exit at the boundaries of the actual strip fired and its neighboring strips. The two strips cluster corresponds to tracks that enter and exit in the center of the two strips fired, so that the deposited charge is equally shared by the two strips.

### 5.2.3 Hit position reconstruction

Further analysis such as track reconstruction and detector alignment are only possible after the hit positions have been correctly reconstructed.

The one-dimensional position reconstruction is based on the charge sharing process between strips. This can be seen through the behavior of the $\eta-$function (see Equation (4.13)). The two-dimensional position reconstruction matches the charge measured on both sides of the sensor. Since no charge correlation can be expected between layers of the single-sided modules, the charge matching is only used for the double-sided modules.

#### 5.2.3.1 $\eta-$distribution

The charge sharing between strips is mainly determined by the charge diffusion process as described in the previous chapter. The parameter $\sigma_{diff}$ representing the charge smearing is characteristic of the material and does not depend on the incident particle energy. In order to estimate the value of $\sigma_{diff}$, the $\eta-$distribution in the beam test data and simulation have been compared.

Data taken at $p_{beam} = 0.893\,GeV/c$ were used since they have a large fraction of multi-strip clusters as seen in Figure 5.9. In the simulation, the threshold and noise were set to the values

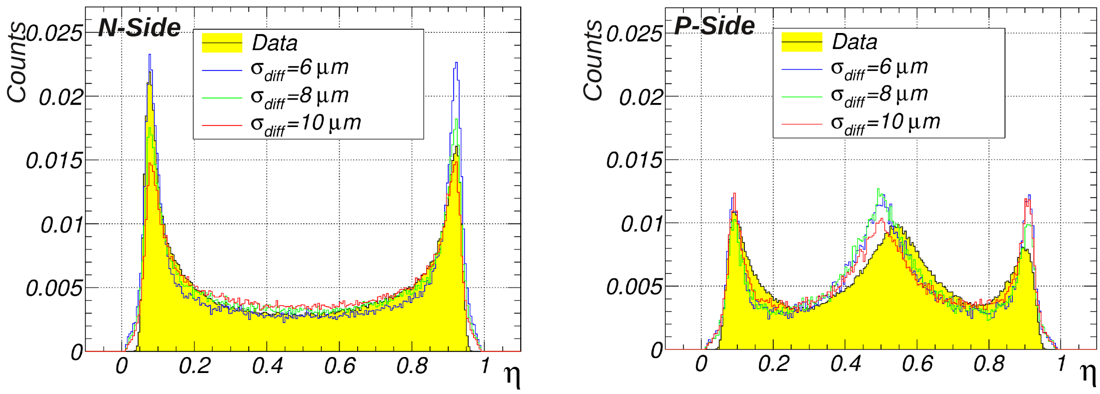


**Figure 5.14**: Distribution of the $\eta-$function on the N-side (*left*) and P-side (*right*) of the double-sided sensor in module 1. For both cases, the measured data (yellow filled area) are compared with the simulation (colored lines) in which different values of $\sigma_{diff}$ were used.

reconstructed in this analysis. The comparisons were performed for different values of $\sigma_{diff}$. The distributions of the $\eta-$function are shown in Figure 5.14 for the P- and N-sides of the double-sided sensor of module 1.

The distribution of the $\eta-$function for the N-side sensor, shown by the left plot of Figure 5.14, has two peaks located at $\eta \simeq 0.07$ and $\eta \simeq 0.93$ which correspond to the ratio of the threshold to the most probable value ratio. The distribution was compared to the output of the simulations in which $\sigma_{diff}$ was set to 6, 8 and 10 $\mu m$.

In the right part of Figure 5.14, the $\eta-$distribution at the P-side is shown. The distribution exhibits three peaks. This is due to the big fluctuation of the charge threshold for the channels on this side. In fact, the three-peak structure can be attributed as the result of the superposition of two distributions: one corresponding to a lower threshold ($threshold/\Delta_p \sim 0.1$) which generates the two peaks at the edges, and another with a higher threshold ($threshold/\Delta_p \sim 0.5$) generating the bump in the center. The simulations were performed for the two values of the thresholds corresponding to the $threshold/\Delta_p$ ratio measured above.

For both sides of the sensor, the measured data are quite well reproduced by using $\sigma_{diff} = 8$ or 10 $\mu m$. However, for the measured data, different peak heights for both sides and also a shift of the central peak to the right can be noted. These have been observed before by other measurements [Tre02] and are potentially due to the small rotation of the sensor.

#### 5.2.3.2 Double-sided sensors charge correlation

The passage of an ionizing track through the sensor generates an identical number of holes and electrons. Thus, a strong correlation between the P-side and N-side cluster charges is expected. As a result, charge matching between the two sides should be very helpful to reduce hit ambiguity.

Here the charge correlation between the reconstructed clusters on both sides of the sensors in module 1 and module 4 was investigated for both beam momenta. Scatter plots of the P- versus N-side cluster charges were used to study the correlation between both charges. Such distributions are shown in the upper row of the two groups of plots in Figure 5.15. They exhibit a strong correlation between the reconstructed clusters on both sensor sides. The departure of the distributions from the perfect correlation, in which the cluster charge on the P-side is exactly equal to the cluster charge on the N-side, is mainly due to the readout electronics noise. The noise on the N-side is slightly higher than on the P-side.

The difference of the cluster charges on both sides are plotted in the lower row of the two groups of plots in Figure 5.15. These results have been fit with a Gaussian distribution of the charge difference in both sides. A small dispersion of about $11\,keV$ is obtained except for the module 4 at $p_{beam} = 2.95\,GeV/c$ beam momentum. The larger spread in this module is due to the lower gain compared to the threshold. This also explains the more pronounced deviation from the perfect correlation in module 4 than in module 1. During the hit position reconstruction, only clusters on both sides with charge difference of $3\sigma$ from the average difference were considered.

### 5.2.4 Sensor alignment

Since the modules were manually mounted, the exact positions of the sensors were known with a limited precision. In order to achieve the best estimation of the tracking station efficiency, it is essential to determine the correct relative position and orientation of each individual sensor during the beam test. For that purpose, a dedicated algorithm was implemented based on particle tracks traversing planar sensors [K+03].

#### 5.2.4.1 Alignment formalism

The alignment method consists of determining iteratively the correct transformation from the global coordinate system (GCS) $(x, y, z)$ to the sensor local coordinate system (LCS) $(u, v, w)$ by minimizing the $\chi^2$ hit residual function written as:

$$\chi^2 = \sum_{j=0}^{N} \varepsilon_j^T \mathbf{V}_j^{-1} \varepsilon_j \,. \tag{5.3}$$

In this formula, the summation is done over all the $N$ tracks, $\varepsilon$ is the residual vector of the measured hit position $\mathbf{q}_m = (u_m, v_m, 0)$ and the corrected track impact position $\mathbf{q}_x^c = (u_x, v_x, 0)$, and $\mathbf{V}_j$ is the covariance matrix associated with the track $j$.

**Expression of the coordinate transformation**

A complete transformation from the GCS to the LCS includes the translation of the origin and the relative rotation of the axis of the LCS with respect to the GCS. The LCS is such that its origin coincides with the geometric center of the sensor, the $u-$ and $v-$axes are parallel to the directions of the strips at the front and the back sides of the sensor, respectively, and the $w-$axis is perpendicular to the sensor surface.

The transformation of a given hit is

$$\mathbf{q} = \mathbf{R}_0 \cdot (\mathbf{r} - \mathbf{r}_0') \,, \tag{5.4}$$

where $\mathbf{r} = (x, y, z)$ and $\mathbf{q} = (u, v, w)$ are the hit positions in the global and local coordinate systems, respectively, $\mathbf{r}_0' = (x_0', y_0', z_0')$ is the actual global coordinates of the sensor center and $\mathbf{R}_0$ is the actual relative rotation of the local coordinate system with respect to the global coordinate system.

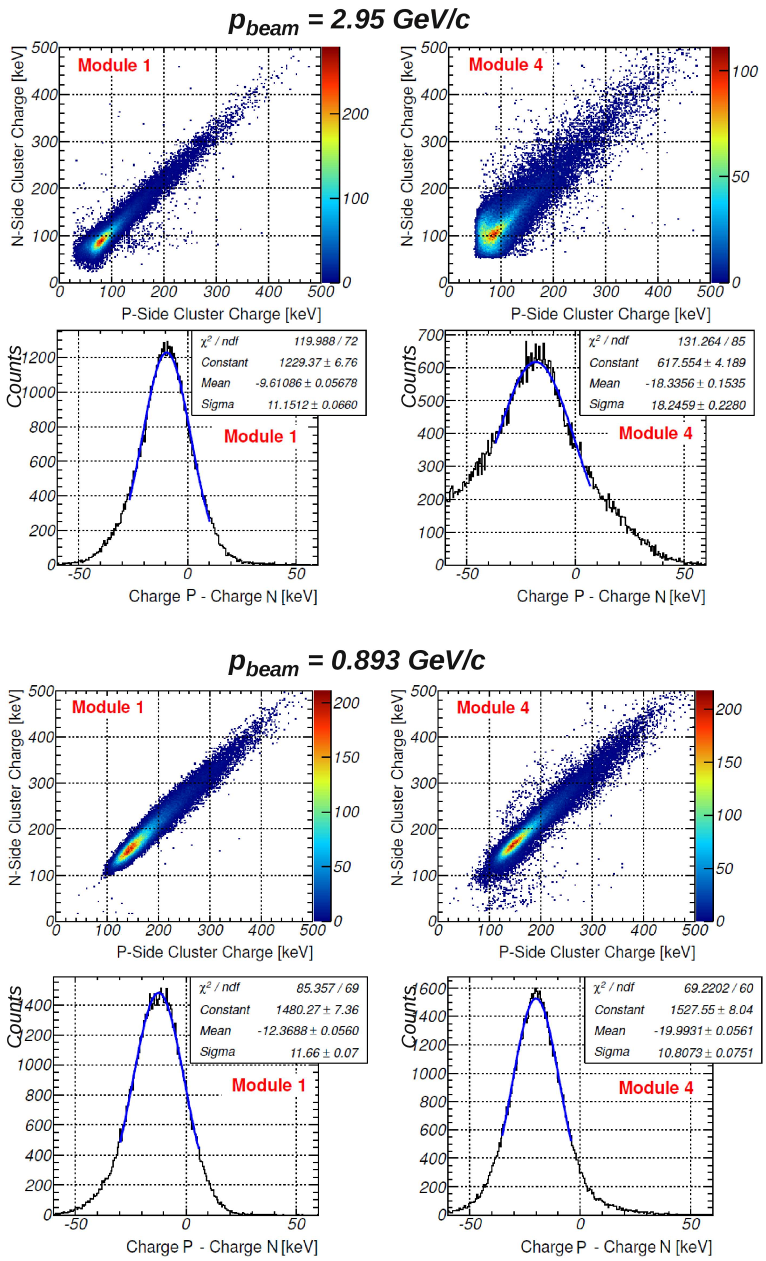


**Figure 5.15**: Scatter plots of charges in the P-side versus the N-side (*upper row*) and distributions of the difference between the P-side and N-side cluster charges (*lower row*) for the two double-sided modules for $p_{beam} = 2.95\,GeV/c$ (*upper group*) and $p_{beam} = 0.893\,GeV/c$ (*lower group*).

These actual transformation matrices are obtained by incrementing the initial measured transformation $\mathbf{r}_0$ and $\mathbf{R}$ with the corrective translation $\mathbf{\Delta r}$ and rotation $\mathbf{\Delta R}$ as following:

$$\mathbf{r}_0' = \mathbf{r}_0 + \mathbf{\Delta r}\,, \tag{5.5}$$

$$\mathbf{R}_0 = \mathbf{\Delta R R}\,, \tag{5.6}$$

where the matrix $\mathbf{\Delta R}$ is the product of the matrices $\mathbf{R}_\alpha$, $\mathbf{R}_\beta$ and $\mathbf{R}_\gamma$ expressing the rotations by small angles $\Delta\alpha$, $\Delta\beta$ and $\Delta\gamma$ around the $w-$axis, the (new) $u-$axis and the (new) $w-$axis, respectively i.e.:

$$\mathbf{\Delta R} = \mathbf{R}_\alpha \mathbf{R}_\beta \mathbf{R}_\gamma = \begin{pmatrix} 1 & \Delta\gamma + \Delta\alpha & 0 \\ -(\Delta\gamma + \Delta\alpha) & 1 & \Delta\beta \\ 0 & \Delta\beta & 1 \end{pmatrix} \tag{5.7}$$

The correct transformation $\mathbf{q}^c$ is then obtained and reads:

$$\mathbf{q}^c = \mathbf{\Delta R R}(\mathbf{r} - \mathbf{r}_0) - \mathbf{\Delta q}\,, \tag{5.8}$$

with $\mathbf{\Delta q} = \mathbf{\Delta R R \Delta r} = (\Delta u, \Delta v, \Delta w)$.

### Expression of the residual

A straight line approximation of the particle trajectory in the vicinity of the sensor plane leads to an expression of the corrected track impact position $\mathbf{q}_x^c$ of

$$\mathbf{q}_x^c = \mathbf{\Delta R R}(\mathbf{r}_x + h\hat{s} - \mathbf{r}_0) - \mathbf{\Delta q}\,, \tag{5.9}$$

where $\hat{s}$ is the unit trajectory direction vector in the GCS and $h$ is the trajectory parameter determined from the condition $\mathbf{q} \cdot \hat{\mathbf{w}} = 0$. Its final expression reads [K+03]

$$\mathbf{q}_x^c = \mathbf{\Delta R q}_x + (\mathbf{\Delta} w - [\mathbf{\Delta R q}_x]_3) \frac{\mathbf{\Delta R \hat{t}}}{[\mathbf{\Delta R \hat{t}}]_3} - \mathbf{\Delta q}\,, \tag{5.10}$$

in which $\hat{t}$ is the uncorrected trajectory direction in the LCS, $\mathbf{q}_x$ is the uncorrected trajectory impact position and the index 3 indicates the third components.

Using the corrective rotation $\mathbf{\Delta R}$ given in Equation (5.7), the residual components are expressed as:

$$\varepsilon_u = u_x - \Delta u + (\Delta\gamma + \Delta\alpha)v_x + (\Delta w + \Delta\beta v_x)\tan\phi - u_m \tag{5.11}$$

$$\varepsilon_v = v_x - \Delta v - (\Delta\gamma + \Delta\alpha)u_x + (\Delta w + \Delta\beta v_x)\tan\theta - v_m \tag{5.12}$$

where $\phi$ is the angle between the $(vw)-$plane and the track and $\theta$ is the angles between the $(uw)-$plane and the track.

In short, the minimization of the $\chi^2$ function defined in Equation (5.3) results in the determination of the values of the alignment parameters. These parameters are explicitly connected to the bivector residual $\varepsilon(\varepsilon_u, \varepsilon_v)$ via the expressions Equations (5.11) and (5.12). There are 6 parameters in total i.e. the three position parameters $(\Delta u, \Delta v, \Delta w)$ and the three orientation parameters $(\Delta\alpha, \Delta\beta, \Delta\gamma)$. This method is known as Hits and Impact Points method (HIP).

| Module Number | Setup 1 (2.95 $GeV/c$) | | Setup 1 (0.893 $GeV/c$) | | Setup 2 (2.95 $GeV/c$) | |
|---|---|---|---|---|---|---|
| | $x$ ($mm$) | $y$ ($mm$) | $x$ ($mm$) | $y$ ($mm$) | $x$ ($mm$) | $y$ ($mm$) |
| 1 | -0.59 | -0.71 | -0.11 | -0.59 | 1.41 | -0.63 |
| 2 | 1.09 | 0.82 | 0.15 | 0.67 | 1.61 | 0.03 |
| 3 | -0.16 | 0.91 | 0.06 | 0.77 | 0.57 | -0.83 |
| 4 | -0.32 | -1.02 | -0.11 | -0.85 | -3.55 | 1.50 |

**Table 5.4**: Start $x-$ and $y-$positions of the four modules for the geometry alignment procedure for the different experimental setups.

#### 5.2.4.2 Tracking station alignment

**Preliminary calibration**

The method of geometry calibration by tracks described previously is only valid for an approximation to a small misalignment. In this case, it is necessary to have an optimal situation in terms of sensor positions before performing the alignment procedure. Therefore, a rough estimation of the position of each individual module in GCS is required. The obtained position will be then used as start positions for the sensors for the alignment process.

Initially, the detector axis ($w-$axis) was assumed to be collinear to the beam direction ($z-$axis). The $z-$positions of the modules were assumed to be relatively accurately measured. Therefore, the position estimation consists of determining the lateral shifts, i.e. in the $x-$ and $y-$directions, that will be performed for each individual detector module. The magnitude of the displacement of a single module is given by the mean value of the hit residual distributions in the two directions. Here, the hit residual is defined by the difference between the measured hit position and the projected track position reconstructed from *equally weighted* hits. This means that during the track fitting, the hit errors were set to a same value and any correlation between modules was not considered. Using the $\chi^2$ function defined in Equation (4.31), one can choose the $4 \times 4$ identity covariance matrices for the $x-$ and $y-$components. The results of this operation are given in Table 5.4 for Setup 1 at $p_{beam} = 2.95$ and $0.893\,GeV/c$ and for Setup 2.

**Sensor alignment**

During the alignment process, several assumption have been made. As already mentioned above, the $z-$position of each individual module was assumed to be accurately measured. In addition, since the tracks are nearly perpendicular to the detector plane, the alignment procedure has very low sensitivity to shifts in the $w-$direction, i.e. $\Delta w = 0$. Also, due to lack of information, the relative displacement between the two sensors in the single-sided modules was neglected. As a consequence, they undergo the same geometrical transformation during the process. Furthermore, since the track fitting process uses the first two modules as a reference, no additional translations were allowed for these modules. The second module was however allowed to be rotated. Consequently, the whole transformation acts only on the two last modules.

The track fitting parameters were calculated from simulation. As developed in Section 4.3.4.2, the hit errors on the two first planes corresponds to the intrinsic detector resolution i.e. $\sigma_1 = \sigma_2 \simeq 14\,\mu m$. The hit errors on the two last planes are given in Table 5.5. The

| | | Parameter | | | | |
|---|---|---|---|---|---|---|
| | $p_{beam}$ $[GeV/c]$ | $\sigma_1$ $[cm]$ | $\sigma_2$ $[cm]$ | $\sigma_3$ $[cm]$ | $\sigma_4$ $[cm]$ | $\rho_{34}$ |
| Setup 1 | 2.95 | $1.4 \times 10^{-4}$ | $1.4 \times 10^{-4}$ | 0.0207 | 0.0404 | 0.64 |
| | 0.893 | $1.4 \times 10^{-4}$ | $1.4 \times 10^{-4}$ | 0.0952 | 0.1865 | 0.68 |
| Setup 2 | 2.95 | $1.4 \times 10^{-4}$ | $1.4 \times 10^{-4}$ | 0.0126 | 0.0157 | 0.71 |

**Table 5.5**: Hit errors and correlation coefficients corresponding to the two experimental setups.

non-zero off-diagonal element of the correlation matrix is also given in this table for both beam momenta.

These errors were assigned to the measured hit position during the $\chi^2-$minimization for the alignment process. The errors for the track impact position were set to the detector resolution. Therefore, the covariance matrix used in Equation (5.3) is independent of the track and for a given module $i$, it is written:

$$V^i = \begin{pmatrix} \sigma_{res}^2 + \sigma_i^2 & 0 \\ 0 & \sigma_{res}^2 + \sigma_i^2 \end{pmatrix} \tag{5.13}$$

where $\sigma_{res}$ is the detector resolution and $\sigma_i$ is the hit errors at the $i^{th}$ module. Here it was assumed that there is no correlation between the $u-$ and $v-$coordinates.

The minimization was performed sequentially for each module. Each minimization leads to a correction of the geometry. The full reconstruction chain is repeated for every single module transformation. For each detector setup, about 70,000 tracks were used. For the case of Setup 2, the alignment procedure was only performed at normal incident angle ($\omega = 0°$). The error of the angle at which Module 4 was rotated, was assumed to be small relative to the alignment precision.

An illustration of the geometry calibration is shown Figure 5.16. The evolution of the distributions of the hit residuals $\Delta\vec{x} = (\Delta x, \Delta y)$ in the GCS at each individual module after every complete iteration are plotted in this figure. These plots corresponds to the data taken with Setup 1 at $p_{beam} = 2.95\,GeV/c$. The width and the position of the residual distributions in Module 1 remain unchanged throughout the process since the corresponding hits, with the ones at Module 2, were used as reference for the track fitting procedure. The residual distributions on Module 2 were slightly changed because rotations were allowed to be performed during the calibration. Nevertheless, the width of the distributions remains on the order of $14\,\mu m$. In the two last modules, the distributions moved towards $\Delta x = \Delta y = 0$ and its width narrowed. On both modules, the width of the distribution is limited by the errors of the measured hit position on this module. The width converged quickly to the error values after only 2 iterations. Typically, the sensor alignment was achieved after 3 iterations. This is illustrated by the variation of the fit parameters as a function of the number of iterations shown in Figure 5.17. After 3 iterations, the value of each individual parameter did not change significantly.

The summary of the values of the alignment parameters with respect to the start positions obtained after the complete geometry calibration for detector Setup 1 at $2.95\,GeV/c$ and $0.893\,GeV/c$ beam momenta is given in Table 5.6 and Table 5.7, respectively, and for the detector Setup 2 at the normal incident track ($\omega = 0°$) is given in Table 5.8.

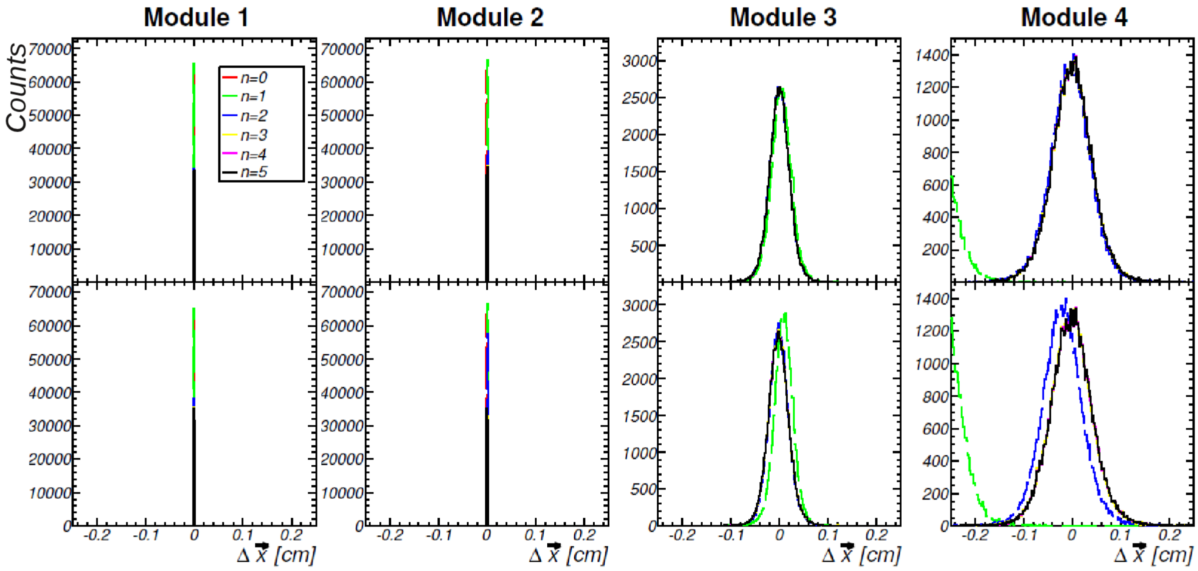


**Figure 5.16**: Distributions of the hits residuals $\Delta x$ (*upper row*) and $\Delta y$ (*lower row*) in each individual module after $n$ iterations.

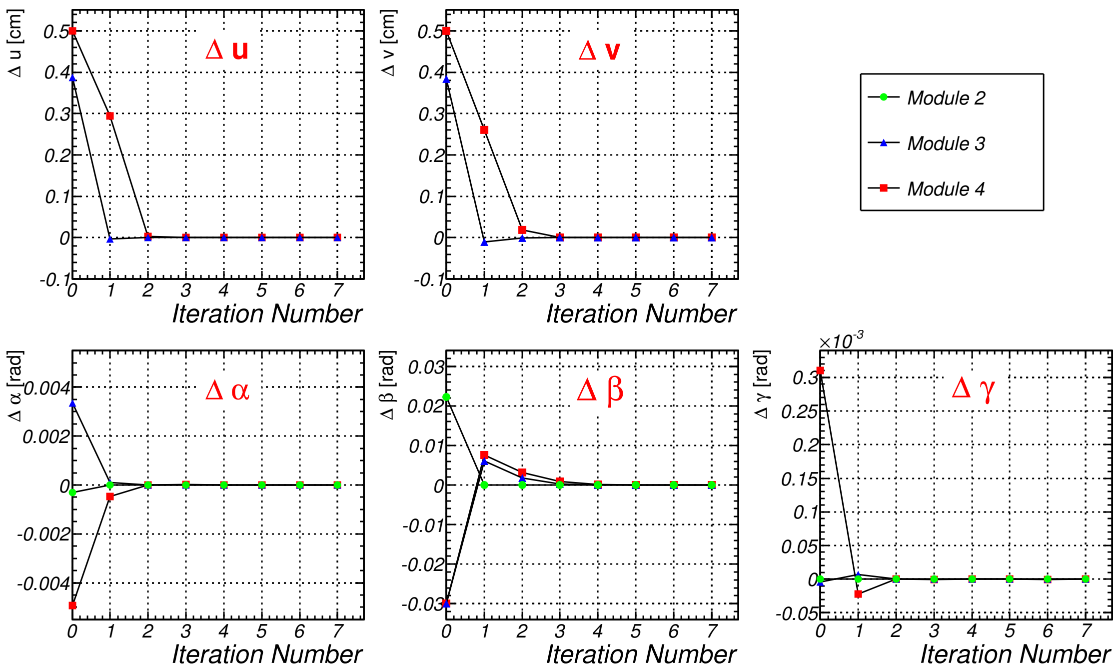


**Figure 5.17**: Variations of the alignment parameters as a function of the number of iterations for the module 2, 3 and 4.

| Setup 1 at $p_{beam} = 2.95\,GeV/c$ | | | | | |
|---|---|---|---|---|---|
| Module Number | $\Delta u$ $(mm)$ | $\Delta v$ $(mm)$ | $\Delta\alpha$ $(mrad)$ | $\Delta\beta$ $(mrad)$ | $\Delta\gamma$ $(mrad)$ |
| 2 | – | – | -0.32 | 22.26 | $-5.71 \cdot 10^{-5}$ |
| 3 | 3.85 | 3.72 | 3.46 | -21.87 | $3.65 \cdot 10^{-3}$ |
| 4 | 7.98 | 7.80 | -5.36 | -18.14 | 0.28 |

**Table 5.6**: Alignment parameters values for the module 2, 3 and 4 for the data taken with the geometry Setup 1 at $p_{beam} = 2.95\,GeV/c$ relative to the start position in Table 5.4.

| Setup 1 at $p_{beam} = 0.893\,GeV/c$ | | | | | |
|---|---|---|---|---|---|
| Module Number | $\Delta u$ $(mm)$ | $\Delta v$ $(mm)$ | $\Delta\alpha$ $(mrad)$ | $\Delta\beta$ $(mrad)$ | $\Delta\gamma$ $(mrad)$ |
| 2 | – | – | $1.27 \cdot 10^{-2}$ | -35.75 | $-2.32 \cdot 10^{-4}$ |
| 3 | 1.24 | 1.25 | 1.22 | 26.33 | 1.20 |
| 4 | 0.78 | 1.82 | -9.42 | -29.99 | 2.55 |

**Table 5.7**: Alignment parameters values for the module 2, 3 and 4 for the data taken with the geometry Setup 1 at $p_{beam} = 0.893\,GeV/c$ relative to the start position in Table 5.4.

| Setup 2 at $\omega = 0°$ | | | | | |
|---|---|---|---|---|---|
| Module Number | $\Delta u$ $(mm)$ | $\Delta v$ $(mm)$ | $\Delta\alpha$ $(mrad)$ | $\Delta\beta$ $(mrad)$ | $\Delta\gamma$ $(mrad)$ |
| 2 | – | – | -1.42 | -10.33 | $-4.22 \cdot 10^{-3}$ |
| 3 | 2.24 | 0.85 | 2.32 | -32.24 | $9.60 \cdot 10^{-3}$ |
| 4 | 8.04 | 7.66 | 6.63 | 13.61 | $4.18 \cdot 10^{-2}$ |

**Table 5.8**: Alignment parameters values for the module 2, 3 and 4 for the data taken with the geometry Setup 2 at normal track incident relative to the start position in Table 5.4.

### 5.2.5 Detector resolution

After the alignment, the resolution of the tracking station can be determined. For a given experimental setup, a *virtual plane* perpendicular to the $z-$direction was placed in the middle of the second and third modules. Two straight lines formed by the hits at the two first modules and by the hits at two last modules, respectively, are projected onto the virtual plane. The detector resolution can be estimated by investigating the bivector residuals $\Delta\vec{x} = (\Delta x, \Delta y)$ of the positions of the two projected lines on that plane. An illustration of the method is shown in Figure 5.18. In this study, the beam test measured data were compared to the simulation.

For Setup 1, the virtual plane is located at $z = +109.85\,cm$. In the simulation, the residuals have Gaussian distributions with means $\overline{\Delta x} = \overline{\Delta y} = 0$. Similar values of means are obtained for the measured data. But the residual distributions for the measured data differ to the simulation by the existence of the long tail on both sides of the central Gaussian distribution. This can be seen through the distributions of of $\Delta r = \sqrt{(\Delta x)^2 + (\Delta y)^2}$ shown in Figure 5.19 for both simulation and measured data. The non-Gaussian tail on this distribution represents the single scattering events.

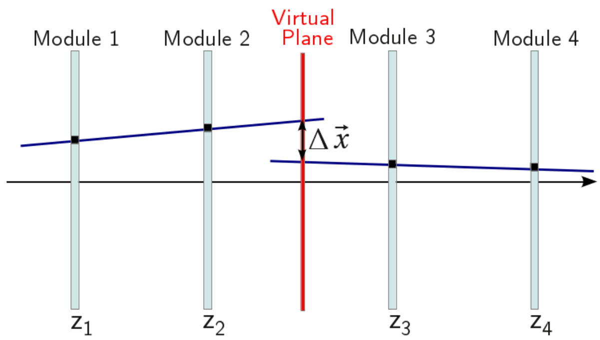


**Figure 5.18**: Illustration of the projections of the lines formed by the hits at the two first modules and by the hits at two last modules onto a virtual plane located at $z = (z_2 + z_3)/2$.

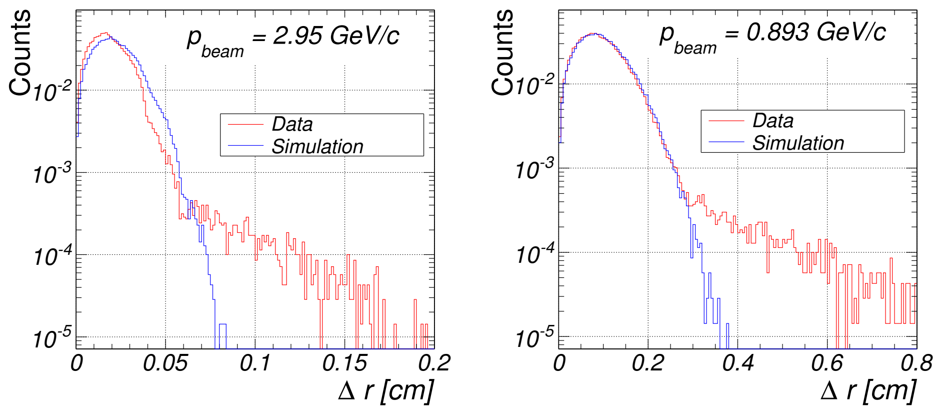


**Figure 5.19**: Distributions of the residuals of the two lines projection points onto the virtual plane located at $z = +109.85\,cm$ corresponding to the detector Setup 1 for $p_{beam} = 2.95\,GeV/c$ (*left*) and $p_{beam} = 0.893\,GeV/c$ (*right*).

If the tails are not considered, the standard deviations of the central Gaussian distribution can be used as an estimate of the resolution in the two directions. In this case slightly better resolutions $\sigma_{data}$ are obtained for the tracking station compared to the resolutions $\sigma_{sim}$ from the simulation. Similar resolutions are obtained in the $x-$ and $y-$directions: $\sigma_{data} \simeq 150 \pm 1.2\,\mu m$ ($\sigma_{sim} = 179\,\mu m$) and $\sigma_{data} \simeq 750 \pm 2.2\,\mu m$ ($\sigma_{sim} = 780\,\mu m$) are obtained for $p_{beam} = 2.95$ and $0.893\,GeV/c$, respectively. These values depend strongly on the position of the virtual plane and, especially for the data, on the precision of the geometry calibration procedure. The agreement between the data and the simulation results reflects the correctness of the alignment procedure and the tracking procedure.

For Setup 2, the position of the virtual plane is at $z = 145\,cm$. The residual distributions of the projected positions on this plane are similar to this results above. Fits to the central Gaussian distribution were used to determine the resolution. The variations of the resolution as a function of the incident angle $\omega$ are shown in Figure 5.20 for the two coordinates. As a reference the results from simulations are also plotted in the same frame. At normal incidence, in the simulation, similar resolutions of about $129\,\mu m$ are obtained in both directions. The

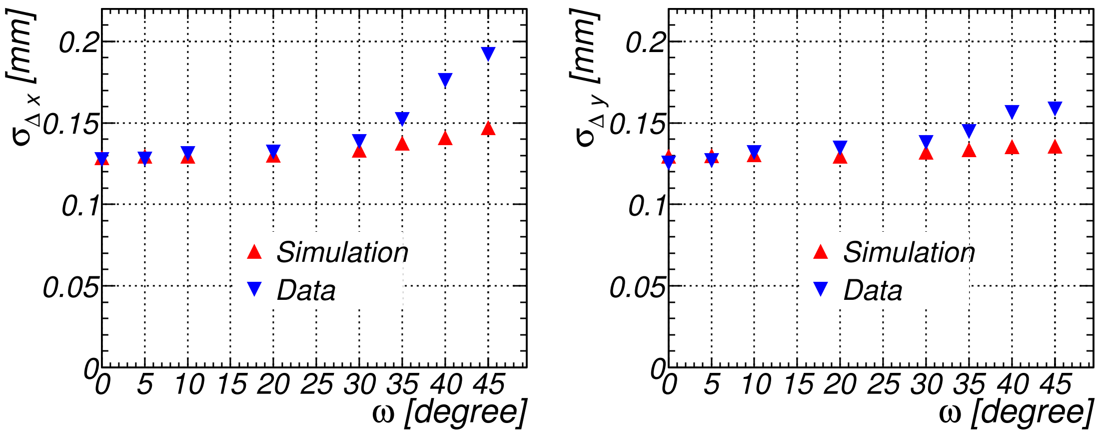


**Figure 5.20**: Variation of the resolution in the $x-$direction (*left*) and the $y-$direction (*right*) as a function of the incident angle for Setup 2.

resolution in $y-$direction is not sensitive to the incident angle. But in the $x-$direction, the resolution decreases at bigger incident angles and worsens by a factor of about 1.5 at $\omega = 45°$.

The measured data agree with the simulation for small incident angles ($\omega < 30°$). Data points stand out from those of the simulation for larger angles and the resolution deteriorates. This may be a consequence of the geometry not being recalibrated at each rotated angle.

### 5.2.6 Tracking station efficiency

The track finding method used for the beam test analysis was the line projection method described in the previous chapter. Since, the method is triggered by the hits found in the outer planes, the combination of the external hits represents the probable number of tracks that can be reconstructed. In this case, the efficiency $\epsilon$ is defined by the ratio of the number of reconstructed track to the number of hits reconstructed at the two outer planes:

$$\epsilon = \frac{\#\, Reconstructed\, Track}{\#Probable\, Track\, Candidate}\,. \tag{5.14}$$

Within the track finding algorithm, a track can only be reconstructed if all four modules are hit, i.e. the efficiency is obtained by the probability of finding hits in the two intermediate planes for a given probable track candidate configuration. Here, the study was only performed over the effective acceptance of the tracking station i.e. only probable tracks candidate belonging to the overlapped area of all modules are considered. Based on this cut, if $\epsilon_2$ and $\epsilon_3$ are the efficiencies of finding hit in the second and third planes, respectively, the total efficiency reads:

$$\epsilon = \epsilon_2 \cdot \epsilon_3\,. \tag{5.15}$$

In the intermediate planes, the hits were searched for over a finite region that was determined for each plane by the simulations. For a given plane, it was deduced from the width of the distribution of the residual between the projected position of the line formed by the outer hits and the hit position on this plane. The distributions in the $x-$ and $y-$directions of such residuals are Gaussian of $\sigma_2$ and $\sigma_3$ widths at the second and third planes, respectively. The values of the width corresponding to the different experimental setups are given in Table 5.9.

| | $\sigma_2$ [$\mu m$] | $\sigma_3$ [$\mu m$] |
|---|---|---|
| Setup 1 | | |
| $p_{beam} = 2.95\,GeV/c$ | 125.85 | 102.34 |
| $p_{beam} = 0.893\,GeV/c$ | 557.63 | 458.88 |
| Setup 2 | | |
| $\omega = 0°$ | 125.85 | 38.13 |
| $\omega = 5°$ | 127.32 | 37.95 |
| $\omega = 10°$ | 127.89 | 37.84 |
| $\omega = 20°$ | 128.54 | 38.17 |
| $\omega = 30°$ | 129.97 | 38.33 |
| $\omega = 35°$ | 133.81 | 38.99 |
| $\omega = 40°$ | 136.17 | 39.08 |
| $\omega = 45°$ | 138.38 | 39.36 |

**Table 5.9**: Widths of the residual distributions between the position of the line formed by the two hits of the outer planes projected onto the second and third planes and the hit positions on these planes.

Here, the searching area was set to $3\sigma$. The efficiencies of the two considered modules are about $\epsilon_2 = \epsilon_3 \simeq 97.7\%$. The average efficiency obtained for the tracking station is about $\epsilon \simeq 95\%$. During this study, the region containing dead channels were omitted. Thus, this result is mainly dominated by the precision of the geometry calibration process.

## 5.3 Summary

Tests of the silicon strip tracking station were performed with proton beams at the COSY accelerator. Two beam energies of $2.95\,GeV/c$ and $0.893\,GeV/c$ were used during a one week beam test. For the $2.95\,GeV/c$ beam momentum, two different detector setups, see Figure 5.2, were tested.

The data analysis was conducted using the simulation software conceived for the luminosity monitor and which has been implemented in PandaRoot. In this way, the beam test provided an opportunity to validate the reconstruction chain in the software. The results of the data analysis were presented throughout this chapter.

It was shown that the width of the clusters are narrower for the high beam momentum since the deposited charge is much lower than in the low beam momentum. The charge calibration was done by setting the most probable deposited charge obtained by a fit to the charge distribution with a Landau convoluted by a Gaussian function to the theoretical calculation given in [N+10].

The analysis of the data taken with the geometry setup that had one module rotated provided the establishment of the linear proportionality of the cluster charge with $1/\cos\omega$ where $\omega$ is the track incident angle with respect to the sensor surface. The study of the angular dependence of the cluster size shows that the rotation affects more the cluster on the side where the strip direction is parallel to the axis of the rotation. In this side, the cluster size varies linearly with the incident angle, especially for $5° < \omega < 35°$. On the opposite side, the cluster size is practically constant.

A validation of the one-dimensional hit position reconstruction was performed by comparing the $\eta-$distribution for the beam test data with simulations where different Gaussian widths modeling the charge diffusion, $\sigma_{diff}$, were used. The simulation used the noise and threshold values reconstructed during the analysis. It follows then that the simulations with $\sigma_{diff} = 8$ to $10\,\mu m$ are good approximations of the measured data. But this only stands for the N-side of the sensor. The existence of the peak near $\eta = 0.55$ makes the $\eta-$distribution at the P-side difficult to reproduce in simulation.

For single-sided sensor modules, the two-dimensional position reconstruction was performed for all possible combinations of the clusters reconstructed on both sides. In this case, it was impossible to discriminate actual hits from ghost hits. However, for double-sided sensor modules, the strong correlation of charges collected in the P- and N-sides was exploited to suppress ghost hits.

The spatial resolution was determined after performing a geometry calibration. An algorithm developed in [K+03] was briefly introduced in the text and was implemented to perform the offline alignment of the modules of the tracking stations. The resolution of the tracking station was estimated relative to a virtual plane located in the middle of the modules placed on the second and the third positions. A good agreement with the simulation was obtained for the data taken with the detector Setup 1 (at both momenta) and with the detector Setup 2 at nearly normal track incidence in which the resolutions were $150\,\mu m$, $750\,\mu m$ and $126\,\mu m$, respectively.

The efficiency of the tracking station was evaluated in terms of the probability of finding hits on the second and third planes for a given track configuration defined by two hits of the outer planes within the effective acceptance of the detector. An individual efficiency of above 97% and a global efficiency of about 95% were obtained for all different experimental setups used during the beam test.

Chapter 6

# Mass and Width Reconstruction of the X(3872) Meson with $\bar{\text{P}}$ANDA

The $\bar{\text{P}}$ANDA experiment will allow the direct formation of the $X(3872)$ meson to be measured via $\bar{p}p$ annihilation. The measurement of its properties, mainly the mass and the width, will be performed by studying its decay products. Despite the narrowness of the $X(3872)$, $\bar{\text{P}}$ANDA is expected to have sufficient resolution to measure the width. A direct analysis of the final states mass spectrum will not be effective to determine the $X(3872)$ meson properties, instead the well-known *resonance scan* method will be used.

Simulation studies on the performance of the $\bar{\text{P}}$ANDA experiment to reconstruct the mass and the width of the $X(3872)$ meson is presented in this chapter. It is focused on the formation and exclusive decay of the $X(3872)$ meson to the $\pi^+\pi^- J/\psi$ final state. The $J/\psi$ state will be identified through its leptonic decay and the dipion system is assumed to be the result of the intermediate $\rho^0$ meson decay. The complete decay chain is then written as

$$\begin{aligned} \bar{p}p &\rightarrow X(3872) \rightarrow J/\psi\rho^0\,; && (6.1)\\ J/\psi &\rightarrow l^+l^-\,,\, l=\{e,\mu\}\,; && (6.2)\\ \rho^0 &\rightarrow \pi^+\pi^-\,. && (6.3) \end{aligned}$$

This study is based on the line shape assumption given in [CM08]. The description of the event generator used for this simulation is given in the first section of this chapter. The next section describes the simulation using the resonance scan method. This is followed by the mass and width determination. And finally, the results will be presented as a summary of this chapter.

## 6.1 Event generator

The resonance scan method is based on the measurement of the count rate for the $\pi^+\pi^- J/\psi$ final state at different center-of-mass energies, called *scan points*. The $\pi^+\pi^- J/\psi$ invariant mass will be generated with a function that has two main components: the *signal* and the *instrumental background*.

For what follows, it is necessary to point out the difference between physical and instrumental background. The physical background is due to measurement of the same $\pi^+\pi^- J/\psi$ final state which does not come from the decay of the considered intermediate state. In this simulation, this type of background is incorporated with the signal. The instrumental background is due to a different final states that were falsely identified as $\pi^+\pi^- J/\psi$ by the detector.

The invariant mass distribution of the $\pi^+\pi^- J/\psi$ final state will be generated by a function which is the weighted sum of the signal and instrumental background probability density functions, $f_{SIG}$ and $f_{BKG}$, respectively. The weights are the number of signal events $N_{SIG}$ and the number of instrumental background $N_{BKG}$, respectively. The function is then written as:

$$f_{M_{inv}}(m) = N_{SIG} \cdot f_{SIG}(m) + N_{BKG} \cdot f_{BKG}(m) \,. \tag{6.4}$$

The distribution of the $\pi^+\pi^- J/\psi$ count rate depends on the resolution of the detector for a given center-of-mass energy. If $\sigma_{SIG}$ is the detector resolution, the signal is a Gaussian distribution with a mean $\sqrt{s}$ and width $\sigma_{SIG}$. The expression of the $f_{SIG}$ is then:

$$f_{SIG}(m, \sqrt{s}, \sigma_{SIG}) = \frac{1}{\sigma_{SIG}\sqrt{2\pi}} \cdot exp\left[-\frac{1}{2} \cdot \left(\frac{m-\sqrt{s}}{\sigma_{SIG}}\right)^2\right] \tag{6.5}$$

The instrumental background will be implemented by using the so-called ARGUS function [A+90]. This function gives a good description of the phase space multi-body decays near the threshold. Its probability density function has the form:

$$f_{ARG}(m, m_0, c) = m \cdot \sqrt{1-\left(\frac{m}{m_0}\right)^2} \cdot exp\left[c \cdot \left(1-\left(\frac{m}{m_0}\right)^2\right)\right] \tag{6.6}$$

in which $c$ is the shape parameter which determines the curvature of the function and $m_0$ is the cutoff parameter which defines the phase space limit.

In the simulation, the phase space limit is shifted down from $\sqrt{s}$ by $2\sigma_{SIG}$ to take into account the finite detector resolution. Thus, the background shape will be described by the function $f_{BKG}$ defined as :

$$f_{BKG}(m, \sqrt{s}, c) = f_{ARG}(m, \sqrt{s} + 2\sigma_{SIG}, c) \,. \tag{6.7}$$

The number of events $N_{BKG}$ of the background is determined from the number $N_{peak}$ of the signal corresponding to the cross section peak i.e. at the resonance mass, and the signal to background ratio $r_{SB}$ as following:

$$\begin{aligned} N_{BKG} &= \frac{N_{peak}}{r_{SB}} \cdot \frac{\mathcal{A}_{SIG}|_{peak}}{\mathcal{A}_{BKG}|_{peak}} \\ &= \frac{N_{peak}}{r_{SB}} \cdot \frac{\int_{M_{in}-\sigma_{SIG}}^{M_{in}+\sigma_{SIG}} f_{SIG}(m, M_{in}, \sigma_{SIG})}{\int_{M_{in}-\sigma_{BKG}}^{M_{in}+\sigma_{SIG}} f_{BKG}(m, M_{in}, c)} \end{aligned} \tag{6.8}$$

Examples of plots of the probability density functions of the $\pi^+\pi^- J/\psi$ invariant mass generator for given values of $\sigma_{SIG}$, $c$ and different values of $r_{SB}$ are drawn in Figure 6.1.

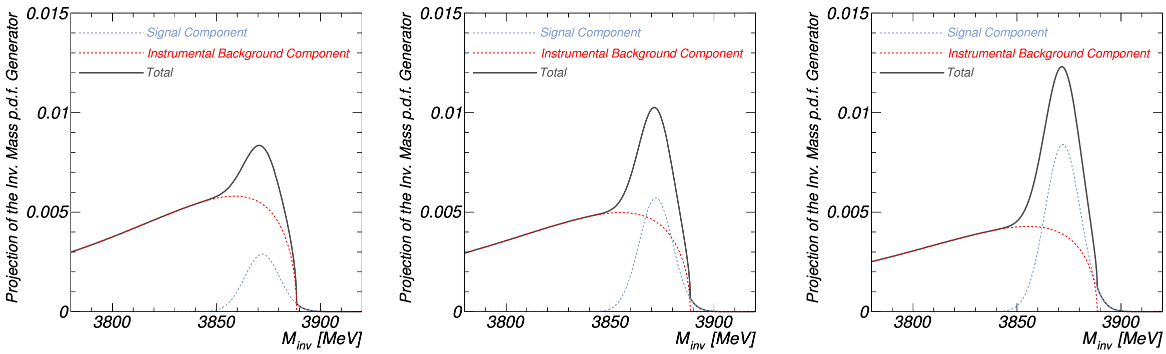


**Figure 6.1**: The *p.d.f.* of $\pi^+\pi^- J/\psi$ invariant mass at $\sqrt{s} = 3872\ MeV$ for signal to background ratios $r_{SB} = 0.5$ (*left*), $r_{SB} = 1$ (*middle*) and $r_{SB} = 2$ (*right*). The red and blue dashed curves are the signal and the instrumental background components of the *p.d.f.*, respectively. Here, The width of the Gaussian signal function is $\sigma_{SIG} = 8.3\ MeV$, and the shape parameter of the ARGUS background function is $c = -10$.

## 6.2 Simulation of $X(3872) \to J/\psi\pi^+\pi^-$

### 6.2.1 Line shape function

The final state production cross section varies as a function of the center-of-mass energy. The corresponding line shape contains information on the nature of the decaying particle. Since the exact nature of the $X(3872)$ meson is still unknown, an assumption must be made to define the line shape.

Numerical predictions of the cross section of the $\bar{p}p \to \pi^+\pi^- J/\psi$ reaction near the $X(3872)$ threshold are described in [CM08]. Two different cases were investigated corresponding on the interpretations of the $X(3872)$ meson being a loosely bound $D^0\bar{D}^{*0}$ molecule and being the first excited state of the $\chi_{c1}$ state. The cross section estimations take into account the non-resonant final state and assume the dipion system comes from the $\rho$ meson resonance.

The outcome of the calculations can be summarized by the determination of the line shape as a superposition of a Breit-Wigner resonance peak and a first order polynomial physical background. In the simulation described below the corresponding probability density function $\sigma_{pdf}$ was used to estimate to cross section at a given center-of-mass energy $\sqrt{s}$:

$$\sigma_{pdf}(\sqrt{s}) = (1-q) \cdot \frac{\Gamma_{in}/2}{(\sqrt{s} - M_{in})^2 + (\Gamma_{in}/2)^2} + q \cdot f_{pol}(\sqrt{s})\,, \tag{6.9}$$

where the first term refers to the non-relativistic Breit-Wigner $X(3872)$ resonance, $f_{pol}$ is the polynomial term for the non-resonant background. $M_{in}$ and $\Gamma_{in}$ are the input mass and width, respectively, and $q$ is the relative fraction between the resonance signal and the physical background.

It was assumed in this study that the $X(3872)$ resonance occurs at $\sqrt{s} = M_{in} = 3872\,MeV$. The resonance scan simulations were performed for three different supposed values of the width: $\Gamma_{in} = 136\,keV$, $0.5\,MeV$ and $1\,MeV$. The choice of these values are essentially based on the

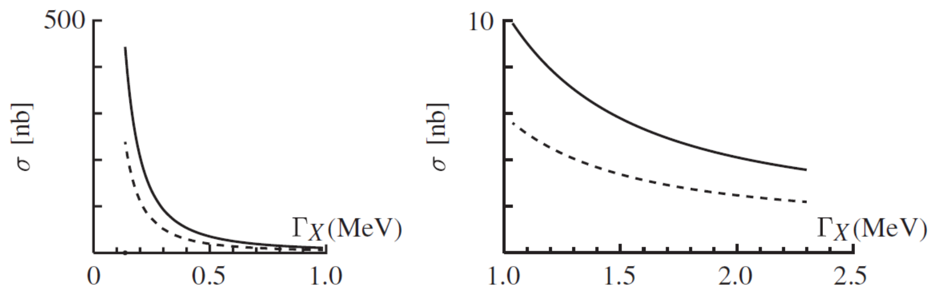


**Figure 6.2**: The $\pi^+\pi^- J/\psi$ production cross section as a function of the total width of the $X(3872)$ meson at the resonance mass location. The solid and dashed curves correspond to the $D^0\bar{D}^{*0}$ bound state and $\chi_{c1}(2P)$ charmonium interpretations, respectively. Picture taken from [CM08].

calculations performed in [CM08] in which an upper and a lower bound of the total width are estimated to be:

$$\begin{aligned} 2\Gamma_{D^*} &< \Gamma_X < \Gamma_{X,max} \\ 136 \pm 32\,keV &< \Gamma_X < 2.3 MeV. \end{aligned} \tag{6.10}$$

According to [CM08], the $\pi^+\pi^- J/\psi$ final state production cross section depends strongly on the total width of the $X(3872)$ meson. This is explicitly shown in Figure 6.2 in which the peak cross section corresponding to the two models ($D^0\bar{D}^{*0}$ bound state and $\chi_{c1}(2P)$ charmonium) is drawn within the width range given in Equation (6.10). It is also shown the relatively higher cross section in the $D^0\bar{D}^{*0}$ bound state interpretation comparing to the $\chi_{c1}$ charmonium interpretation.

Based on these results, the $X(3872)$ *interpreted as a* $\chi_{c1}(2P)$ *state* was adopted, in which the cross section of the final state production is lower and the peak cross section $\sigma_{peak}$ is within the range:

$$\sigma_{peak} = 2.19 - 238\,nb \quad \text{for} \quad \Gamma_X = 2.3 - 0.136\,MeV\,. \tag{6.11}$$

In contrast, the cross section for the physical background has a very small variation over the width of the $X(3872)$. As a consequence, one can assume that in the vicinity of the $X(3872)$ threshold (e.g within a range of $\pm 2\ MeV$), the physical background cross section is constant. The value of 1.2 $nb$ was used in the simulation.

After combining this information, the line shapes for the three simulated widths are presented in Figure 6.3.

### 6.2.2 Input simulation parameters

The expected number of events in the signal, $N_{SIG}$, at a given scan point $\sqrt{s}$ is given by

$$N_{SIG} = \varepsilon \cdot f_{\mathcal{B}} \cdot \sigma \cdot \mathcal{L} \cdot T_{beam} \tag{6.12}$$

where $\sigma$ is the cross section, $\varepsilon$ includes the geometry acceptance of the detector and the final state reconstruction efficiency, $\mathcal{L} = \int \mathring{\mathcal{L}} \cdot dt$ and $T_{beam}$ are the integrated luminosity and the

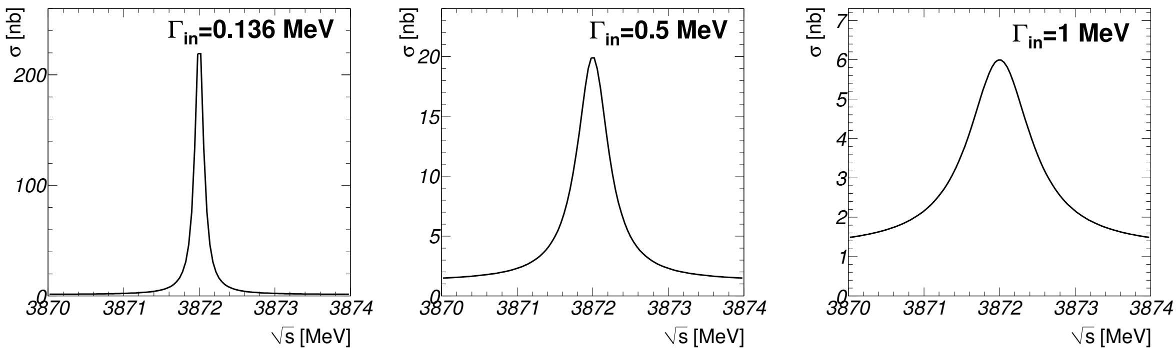


**Figure 6.3**: The line shapes used in the event generator for the three input widths.

beam time spent for the measurement, respectively, and $f_B$ is the combined branching ratios of the decay chain, which is, for the channel of interest, expressed as:

$$f_{\mathcal{B}} = \underbrace{\mathcal{B}(X \to \bar{p}p)}_{\mathcal{B}_{in}} \times \underbrace{\mathcal{B}(X \to \rho J/\psi) \times \mathcal{B}(\rho \to \pi^+\pi-) \times \mathcal{B}(J/\psi \to l^+l^-)}_{\mathcal{B}_{out}} . \tag{6.13}$$

Given that the cross section calculations performed in [CM08] include the Equations (6.1) and (6.3) decay channels, the combined branching ratio $f_{\mathcal{B}}$ was reduced to the leptonic decay of the $J/\psi$ branching ratio as:

$$\begin{aligned} f_{\mathcal{B}} &= \mathcal{B}(J/\psi \to e^+e^-, \mu^+\mu^-) \\ &= 12\%. \end{aligned} \tag{6.14}$$

Since the $\bar{\text{P}}$ANDA detector has nearly $4\pi$ solid angle coverage, the product of the geometry acceptance with the reconstruction efficiency $\varepsilon$ for the $\pi^+\pi^-J/\psi$ final state is taken to be about 0.3 at $\sqrt{s} = 3872\,MeV$ [pC09a].

For these simulations, the $\bar{\text{P}}$ANDA high resolution mode with a relative momentum spread $\delta p/p \simeq 3 \times 10^{-5}$ corresponding to an instantaneous luminosity of $2 \times 10^{31}\,cm^{-1} \cdot s^{-1}$. Assuming a 50% duty cycle of the HESR accelerator, the integrated luminosity used for the simulation is about $864\,nb^{-1}/day$.

The resonance scan was performed at 10 different scan points within the interval $\pm 2\,MeV$ around $M_{in}$. The time spent for each scan point was set to 4 days. At each scan point, the Gaussian signal function has a width of $\sigma_{SIG} = 8.3\ MeV$ corresponding to the detector resolution. This value is taken from the simulation study on the benchmark channel $\bar{p}p \to \pi^+\pi^-J/\psi \to \pi^+\pi^-e^+e^-$ exclusive process at 3872 $MeV$ center-of-mass energy with the PandaRoot framework analysis and described elsewhere [pC09a]. The shape parameter of the ARGUS instrumental background function was set to $-10$.

A summary of the input parameters of the resonance scan simulation is given in Table 6.1 and the expected daily rates at peak for the different input widths obtained from the peak cross section and the relation (6.12) in Table 6.2.

| Parameter Name | Symbol | Value |
|---|---|---|
| Input resonance mass | $M_{in}$ | $3872\, MeV$ |
| Input resonance widths | $\Gamma_{in}$ | $0.136\,, 0.5\,, 1\, MeV$ |
| Acceptance × Efficiency | $\varepsilon$ | 0.3 |
| Integrated luminosity | $\mathcal{L}$ | $864\, nb^{-1}/day$ |
| Combined branching ratio | $f_{\mathcal{B}}$ | 0.12 |
| Physical background cross section | $\sigma_{PHYS.BKG.}$ | $1.2\, nb$ |
| Number of scan points | $n_{SP}$ | 10 |
| Energy range scan around the resonance | $\Delta E$ | $2\, MeV$ |
| Time spent per scan | $T_{beam}$ | $4\, days$ |
| Gaussian signal width | $\sigma_{SIG}$ | $8.3\ MeV$ |
| Instrumental background shape parameter | $c$ | $-10$ |

**Table 6.1**: Input parameters for the event generator of the simulation.

| $\mathbf{\Gamma_{in}}$ **(MeV)** | **0.136** | **0.5** | **1** |
|---|---|---|---|
| $\sigma_{peak}\ (nb)$ | 238 | 20 | 6 |
| $N_{peak}\ (/day)$ | 7042 | 622 | 186 |

**Table 6.2**: Expected daily rate of the $\pi^+\pi^- J/\psi$ final state at $\bar{\text{P}}$ANDA at the $X(3872)$ resonance mass, where the $X(3872)$ meson is interpreted as $\chi_{c1}(2P)$ charmonium. The peak cross section value have been deduced from Figure 6.2.

### 6.2.3 Resonance scan simulation

The resonance scan simulation consists on generating the $\pi^+\pi^- J/\psi$ invariant mass spectra at the 10 different scan points around the expected resonance mass by using the $f_{M_{inv}}$ function defined in Equation (6.4). The input number of signal events and instrumental background events are generated according to Poisson distributions with expectation values $N_{SIG}$ calculated from Equation (6.12), and $N_{BKG}$ calculated from Equation (6.8), respectively. For the later, the value of the signal to background ratio needs to be set.

## 6.3 Mass and width reconstruction

### 6.3.1 Reconstruction of the $X(3872)$ yield

A systematic Monte Carlo simulation on the $\pi^+\pi^- J/\psi$ final state invariant mass distribution has been carried out at each individual scan point. At every scan point, the invariant mass distribution is fitted using the $f_{M_{inv}}$ function. During the fit, the parameters such as the resonance mass and the ARGUS cutoff parameter $m_0$ (the phase space limit) were kept constant. The remaining floating fit parameters were:

- the number of signal events: $N_{SIG}$,
- the number of instrumental background events: $N_{BKG}$,
- the width of the Gaussian signal function: $\sigma_{SIG}$, and

- the ARGUS shape parameter: $c_{ARG}$.

Examples of generated $\pi^+\pi^- J/\psi$ invariant mass spectra fitted with $f_{M_{inv}}$ are shown in Figure 6.4. The spectra correspond to the resonance width of $1\,MeV$ and a signal to background ratio of 2. The top of each panel includes the corresponding center-of-mass energy at which the resonance scan point is perfomed.

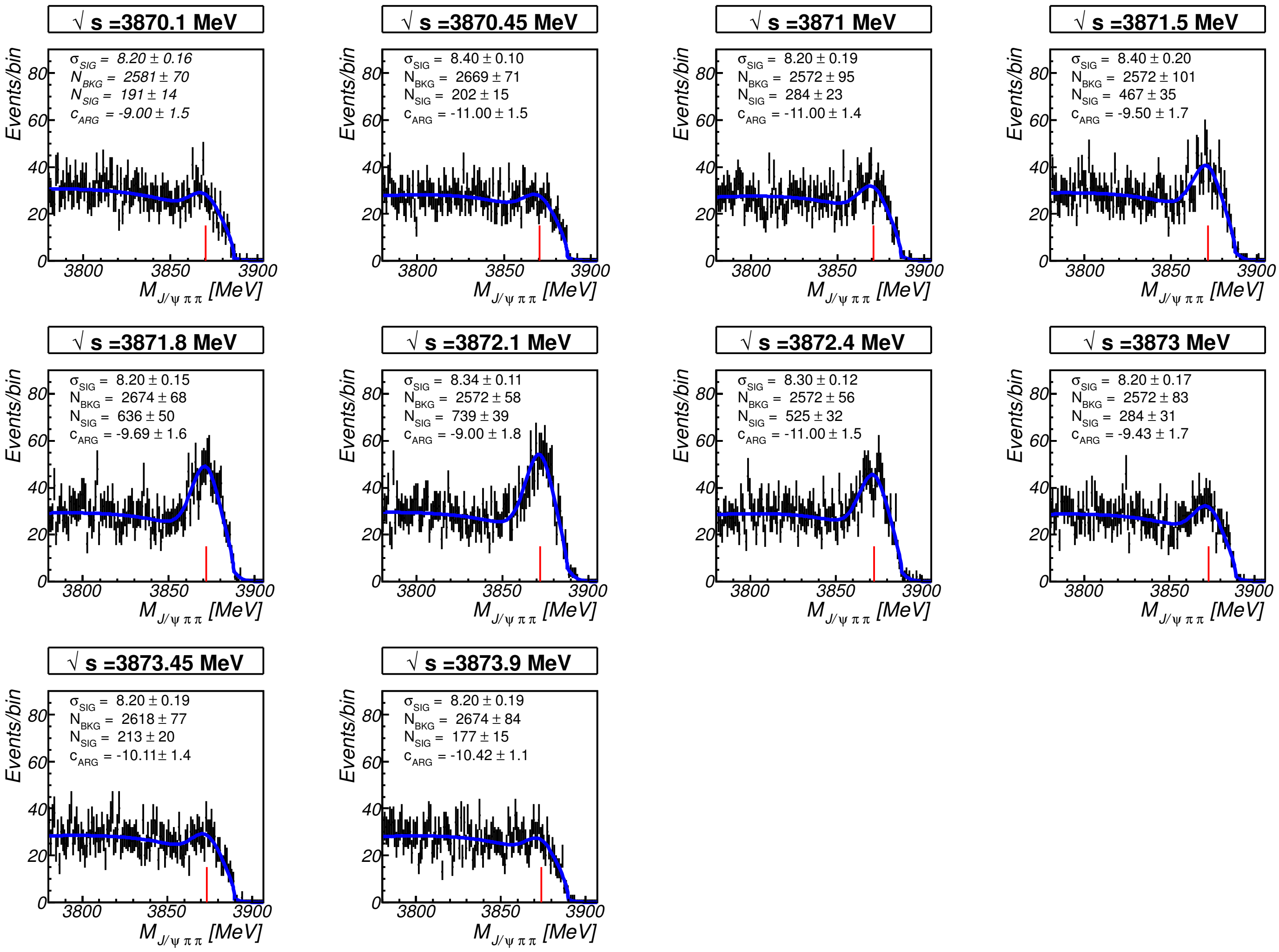


**Figure 6.4**: Final state invariant mass spectra at 10 scan points around the resonance mass of $3872\,MeV$. On each individual histogram, the vertical red line indicates the energy scan position and the blue curve is a fit to the distribution in Equation (6.4).

To account for the statistical fluctuation, the $M_{inv}$ spectra have been generated 1000 times at each scan point. The distribution of the fit values are plotted in Figure 6.5 for the $N_{SIG}$ parameter and in Figure 6.6 for its error $\sigma_{N_{SIG}}$. These figures correspond to the same simulation setup as in Figure 6.4, i.e. $\Gamma_{in} = 1\,MeV$ and $r_{SB} = 2$.

The reconstructed $X(3872)$ yield at a given center-of-mass energy, $\sqrt{s}$, corresponds to the mean values of $N_{SIG}$. The distributions of the reconstructed $N_{SIG}$ as a function $\sqrt{s}$ are shown

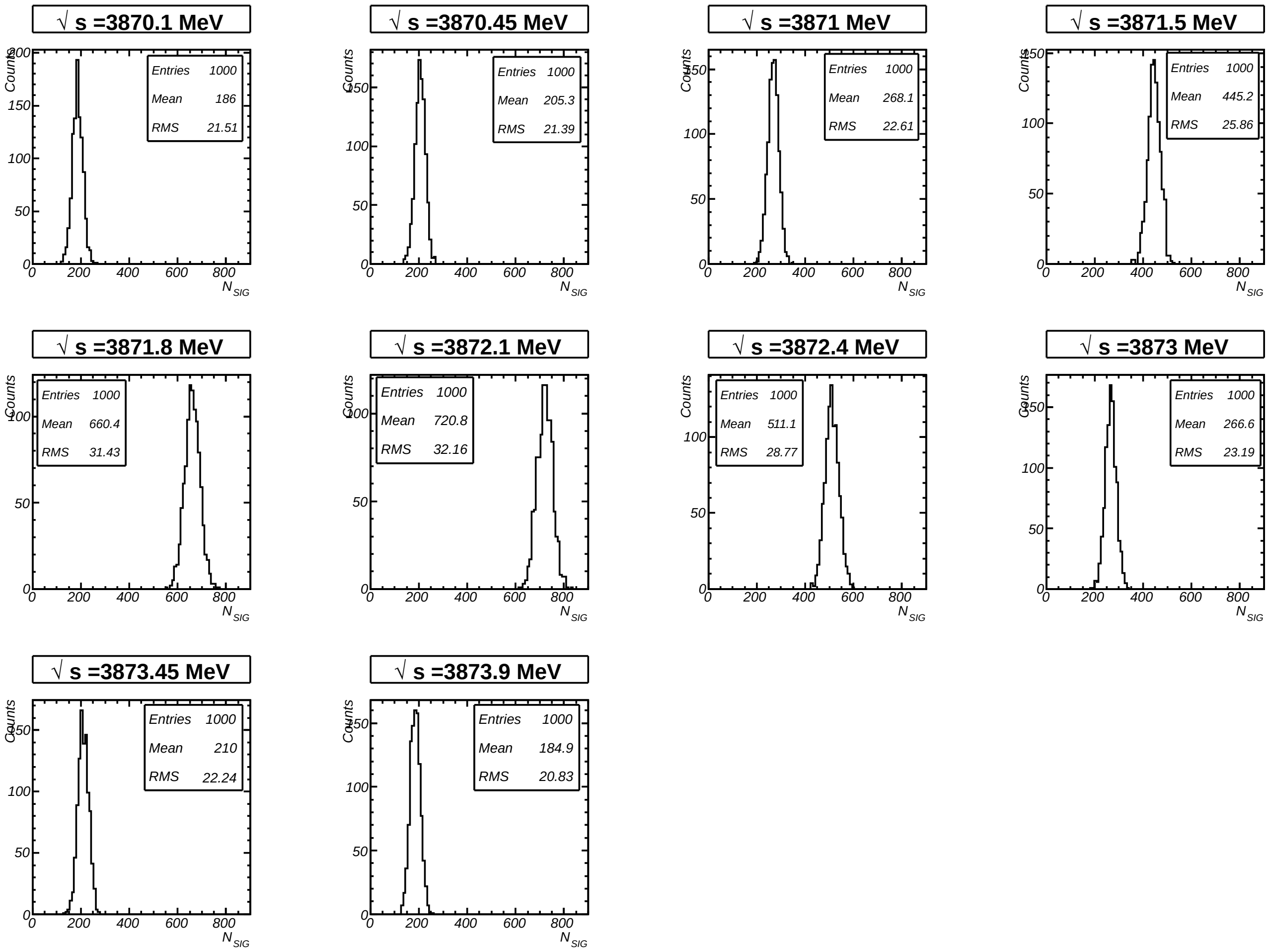

**Figure 6.5**: Distribution of the reconstructed number of signal event for 1000 Monte Carlo events at each of the 10 scan points corresponding to $\Gamma_{in} = 1\,MeV$ and $r_{SB} = 2$.

in Figure 6.7 for the three simulated resonance widths and a signal to background ratio of 2. On these plots, the vertical error bars are the measured errors on the reconstructed number of signal events, and the horizontal error bars are the center-of-mass resolutions that will be discussed in the next paragraph.

### Accuracy of the fit procedure

This section presents an analysis of the precision of the signal and background extraction procedure. The analysis was done by calculating the pull distribution for each fit parameter. The pull of a parameter $p$ is given by:

$$Pull_p = \frac{\Delta p}{\sigma_p}, \tag{6.15}$$

in which $\Delta p = p_{reco} - p_{in}$ where $p_{reco}$, $p_{in}$ are the reconstructed value and the input value, respectively, and $\sigma_p$ and the uncertainty on the reconstructed value of the parameter. A standard normal distribution of the pull indicates that the fit procedure works correctly.

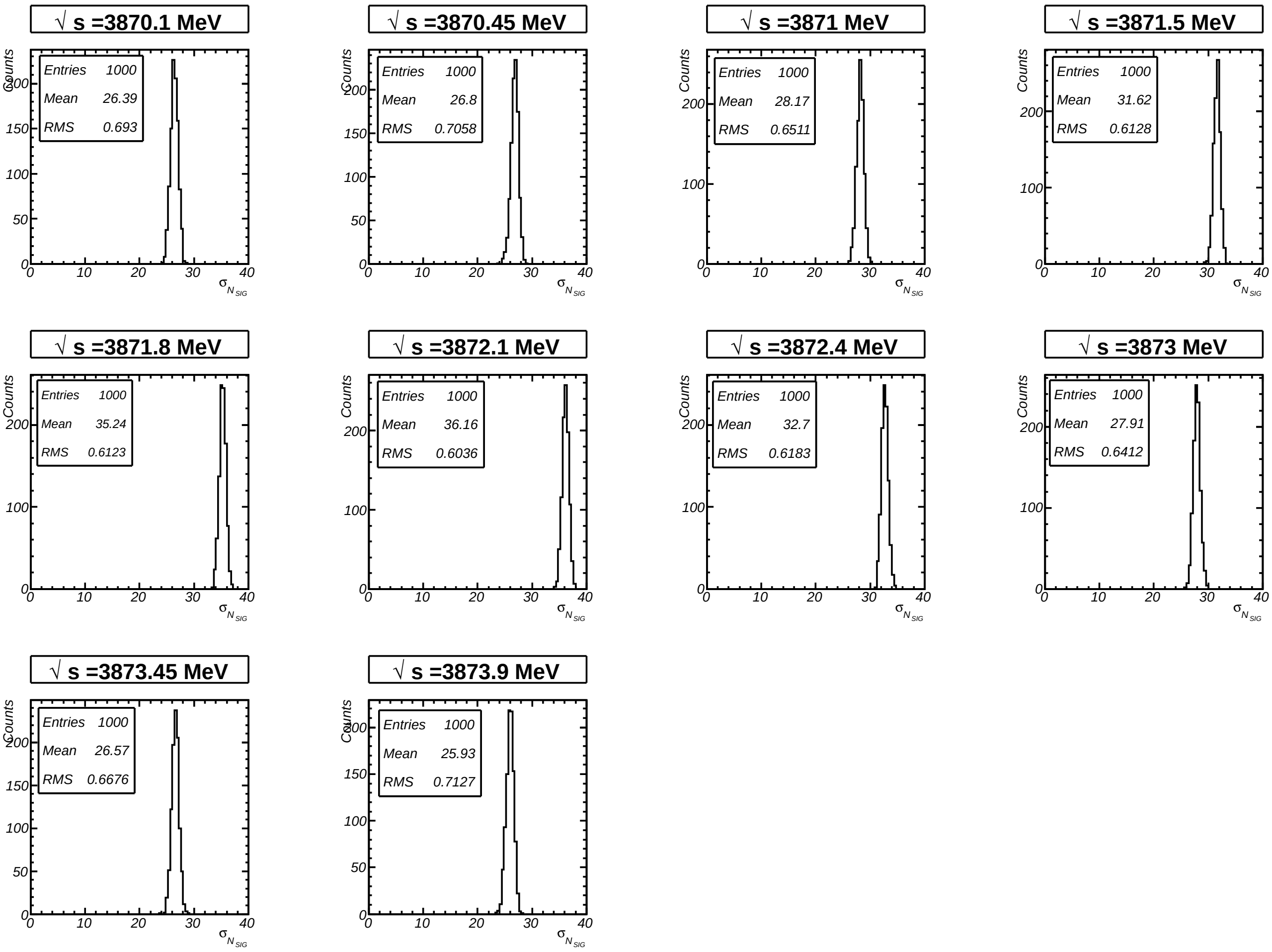


**Figure 6.6**: Distribution of the errors on the fitted number of signal for 1000 Monte Carlo events at each of the 10 scan points corresponding to $\Gamma_{in} = 1\,MeV$ and $r_{SB} = 2$.

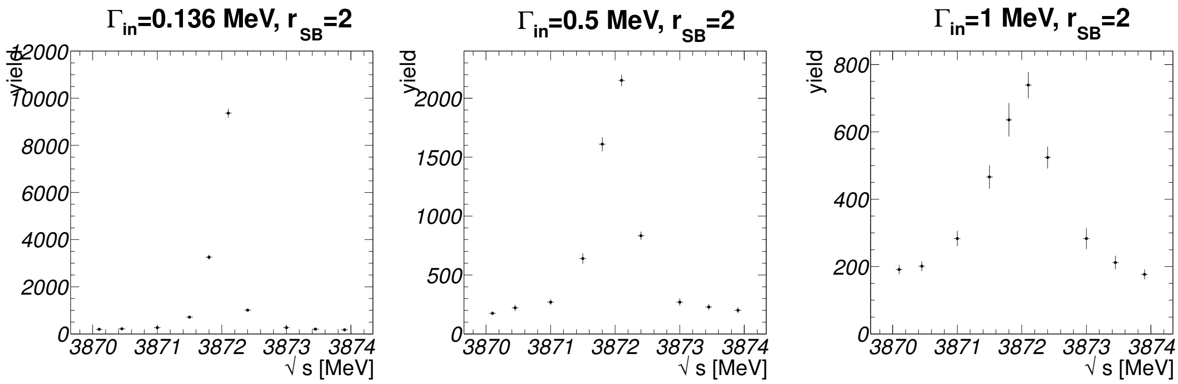


**Figure 6.7**: Reconstructed yield distribution of the $X(3872)$ meson as a function of the center-of-mass energy for the three input widths.

The pull distributions of the free parameters of the fit function are presented in Figure 6.8 for $\sqrt{s} = 3871.8\ MeV$ scan point. Gaussian fits are applied to each distribution. As it can be seen in the figure, the means and widths of the Gaussian distributions are close to the expected values of zero and one, respectively.

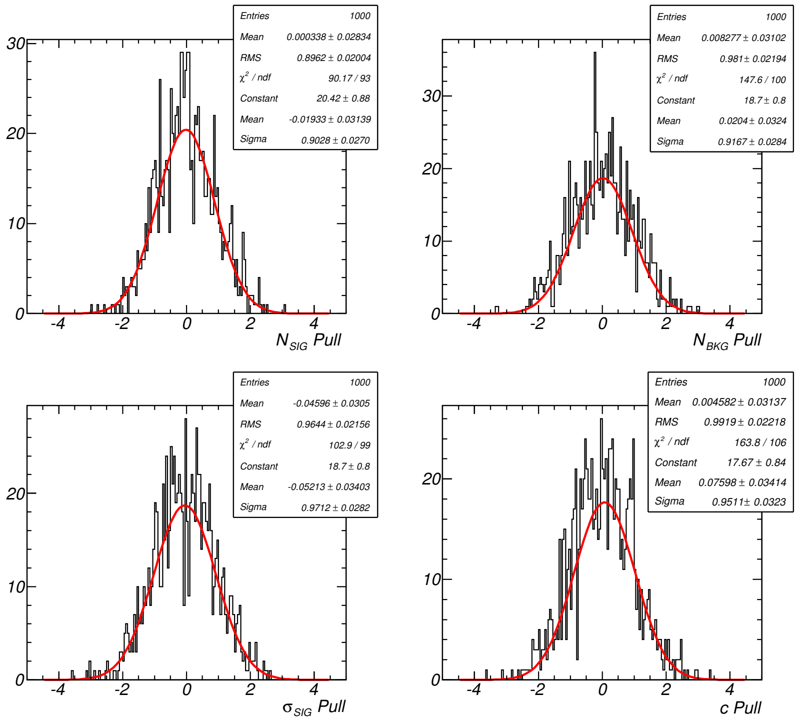


**Figure 6.8**: Pull distributions of the $N_{SIG}$, $N_{BKG}$, $\sigma_{SIG}$ and $c$ parameters of the $f_{M_{inv}}$ invariant mass fit function at $\sqrt{s} = 3871.8\ MeV$.

Furthermore, potential correlations between the fit parameters were investigated. The correlation coefficient $\rho_{ij}$ between the parameters $p_i$ and $p_j$ is expressed as:

$$\rho_{ij} = \frac{\sum_{k=1}^{n} (\Delta p_{i,k} - \bar{\Delta} p_i)(\Delta p_{j,k} - \bar{\Delta} p_j)}{(n-1)\sigma_{p_i}\sigma_{p_j}} . \tag{6.16}$$

where $n$ are the number of Monte Carlo events $\sigma_p$ is the fit error on the parameter $p$. The correlation between any two parameters can be seen through the scatter plots of the corresponding residuals. These plots are shown in Figure 6.9 for four involved fit parameters.

The correlation coefficients were calculated for all distributions and found to be about zero except for the $N_{SIG}$-$N_{BGK}$. Its value is about $-0.15$. This is because the $N_{SIG}$ and $N_{BGK}$ parameters were used as the weights on the sum of the two components function of the invariant mass generator function in Equation (6.4).

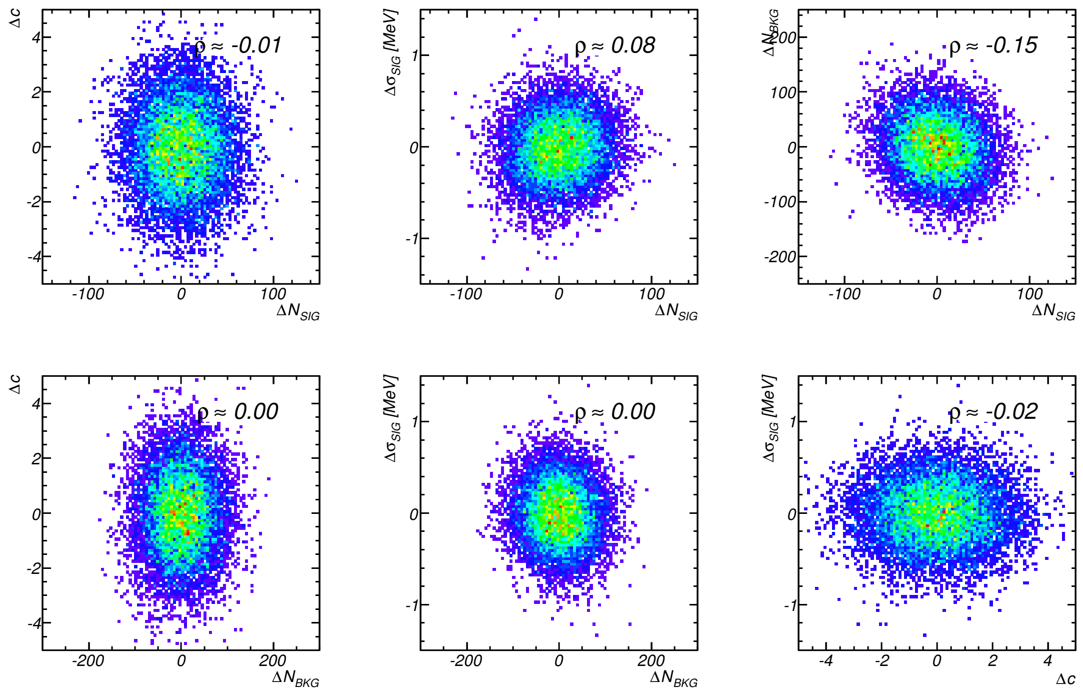


**Figure 6.9**: Scatter plots of the residuals showing the correlations between the fit parameters. For each individual plot, the correlation coefficient $\rho$ is printed on its upper right corner.

### 6.3.2 Mass and width determination

Since the mass and the width are incorporated in the expression of the cross section, its distribution as a function of $\sqrt{s}$ must be provided. The cross section distribution is determined from the reconstructed yield by using the relation (6.12) at each scan point. Using the same formula the uncertainty $\Delta\sigma$ on the cross section at $\sqrt{s}$ is:

$$\Delta\sigma = \left[\frac{1}{\mathcal{A}} \cdot \left(\frac{1}{\mathcal{L}^2} \cdot (\Delta N)^2 + \left(\frac{N}{\mathcal{L}^2}\right)^2 \cdot (\Delta\mathcal{L})^2\right)\right]^{1/2} \tag{6.17}$$

where $\mathcal{A} = \varepsilon \cdot f_{\mathcal{B}} \cdot T_{beam}$, $\Delta N$ and $\Delta\mathcal{L}$ are the uncertainties on the reconstructed count rate and on the integrated luminosity, respectively.

A fit to the cross section distribution gives the mass and the width of the $X(3872)$ meson. The fit function must consider the center-of-mass energy resolution. Therefore, the reconstructed cross section will be fitted with the line shape function $\sigma_{pdf}$ convoluted with $G_{beam}$ a Gauss describing the resolution function with $\sigma_{\sqrt{s}}$ width. The resulting function is thus:

$$(\sigma_{pdf} \otimes G_{beam})(\sqrt{s}') = \int_{-\infty}^{+\infty} \sigma_{pdf}(\sqrt{s}) \cdot G_{beam}(\sqrt{s}' - \sqrt{s}, \sigma_{\sqrt{s}}) \cdot d\sqrt{s}\,. \tag{6.18}$$

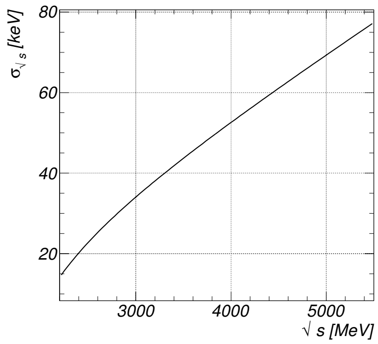


**Figure 6.10**: Resolution of $\sqrt{s}$ for the P̄ANDA high resolution mode.

### Center-of-mass energy resolution

The center-of-mass energy is related to the incident antiproton beam momentum by the following relation:

$$\sqrt{s} = \left[2m_p \cdot \left(m_p + \sqrt{p^2 + m_p^2}\right)\right]^{1/2} \tag{6.19}$$

where $m_p$ is the (anti)proton mass and $p$ is the nominal beam momentum. For the P̄ANDA beam momentum range, the center-of-mass energy is within the range of 2.3 to 5.5 $GeV/c^2$.

For a Gaussian distribution of the incident antiproton beam momentum with a spread of $\delta p$, the center-of-mass energy will follow a Gaussian distribution of $\sigma_{\sqrt{s}}$ width which is the center-of-mass energy resolution and computed as

$$\sigma_{\sqrt{s}} = \frac{m_p p^2}{\sqrt{p^2 + m_p^2}} \cdot \frac{1}{\sqrt{s}}.\delta p/p\,. \tag{6.20}$$

The variation of $\sigma_{\sqrt{s}}$ as a function of the beam energy is shown in Figure 6.10 for the P̄ANDA high resolution mode. One can note from this figure the nearly linear behavior of the $\sigma_{\sqrt{s}}$ variation for the beam energy relevant for P̄ANDA and in particular in the vicinity of $\sqrt{s} = 3872\,MeV$, it can be approximated as a constant of $\sigma_{\sqrt{s}} \sim 50.4\,keV$.

### Cross section fit process

The fit procedure minimized the $\chi^2-$function with respect to the mass and the width of the resonance. Two-dimensional histograms of $\chi^2$ for various scans mass and width values are shown in Figure 6.11 for the three input widths corresponding to the simulation setup described previously. The minimization procedure found several local minima with respect to the mass which explains the non-parabolic variation of the projected $\chi^2-$function in the $y-$axis over the considered mass range for these plots. The global minimum corresponds to the reconstructed values of the mass and the width of the $X(3872)$.

The reconstructed cross section distributions with which the above scans have been performed are plotted in Figure 6.12. The horizontal error bars corresponds to the center-of-mass resolution calculated from Equation (6.20). The vertical error bars are the uncertainties $\Delta\sigma$ computed by the relation (6.18).

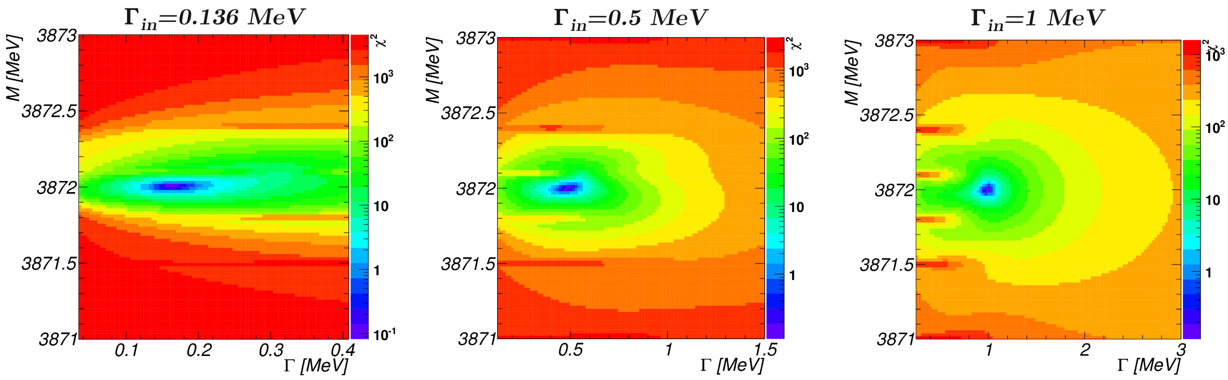


**Figure 6.11**: The $\chi^2$ variation as functions of the mass and the width parameters for the three input widths.

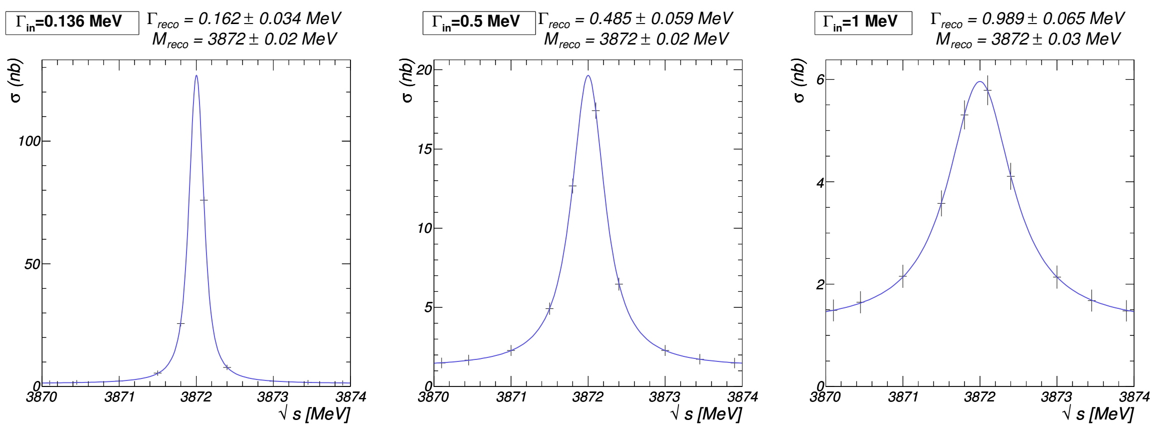


**Figure 6.12**: Reconstructed cross section distributions corresponding to the three input widths for $\Delta\mathcal{L} = 0$ and $r_{SB} = 2$. The blue curve corresponds to the fit function given by Equation (6.18).

These simulations are based on the assumptions of the zero relative luminosity i.e. $\Delta\mathcal{L} = 0$ and $r_{SB} = 2$. However, $r_{SB}$ is unknown. Its effect on the extraction of the mass and the width of the resonance was investigated by assuming other values. Also the $\Delta\mathcal{L} = 0$ assumption represents only an idealistic situation. Actually, the integrated luminosity will not be measured with perfect accuracy. The studies influence of these two parameters on the measurements of the width and the mass were performed separately and are presented in the subsequent sections.

### 6.3.3 Effect of the signal to background ratio

Apart from the simulations using $r_{SB} = 2$ which have been described so far, several values of the signal to background ratio were considered. In these simulations, the relative error on the luminosity was set to $\Delta\mathcal{L} = 0$. The distributions of the reconstructed cross section corresponding to $r_{SB} = 0.5$, 1 and 5 are shown in Figures 6.13 to 6.15.

For a small value of $r_{SB}$ the signal is merged with the instrumental background. As a result, $N_{SIG}$ and thus the cross section, are extracted with large error bars. The reconstruction of the

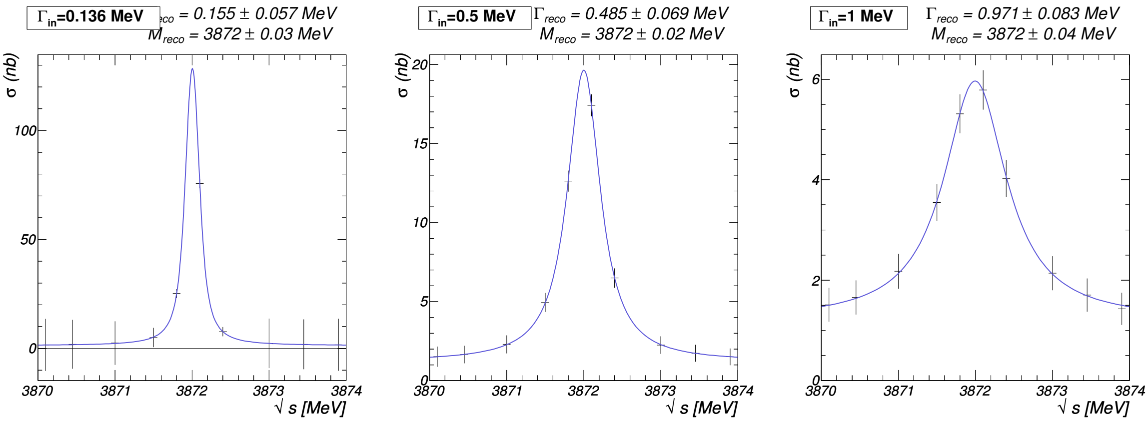


**Figure 6.13**: Reconstructed cross section distributions for the three input widths and $r_{SB} = 0.5$.

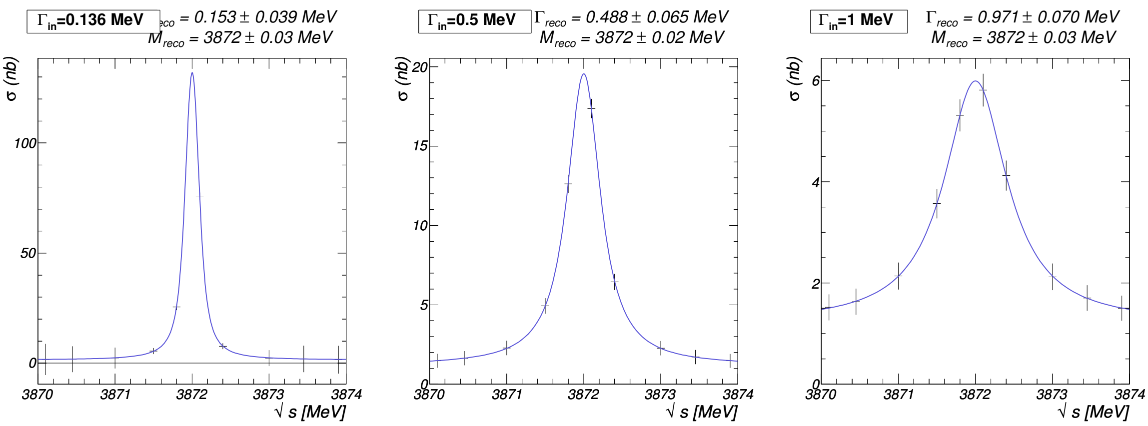


**Figure 6.14**: Reconstructed cross section distributions for the three input widths and $r_{SB} = 1$.

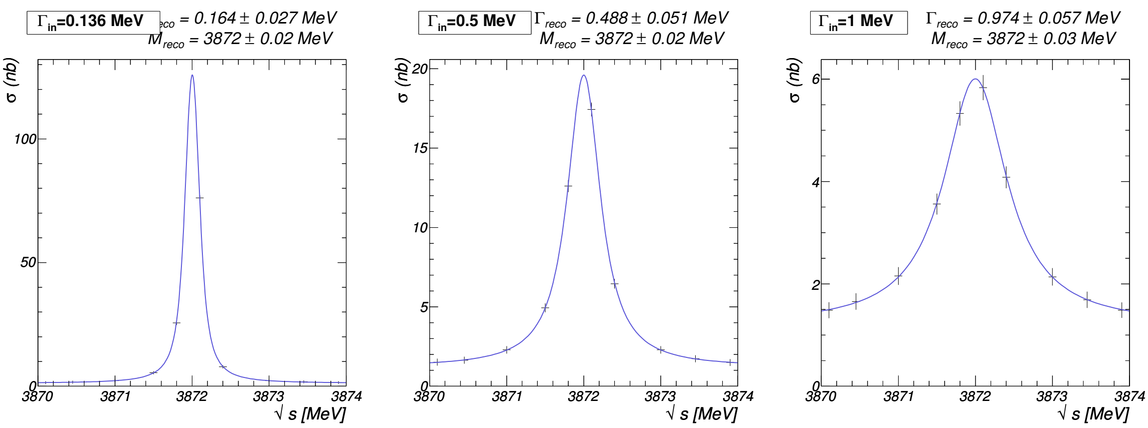


**Figure 6.15**: Reconstructed cross section distributions for the three input widths and $r_{SB} = 5$.

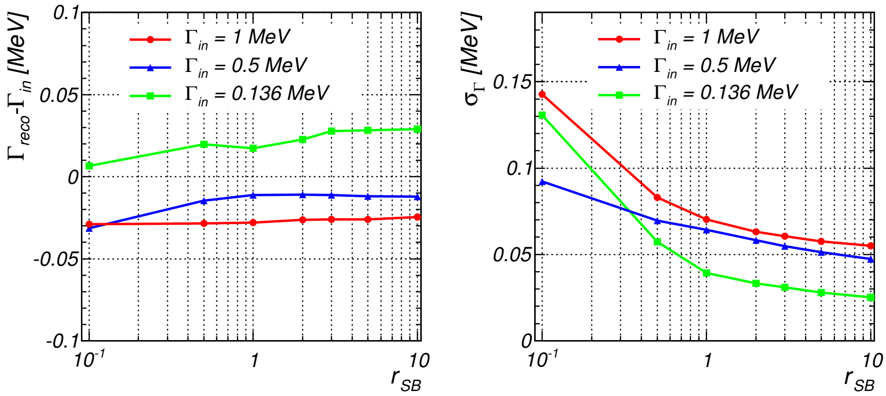


**Figure 6.16**: Variations of the reconstructed width $\Gamma_{reco}$ and its respective precision $\sigma_\Gamma$ as a function of the signal to background ratio $r_{SB}$ with $\frac{\Delta\mathcal{L}}{\mathcal{L}} = 0\%$.

mass seems not to be influenced by $r_{SB}$. However, the width was affected. In particular, as expected the precision on which the width is reconstructed deteriorates when the $r_{SB}$ decreases.

The variations of the reconstructed width and its precision are summarized in Figure 6.16. The worst precision obtained corresponds to the simulation setup $\Gamma_{in} = 0.136\,MeV$ and $r_{SB} = 0.1$ in which a couple of points near the resonance mass contribute into the fit.

### 6.3.4 Effect of the luminosity uncertainty

The effect of finite uncertainty of the integrated luminosity $\frac{\Delta\mathcal{L}}{\mathcal{L}}$ on the extracted mass and width has been has studied for $\frac{\Delta\mathcal{L}}{\mathcal{L}} = 3\%$, 5% and 10% at each individual scan point. $\frac{\Delta\mathcal{L}}{\mathcal{L}} = 3\%$ is the design goal of the LuMo, $\frac{\Delta\mathcal{L}}{\mathcal{L}} = 10\%$ corresponds to the precision by which HESR will measure the luminosity and $\frac{\Delta\mathcal{L}}{\mathcal{L}} = 5\%$ corresponds to the case in which the design precision of the LuMo will not be reached.

The plots showing the distributions of the reconstructed cross sections as a function of $\sqrt{s}$ for all three assumed input widths and luminosity errors mentioned above are presented in Figures 6.17 to 6.19 for $r_{SB} = 2$.

As expected, the relative uncertainty of the luminosity mainly deteriorates the precision of the width measurement. The precision on the mass measurement is not strongly affected. However, the changes are more pronounced for the bigger input widths. In fact, the luminosity acts as a scaling factor on the cross section distribution. But due to the relative high value of the cross section near the resonance mass, the case of $\Gamma_{in} = 0.136\,MeV$ is less affected by the relative uncertainty of the luminosity. The measured width and its precision are shown in Figure 6.20 for different values of $\frac{\Delta\mathcal{L}}{\mathcal{L}}$.

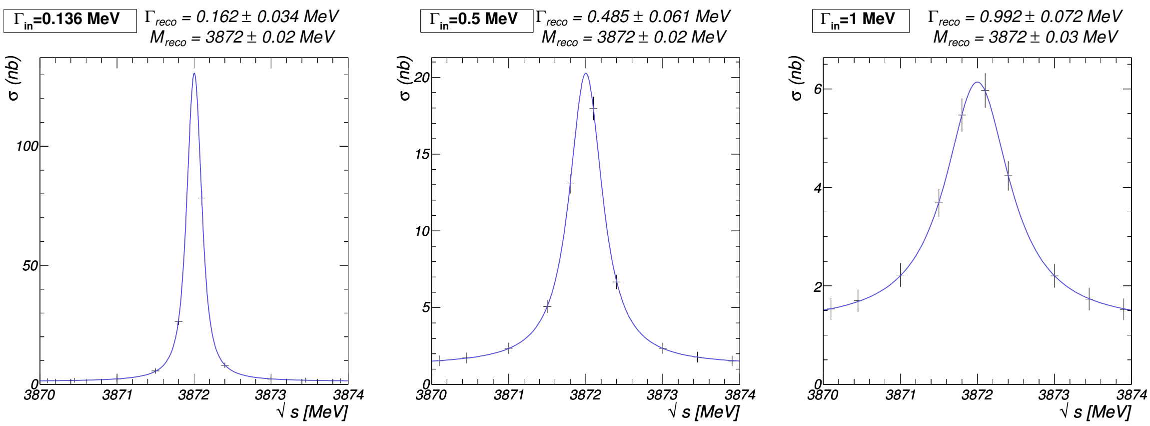


**Figure 6.17**: Reconstructed cross section distributions for the three input widths and $\frac{\Delta\mathcal{L}}{\mathcal{L}} = 3\%$.

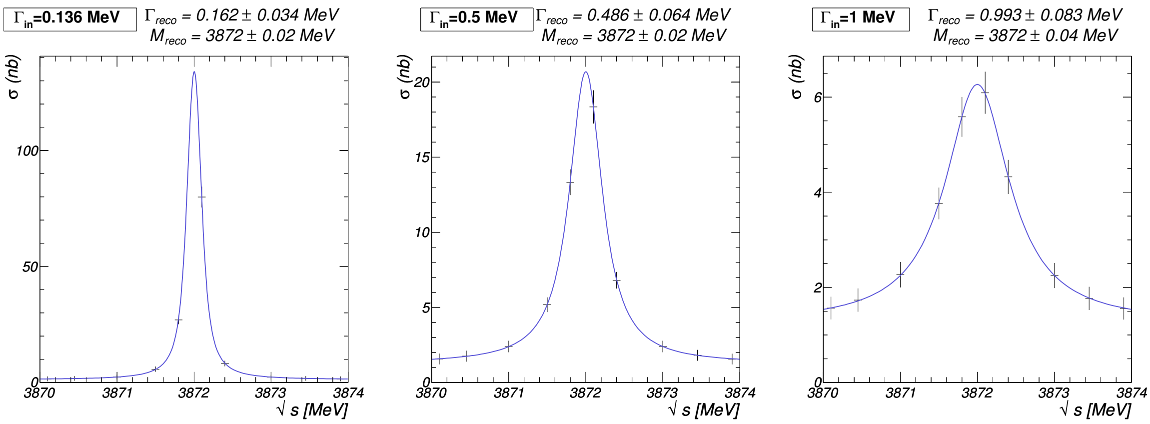


**Figure 6.18**: Reconstructed cross section distributions for the three input widths and $\frac{\Delta\mathcal{L}}{\mathcal{L}} = 5\%$.

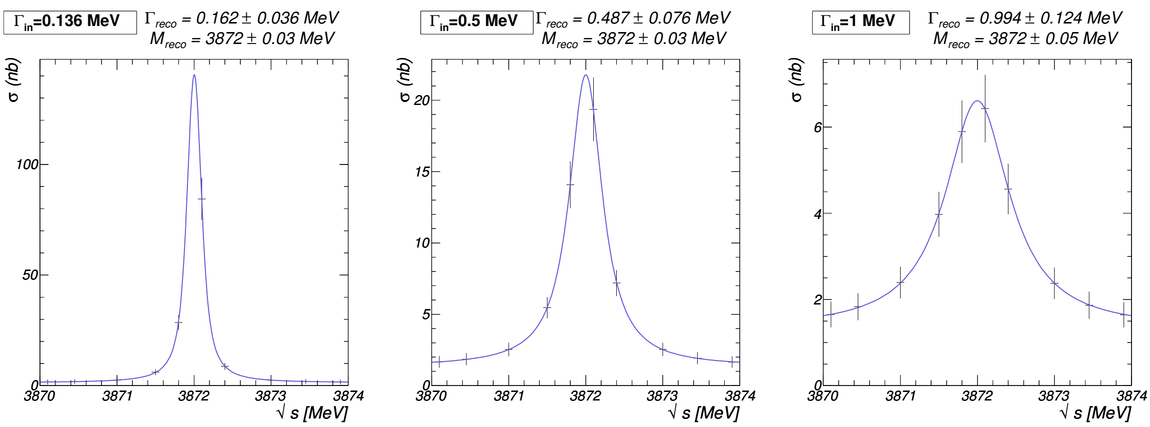


**Figure 6.19**: Reconstructed cross section distributions for the three input widths and $\frac{\Delta\mathcal{L}}{\mathcal{L}} = 10\%$.

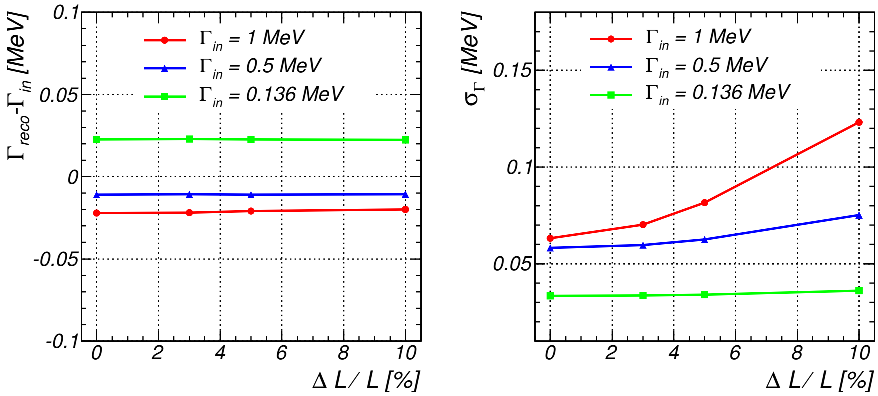


**Figure 6.20**: Variations of the reconstructed width $\Gamma_{reco}$ and its respective precision $\sigma_\Gamma$ as a function of the relative uncertainty of the luminosity measurement at each individual scan point $\frac{\Delta\mathcal{L}}{\mathcal{L}}$ with $r_{SB} = 2$.

## 6.4 Summary and discussion

Simulation studies on the mass and the width measurements of the $X(3872)$ meson were described in this chapter taking into account the $\bar{\text{P}}$ANDA detector and the HESR accelerator specifications. The resonance scan method has been used to perform the measurement. The studies were based on the more conservative estimate of the $\pi^+\pi^- J/\psi$ final state production cross section assuming the $\chi_{c1}(2P)$ charmonium interpretation of the $X(3872)$ state [CM08]. Other interpretations with higher cross section will have a higher precision to measure the width.

The reconstruction considers that $\bar{\text{P}}$ANDA is running in the high resolution mode. The effect of the signal to background ratio $r_{SB}$ and the error on the relative luminosity measurement $\frac{\Delta\mathcal{L}}{\mathcal{L}}$ at each scan point on the mass and the width measurements have been investigated. The mass was almost perfectly reconstructed with a precision of an order of $20\,keV$ independently on the simulation parameters setup. However, the width and its precision were most effected by the value of $r_{SB}$ and $\frac{\Delta\mathcal{L}}{\mathcal{L}}$. As expected, $\sigma_\Gamma$ is better for higher $r_{SB}$. Also it gets worse as $\frac{\Delta\mathcal{L}}{\mathcal{L}}$ increases.

As a conclusion, a statistically based method was used to estimate the performance of $\bar{\text{P}}$ANDA on the mass and width reconstruction of the $X(3872)$ meson. The method presents a strong dependence on the signal to background ratio parameter.

In this study, the width of the signal was determined by the detector resolution. However, the instrumental background shape model is an assumption. That needs further investigation to obtain a more realistic estimation of $r_{SB}$. This can be done by performing a full detector simulation using an adequate event generator. Detailed knowledge of the signal to background ratio is needed for a precise measurement of the mass and the width of the $X(3872)$ state and further details of the line shape, and thus a better understanding of the nature of the resonance.

CHAPTER 7

# Conclusion and Outlook

The upcoming FAIR facility at Darmstadt will host the $\bar{\text{P}}$ANDA experiment which is dedicated to some of the most relevant topics predicted by QCD in the low momentum transfer region. It will perform very precise spectroscopy of hadronic systems resulting from $\bar{p}p$ annihilation in the charmonium mass range, corresponding to an antiproton beam momentum range of 1.5 to $15\,GeV/c$. In particular the phase space cooled HESR antiproton beam will allow unprecedented precision for the mass and width determination of narrow states such as charmonium-like and open charm states, by using the resonance scan technique. This technique will not be effective to extract the properties of a given state unless the luminosity is known with high precision.

For this purpose a detector was designed to monitor the luminosity. It will provide the cross section normalization for a given process by using the $\bar{p}p$ elastic scattering as the reference channel. The conceptual design of the detector is based on the reconstruction of the scattered antiproton track in the Coulomb-nuclear interference region. Due to some constraints imposed by the $\bar{\text{P}}$ANDA detector and the HESR accelerator, the LuMo will be located between $z = +10$ and $+13\,m$ downstream of the interaction point. It will consist of four layers of double-sided silicon strip sensors. Two sensor shapes are proposed by the collaboration: rectangular and trapezoidal. This thesis was focused on the implementation of the LuMo with rectangular sensors. The strip sensors have $50\,\mu m$ pitch, with a dimension of $2\,cm \times 5\,cm \times 300\,\mu m$ each, arranged radially from the beam axis. The first plane is located at $z = +10.5\,cm$ and the subsequent planes are separated by $20\,cm$. Therefore, the detector covers a polar angle region from about 2.8 to $7.5\,mrad$.

The LuMo has been implemented inside the PandaRoot framework with which Monte Carlo performance studies were carried out. This results in the determination of the spatial resolution and angular resolution of the telescope. The detector resolution depends mainly on the small angle scattering and the charge diffusion process. The charge diffusion was implemented at the digitization level using a Gaussian charge smearing of $8\,\mu m$ width. This improved the average spatial resolution from $14\,\mu m$ to $8\,\mu m$. The track reconstruction algorithm used the first two planes to define the polar angle and led to an angular resolution proportional to $1/p_{beam}$ of $0.5\,mrad$ and $0.05\,mrad$ at $p_{beam} = 1.5$ and $15\,GeV/c$, respectively. The effect of external parameters such as the HESR beam emittance and the magnetic field has been investigated. The magnetic field effects only the acceptance of the detector but the beam emitance deteriorates both the acceptance and the angular resolution of the detector. Using the expected properties of the HESR antiproton beam at the interaction region, a lower limit of the angular resolution of $0.2\,mrad$ at $p_{beam} = 15\,GeV/c$ was obtained.

A simulation of the luminosity measurement was performed using the DPM event generator. Basically, it consists of the reconstruction of the $\bar{p}p$ elastic scattering $t-$spectrum and a fit to it with the corresponding differential cross section formula. Using the same parameter values as the input ones, a systematic uncertainty on the luminosity due to the intrinsic detector resolution, the beam emittance and the magnetic field, of 4.53% and 1.33% were obtained at the lowest and the highest beam momenta, respectively. The influence of the uncertainty on the cross section parameters ($\rho$, $b$ and $\sigma_{tot}$) was investigated which led to the determination of the correlation between these parameters and the luminosity. The study of the effect of the $\bar{p}p$ inelastic scattering, expected to be a source of background, showed that it is negligible because of its low rate in the detector due to the high discriminating power of the dipole magnetic field. The statistical uncertainty was determined to be less than 1% after about 25 seconds experimental running time. The results of this study showed that a precision of about 3% on the measurement of the absolute luminosity is feasible.

The implemented algorithms were checked using the measured data from the beam test of a prototype of a silicon strip tracking station perfomed with the COSY proton beam at 0.893 and 2.95 $GeV/c$. The two different detector setups adopted during the beam test also allow to investigate the cluster behavior dependence on the beam momentum and the incident angle. The width of the charge smearing was determined by comparing the $\eta-$distribution obtained by the measured data with the simulation with the same setup parameters (noise and threshold values) as the beam test. For a 300 $\mu m$ thick silicon sensor $\sigma_{diff} = 8 - 10\,\mu m$ was measured. The geometry calibration was performed using the HIP method allowing to achieve the alignment of the sensors after 3 iterations. The detector resolution at a virtual plane placed in the center between the second and third modules was determined to be similar to the one obtained from the simulation and about 750 $\mu m$ and 150 $\mu m$ at $p_{beam} = 0.893$ and 2.95 $GeV/c$, respectively, for Setup 1 and 126 $\mu m$ at normal incidence for Setup 2. The global efficiency of the tracking station was about 95%.

The last chapter of this thesis was dedicated for the development of a strategy to measure the width and mass of the $X(3872)$ state. The study was based on the $\chi_{c1}(2P)$ interpretation of the state. The line shape was taken to be a Breit-Wigner resonance with a constant physical background. Additional instrumental background following the ARGUS function was used at each individual scan point. The measurements were performed considering the HESR high resolution mode. The effect of the signal to (instrumental) background ratio $r_{SB}$ and the error on the relative luminosity measurement $\frac{\Delta\mathcal{L}}{\mathcal{L}}$ at each scan point on the mass and width measurements have been investigated separately for $\frac{\Delta\mathcal{L}}{\mathcal{L}} = 0\%$ and $r_{SB} = 2$, respectively. As expected, the precision on the width measurement worsens as $r_{SB}$ decreases and best precision is then achieved for $r_{SB} = 10$ with $\sigma_\Gamma/\Gamma_{in} < 1\%$ for $\Gamma_{in} = 0.5$ and $1\,MeV/c^2$ and $\sigma_\Gamma/\Gamma_{in} \sim 2\%$ for $\Gamma_{in} = 136\,keV/c^2$. These resolutions were almost reached already with $r_{SB} = 2$. The uncertainty of the luminosity determination does not affect the resolution of the small width state ($\Gamma_{in} = 136\,keV/c^2$) and causes a deterioration of those of larger widths by a factor of 1.5 for $\frac{\Delta\mathcal{L}}{\mathcal{L}} = 10\%$. Here it has to be noted that with the design luminosity precision of the LuMo ($\frac{\Delta\mathcal{L}}{\mathcal{L}} = 3\%$) the best precision on the width measurement is achieved.

Further optimization of the LuMo are still under study as well for the geometry as for the electronic readout system. The latter is undertaken by the LuMo Mainz group. As seen in this thesis, the most influential factors on the measurement of luminosity are the detector intrinsic resolution, the HESR beam emittance and the differential cross section parameters $\rho$, $b$ and $\sigma_{tot}$. According to the track reconstruction algorithm, the angular resolution of the

LuMo depends strongly on the spatial resolution at the two first detector plane. Indeed, a main issue on the geometry optimization is the reduction the effect of multiple scattering, especially at the first plane, to achieve better resolution especially for low beam momenta. This could be done by decreasing the thickness of the sensors at the first plane and/or by reducing the distance between the two first planes.

The knowledge of $\rho$, $b$ and $\sigma_{tot}$ is also crucial to the precision with which the luminosity will be determined. To measure these parameters with high accuracy, the HESR Day-One Experiment was designed. It will measure these parameter in an independent way. An overview of this experiment was given in this thesis, more details can be found in [X+11]. In the near future, the apparatus will be tested by a COSY proton beam that will assess its performance.

Appendix A

# List of Figures

Appendix B

# List of Tables

Appendix C

# List of Abbreviations

| | |
|---|---|
| **ADC** | Analog-to-Digital Conveter |
| **CERN** | Centre Européen pour la Recherche Nucléaire |
| **CDF** | Collider Detector at Fermilab |
| **COSY** | Cooler Synchrotron |
| **CR** | Collector Ring |
| **DPM** | Dual Parton Model |
| **EMC** | Electromagnetic Calorimeter |
| **FAIR** | Facility for Antiproton and Ion Research |
| **FIFO** | First In First Out |
| **FPGA** | Field Programmable Gate Array |
| **FWHM** | Full Width at Half Maximum |
| **GCS** | Global Coordinate System |
| **GSI** | Gesellschaft für Schwerionenforschung |
| **HESR** | High Energy Storage Ring |
| **HISKP** | Helmholtz Institut für Strahlen- und Kernphysik |
| **LGS** | Local Coordinate System |
| **LHC** | Large Hadron Collider |
| **LQCD** | Lattice Quantum Chromodynamics |
| **LuMo** | Luminosity Monitor |
| **$\bar{\text{P}}$ANDA** | Antiproton Annihilation at Darmstadt |
| **PCB** | Printed Circuit Board |
| **PDG** | Particle Data Group |
| **p.d.f** | Probability Density Function |
| **QCD** | Quantum Chromodynamics |
| **RF** | Resonant Frequencies |
| **SM** | Standard Model |
| **STT** | Straw Tube Tracker |
| **TOF** | Time-Of-Flight |

# Bibliography


[A$^+$74] I. Ambats et al. Systematic Study of $\pi^{\pm}p$, $K^{\pm}p$, $pp$, and $\bar{p}p$ Forward Elastic Scattering from 3 to 6 $GeV/c$. *Phys. Rev. D*, 9:1179–1209, 1974.

[A$^+$90] H. Albrecht et al. Search for Hadronic $b \to u$ Decays. *Phys. Lett. B*, 241:278–282, 1990.

[A$^+$94a] F. Abe et al. Measurement of Small Angle Antiproton-Proton Elastic Scattering at $\sqrt{s} = 546$ and $1800GeV$. *Phys. Rev. D*, 50:5518–5534, 1994.

[A$^+$94b] C. Augier et al. Measurement of the Proton-Antiproton Total Cross Section at the $S\bar{p}pS$ Collider by a Luminosity Dependent Method. *CERN/PPE 94-190*, 1994.

[A$^+$96] T.A. Armstrong et al. Precision Measurements of Antiproton-Proton Forward Elastic Scattering Parameters in the 3.7 to 6.2 $GeV/c$ Region. *Phys. Lett. B*, 385:479–486, 1996.

[A$^+$03] S. Agostinelli et al. G4- A Simulation Toolkit. *Nucl. Instr.and Meth. A*, 506:250–303, 2003.

[A$^+$04a] V.M. Abazov et al. Observation and Properties of the $X(3872)$ Decaying to $J/\psi\pi^+\pi^-$ in $p\bar{p}$ Collisions at $\sqrt{s} = 1.96\,TeV$. *Phys. Rev. Lett*, 93(162002), 2004.

[A$^+$04b] D. Acosta et al. Observation of a Narrow State $X(3872) \to J/\psi\pi^+\pi^-$ in $p\bar{p}$ Collisions at $\sqrt{s} = 1.96\,TeV$. *Phys. Rev. Lett*, 93(072001), 2004.

[A$^+$05a] B. Abe et al. Experimental Constraints on the Possible $J^{PC}$ Quantum Number of the $X(3872)$. *hep-ex*, (0505038), 2005.

[A$^+$05b] K. Abe et al. Evidence for $X(3872) \to \gamma J/\psi$ and Sub-Threshold Decay $X(3872) \to \omega J/\psi$. *hep-ex*, (0505037), 2005.

[A$^+$05c] B. Aubert et al. Study of the $B^- \to J/\psi K^-\pi^+\pi^-$ Decay and Measurement of $B^- \to X(3872)K^-$ Branching Fraction. *Phys. Rev. D*, 71(071103), 2005.

[A$^+$06] D. Abulancia et al. Measurement of the Dipion Mass Spectrum in $X(3872) \to J/\psi\pi^+\pi^-$ Decays. *Phys. Rev. Lett*, 96(102002), 2006.

[A$^+$08a] B. Aubert et al. Study of $B \to X(3872)K$, with $X(3872) \to J/\psi\pi^+\pi^-$. *Phys. Rev. D*, 77(111101), 2008.

[A$^+$08b] B. Aubert et al. Study of Resonances in Exclusive $B$ Decays to $\bar{D}^{(*)}D^{(*)}K$. *Phys. Rev. D*, 77(011102), 2008.

[A$^+$09a] T. Aaltonen et al. Precision Measurement of the $X(3872)$ Mass in $J/\psi\pi^+\pi^-$ Decays. *hep-ex*, (0906.5218), 2009.

[A$^+$09b] B. Aubert et al. Evidence for the $X(3872) \to \psi(2S)\gamma$ in $B^{\pm} \to X(3872)K^{\pm}$ Decays and a Study of $B \to c\bar{c}\gamma K$. *hep-ex*, (0809.0042), 2009.

[ATU09] M. Al-Turany and F. Uhlig. Status of the FairRoot Simulation and Analysis Framework. *GSI Scientific Report 2008*, page 236, 2009.

[B+69] D. Birnbaum et al. $\bar{p}p$ Elastic Scattering at 8 and 16 $GeV/c$. *Phys. Rev. Lett.*, 23:663–666, 1969.

[B+75] H. Braun et al. Analysis of Two-Prong Events in Antiproton-Proton Interactions at 5.7 $GeV/c$. *Nucl. Phys. B*, 95:481–502, 1975.

[B+87] C. Baglin et al. $J/\psi$ Resonance Formation and Mass Measurement in Antiproton-Proton Annihilations. *CERN-EP*, pages 87–30, 1987.

[B+02] S. Bagnasco et al. New Measurements of the Resonance Parameters of the $\chi_{c0}(1^3P_0)$ State of Charmonium. *Phys. Lett. B*, 533:237–242, 2002.

[Bel83] E. Belau. Charge Collection in Silicon Strip Detectors. *Nucl. Instr. Meth.*, 214:253–260, 1983.

[BG03] T. Barnes and S. Godfrey. Charmonium Options for the $X(3872)$. *hep-ph*, (0311162), 2003.

[Bic88] H. Bichsel. Straggling in Thin Silicon Detectors. *Rev. Mod. Phys.*, pages 663–699, 1988.

[BL07] E. Brateen and M. Lu. Line Shape of the X(3872). *Phys. Rev. D*, 76(094028), 2007.

[BP02] V. Barone and E. Predazzi. *High-Energy Particle Diffraction.* Springer, Berlin, 2002.

[C+03] S.K. Choi et al. Observation of a Narrow Charmoniumlike State in Exclusive $B^\pm \to K^\pm\pi^+\pi^- J/\psi$ Decays. *Phys. Rev. Lett*, 91(262001), 2003.

[CM08] G.Y. Chen and J.P. Ma. Production of X(3872) at $\bar{\text{P}}$ANDA . *Phys. Rev. D*, 77(097501), 2008.

[CP04] F.E. Close and P.R. Page. The $D^{*0}\bar{D}^0$ Threshold Resonance. *Phys. Rev. B*, 578:119–123, 2004.

[D+67] V. Domingo et al. Elastic Scattering of 2.7 $GeV/c$ Antiprotons on Protons. *Phys. Lett. B*, 24:642–644, 1967.

[dAS+10] P. del Amo Sanchez et al. Evidence of the Decay $X(3872) \to J/\psi\omega$. *hep-ex*, (1005.5190), 2010.

[DF03] A. Das and T. Ferbel. *Introduction to Nuclear and Particle Physics.* World Scientific, Berlin, 2003.

[DL02] L. Demortier and L. Lyons. Everything You Always Wanted To Know About Pulls. (5776), 2002.

[EVE] The ROOT Event Display Webpage. `http://root.cern.ch/root/html/GRAF3D_EVE_Index.html`.

[F$^+$63] K.J. Foley et al. Antiproton and Kaon Elastic Scattering at High Energies. *Phys. Rev. Lett*, 11:503–506, 1963.

[F$^+$65a] T. Ferbel et al. Pion Production and the One-Particle-Exchange Mechanism in $\bar{p}p$ Interactions at $3-4BeV/c$. *Phys. Rev.*, 138:B1528–B1536, 1965.

[F$^+$65b] K.J. Foley et al. Elastic Scattering of Proton, Antiprotons, Negative Pions and Negative Kaons at High Energies. *Phys. Rev. Lett.*, 15:45–50, 1965.

[F$^+$07] A. Fontana et al. Track Following in Dense Media and Inhomogeneous Magnetic Fields. *PANDA Report PV/01*, 2007.

[F$^+$08] A. Fontana et al. Use of GEANE for Tracking in Virtual Monte Carlo. *J. Phys.: Conf. Ser.*, (119 032018), 2008.

[FAI] The FAIR Webpage. www.fair-center.de.

[FRO] The FairRoot Webpage. http://cbmroot.gsi.de/.

[G$^+$06] G. Gokhroo et al. Observation of a Near-Threshold $D^0\bar{D}^0\pi^0$ Enhancement in $B \to D^0\bar{D}^0\pi^0K$ Decays. *Phys. Rev. Lett*, 97(162002), 2006.

[G$^+$08] A.S Galoyan et al. Parametrization of the $\bar{p}p$ Elastic Scattering Differential Cross Section between $2\,GeV/c \le P_{lab} \le 16\,GeV/c$. *hep-ex*, (0809.3804), 2008.

[GEA93] GEANT-Detector Description and Simulation Tool. *CERN Program Library Long Writeup, W5013*, 1993.

[Gia10] P. Gianotti. The $\bar{\text{P}}$ANDA Experiment at FAIR. *Nucl Phys A*, 835:96–101, 2010.

[GO08] S. Godfrey and S.L. Olsen. The Exotic XYZ Charmonium-like Mesons. *hep-ph*, (0801.3867), 2008.

[GP03] A.S. Galoyan and A. Polanski. Simulation of Antiproton-Nucleus Interactions in the Framework of the UrQMD Model. *hep-ph*, (0304196), 2003.

[GU05] A. Galoyan and V.V. Uzhinsky. New Monte Carlo Implementation of Quark-Gluon-String Model of the $\bar{p}p$ -Interactions. *AIP Conf. Proc.*, 796, LEAP'05:79–82, 2005.

[H$^+$84a] S. Hancock et al. Energy Loss and Energy Straggling of Protons and Pions in Momentum Range 0.7 to 115 $GeV/c$. *Phys. Rev. A*, 28-2, 1984.

[H$^+$84b] S. Hancock et al. Energy Loss Distributions for Single Particles and Several Particles in a Thin Silicon Absorber. *Nucl. Instr. and Meth. B*, 1:16–22, 1984.

[H$^+$07] C. Hanhart et al. Reconciling the $X(3872)$ with the Near-Threshold Enhancement in the $D^0\bar{D}^{*0}$ Final State. *Phys. Rev. D*, 76(034007), 2007.

[HŎ3] I. Hšivnàčová. The Virtual Monte Carlo. In *Proc. of Computing in High Energy and Nuclear Physics, La Jolla, California*, 2003.

[HŎ8] I. Hšivnàčová. The Geant4 Virtual Monte Carlo. *J. Phys.: Conf. Ser.*, (119 032035), 2008.

[I+91] V. Innocent et al. GEANE: Average Tracking and Error Propagation Package. *CERN Program Library Long Writeup, W5013-E*, 1991.

[J+75] P. Jenni et al. Measurement of the Real Part of the Forward Amplitude in $\bar{p}p$ Elastic Scattering. *Nucl. Phys. B*, 94:1–20, 1975.

[J+77] P. Jenni et al. $\bar{p}p$ and $pp$ Forward Elastic Scattering between 4 and 10 $GeV/c$. *Nucl. Phys. B*, 129:232–252, 1977.

[Jam98] F. James. MINUIT: Function Minimization and Error Analysis. *CERN Program Library Long Writeup, D506*, 1998.

[Jon01] L Jones. APV25-S1 User Guide Version 2.2. 2001. http://www.te.rl.ac.uk/med.

[JR10] V. Jha and J. Ritman. Vertex and Kinematic Fitting for the $\bar{\text{P}}$ANDA Experiment. *DAE Symp. Nucl. Phys.*, (55), 2010.

[K+68] T. Kitagaki et al. $\bar{p}p$ Elastic Scattering at 6.9 $GeV/c$. *Phys. Rev. Lett.*, 21:175–177, 1968.

[K+03] V. Karimäki et al. Sensor Alignment by Tracks. *CMS CR*, 022, 2003.

[L+06] A. Lehrach et al. Beam Performance and Luminosity Limitations in the High-Energy Storage Ring (HESR). *Nucl. Instr. Meth. A*, 561(2):289–296, 2006.

[L+08] Y.R. Lui et al. Is $X(3872)$ Really a Molecule State? *Eur. Phys. J. C.*, 56:63–73, 2008.

[L+09] X. Lui et al. $X(3872)$ and Other Possible Heavy Molecular States. *Eur. Phys. J. C.*, 61:411–428, 2009.

[Lan01] D.J. Lange. The EvtGen Particle Decay Simulation Package. *Nucl. Instr. Meth. A*, 462:152–155, 2001.

[Li05] B.A. Li. Is $X(3872)$ a Possible Candidate as Hybrid Meson? *Phys. Lett. B*, 605:306–310, 2005.

[M+05] L. Maiani et al. Diquark-Antidiquark States with Hidden or Open Charm and the Nature of X(3872). *Phys. Rev. D*, 71(014028), 2005.

[Mai11] R. Maier. The High-Energy Storage Ring (HESR). *Proc. of Particle Accelerator Conf., New York*, THOCN2, 2011.

[MPR07] L. Maiani, A.D Polosa, and V. Riquer. Indications of a Four-Quark Structure for the X(3872) and X(3876) Particles from Recent Belle and BaBar Data. *Phys. Rev. Lett.*, 99(0182003), 2007.

[N+10] N. Nakamura et al. Review of Particle Physics. *Particle Data Group*, 2010. pdg.lbl.gov/.

[PAN] The $\bar{\text{P}}$ANDA Experiment Webpage. http://www-panda.gsi.de/.

[pC05] The $\bar{\text{P}}$ANDA Collaboration. Strong Interaction Studies with Antiprotons, Technical Progress Report for $\bar{\text{P}}$ANDA . 2005.

[pC09a] The $\bar{\text{P}}$ANDA Collaboration. Physics Performance Report for $\bar{\text{P}}$ANDA , Strong Interaction Studies with Antiprotons. *hep-ex*, (0903.3905), 2009.

[pC09b] The $\bar{\text{P}}$ANDA Collaboration. Solenoid and Dipole Spectrometer Magnet, Strong Interaction Studies with Antiprotons, Techincal Design Report for the $\bar{\text{P}}$ANDA . 2009.

[Pei93] A. Peisertm. Silicon Microstrip Detector. *Instr. HEP*, 9:1–81, 1993.

[PPE10] G.V. Pakhlova, P.N. Pakhlov, and S.I. Eidel'man. Exotic Charmonium. *Phys. Usp.*, 53:219–241, 2010.

[R+07] D. Reistad et al. Calculations on High-Energy Electron Cooling in the HESR. *Proc. of COOL, Bad Kreuznach*, MOA2C05:44–47, 2007.

[Ran84] P. G. Rancoita. Silicon Detectors and Elementary Particle Physics. *J. Phys. G: Nucl. Phys.*, 10:299–319, 1984.

[RHO] Rho: A Set of Analysis Tools for ROOT. `http://savannah.fzk.de/websites/hep/rho/`.

[ROO] ROOT: An Object-Oriented Data Analysis Framework. `http://root.cern.ch/drupal/`.

[Sch07] F. Scheck. *Quantum Physics*. Springer, Berlin, 2007.

[Set05] K.K Seth. An Alternative Interpretation of $X(3872)$. *Phys. Lett. B*, 612:1–4, 2005.

[T+95] S. Trokenheim et al. A $\bar{p}p$ Luminosity Monitor for Fermilab Experiment E760. *Nucl. Inst. Meth.A*, 355:308–319, 1995.

[T04] N.A. Törnqvist. Isospin Breaking of the Narrow Charmonium State of Belle at 3872 $MeV$ as a Deuson. *Phys. Lett. B*, 590:209–215, 2004.

[T+11] A. Täschner et al. High Density Cluster Jet Target for Storage Ring Experiments. *physics.ins-det*, (1108.2653), 2011.

[Tre02] J. Treis. *Development and Operation of a Novel PC-based High Speed Beam Telescope for Particle Tracking Using Double Sided Silicon Microstrip Detectors*. PhD Dissertation, Universität Bonn, Physikalisches Institut, August 2002.

[UG02] V.V. Uzhinsky and A.S. Galoyan. Cross Sections of Various Processes in $\bar{p}p$ - Interactions. *hep-ph*, (0212369), 2002.

[VMC] The ROOT Virtual Monte-Carlo Webpage. `http://root.cern.ch/drupal/content/vmc`.

[W+10] T. Würschig et al. Setup of a Test-Station for Double-Sided Silicon Microstrip Detectors. *PANDA -MVD Note*, 005, 2010.

[WW11] T.H. Wang and G.L. Wang. Radiative E1 Decays of $X(3872)$. *hep-ph*, (1006.3363), 2011.

[X+10] H. Xu et al. Study of the Effect of Solenoid Field on the $\bar{\text{P}}$ANDA Luminosity Monitor. *DPG Frühjahrstagung Bonn*, (HK 36.66), 2010.

[X+11] H. Xu et al. Antiproton-Proton Elastic Scattering as Day-1 Experiment at HESR. *DPG Frühjahrstagung Münster*, (HK 46.3), 2011.

[Zie06] V. Ziemann. On Pellet Target Luminosity Modulation. *Nucl. Instr. Meth. A*, 556:641–643, 2006.

# Acknowledgments

With my enthusiasm the deepest and most sincere I would like to thank everyone who directly or indirectly, helped, supported and encouraged me to the realization of this thesis.

I desire to express my deep gratitude to my supervisor, Prof. James Ritman, for his excellent guidance, advice, patience and willingness to always help not only on my work but also in my life in general. I am very thankful to Prof. Ulrich Wiedner for kindly accepting to be my second advisor.

I am also grateful to Dr. Tobias Stockmanns and Dr. Huagen Xu for their precious comments and advices, their strong support and also their help in improving the content of this thesis and Dr. Andrei Sokolov who initiates me with PandaRoot.

I would like to thank PD Dr. Andreas Lehrach for providing a lot of helpful information concerning the HESR accelerator, Dr. Marius Mertens for many fruitful discussions about the resonance scan method and Mr. Günter Sterzenbach for being always available to fix my frequent problems of computer and Matthias Röder for his help for the submission of the thesis.

I acknowledge Mrs. Sandra Müller for handling all administrative issue and her own way to contribute to the completion of this thesis, Mr. Herbert Jäger for his friendly assistance during my first days at Jülich, the FZJ-IKP1 $\bar{\text{P}}$ANDA group for all valuable discussions and suggestions and FZJ-IKP1 team for the hearty welcome.

I am thankful to the $\bar{\text{P}}$ANDA LuMo Group and the HISKP Bonn $\bar{\text{P}}$ANDA MVD Group for their precious collaboration.

I thank my father and my family who, despite the distances, always supports me throughout my thesis.

I deserve a special mention to the one who accompanies me day and night.

Last but not least, thanks be to God for my life. May your name be exalted, honored, and glorified.

*This work is partially supported by German Academic Exchange Service (DAAD) and Forchungszentrum Jülich.*

# Tsitohaina Hary Randriamalala

## PERSONAL

Born on 11.04.1981 in Antananarivo Madagascar
Address : Kopernikusstrasse 33, D-52428 Jülich
Nationality : Malagasy
Married

## EDUCATION

**Scientific baccalaureat**, *July 1998*
Lycee Jules Ferry Faravohitra - Antananarivo

**CAPEN in Physics and Chemistry**, *December 2003*
Ecole Normale Superieure - University of Antananarivo

**DEA in Physics**, *March 2006*
Faculty of Sciences - University of Antananarivo

## PhD PROJECT

Conceptual Design of the PANDA Luminosity Monitor
and Reconstruction Strategy to Measure the Width
of the $X(3872)$ State, *October 2007 - December 2011*
Institut für Kernphysik - Forchungszentrum Jülich